# The Evolution of Halo Properties Through Binary Major Mergers

by

Justin Marchioni

A thesis
presented to the University of Waterloo
in fulfillment of the
thesis requirement for the degree of
Master of Science
in
Physics

Waterloo, Ontario, Canada, 2024

© Justin Marchioni 2024

## Author's Declaration

I hereby declare that I am the sole author of this thesis. This is a true copy of the thesis, including any required final revisions, as accepted by my examiners.

I understand that my thesis may be made electronically available to the public.

## Abstract

Galaxy clusters are massive, gravitationally bound objects composed of a large population of galaxies. Each of these galaxies occupies a dark matter halo and collectively the cluster has its own extended halo. Cluster halos can be described by many structural properties including their mass, concentration, shape, spin, and asymmetry. These properties, among others, can be used as proxies to constrain cosmology. The issue with galaxy clusters is that they are still assembling at the present-day. These clusters primarily grow through mergers, where smaller systems coalesce to form larger ones. If the mass ratio between the two merging components is sufficiently large (i.e. 3:1 or below), this is known as a major merger. The effect of major mergers is to significantly redistribute the matter distribution in the host system. This leads to pronounced fluctuations in the cluster's structural properties during the merger, making measurements of these properties hard to interpret. Therefore, accurately predicting how cluster properties vary during mergers is important in order to use them as a cosmological tool.

In this thesis, we use simulations to study how the structure of remnant systems evolves during mergers. These simulations consider the merger of two isolated components, each represented by truncated Navarro-Frenk-White (NFW) profiles. We find that mergers produce oscillations in structural parameters for both the overall remnant and the host system. For example, the host halo's concentration experiences one of two types of responses to the satellite's motion depending primarily on the pericentric passage distance of the orbit. Given the simulation results, we present a semi-analytic model for the evolution of structure in remnant systems due to isolated, binary mergers. The model consists of two components, a treatment for the orbital evolution of the satellite and a prescription for changes in the host halo's potential. This second component is often neglected when modeling satellite orbits in minor mergers. Interestingly, we find that adding a host halo response model has little impact on the orbital evolution of the satellite and its mass loss. In contrast, this model must be incorporated in order to accurately predict how the remnant's structure changes after the satellite first passes pericentre. While our model generally works well at replicating the median concentration for the first two orbits, it is unable to recreate any of the remnant's anisotropy properties (i.e. shape, spin, and asymmetry). Overall, our results provide a framework for analyzing the response of cluster halo properties to mergers in more realistic scenarios.

**Acknowledgements**

First, I would like to thank my advisor Dr. James Taylor for his advice, patience, and encouragement. I am grateful for the guidance and mentorship you have provided me over the last three years. Next, I would like to thank the members of my advisory committee Dr. Michael Balogh and Dr. Brian McNamara for their comments and suggestions that undoubtedly improved this thesis. All the other members of the astrophysics group at the University of Waterloo should be recognized as well for their contributions to my education.

Lastly, and most importantly, I would like to acknowledge the support of my family. To my parents, grandparents, brothers, and cats, thank you so much for all that you have given me. This would not have been possible without all of you.

# Table of Contents

**Author's Declaration** ii

**Abstract** iii

**Acknowledgements** iv

**List of Figures** viii

**List of Tables** xii

**1 Introduction** 1

1.1 ΛCDM and Dark Matter Halos . . . . . 1

1.2 Galaxy Clusters and Their Properties . . . . . 6

1.3 Mergers . . . . . 9

1.4 Motivation . . . . . 13

1.5 Outline of the Thesis . . . . . 15

**2 Simulations** 16

2.1 *N*-body Codes . . . . . 16

2.2 Initial Conditions . . . . . 17

2.2.1 Generating Halos . . . . . 18

2.2.2 Placing the Satellite on its Orbit . . . . . 23

2.2.3 Distribution of Orbital Parameters . . . 25
2.3 Measuring Properties of the Simulations . . . 29
2.3.1 Satellite Position and Mass . . . 29
2.3.2 Concentration and Scale Radius . . . 35
2.3.3 Shape . . . 42
2.3.4 Spin . . . 44
2.3.5 Asymmetry . . . 47
2.4 Fiducial Simulation Set . . . 49

**3 Orbital Evolution Model** **51**
3.1 Primary Components . . . 51
3.1.1 Satellite Mass and Unbound Mass . . . 51
3.1.2 Dynamical Friction . . . 56
3.1.3 Reduced Mass . . . 59
3.2 Evaluating the Model . . . 61
3.3 Machine Learning to Predict Model Parameters . . . 71

**4 Disruption of the Central Halo** **77**
4.1 Semi-analytic Model to Describe the Response . . . 77
4.1.1 Classifying the Response Types . . . 77
4.1.2 Modeling the Central Halo Scale Radius . . . 83
4.2 Orbital Model Predictions . . . 88
4.3 Remnant System Structural Property Predictions . . . 93
4.3.1 Concentration and Scale Radius . . . 96
4.3.2 Other Parameters . . . 101

**5 Conclusion** **113**

5.1 Summary of the Thesis . . . 113

5.2 Discussion . . . 114

5.2.1 Potential Applications . . . 117

5.2.2 Issues and Shortcomings . . . 121

5.3 Future Work . . . 123

**References** **125**

**APPENDICES** **137**

**A Supplemental Simulation Results** **138**

A.1 Evolving the Central Halo in Isolation . . . 138

A.2 Fitting NFWT Parameters Using a Fixed Truncation Scale $y_d$ . . . 140

A.3 Investigating the Central Halo Response Type Separation Using Other Initial Conditions . . . 144

A.4 Measuring Orbits for a Point Mass Satellite with Various Mass Resolutions 146

A.5 Measuring Changes in Structural Properties for Different Satellite Masses . 148

**B Supplemental Modeling Results** **159**

B.1 Static Orbit in a Spherically Symmetric Potential . . . 159

B.2 Testing Integration Schemes for Evaluating Ordinary Differential Equations (ODEs) . . . 163

B.3 Rejection Sampling to Generate NFWT Profiles . . . 167

B.4 Model Predictions for the Fiducial Simulations . . . 169

# List of Figures


1.1 Simulated large-scale structure of the Universe . . . . . 3
1.2 Composite image of the Bullet Cluster . . . . . 10
1.3 Oscillations in structural parameters due to mergers . . . . . 12
1.4 $S_8$ tension and breaking the $\Omega_m$-$\sigma_8$ degeneracy . . . . . 14

2.1 Example initial halo positions . . . . . 19
2.2 Comparing NFW and NFWT density profiles . . . . . 21
2.3 Orbital property distributions for the simulations . . . . . 27
2.4 Example merger between the satellite and central halo in a simulation . . . 30
2.5 Unbinding time of satellite halo particles in a set of simulations . . . . . 32
2.6 Satellite position and mass measurements for a set of simulations . . . . . 34
2.7 Example remnant system circular velocity profiles in a simulation . . . . . 36
2.8 Central halo and remnant system scale radius for a set of simulations . . . 39
2.9 Central halo and remnant system NFWT parameters for a set of simulations 40
2.10 Central halo and remnant system shape parameters for a set of simulations 43
2.11 Central halo and remnant system spin parameters for a set of simulations . 46
2.12 Central halo and remnant system asymmetry for a set of simulations . . . 48

3.1 Satellite density profiles considering the bound, unbound, and total components for a set of simulations . . . . . 55
3.2 Model and simulation dynamical friction deceleration for a set of simulations 57

3.3 Diagram illustrating the two-body problem . . . . . 60
3.4 Model and simulation motion of the satellite in the orbital plane for a set of simulations . . . . . 65
3.5 Model and simulation satellite radial separation for a set of simulations . . 66
3.6 Model and simulation satellite mass loss for a set of simulations . . . . . 67
3.7 Modeled satellite radial separation neglecting certain components . . . . . 70
3.8 Model parameters vs. initial conditions for all simulations . . . . . 72
3.9 XGBoost model predictions vs. initial conditions for the training and test sets . . . . . 75

4.1 Classifying the central halo response into two types . . . . . 78
4.2 Drawing a plane using the initial conditions to classify the central halo response 80
4.3 Predictions for the central halo response types from the SVM derived plane 82
4.4 Median central halo response for both types . . . . . 84
4.5 Predictions for the central halo response model parameters from the scaling relations . . . . . 85
4.6 Model and simulation central halo scale radius for a set of simulations . . . 87
4.7 Model and simulation motion of the satellite in the orbital plane for a set of simulations . . . . . 89
4.8 Model and simulation satellite radial separation for a set of simulations . . 90
4.9 Model and simulation satellite mass loss for a set of simulations . . . . . 91
4.10 Effect of the transferred $M_{\rm ub}$ fraction on the remnant system scale radius . 95
4.11 Model and simulation remnant system scale radius for a set of simulations 97
4.12 Model and simulation remnant system concentration for a set of simulations 98
4.13 Median remnant system scale radius and concentration for all simulations . 100
4.14 Model and simulation remnant system minor-to-major axis ratio for a set of simulations . . . . . 102
4.15 Model and simulation remnant system minor-to-intermediate axis ratio for a set of simulations . . . . . 103

4.16 Model and simulation remnant system asymmetry for a set of simulations . 104
4.17 Ellipse unbound mass model remnant system shape parameters and asymmetry . . . 108
4.18 Ellipse unbound mass model remnant system scale radius . . . 109
4.19 Simulation remnant system shape parameters and asymmetry neglecting certain components . . . 111

5.1 Remnant system properties after the merger vs. select initial conditions for all simulations . . . 116
5.2 Remnant system concentration and its correlation with other parameters . 119
5.3 Remnant system concentration maximum change vs. its overall change . . 120

A.1 Testing the stability of the central halo scale radius . . . 139
A.2 Remnant system NFWT parameters using a fixed truncation scale $y_d$ . . . 141
A.3 Remnant system scale radius estimated from the peak circular velocity . . 143
A.4 Anti-correlation between the scale radius and truncation scale . . . 144
A.5 Testing the central halo response classification using other initial conditions 145
A.6 Simulation satellite orbit and radial separation for different particle mass resolutions . . . 147
A.7 Effect of the satellite mass on its orbit . . . 149
A.8 Effect of the satellite mass on its radial separation . . . 150
A.9 Effect of the satellite mass on its mass loss . . . 151
A.10 Effect of the satellite mass on the central halo scale radius . . . 152
A.11 Effect of the satellite mass on the remnant system scale radius . . . 153
A.12 Effect of the satellite mass on the remnant system concentration . . . 154
A.13 Effect of the satellite mass on the remnant system minor-to-major axis ratio 155
A.14 Effect of the satellite mass on the remnant system minor-to-intermediate axis ratio . . . 156
A.15 Effect of the satellite mass on the remnant system spin . . . 157
A.16 Effect of the satellite mass on the remnant system asymmetry . . . 158

B.1 Leapfrog integration scheme . . . . . 164
B.2 Example orbit in an NFW potential . . . . . 165
B.3 Relative changes in orbital energy and angular momentum for various integration schemes . . . . . 166
B.4 Comparing the initial mass profiles from rejection sampling to ICICLE . . 168
B.5 Model predictions for all properties in the simulation $\xi 1\,\eta 2\,\epsilon 2\,T1$ . . . . . 170
B.6 Model predictions for all properties in the simulation $\xi 2\,\eta 2\,\epsilon 2\,T1$ . . . . . 171
B.7 Model predictions for all properties in the simulation $\xi 3\,\eta 2\,\epsilon 2\,T1$ . . . . . 172
B.8 Model predictions for all properties in the simulation $\xi 4\,\eta 2\,\epsilon 2\,T1$ . . . . . 173
B.9 Model predictions for all properties in the simulation $\xi 2\,\eta 1\,\epsilon 2\,T1$ . . . . . 174
B.10 Model predictions for all properties in the simulation $\xi 2\,\eta 3\,\epsilon 3\,T1$ . . . . . 175
B.11 Model predictions for all properties in the simulation $\xi 2\,\eta 1\,\epsilon 1\,T1$ . . . . . 176
B.12 Model predictions for all properties in the simulation $\xi 2\,\eta 2\,\epsilon 3\,T1$ . . . . . 177
B.13 Model predictions for all properties in the simulation $\xi 1\,\eta 2\,\epsilon 2\,T2$ . . . . . 178
B.14 Model predictions for all properties in the simulation $\xi 2\,\eta 2\,\epsilon 2\,T2$ . . . . . 179
B.15 Model predictions for all properties in the simulation $\xi 3\,\eta 2\,\epsilon 2\,T2$ . . . . . 180
B.16 Model predictions for all properties in the simulation $\xi 4\,\eta 2\,\epsilon 2\,T2$ . . . . . 181
B.17 Model predictions for all properties in the simulation $\xi 2\,\eta 1\,\epsilon 1\,T2$ . . . . . 182
B.18 Model predictions for all properties in the simulation $\xi 2\,\eta 3\,\epsilon 2\,T2$ . . . . . 183
B.19 Model predictions for all properties in the simulation $\xi 2\,\eta 2\,\epsilon 1\,T2$ . . . . . 184
B.20 Model predictions for all properties in the simulation $\xi 2\,\eta 3\,\epsilon 3\,T2$ . . . . . 185

# List of Tables

2.1 Summary of the initial conditions for the fiducial set. The columns list (1) the simulation name, (2) the mass ratio, (3) the relative energy, (4) the circularity, (5) the radial-to-total velocity ratio, (6) the total-to-virial velocity ratio, (7) the time to pericentre, (8) the pericentric passage distance, and (9) the class of central halo response. The simulations listed in bold are a subset of the fiducial set used for select plots. Note that the radial-to-total velocity ratio is negative since we require the satellite's radial velocity to point towards the central halo for them to merge. . . . . 50

3.1 Summary of the hyperparameters calibrated for training the XGBoost regression model. The columns list (1) the hyperparameter, (2) the values investigated for a given hyperparameter, and (3) their optimal values. . . . 73

3.2 Median percent difference between the XGBoost model predictions and the values of the parameters when calibrated directly from the simulations. The sets of simulations considered are the training set, the test set, and the total set consisting of all simulations. . . . . 76

4.1 Central halo response model parameters used to scale the median $r_{s,c}$ evolution curve. Each type of central halo response, given in the second column, had different best-fit model parameters. The variables ($\alpha$, $\beta$, $\delta$) relate the model parameters to the initial conditions of the simulations. Their values are depicted in the labels of Fig. 4.5 as well. . . . . 86

# Chapter 1

# Introduction

## 1.1 ΛCDM and Dark Matter Halos

To date, the prevailing theory is that the Universe follows a Lambda Cold Dark Matter (ΛCDM) cosmological model, a parameterization of the Big Bang cosmological model in which the Universe is spatially flat and consists of three major constituents: radiation, matter, and dark energy (Ostriker & Steinhardt, 1995; Carroll, 2001; Spergel et al., 2007). The radiation component is composed of photons and neutrinos, and contributes the least to the total energy density. The matter component is split between two types: ordinary matter (baryons and leptons) and cold dark matter. In this context, *cold* indicates the matter is non-relativistic, moving slowly compared to the speed of light, while *dark* means the matter weakly interacts with ordinary matter and electromagnetic radiation. The largest component is dark energy, a uniform vacuum energy density with negative pressure (Copeland et al., 2006). It is widely considered to be a cosmological constant, denoted by $\Lambda$, causing the accelerated expansion of the Universe. While the ΛCDM model has its discrepancies (see e.g. Bullock & Boylan-Kolchin, 2017; Perivolaropoulos & Skara, 2022, for reviews), it successfully explains many observed features of the Universe including the abundances of light elements (Cyburt et al., 2016), the large-scale structure (Reid et al., 2010), and the acceleration of cosmic expansion (Astier et al., 2006).

Recent analysis of the cosmic microwave background (CMB) observed by the Planck satellite place constraints on the present-day density of each component (Planck Collaboration et al., 2020). Analysis of the shape of the CMB power spectrum constrains the late Universe densities to be: a radiation density $\Omega_\gamma = 5.4 \times 10^{-5}$, a baryon density $\Omega_b = 0.049$, a matter density $\Omega_m = 0.315$, and a dark energy density $\Omega_\Lambda = 0.684$. Here, these are

defined in terms of dimensionless density parameters,

$$\Omega_i = \frac{\rho_i}{\rho_{\rm crit}} \tag{1.1}$$

where $\rho_i$ is the physical density of the $i^{\rm th}$ component, $\rho_{\rm crit} = 3H_0^2/(8\pi G)$ is the critical density of the Universe (Mo et al., 2010), and $G = 4.498 \times 10^{-15}$ Mpc$^3$/(Gyr$^2 M_\odot$) is Newton's constant. Both of these quantities are measured at the present time. The critical density describes the required density of the Universe for it to stop expanding in the case of zero cosmological constant. It depends on the Hubble constant, $H_0$, which quantifies the expansion rate of the Universe. This parameter itself is often written in a dimensionless form as well, $h = H_0/(100$ km s$^{-1}$ Mpc$^{-1})$.

Evidence supporting the existence of dark matter has increased substantially over the last century. The earliest of this comes from observations of the Coma cluster by Zwicky (Zwicky, 1933). His findings suggested that there needed to be 20 times more mass present than inferred from the distribution of visible stars and gas in order to keep the cluster dynamically stable given its large velocity dispersion. Almost 40 years later, Rubin & Ford (1970) would eventually establish that a significant component of dark material was required in order to explain why the rotation speeds in the outskirts of galaxies were far higher than could be accounted for by the visible matter alone. In the modern day, the best evidence for dark matter relates to the CMB power spectrum, where the ratio of the second to third acoustic peaks constrains the ratio of the baryonic to non-baryonic matter (Mo et al., 2010). As discussed above, the most recent CMB measurements (Planck Collaboration et al., 2020) suggest there is $\sim 5.4$ times more dark matter than baryonic matter in the Universe.

In the early Universe, the dark matter distribution (and the overall matter distribution) was homogeneous with only small fluctuations about the average density (Carroll, 2001). The growth of structure then comes from the gravitational collapse of regions around these density fluctuations. This occurs hierarchically, where the smallest objects form first and grow through mergers. Suppose the density perturbation of a region of space is defined as $\delta = (\rho - \bar{\rho})/\bar{\rho}$, where $\bar{\rho}$ is the average density. Then, overdense regions of space ($\delta > 0$) will collapse to form structure, while underdense regions of space ($\delta < 0$) will become largely void of matter. If the fluctuations are small ($\delta \ll 1$), linear perturbation theory can be used to describe their growth (see e.g. Peacock, 1999; Mo et al., 2010). Only structures on the largest of scales fall into this regime.

On small scales ($\delta > 1$), the growth of structure is highly non-linear and requires numerical simulations to predict. Qualitatively, the results of these simulations demonstrate that dark matter clusters into sheets and filaments. Between these structures are voids,

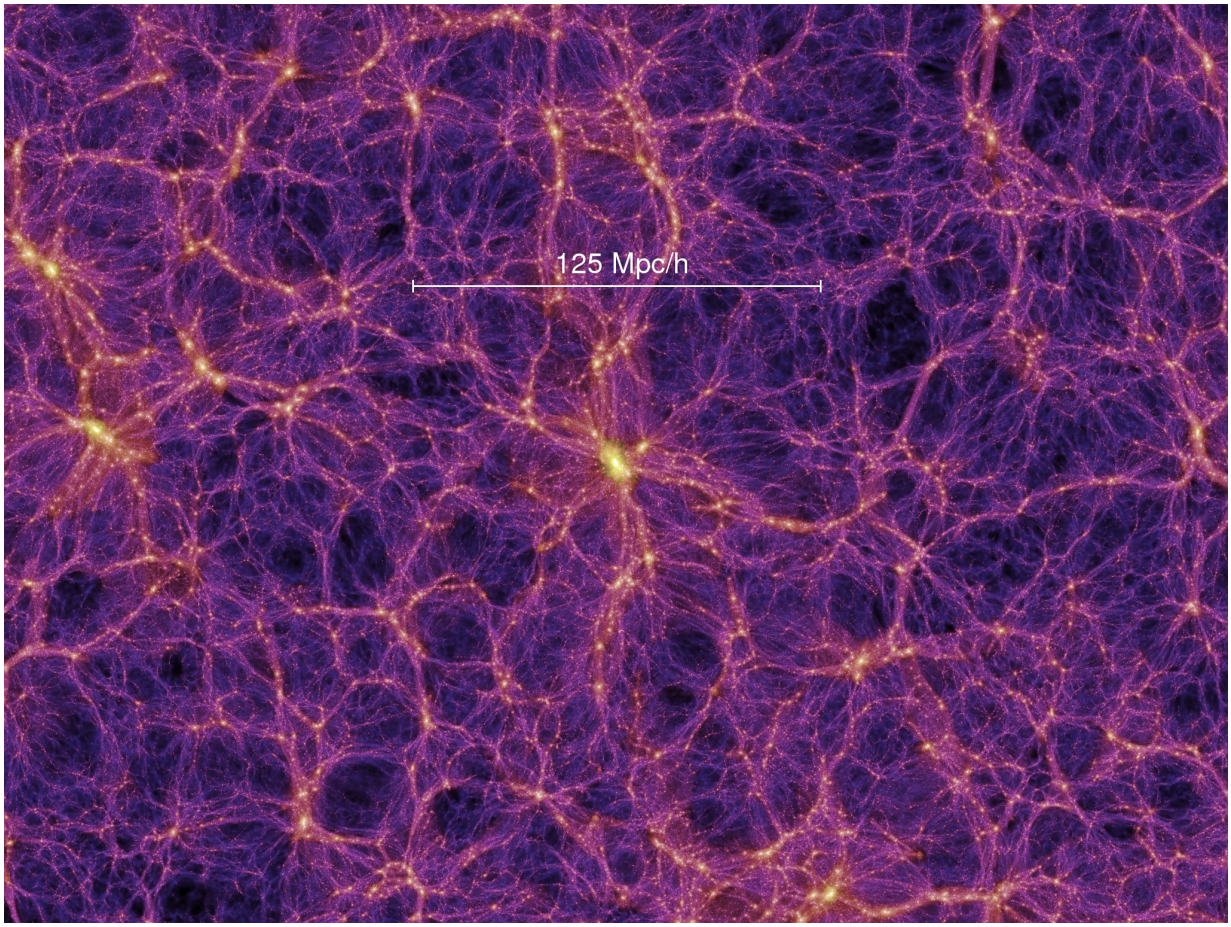



Figure 1.1: Large-scale structure of the Universe at the present day depicted through its dark matter distribution, based on the Millennium Simulation (Springel et al., 2006). The scale bar illustrates a length scale of 125 Mpc/$h$.

largely empty space originating from the expansion of underdense regions. The points where filaments intersect are known as nodes, and dark matter halos correspond to the higher density, roughly spherical regions in the nodes. Within larger halos, smaller subhalos may exist as they merge from the surrounding filaments. Overall, the underlying structure of the Universe is known as the cosmic web (Bond et al., 1996). Fig. 1.1 depicts a snapshot of the Universe at the present-day from a dark-matter-only simulation (Springel et al., 2006), illustrating the cosmic web. Simulations including baryons find the same general structure (see e.g. EAGLE in Schaye et al. 2014, IllustrisTNG in Vogelsberger et al. 2014, and FLAMINGOs in Schaye et al. 2023).

In the non-linear regime, the nature of structure formation is complex and cannot be determined analytically. However, simple analytic models for the formation of dark matter halos have been proposed. One of these is the spherical collapse model introduced by Gunn & Gott (1972). Consider a small positive spherical perturbation of density $\rho = \bar{\rho}(1+\delta)$ at time $t$ in an otherwise homogeneous Einstein-de Sitter Universe (i.e. no curvature, $\Omega_m = 1$, $\Omega_\Lambda = 0$). Of this mass, consider a shell of radius $r$ encompassing a mass $M_i$. We are assuming the mass enclosed by the shell remains constant as its radius evolves. The equation of motion of the shell is then,

$$\frac{d^2r}{dt^2} = -\frac{GM_i}{r^2} \tag{1.2}$$

which can be integrated once to find,

$$\left(\frac{dr}{dt}\right)^2 = \frac{2GM_i}{r} - \varepsilon \tag{1.3}$$

where $\varepsilon$ describes the specific energy of the shell. For the case $\varepsilon > 0$ corresponding to a shell that expands to some maximum radius, the solution to $dr/dt$ can be expressed in parametric form,

$$r(\theta) = \frac{GM_i}{\varepsilon}\left[1 - \cos(\theta)\right] \qquad\qquad t(\theta) = \frac{GM_i}{\varepsilon^{3/2}}\left[\theta - \sin(\theta)\right] \tag{1.4}$$

where $r(t_0) = 0$. From these equations, we can see that the shell reaches a maximum radius at $\theta = \pi$, denoted by $r_{\rm ta} = r(t_{\rm ta})$ (the turnaround radius). The shell then fully collapses back at $\theta = 2\pi$ ($t_{\rm col} = 2t_{\rm ta}$). However, this calculation assumes the shells of mass do not cross each other as they recollapse. Rather than fully collapsing, the overdensity instead mixes and relaxes until it reaches virial equilibrium at $r_{\rm vir}$. Using the virial theorem (see e.g. Binney & Tremaine, 2008, Eq. 4.248), we find $r_{\rm vir} = r_{\rm ta}/2$ given that the kinetic energy is zero at the turnaround radius. During this time, the Universe expands and the background density decreases. This process can be described by the solution to Eq. 1.3 when $\varepsilon = 0$,

$$\bar{r} = \frac{1}{2}\left(GM_i\right)^{1/3}\left(6t\right)^{2/3} \tag{1.5}$$

Putting everything together, the density contrast of a virialized halo relative to the background is,

$$\Delta_{\rm vir} \equiv \frac{\rho_{\rm vir}}{\bar{\rho}} = \frac{\left[\bar{r}(t_{\rm col})\right]^3}{r_{\rm vir}^3} = \frac{1}{8}(12\pi)^2 \approx 178 \tag{1.6}$$

Therefore, the model states that overdense regions of space will collapse into virialized objects with a characteristic overdensity of roughly 178. Note that this calculation can be done for more realistic cosmologies (see e.g. Bryan & Norman, 1998). In practice, a commonly used definition for the virial radius of dark matter halos is the radius within which the mean density is 200 times the critical density of the Universe (White, 2001).

The spherical collapse model allows for the outer boundary of dark matter halos to be defined. The matter within this boundary is stable and has broken away from the cosmic expansion. Through cosmological simulations, dark matter halos were found to have a matter density which is well described by the two parameter Navarro-Frenk-White (NFW) profile (Navarro et al., 1996, 1997),

$$\rho_{\rm NFW}(r) = \frac{\rho_0 r_s^3}{r\left(r + r_s\right)^2} \tag{1.7}$$

where $\rho_0$ is the characteristic density of the profile and $r_s$ is the scale radius corresponding to the point where the logarithmic slope is $d\ln(\rho)/d\ln(r) = -2$. Qualitatively, the scale radius characterizes the transition point between the inner halo ($\rho \propto r^{-1}$) and the outer halo ($\rho \propto r^{-3}$). The NFW profile is a spherically symmetric distribution, where the enclosed mass, potential, and gradient in these quantities are related to the density by (Binney & Tremaine, 2008),

$$M(<r) = 4\pi \int_0^r \rho(r') r'^2 dr' \qquad \frac{dM(<r)}{dr} = 4\pi\rho(r) r^2 \tag{1.8}$$

$$\Phi(r) = -\int_r^\infty \frac{GM(<r')}{r'^2} dr' \qquad \frac{d\Phi(r)}{dr} = \frac{GM(<r)}{r^2} \tag{1.9}$$

The profile is also universal in that the profiles of dark matter halos follow the same shape regardless of their mass, formation time, or the specific cosmology. More recent work has suggested refinements to the NFW profile (see e.g. Moore et al., 1998; Navarro et al., 2010), implying halos are better approximated by the three parameter Einasto profile (Einasto, 1965). Regardless, the NFW profile successfully describes the general structure of halos found in simulations and is still the most commonly used halo profile today.

Finally, note that on large scales, distance and time are usually expressed in terms of redshift, $z$. This quantity refers to the relative change in the wavelength of light due to the Doppler effect. Cosmic expansion causes objects to recede faster the further away they are. As a result, light emitted by these objects appears redder. Redshift is related to the cosmological epoch that light is emitted since it takes a finite amount of time to reach an

observer. The formula to calculate redshift is quite simple, $a \propto 1/(1+z)$, where $a$ is the scale factor relating distances in physical units to comoving units (i.e. units that grow with the expansion of the Universe). This expression becomes an equality if $a(t_0) \equiv 1$. At the present time, $z = 0$, and it increases when observing more distant objects corresponding to earlier epochs.

## 1.2 Galaxy Clusters and Their Properties

Galaxy groups and clusters are among the largest gravitationally bound structures in the Universe. These objects contain tens to thousands of galaxies and have total masses between $10^{13} - 10^{15} M_{\odot}$. Their sizes are typically between $0.5 - 2.5$ Mpc in radius with a wide range of velocity dispersions (i.e. $\sim 300 - 1000$ km/s). Clusters themselves correspond roughly to halos and their overall structure can be represented by one. However, they also consist of substructures (or subhalos) that each occupy their own dark matter halos. The galaxies that are found within clusters trace the underlying substructure.

Galaxy clusters primarily form through the accretion of groups and individual galaxies. These galaxies themselves are built from free gas that has cooled and condensed in the potential wells supplied by the dark matter halos (Blumenthal et al., 1984). There are three main components to galaxy clusters: (1) stellar material in and around galaxies, (2) hot X-ray emitting gas in the intracluster medium (ICM), and (3) dark matter. The stellar-to-gas mass fraction in clusters ranges from $0.05 - 0.2$, decreasing as total mass increases (Kravtsov & Borgani, 2012). Moreover, the ratio of stellar mass to total mass is roughly 1% on cluster scales, and this increases to about 3% on group scales (see e.g. Leauthaud et al., 2012, Fig. 16). Thus, the vast majority of the mass in clusters is in the form of dark matter.

The properties of galaxy clusters can be studied through cosmological simulations. At any given time, these simulations output snapshots consisting of the 3D positions and velocities of the particles used to represent the matter in the Universe. However, the snapshots do not indicate which set of particles belong to which structures. Some technique must be employed to group particles together. To identify galaxy clusters, one of two approaches are mainly used, the Friends of Friends (FoF) algorithm (Huchra & Geller, 1982; More et al., 2011) or the Spherical Overdensity (SO) algorithm (Lacey & Cole, 1994). The former links together particles within some distance, while the latter attempts to detect regions of particles with a density above some chosen threshold. A detailed comparison between the methods, and others, is presented in Knebe et al. (2011).

A basic property of galaxy clusters is their mass. This is typically defined as the mass of all particles within the virial radius, $M_{\rm vir} = M(< r_{\rm vir})$. A related property is the concentration of a cluster's halo which quantifies the size of its central core relative to its outer envelope. For an NFW halo, concentration is defined as $c = r_{\rm vir}/r_s$ (Navarro et al., 1996). There exists a relationship between concentration and mass known as the concentration-mass ($c-M$) relation after averaging over many systems (see e.g. Wechsler et al., 2002; Macciò et al., 2008; Klypin et al., 2011; Ludlow et al., 2012; Dutton & Macciò, 2014; Sánchez-Conde & Prada, 2014; Groener et al., 2016; Biviano et al., 2017; Shan et al., 2017; Diemer & Joyce, 2019). At fixed redshift and cosmology, it is more or less a power law with negative slope, meaning more massive halos have lower concentrations. At fixed halo mass, concentration generally decreases with increasing redshift although there is a lot of scatter at any particular redshift. In the absence of any physical process, halo concentration will evolve through pseudo-evolution: as the Universe expands, the background density decreases leading to growth in the virial radius and thus an increase in concentration. This process is largely responsible for the present-day growth of halos on galaxy scales (Diemer et al., 2013).

Other spatial properties of cluster halos include their shape and spin. The shapes of halos are generally described by ellipsoids which are characterized by the lengths of their axes. On cluster-scales, the objects are more prolate (cigar-shaped) than oblate (disk-shaped) with typical values for their axis ratios in the range $0.5 - 0.7$ (Jing & Suto, 2002; Allgood et al., 2006). The spin of halos quantifies their bulk rotation. These objects often have little spin (i.e. values in the range $0.03 - 0.05$) with more massive halos spinning more slowly (Bett et al., 2007). More information on calculating these quantities in simulations can be found in Section 2.3. Clusters are also described by temporal properties. These parameters usually attempt to summarize how material in the halo built up. For example, $z_{50}$ is a measure for the age of a halo given by its half-mass assembly time, while $\gamma$ gives the mass accretion rate. Exact definitions of these and other cluster halo properties can be found in Haggar et al. (2024).

Observational surveys detect clusters through one of four modalities. Each method probes a different source in the cluster. As a result, they can be combined to produce a full map of the system (see e.g. the Bullet Cluster in Section 1.3).

1. *Optical*: The luminous matter of galaxies in a cluster is detected through optical and infrared imaging. The galaxies provide a sampling of the underlying matter distribution, which allows for estimates of its density profile and concentration. However, foreground and background interlopers (i.e. galaxies that are not a part of the cluster) can impact estimates of these quantities, particularly for galaxies with imprecisely

measured redshifts. Thus, membership corrections are used to minimize their influence (see e.g. Castignani & Benoist, 2016; van der Burg et al., 2020).

2. *Gravitational Lensing*: The overall matter distribution of clusters, the majority of which is dark matter, can be mapped using gravitational lensing. As light from distant sources travels towards an observer, it can be deflected if there exists a massive object along its path. The lensing effect on the source is then related to the mass distribution of foreground system (Bartelmann, 2010). The main advantage of this technique is that it is the only one that measures the dark matter mass directly.

3. *X-ray Emission*: The hot gas in the ICM (at temperatures $10^7 - 10^8$ K) is detected at X-ray wavelengths. This emission is characterized by thermal bremsstrahlung. As free electrons in the gas are decelerated by ions, the lost energy is converted into radiation. The X-ray spectrum of clusters can be used to constrain their total mass through models of the gas density and temperature (see e.g. Vikhlinin et al., 2006), and assuming hydrostatic equilibrium (i.e. the internal pressure of the gas balances its self-gravity).

4. *Sunyaev-Zel'dovich (SZ) Effect*: The hot gas in the ICM can also be detected at millimeter wavelengths through the thermal SZ effect (Sunyaev & Zeldovich, 1972). In short, this is an inverse Compton scattering process where low energy CMB photons are deflected by high energy electrons in the ICM gas producing distortions in the CMB spectrum at the positions of clusters. Since the SZ effect is redshift independent, it is a useful probe for high redshift clusters. Furthermore, it can be used to directly measure the enclosed gas mass along the line of sight (Myers et al., 1997). On the other hand, the SZ signal can be contaminated by radio or infrared sources (Sehgal et al., 2010).

When we observe the structure of a cluster, it is projected into the plane of the sky. Any measurement of their properties is integrated along the line-of-sight. Moreover, we only observe the cluster at a single moment in time. This is different from simulations where we have access to the full 3D distribution of the particles and their time evolution. Thus, simulation based quantities are not directly comparable to real observations. To reconcile this, 3D spatial properties can be projected into the plane of the sky to obtain 2D equivalents suitable for observing data (see e.g. Coe, 2010; Coe et al., 2012). However, some of these properties are sensitive to projection effects. For example, halo concentration depends on the viewing angle. Concentration would be overestimated for clusters with large subhalos along the line-of-sight if their actual 3D position indicates they are much further from the cluster's centre, as in the case of a recent merger. In contrast, temporal

properties cannot be measured at all since they require knowledge of the cluster's growth history. Instead, they are inferred from other properties. For instance, halo age is strongly correlated with concentration (Wechsler et al., 2002). Thus, measurements of concentration can be turned into predictions for age.

Recent and upcoming surveys will improve the statistics of cluster properties. By modality, these missions and surveys include but are not limited to: *Euclid* (Sartoris et al., 2016) and *UNIONS* (Chambers et al., 2020) in the optical, *LSST* (LSST Dark Energy Science Collaboration et al., 2021) and *Roman* (Akeson et al., 2019) through lensing, *eROSITA* (Merloni et al., 2012) and *XRISM* (XRISM Science Team, 2020) in the X-ray, and *CMB-S4* (Abazajian et al., 2019) and *CCAT* (CCAT-Prime Collaboration et al., 2023) through the SZ effect. This new data will be composed of large samples of clusters with sufficient signal-to-noise to measure structural properties (see e.g. *Euclid*). Furthermore, detailed multi-modal studies of low redshift systems will be available (see e.g. *CLASH* in Postman et al. 2012 and *CHEX-MATE* in CHEX-MATE Collaboration et al. 2021) providing a pathway to study interactions between the different components of clusters.

## 1.3 Mergers

Dark matter halos primarily grow through repeated hierarchical merging. The results of cosmological simulations have shown these mergers mainly follow radial orbits with a median apocentre-to-pericentre ratio of approximately $5-6$ (Ghigna et al., 1998; van den Bosch et al., 1999). Analytic expressions have been developed to estimate the rate at which mergers occur as a function of halo mass, mass ratio, and redshift (see e.g. Lacey & Cole, 1993; Sheth & Tormen, 2002; Zhang et al., 2008). In addition, $N$-body simulations have led to the development of a universal fitting formula for the merger rate (Fakhouri & Ma, 2008). As stated, the merger rate depends on the mass ratio between the two merging halos. For instance, suppose a satellite halo of mass $M_s = 2.5 \times 10^{13} M_\odot$ merged with a larger central halo at the present-day. Accounting for effects on the satellite's dynamics, the typical orbital period is $\sim 6$ Gyr, corresponding to a redshift change of $\Delta z \approx 0.62$ assuming *Planck-18* cosmology. Considering the Fakhouri & Ma (2008) merger rate, the number of mergers following this scenario is roughly 1.2 per halo for a 3:1 mass ratio and 7.5 per halo for a 10:1 mass ratio. Thus, more unequal mergers are much more common.

An example of two galaxy clusters colliding is the well-known Bullet Cluster shown in Fig. 1.2. Here we have a composite image with the galaxies in the optical, the ICM gas in pink, and the matter distribution inferred from gravitational lensing in blue. During the merger, the cluster on the right passed through the larger cluster on the left. While the

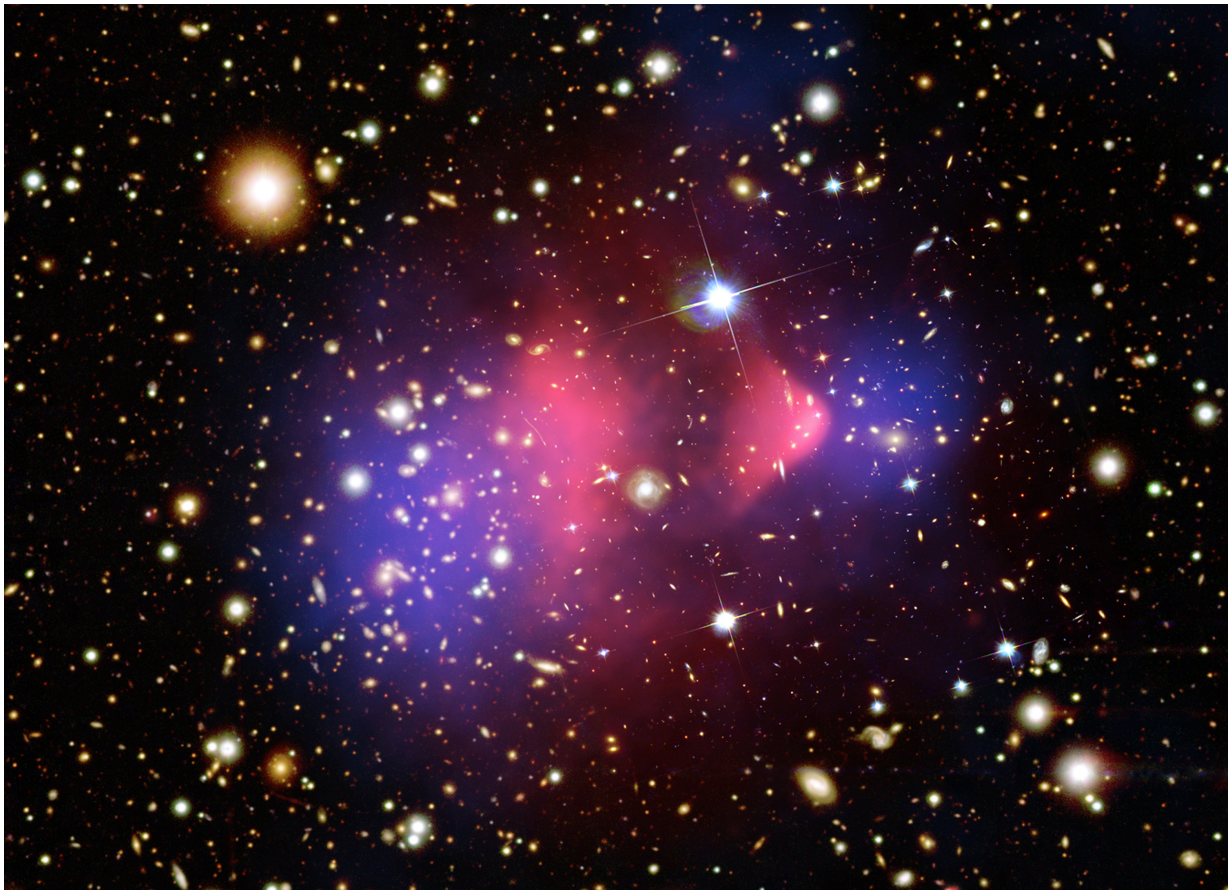


Figure 1.2: Composite image of the Bullet Cluster located at $z = 0.296$ (Clowe et al., 2004). The pink clumps are hot gas from the intracluster medium which consists of the majority of the visible matter in the cluster. The blue regions are a map of the mass inferred from gravitational lensing. Credit: X-ray: NASA/CXC/CfA/Markevitch et al. (2004); Optical: NASA/ST-ScI; Magellan/U.Arizona/Clowe et al. (2006); Lensing Map: NASA/STScI; ESO WFI; Magellan/U.Arizona/Clowe et al. (2006).

galaxies of each cluster passed through one another without affect, the ICM gas, which encompasses a majority of the visible matter, collided, dragged, and separated from the bulk of the mass in the cluster. The bulk material is traced through gravitational lensing and is concentrated in the two lobes centred on each group of galaxies. This result demonstrates most of the matter in the cluster is collisionless (i.e. non-baryonic dark matter) since it did not shock with the gas during the encounter.

In the literature, mergers are often classified as one of two types, minor or major, depending on the mass ratio of the two systems. However, the exact threshold used to separate the two categories is not universal. The most widely used classification defines major mergers as systems with a mass ratio smaller than 3:1 (see e.g. Cox et al., 2008; Hopkins et al., 2009; Wang et al., 2020, 2023). For example, the Bullet Cluster, which is thought to be $\sim$ 10:1 merger (Bradač et al., 2006; Mastropietro & Burkert, 2008), would be a minor merger with this definition. Rather than separate mergers based on some specific threshold, a better criteria would be to examine the perturbation caused by the satellite on the more massive system in which they sink. In minor mergers, the host halo remains largely unaffected during the encounter, while the satellite evolves through a combination of effects.

1. *Dynamical Friction*: This refers to the systematic loss of energy and angular momentum as the satellite moves through a distribution of background particles (Chandrasekhar, 1943). Energy is transferred from the satellite to the random motions of the background particles that make up the host halo through gravitational interactions. The net effect is to create a wake of higher density behind the satellite, leading to a drag force that slows it and thus causes its orbit to shrink. However, this effect is only expected to be significant for satellites with masses larger than a few percent of the host halo's mass (Mo et al., 2010). Dynamical friction results in mass segregation, where more massive satellites reside closer to the centre of the host.

2. *Tidal Mass Loss*: This refers to the loss of material from the outer regions of satellites due to tidal forces in a steady or slowly varying gravitational field (King, 1962). The satellite is stretched along the line towards the centre of the host halo due to the gradient in the gravitational field. Material that is stripped off the satellite either unbinds from the system or is incorporated into the host halo. Haggar et al. (2022) find that during group mergers with large clusters, 50% of group members are lost by the first pericentre indicating rapid mass loss. Ultimately, the fate of the satellite depends on the mass ratio of the merger. Satellites rapidly disrupt completely in major mergers, whereas they can survive for many orbits in minor mergers.

3. *Tidal Heating*: This refers to heating in the inner regions of satellites due to tidal shocks (Gnedin & Ostriker, 1999; Taylor & Babul, 2001). These shocks result from a gravitational field that varies rapidly compared to the typical orbital period of the particles in the satellite. In clusters, encounters between the satellite and other substructures, as well as interactions with the host halo during pericentric passages, will induce gravitational shocks (Peñarrubia & Benson, 2005). Tidal heating adds energy to satellites, modifying their internal structure and accelerating mass loss.

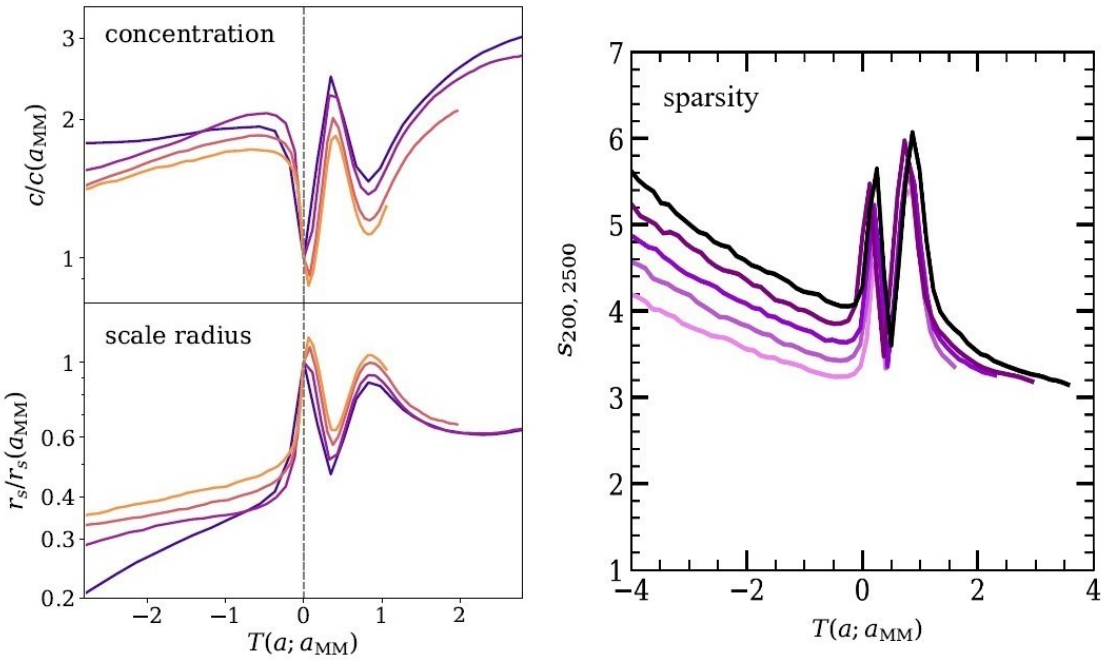



Figure 1.3: Response of concentration (left-top), scale radius (left-bottom), and halo sparsity (right) due to major mergers in cosmological simulations. Each curve depicts the median response for a sample of systems selected to merge at the same epoch. The timescale in these plots is shown in units of dynamical time, with the merger time as a reference. This figure was adapted from Wang et al. (2020) and Richardson & Corasaniti (2022).

Thus, the effect of minor mergers is to introduce small, bound substructures (or subhalos) into the host system. On the other hand, major mergers are disruptive events that significantly redistribute the matter distribution in the parent system. The long-term effects of major mergers on the spatial structural properties of halos has been studied in Drakos et al. (2019a,b). Major mergers also cause short-term, transitory effects on the combined system (i.e. the host and satellite) as illustrated in Fig. 1.3. This plot shows the median response of concentration, scale radius, and halo sparsity (i.e. the virial mass ratio at two different $\Delta_{\rm vir}$) due to major mergers in cosmological simulations. To remove the effect of merger phase, the timescale is given in units of dynamical time, the time required to cross an equilibrium dynamical system (see e.g. Wang et al., 2020, Eq. 5). These studies find that major mergers produce oscillations in structural parameters caused by the orbital evolution of the satellite. The response itself is short-lived and only lasts $1-2$ orbits. This behaviour is not limited to spherically symmetric quantities as other studies

have demonstrated a similar response in halo anisotropy properties (i.e. shape, spin, and asymmetry) (see e.g. Power et al., 2011; Wang et al., 2023). These results as discussed in more detail in Section 5.2.

## 1.4 Motivation

Forthcoming surveys of clusters will lead to large samples of structural property measurements that can be used as proxies to constrain cosmology. For example, the cluster mass function, which describes the number of clusters found at a particular redshift with a particular mass, depends on a combination of cosmological parameters: $\Omega_m$, the matter density and $\sigma_8$, the root mean squared of the density field at the present-day smoothed to a scale of 8 Mpc/$h$ (see e.g. Press & Schechter, 1974; Tinker et al., 2008; Allen et al., 2011). The parameters $\Omega_m$ and $\sigma_8$ are degenerate when constrained through low redshift probes since the same set of structures can be created through one of two modes, more early power (low $\Omega_m$, high $\sigma_8$) or more late growth (high $\Omega_m$, low $\sigma_8$). Due to this degeneracy, a related parameter called the structure growth parameter, $S_8 \equiv \sigma_8\sqrt{\Omega_m/0.3}$, which quantifies the amount of clustering in the Universe, is commonly used instead.

Currently, there exists tension between the value of $S_8$ inferred from measurements of the CMB and through late Universe probes of the matter density field (see Abdalla et al., 2022; Perivolaropoulos & Skara, 2022, for reviews). This is demonstrated in the left-hand panel of Fig. 1.4. The larger contours show cosmological constraints obtained from KiDS-450 (de Jong et al., 2013) 3x2pt weak lensing analysis (i.e. a combination of galaxy clustering, galaxy-galaxy lensing, and cosmic shear as described in Joudaki et al., 2017) made at low redshift, while the small contours depict early Universe CMB constraints. This plot illustrates a $3\sigma$ tension between the two measurements. Using cluster structural properties has been proposed as a means to break this degeneracy (Amoura et al., 2021, 2023). In particular, cluster age seems to vary perpendicular to the contours (see the right-hand panel of Fig. 1.4). While age itself is not directly observable, it can be related to other parameters such as concentration or asymmetry. Thus, measurements of median age could dramatically improve cosmological constraints made at low redshifts. Beyond testing cosmology, clusters are used to study galaxy formation and evolution, and its dependence on environment (see e.g. Moore et al., 1996; Kauffmann et al., 2004; Peng et al., 2010).

The issue with galaxy clusters is they are still assembling at the present-day. As a result, a large fraction of them are expected to be disturbed or irregular (see De Luca et al., 2021, Section 5.5 for a summary). This follows from the merger rate being high. As discussed in Section 1.3, on cluster scales, 1.2 major mergers per halo and 7.5 minor mergers per

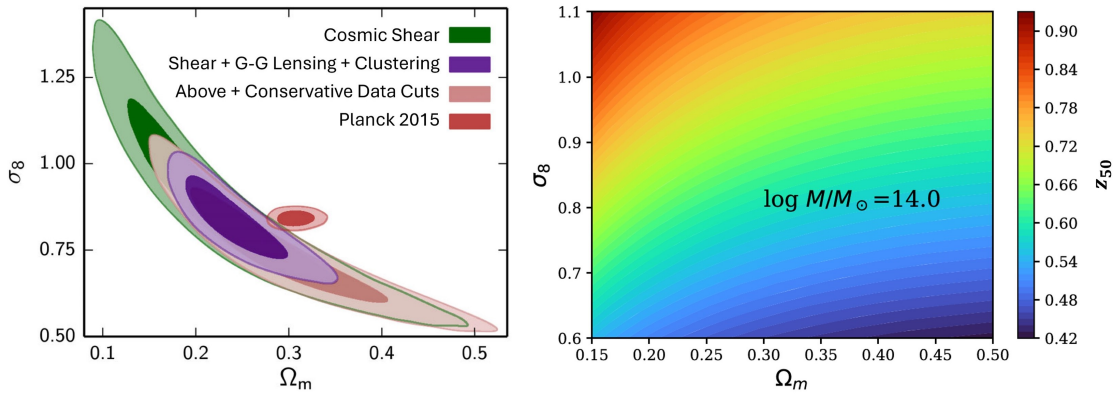



Figure 1.4: Left: Confidence contours for the cosmological parameters $\Omega_m$ and $\sigma_8$ derived from low redshift weak gravitational lensing observations adapted from Joudaki et al. (2017). Right: Median $z_{50}$ for present-day halos at cluster masses as a function of $\Omega_m$ and $\sigma_8$ adapted from Amoura et al. (2021).

halo are expected to occur within the first orbit of a satellite. The effect of mergers is to produce oscillations in the structural features. This behaviour is observed regardless of the type of merger as even more minor ones can create disturbances in the underlying potential (Wang et al., 2020). These oscillations will smooth out when examining median quantities (see e.g. Amoura et al., 2021, Fig. 10 for the concentration-age relation), but there will be intrinsic scatter in the median caused by mergers. As a result, if concentration is used as a proxy for age, this scatter will be passed onto the median age, which in turn would propagate to the cosmological parameter measurements, enlarging the constraints.

In addition, the dynamical state of clusters (i.e. whether or not it is dynamically relaxed) has consequences for their mass estimates. Cluster masses measured from X-ray imaging are often biased low for unrelaxed clusters due to assumptions of hydrostatic equilibrium (see e.g. Nagai et al., 2007; Mahdavi et al., 2013; Hoekstra et al., 2015). Several other properties, including those related to the ICM, are also affected (see Haggar et al., 2024, for a review). Thus, we need to accurately access cluster dynamical states in order to use them as a cosmological tool.

This thesis presents a semi-analytic model for the evolution of structure in remnant systems due to mergers. The model functions by tracking the motion of a satellite halo as it undergoes a merger with a central halo. It includes a prescription for how the material in the central halo responds as the satellite passes through it. We are interested in predicting changes to the structural properties of individual systems during mergers as well as modeling their median behaviour in a large sample. Many models of satellite evolution

and mass loss have been proposed previously (see e.g. Taylor & Babul, 2001; Hashimoto et al., 2003; Hayashi et al., 2003; Zentner & Bullock, 2003; Peñarrubia & Benson, 2005; Fujii et al., 2006; Fellhauer & Lin, 2007; Peñarrubia et al., 2010; Drakos et al., 2017, 2020), but all of these were applied to minor mergers (i.e. the satellite mass $\ll$ the host mass) and assumed the host halo was static. Ultimately, we want to study the impact of a dynamic central halo on satellite orbits and determine how mergers affect the statistics of the remnant structural parameters. On top of this, we want to identify if any remnant properties can constrain the dynamical state of the system or its merger phase. Because if we can model mergers effectively, we should be able to better control the scatter in median relations, like the concentration-age relation, and better predict $\Omega_m$ amd $\sigma_8$.

To construct and test our model, we perform $N$-body simulations of the merger of two isolated halos, represented by collisionless particles using truncated NFW profiles, to study the evolution of the total mass distribution. We consider isolated simulations in order to investigate the impact of mergers at increased resolution without incorporating additional complicating factors associated with halo growth. Our basic setup involves choosing a fixed, cluster-scale satellite mass and selecting cosmologically motivated values for the mass ratio, orbital energy, and angular momentum as the initial conditions. The merger starts at the present-day and the system is evolved for several pericentric passages. Finally, note that all calculations are done in code units, but we convert to physical units in this thesis for convenience.

## 1.5 Outline of the Thesis

The main goal of this thesis is to develop a model for the structural evolution of dark matter halos in major mergers with a particular emphasis on replicating the median evolution. First in Chapter 2, we describe the initial conditions for the set of simulations used to tune and evaluate our proposed model. The specific subset of simulations shown in the thesis is given in Section 2.4. All parameters measured for the satellite, central halo, and remnant system are outlined as well. Next in Chapter 3, we introduce the orbital evolution model used to trace the satellite's position and quantify its mass loss. Moreover, we train a machine learning model to predict the model parameters, and evaluate its functionality. Then in Chapter 4, we propose a semi-analytic model to capture how the central halo responds to the motion of the satellite as it merges. We explore the implications of incorporating this process on modeling the satellite's trajectory and the remnant system's properties. Finally in Chapter 5, we summarize the main findings, suggest potential applications, and detail next steps.

# Chapter 2

# Simulations

## 2.1 $N$-body Codes

$N$-body simulations are commonly used in astronomy to study the gravitational interactions within an extended mass distribution, such as a galaxy or cluster, via a discrete set of points. These simulations provide a method to directly study the structure of a system through the evolution of its particle distribution. The primary component of the simulations are the particles which represent some physical quantity. In our case, particles represent dark matter in the halos, and they are given a set mass. For exact codes, the particles' masses, positions, and velocities are directly used to numerically integrate the equations of motion of the system to determine their subsequent motion. Since this involves computing mutual gravitational forces, at a minimum this requires $N^2$ calculations. Thus, the computational resources used to run an $N$-body simulation grow quickly with the number of particles.

Directly integrating the equations of motion can be extremely computationally expensive. Therefore, methods that approximate these calculations are instead employed. Two such schemes that are commonly used are tree and mesh methods (Bode et al., 2000). In both schemes, the simulation volume is split into a grid of cubic cells. Tree methods only consider individual particle-particle interactions between particles in nearby cells. Each distant cell is treated as a single particle located at the center of the cell with a total mass equal to the sum of the masses of all particles in the cell. On the other hand, mesh methods determine the density of the particles in each cell from the particle positions. Typically, the cell size is adaptively set where smaller cells are required in denser parts of the simulation. This gives a sample of the density field. The potential of the grid, and thus the force field,

is then calculated in Fourier space using the Fast Fourier Transform, drastically speeding up calculations. Both methods reduce the number of computations to $N \log(N)$ or better, a great improvement over the naive approach, at the cost of accuracy.

In this work, our dark matter halo merger simulations were performed using `GADGET-2`, a cosmological $N$-body simulator (Springel, 2005). The code can be used to study isolated systems or cosmological simulations where space expands. This program is massively parallel allowing calculations for each simulation to be spread over many processors. The code makes use of a hybrid approach for calculating particle-particle forces, a tree method for short-range forces and a mesh method for long-range ones. Additional physical processes such as gas dynamics or radiative cooling can be included in the simulations as well. These baryonic processes were not incorporated in our case since our simulations are dark-matter-only.

The code uses spline softening for particle interactions below some threshold separation. This prevents force calculations from diverging when particles come too close to one another. For a softening length, $\varepsilon$, at zero separation the potential is given by $GM_{\rm p}/\varepsilon$ as for a Plummer model (Springel et al., 2001). The gravitational potential is exactly Newtonian at particle separations larger than $2.8\varepsilon$. The softening length selected for our simulations follows that proposed by van Kampen (2000), $\varepsilon = 0.5\, r_h\, N^{-1/3}$, where $r_h$ is the half-mass radius and $N$ is the number of particles in a halo. The value of $\varepsilon$ was calculated for each halo in the system, and the minimum value was used.

## 2.2 Initial Conditions

To run a simulation, one must start with initial conditions. The initial conditions for our simulations were generated using three primary parameters: (1) the mass ratio between the halos, (2) the radial-to-total velocity ratio, and (3) the total-to-virial velocity ratio. The mass ratio is related to how the particles in each halo were created, while the latter two parameters trace the energy and angular momentum of the system. All three parameters are used to place the satellite on its orbit. Each simulation consists of the merger of two isolated, spherically symmetric systems that are modeled by truncated NFW profiles at the present-day, $z = 0$. The particles in the simulations were dark-matter-only. In total there were **729** simulations, resulting in a sampling of nine per parameter (i.e. $9^3 = 729$).

Note that the simulations shown in this thesis all have a standard naming convention to reflect the initial conditions of the merger. For example, a simulation may be labeled "$\xi 1\, \eta 2\, \epsilon 2\, T1$", where $\xi$ describes the mass ratio, $\eta$ the relative energy, $\epsilon$ the circularity, and

$T$ the type of central halo response (of which there were two). For the orbital parameters, the number immediately following the parameter represents a qualitative measure of its value. These numbers are integers and can vary from 1 to 4 for $\xi$ and 1 to 3 for $\eta$ and $\epsilon$. Low numbers indicate a small value for the orbital parameter, while the opposite is true for higher numbers. Thus, a simulation labeled "$\xi 1\, \eta 2\, \epsilon 2\, T 1$" has a low mass ratio, a medium relative energy, a medium circularity, and a type 1 central halo response. For more details, refer to Section 2.4.

### 2.2.1 Generating Halos

The positions and velocities of the particles in the halos follow truncated NFW (or NFWT) profiles. The particles themselves were generated using the code ICICLE (Drakos et al., 2017). To create the particles, the code samples the radial position of each particle from the target mass distribution. Random angles are assigned to give each particle its full 3D coordinates. Next, the total energy of each particle is sampled using the distribution function. In the case of a spherical, isotropic, and self-gravitating system, the distribution function can be written in terms of the total energy and related to the target density profile (see Binney & Tremaine, 2008, Section 4.3). Then, the potential energy of each particle is calculated using their positions given the target mass distribution. The total and potential energies set the kinetic energy of each particle, and thus their velocities. Similar to position, a random direction is assigned to the velocity. Finally, the code truncates the particles to a truncation radius, $r_t$, by iteratively removing any particles that are not self-bound and are outside $r_t$ (see Section 2.3.1 for the definition of self-bound particles).

We need to consider truncated NFW profiles for a few reasons. First, the mass of the standard NFW profile diverges at large radii, so it cannot be represented by a finite number of particles. In addition, the standard NFW profile is not stable in isolated simulations. If we were to evolve an isolated halo with an NFW profile, individual particle-particle interactions would lead to deformation of the halo away from the initial structure, most noticeably in the halo's centre where the profile is densest. Using a truncated NFW profile overcomes this issue as they are very stable long-term (Drakos et al., 2017).

An approximate analytic description for the NFWT profile that yields a good fit to the truncation procedure performed by ICICLE is given by Drakos et al. (2022),

$$\rho(r) = \frac{e^{-q/y_d}}{[1 + (q/y_d)]^a}\, \rho_{\mathrm{NFW}}(r) \tag{2.1}$$

where $q = r/r_e$ is the radius normalized by an effective radius, $r_e$, the truncation scale $y_d$ roughly corresponds to the radius where the profile starts truncating exponentially, and

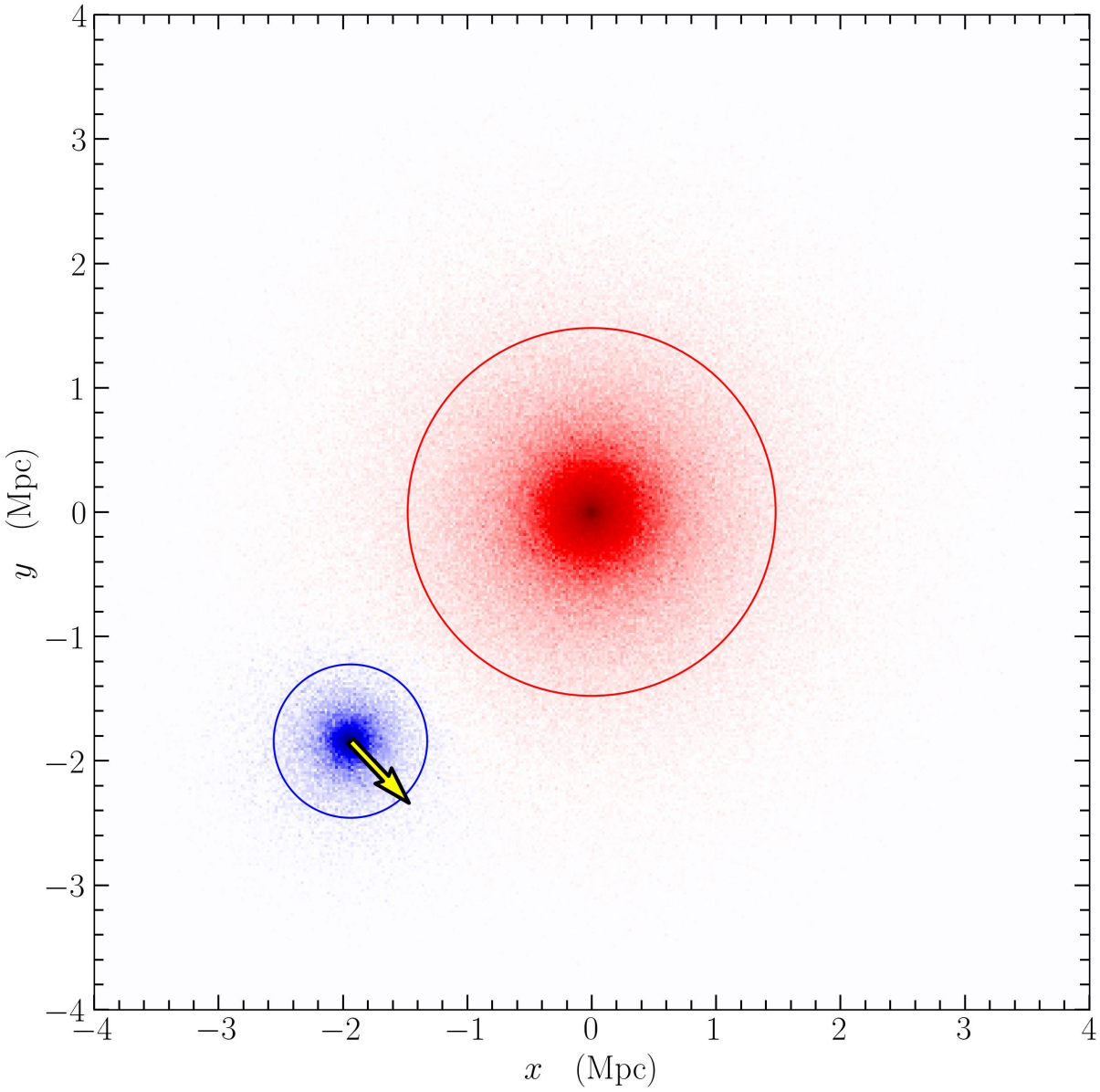



Figure 2.1: Initial setup of the halos in a simulation. The central halo (red) is placed at the centre of the frame and the satellite (blue) is given some initial separation and velocity (yellow arrow, magnitude not to scale). The virial radii of both halos are shown by the circles with their respective colours.

$\rho_{\rm NFW}$ is the standard NFW profile (see Fig. 2.2 for an illustration of the profile). Note that the NFWT profile has a similar functional form to the density profile of stripped halos proposed in Hayashi et al. (2003). This form in particular conserves the central density as $r \to 0$, and the central regions of these profiles resemble dark matter halos in cosmological simulations. The parameters $r_e$ and $a$ are parameterized as follows (Drakos et al., 2022),

$$\log(r_e) = 0.0811 y_d^3 + 0.358 y_d^2 + 0.0781 y_d - 0.201 \tag{2.2}$$

$$a = 0.179 y_d^3 + 0.379 y_d^2 - 0.524 y_d - 0.952 \tag{2.3}$$

In practice, ICICLE requires several choices for creating a halo, most notably the total mass of the halo, the number of particles in the halo, its scale radius, and its truncation radius. For the satellite halo, the first two of these four variables are free parameters. Since we are interested in studying halos on cluster scales, we set the satellite mass to $M_s = 2.5 \times 10^{13} M_\odot$. This will lead to central halos with masses of $\sim 10^{14} M_\odot$. The number of particles in the satellite halo before the truncation procedure is set to 48 884, leading to 35 024 after truncation. This ensures the central halo in each simulation will have sufficient particle resolution to implement dynamical friction accurately (see e.g. Wahde & Donner, 1996; Spinnato et al., 2003). The satellite mass and number of particles then sets the mass per particle, $M_p = 7.138 \times 10^8 M_\odot$.

The central halo mass, $M_c$, is related to the satellite halo mass given the mass ratio of the simulation. The mass ratio, $\xi = M_s/M_c$, is sampled using the Fakhouri & Ma (2008) merger rate. Here, the authors propose a universal form for the merger rate (per halo),

$$\frac{B(M_0, \xi, z)}{n(M_0, z)} = A \left(\frac{M_0}{\tilde{M}}\right)^{\alpha} \xi^{\beta} \exp\left[\left(\frac{\xi}{\tilde{\xi}}\right)^{\gamma}\right] \left(\frac{d\delta_c}{dz}\right)^{\eta} \tag{2.4}$$

where $\tilde{M} = 1.2 \times 10^{12} M_\odot$ is a constant, $\delta_c(z)$ is the standard density threshold normalized to $\delta_{c,0} = 1.686$ at $z = 0$, and $M_0$ is the remnant halo mass after the merger. Since we are interested in studying major mergers, we choose a remnant halo mass of $M_0 = 1 \times 10^{14} M_\odot$ corresponding to a 3:1 merger. The rest of the parameters are tuned fitting parameters: $A = 0.0289$, $\tilde{\xi} = 0.098$, $\alpha = 0.083$, $\beta = -2.01$, $\gamma = 0.409$, and $\eta = 0.371$. The final term in the expression can be simplified using,

$$\frac{d\delta_c}{dz} = -\frac{\delta_{c,0}}{[D(z)]^2} \frac{dD(z)}{dz} \tag{2.5}$$

where $D(z)$ is the linear growth factor which depends on the choice of cosmology. For simplicity, we choose *Planck-18* cosmology (Planck Collaboration et al. 2020, $\Omega_m = 0.31$,

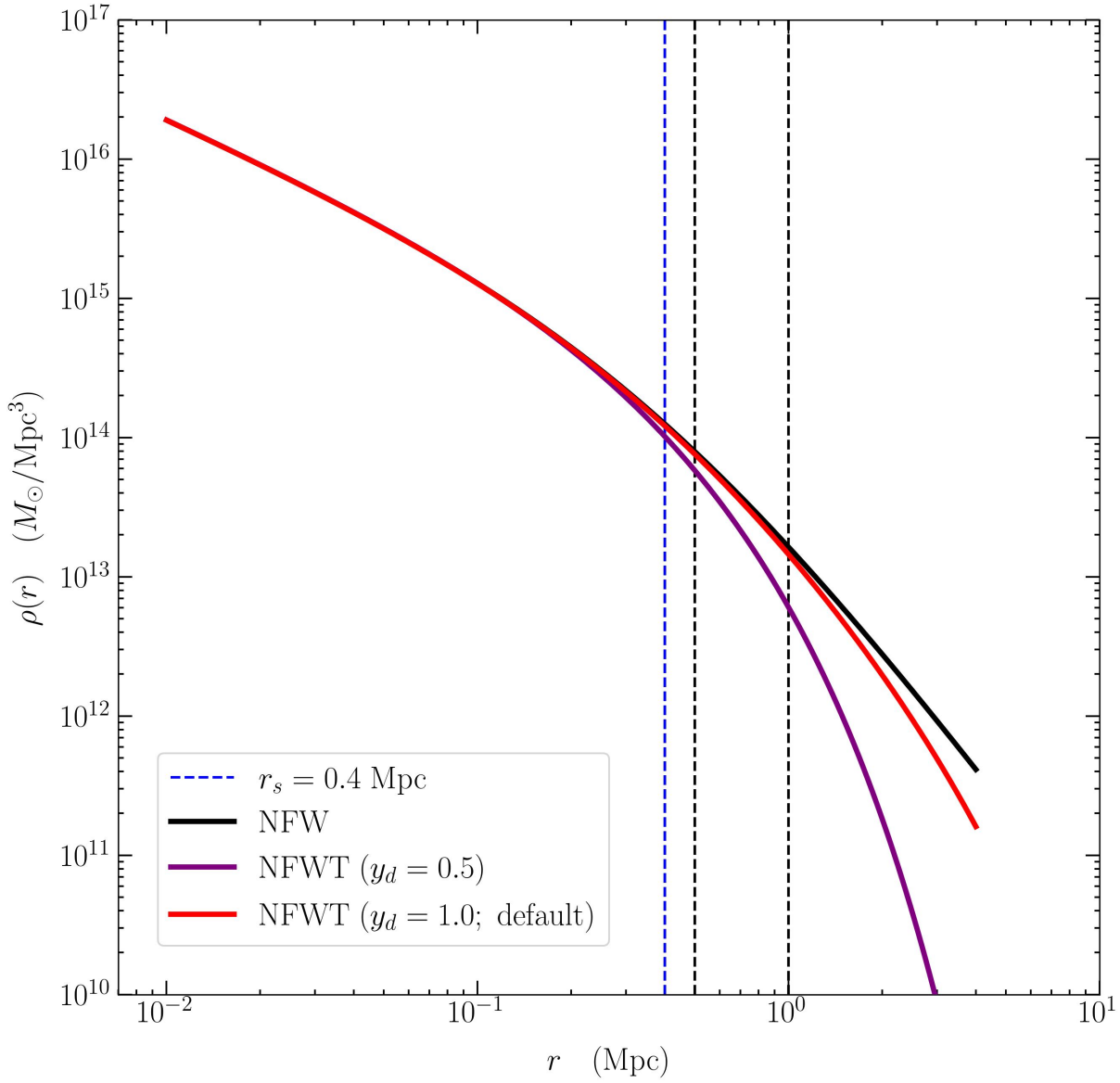



Figure 2.2: Comparison between the NFW (black) and NFWT (red, purple) density profiles. All three profiles consider the same NFW parameters, $r_s = 0.4$ Mpc and $\rho_0 = 5 \times 10^{14} M_\odot/\mathrm{Mpc}^3$, and are truncated to a radius $r_t = 4$ Mpc. The NFWT profile shown in red uses a truncation scale, $y_d$, that is typical in our simulations. The dashed vertical lines mark the radii where $r = y_d$.

$\Omega_b = 0.049$, $h = 0.676$, $\sigma_8 = 0.81$, and $n_s = 0.966$). We can use the merger rate to sample cosmologically consistent mass ratios for our isolated simulations. For our major mergers simulations, we consider mass ratios $\xi \in [0.05, 0.5]$. Then, the probability density function we sample $\xi$ from is given by,

$$P(\xi) = \left[\frac{1}{\int_\xi \frac{B(M_0,x,z)}{n(M_0,z)}dx}\right] \frac{B(M_0,\xi,z)}{n(M_0,z)} \tag{2.6}$$

The central halo mass is finally calculated using $\xi$ and $M_s$. This is the target mass we want for the central halo given the mass ratio. However, ICICLE uses the number of untruncated particles, $N_{ut}$, as an input to generate the particles, and then applies an iterative method to remove unbound particles. The central halo mass we want has the correct number of particles after truncation (i.e. $N_t = M_c/M_p$). There does not exist a simple scaling between $N_{ut}$ and $N_t$. As a result, we cannot generate a central halo with the number of particles equivalent to the target mass. Instead, we apply an iterative procedure where we vary the value of $N_{ut}$ accordingly until the number of particles in the central halo gives a mass ratio to within 1% of the sampled mass ratio.

The scale radius and truncation radius of each halo are calculated from their respective concentrations and virial radii. The concentration is calculated using the $c-M$ relation proposed by Diemer & Joyce (2019). Their model derives an analytic expression for the $c-M$ relation that is valid assuming pseudo-evolution, while incorporating deviations from an Einstein-de Sitter expansion history. For ΛCDM cosmology, it accurately matches simulated concentrations to within 5% agreement at all halo masses with few exceptions. For our purposes, we use the COLOSSUS (Diemer, 2018) implementation of the model to generate halo concentrations from their masses. The corresponding virial radii are given by (Navarro et al., 1997),

$$\bar{\rho}(< r_{200}) = 200\rho_{\text{crit}} \tag{2.7}$$

$$r_{200} = \left(\frac{M}{\frac{4\pi}{3} \times 200\rho_{\text{crit}}}\right)^{1/3} \tag{2.8}$$

where $M$ is the mass of the halo and $\rho_{\text{crit}} = 3H^2/(8\pi G)$ is the critical density of the Universe. Note that $H = H_0$ since our simulations assume that $z = 0$. Defining the virial radius in this way ensures that both halos have the same mean density, as expected. Finally, using the concentration and virial radius, the scale radius of each halo is simply $r_s = r_{200}/c$ and their truncation radii are simply $r_t = 3\,r_{200}$. With these parameters, we can generate the particle positions and velocities for both the satellite and central halos.

### 2.2.2 Placing the Satellite on its Orbit

Once we generate the satellite and central halo particles, we need to place the satellite on an orbit for it to merge. To do this, we give the satellite halo an initial velocity and an initial separation from the central halo. In Cartesian coordinates, no $z$-component was given to the satellite's starting position and velocity. This does not affect the generality of our orbits since the NFWT profile is spherically symmetric. Spherically symmetric distributions in static potentials result in planar orbits (see Appendix B.1 for details), and any general 3D orbit can be obtained by rotating the orbital plane. Thus, the initial conditions for the satellite's orbit are limited to $x$, $y$, $v_x$, and $v_y$.

For our simulations the orbital properties are sampled using empirical fits determined in Jiang et al. (2015). Here the authors present distributions of orbital parameters for satellites infalling towards hosts in the mass range $M_c = 10^{12} - 10^{14} M_\odot$. These distributions represent the initial conditions for the evolution of substructures within a host halo, and feature significant trends with $M_c$ and $\xi$. From their fitted distributions, we sample two orbital properties which uniquely define our orbits. The first is the radial-to-total velocity ratio, modeled using an exponential distribution and sampled in the range $v_r/v \in [0.05, 0.95]$,

$$P\left(v_r/v\right) = \left[\frac{1}{\int_{\frac{v_r}{v}} \left(e^{Bx} - 1\right) dx}\right] \left(e^{B(v_r/v)} - 1\right) \tag{2.9}$$

where $B = 2.982$ is a fitted parameter. The second is the total-to-virial velocity ratio, modeled using a Voigt profile and sampled in the range $v/v_{200} \in [0.5, 1.7]$,

$$P\left(v/v_{200}\right) = \int_{-\infty}^{\infty} P_G(x) P_L(v/v_{200} - x) dx \tag{2.10}$$

where $P_G(x)$ and $P_L(x)$ are the Gaussian and Lorentz distributions, respectively,

$$P_G(x) = \frac{1}{\sqrt{2\pi}\sigma} \exp\left(\frac{-(x-\mu)^2}{2\sigma^2}\right) \qquad P_L(x) = \frac{\gamma}{\pi(x^2 + \gamma^2)} \tag{2.11}$$

and $\mu = 1.084$, $\sigma = 0.187$, and $\gamma = 0.012$ are fitted parameters. Values for the fit parameters were obtained from the $M_c = 10^{14} M_\odot$, $\xi \in [0.05, 0.5]$ bin in Jiang et al. (2015).

Given $v_r/v$ and $v/v_{200}$, we can convert these into polar coordinates for the initial velocity of the satellite using,

$$\frac{v_r}{v_{200}} = \left(\frac{v_r}{v}\right)\left(\frac{v}{v_{200}}\right) \qquad \frac{v_\theta}{v_{200}} = \left(\frac{v}{v_{200}}\right)\sqrt{1 - \left(\frac{v_r}{v}\right)^2} \tag{2.12}$$

where $v_{200} = \sqrt{GM_{200}/r_{200}}$ is the circular velocity at $r_{200}$ and $M_{200} = M_c(< r_{200})$ is the virial mass. The initial radial separation of the satellite is related to its angular momentum, $r = L_{\rm orb}/v_\theta$, while the initial angular position of the satellite relative to the central halo is a free parameter, picked to be $\theta = 0$ for simplicity. The angular momentum of the satellite can be calculated from our other properties using,

$$L_{\rm orb} = \frac{L_{\rm orb}}{L_c(E_{\rm orb})} \times v_{200} \times r_c(E_{\rm orb}) \tag{2.13}$$

where $L_{\rm orb}/L_c(E_{\rm orb})$ is the angular momentum of the satellite relative to the angular momentum of a circular orbit with the same energy. For orbits in an NFW potential, this is given by (Jiang et al., 2015),

$$\frac{L_{\rm orb}}{L_c(E_{\rm orb})} = \frac{v_\theta}{v_{200}} \left( \frac{f(c\, r_c(E_{\rm orb})/r_{200})}{f(c)} \right)^{1/2} \left( \frac{r_c(E_{\rm orb})}{r_{200}} \right)^{-1/2} \tag{2.14}$$

where $f(c) = 1/[\ln(1+c) - c/(c+1)]$ and $c$ is the concentration of the central halo. In this expression, $r_c(E_{\rm orb})$ is the radius of a circular orbit with the same energy.

$$\frac{r_c(E_{\rm orb})}{r_{200}} = \frac{2\ln(1 + c\, r_c(E_{\rm orb})/r_{200}) - 1/f(c\, r_c(E_{\rm orb})/r_{200})}{2\ln(1+c) - (v/v_{200})^2 f(c)} \tag{2.15}$$

This is an implicit equation for $r_c(E_{\rm orb})$ that can be solved using root-finding algorithms. Finally, our initial conditions for the satellite's orbit can be converted from polar into Cartesian coordinates using,

$$x = r\cos(\theta) \qquad v_x = v_r\cos(\theta) - v_\theta \sin(\theta) \tag{2.16}$$

$$y = r\sin(\theta) \qquad v_y = v_r\sin(\theta) + v_\theta \cos(\theta) \tag{2.17}$$

Note that in the above expressions, $v_\theta$ is not multiplied by a factor of $r$ due to how it was originally defined in Eq. 2.12.

Randomly sampling orbital properties from the distributions in Jiang et al. (2015) does not guarantee the satellites will follow bound orbits. For combinations of parameters that result in an unbound orbit (i.e. no defined apocentre), we resample $v_r/v$ and $v/v_{200}$ simultaneously until we obtain a bound orbit. Additionally, the procedure for calculating the initial position and velocity of the satellite we use above does not place the satellite at the apocentre of the orbit. In cosmological simulations, subhalos orbiting within the host system would have already been disturbed during the initial infall. Therefore, the satellite in our isolated simulations must be initially placed at the apocentre of the orbit to capture this effect.

To do this, we numerically integrate the satellite's orbit forward using a Leapfrog method assuming its initial position and velocity are given by Eqs. 2.16-2.17 (see Appendix B.2 for how Leapfrog operates). We do this until the satellite reaches its apocentre position, when it is located furthest from the central halo. In this procedure, we assume the satellite is a point-mass orbiting in a static central halo represented by the particles we generated for it in Section 2.2.1. At apocentre, we record the satellite's position and velocity. These are the orbital properties we ultimately use in our simulations. This method works since in the static case, the energy and angular momentum of the orbit are conserved. The satellite on this new orbit will still have the same values of $v_r/v$ and $v/v_{200}$ we sampled when it crosses the virial radius.

The final step to setting up the simulations involves taking the satellite halo particles and shifting them onto the proper orbit. The default frame of the simulation places the central halo at rest relative to the satellite. The satellite is then combined with the central halo particles, and all particles are written to a file. Before the particle positions and velocities are saved, they are converted into the internal units used by `GADGET-2`. These are user defined and were selected to be: (1) a length unit $\ell_{\rm unit} = 1$ Mpc, (2) a mass unit $M_{\rm unit} = 10^{14} M_\odot$, and (3) a time unit $t_{\rm unit} = 1$ Gyr, for our simulations.

The primary output from the simulations are snapshot files recording particle position and velocity data for the two halos during the merger. These snapshots were output at regular time intervals. There were 500 snapshots in total per simulation, and the time between snapshots was set such that the final snapshot occurred at $t = 1.5\, t_r$, where $t_r$ is the static radial orbital period (see Appendix B.1 for the definition of $t_r$). We set the final snapshot time relative to the orbital period since it varies between simulations depending on the specific initial conditions for the satellite. For example, satellites on radial orbits with small initial separations would require less time to complete one orbit compared to satellites on tangential orbits with large initial separations.

### 2.2.3 Distribution of Orbital Parameters

In cosmological simulations, subhalo orbits are often expressed in terms of their orbital energy and angular momentum rather than the position and velocity of the satellite. In general, converting between these properties for our two halo system is complex since each halo is composed of individual particles that overlap in space. The full treatment of this calculation requires determining the kinetic and potential energies of the entire system and subsequently removing the components of the energy associated with the internal motions of the individual halos.

A far simpler and much less time consuming approximation to this calculation can be made. Instead of being comprised of individual particles, suppose the satellite was a point mass located at the position $\vec{x} = (x, y, z)$ with velocity $\vec{v} = (v_x, v_y, v_z)$. The central halo in this picture is still an extended distribution of particles. The orbital energy of the satellite then simplifies to,

$$E_{\rm orb} = -\sum_i \frac{GM_sM_p}{\|\vec{x}_i - \vec{x}\|} + \frac{1}{2}M_s \|\vec{v}\|^2 \tag{2.18}$$

where in the first term above, we sum over all central halo particles located at positions $\vec{x}_i$. The angular momentum of the satellite has a similar simplified form,

$$L_{\rm orb} = M_{\rm s} \|\vec{x} \times \vec{v}\| \tag{2.19}$$

Our tests have shown that this approximate calculation and the full calculation for the orbital energy result in nearly identical distributions of the orbital parameters for our simulations. Furthermore, we find that calculating the satellite halo's orbital energy using Eq. 2.18 compared to the full treatment that requires considering the internal motions of each halo agree to within 12% on average. In addition, Drakos et al. (2019a) demonstrate that calculating the angular momentum of the satellite using Eq. 2.19 compared to using the satellite's individual particles are equivalent to within 0.5%.

In many studies (e.g. Tormen et al., 1997; Benson, 2005; Wetzel, 2011; Jiang et al., 2015; van den Bosch et al., 2018), the orbital energy is defined by the radius of a circular orbit with the same energy, $r_c(E_{\rm orb})$, relative to the virial radius of the host halo,

$$x_{\rm c} = \frac{r_c(E_{\rm orb})}{r_{200}} \quad \text{where} \quad r_c = -\frac{GM_sM_c}{2E_{\rm orb}} \tag{2.20}$$

Alternatively, the orbital energy can be parameterized as a relative energy, $\eta$, defined as the energy of the satellite divided by the energy of a circular orbit at the virial radius of the host halo,

$$\eta = \frac{E_{\rm orb}}{E_{\rm c}(r_{200})} \quad \text{where} \quad E_{\rm c} = -\frac{GM_sM_c}{2r_{200}} \tag{2.21}$$

Similarly, the angular momentum is often expressed in terms of the circularity, $\epsilon$, defined as the angular momentum of the satellite relative to the angular momentum of a circular orbit with the same energy (Lacey & Cole, 1993),

$$\epsilon = \frac{L_{\rm orb}}{L_{\rm c}(E_{\rm orb})} \quad \text{where} \quad L_{\rm c} = M_s\sqrt{GM_c\, r_c} \tag{2.22}$$

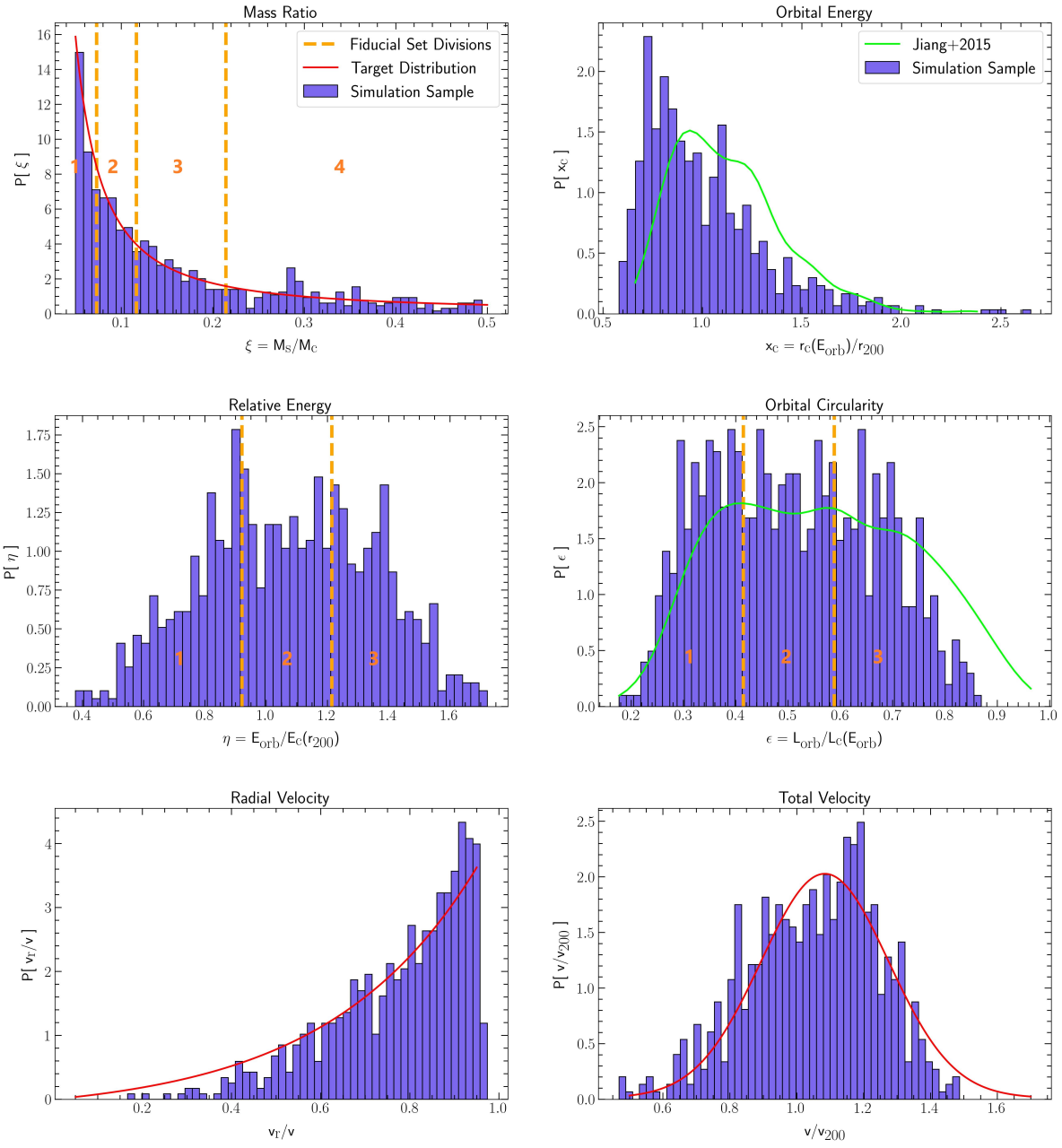



Figure 2.3: Distributions of the orbital parameters for the simulations. From top to bottom, left to right, the parameters depicted in each subplot are as follows: (1) the mass ratio, (2) the orbital energy, (3) the relative energy, (4) the circularity, (5) the radial-to-total velocity ratio, and (6) the total-to-virial velocity ratio. See the text for a detailed discussion.

The definitions we use for the circularity and orbital energy parameter to measure the orbital properties of our simulations are different than that in Jiang et al. (2015) used to sample the initial conditions, given by Eqs. 2.14 and 2.15, respectively. While both our definitions assume a point-mass for the satellite halo, the specific treatment in Jiang et al. (2015) models the central halo using an NFW profile and the satellite is initially placed at the virial radius. These assumptions do not hold for our simulations. First, the central halo is instead modeled using an NFWT profile. More importantly, the satellite is initially placed at the apocentre of the orbit. As the satellite falls in, its particles are disturbed by the central halo through tidal forces and it can lose mass. Some of the satellite's energy is transferred to the central halo, rearranging its particles as well. These processes will affect the orbital properties we measure for the satellite when it first reaches the virial radius. For these reasons, we use the satellite's position and velocity at $r_{200}$ directly from the simulations to measure the orbital parameters.

Each panel of Fig. 2.3 depicts the distribution of an orbital property for our isolated simulations in blue. For the three primary parameters used to setup our simulations ($\xi$, $v_r/v$, $v/v_{200}$), we include their target distributions in red. These distributions are given by Eqs. 2.6, 2.9, 2.10, respectively. From the plot, we find that the sampled values for $\xi$ and $v_r/v$ are well matched to their target distributions. There are slight excesses in mass ratio and radial velocity at $\xi \sim 0.3$ and $v_r/v \sim 0.9$, respectively, but these are marginal. The sampled values for $v/v_{200}$ vary more from their target distribution where we find very few simulations with $v/v_{200} > 1.4$. This is due to resampling unbound orbits. Larger values of $v/v_{200}$ are more likely to create unbound orbits given the other parameters. This leads to sampling excess values of $v/v_{200}$ at the lower end.

The top-right and middle-right subplots of Fig. 2.3 illustrate the orbital energy and circularity for our simulations. Identical plots to these can be found in Jiang et al. (2015), Fig. 3 and van den Bosch et al. (2018), Fig. 1. These works study the distributions of orbital parameters for infalling satellites in cosmological simulations. These papers agree fairly well with one another in terms of the shapes and locations of the distributions for $x_c$ and $\epsilon$. We reproduce the results for Jiang et al. (2015) in our plot as lime green lines considering our sample. They find the orbital energy is a skewed distribution with a peak at $x_c \sim 1.1$ and a sharp decline as $x_c$ increases, while the circularity is a more symmetric distribution with a broad peak at $\epsilon \sim 0.5$ and a more gradual decrease moving towards both tails at $\epsilon = 0$ and $\epsilon = 1$.

In contrast, for our set of isolated simulations, the circularity is slightly skewed towards low $\epsilon$. The range of circularity values in our simulations is $\epsilon \in [0.15, 0.85]$, excluding orbits on the very high end found in cosmological simulations. On the other hand, our orbital energy distribution has a nearly identical shape to that found in Jiang et al. (2015). The

main difference is the peak of the distribution is shifted to $x_c \sim 0.8$ in our case, and the range of values is broader. Despite this, our isolated simulations cover a similar range of energy and angular momentum to that expected in a cosmological scenario. One caveat to this comparison is the sampling distributions for $v_r/v$ and $v/v_{200}$ proposed by Jiang et al. (2015) had the poorest fits (i.e. the largest errors on the fitting parameters) for the mass ratio and host mass ranges occupied by our simulations. This was due to a lack of mergers with the correct characteristics in their simulations. While many mergers had the same mass ratio, the vast majority of those had lower host masses, $M \in [5\times10^{11}M_\odot, 2\times10^{13}M_\odot]$. Sampling the values of $v_r/v$ and $v/v_{200}$ poorly would trickle down into the produced orbital energy and circularity distributions, helping to explain some of the discrepancy between our sample and their results.

## 2.3 Measuring Properties of the Simulations

The objective of our model is to reproduce the structural properties of the remnant system during and after the merger of a satellite with a host halo. Here and in all cases, "remnant system" refers to the combined set of particles from both the satellite and central halo. To evaluate how well the model recreates the halo properties, we need to measure a baseline for these properties directly from the particles in the simulations to compare against. Some of the properties are used in tuning the model, while others are used to evaluate how well it functions. In particular, the satellite position and mass are used to calibrate the orbital model, while the remnant concentration, scale radius, shape, spin, and centre of mass offset are target properties we want to reproduce. This section describes which properties were measured, how they were calculated, and illustrates what their variation looks like during and after the merger in some example simulations.

### 2.3.1 Satellite Position and Mass

Fig. 2.4 illustrates the first orbit of the merger between a satellite halo and a central halo in one of our simulations. As shown, the satellite originally starts off at apocentre before falling towards the host halo. As the satellite orbits, its orbit decays due to dynamical friction and mass is stripped from its outer envelope due to tidal forces. The unbound material resides at different orbital radii, moving outwards. On the other hand, the bound core of the satellite will continue to move around and through the host halo during subsequent orbits.

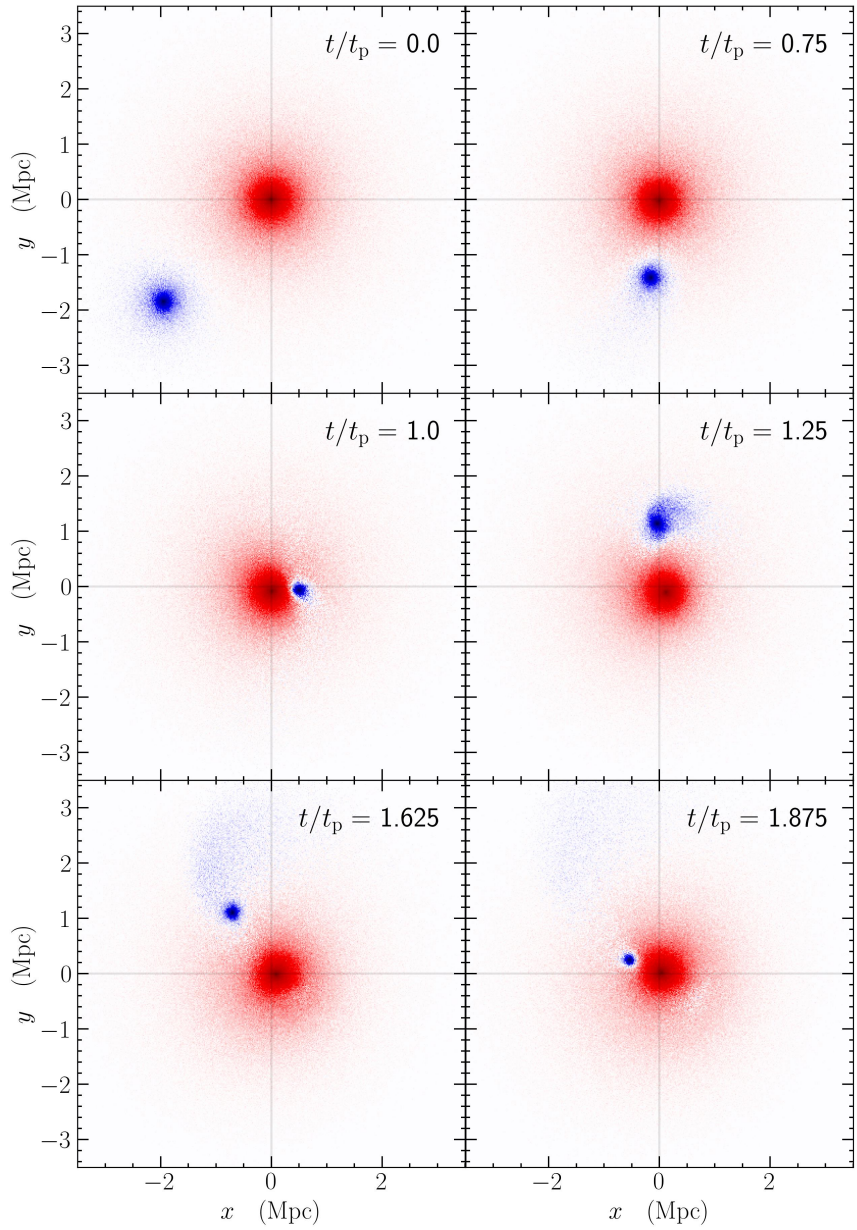



Figure 2.4: The first orbit of the merger between a satellite halo (blue) and a central halo (red) projected into the orbital plane in a simulation. From top to bottom, left to right, each subplot depicts a different snapshot of the orbit with increasing time from the start of the merger. These times are displayed in the top-right hand corner of each subpanel, relative to the time to pericentre. Note that the top-left subplot is the same as Fig. 2.1.

We need to quantify how much mass remains bound to the satellite as the merger progresses to use in our model. However, from just the images in Fig. 2.4 alone, it is not immediately clear which particles are associated with the satellite and which are unbound. To overcome this complication, we define the satellite mass, $M_s$, as the mass of the subset of satellite particles that are gravitationally self-bound in the satellite halo frame. This definition was originally described in Tormen et al. (1998) in order to identify subhalo masses. The subset of particles found is then used to track both the orbit and mass loss of the satellite halo with time.

Following Drakos et al. (2020), the satellite halo frame was identified as the densest point in position and velocity space. The position of highest local density, $\vec{x}_{\rm cod}$, for the satellite was calculated using a variation of the moving centre technique (Tormen et al., 1997). This technique requires calculating the centre of mass (COM) of the particles in progressively smaller spheres. Since each particle has the same mass, the position and velocity of the centre of mass are simply calculated using,

$$\vec{x}_{\rm com} = \frac{1}{N}\sum_i \vec{x}_i \qquad\qquad \vec{v}_{\rm com} = \frac{1}{N}\sum_i \vec{v}_i \tag{2.23}$$

where $\vec{x}_i$ and $\vec{v}_i$ are the positions and velocities of the particles, respectively, and $N$ is the number of particles considered. Initially, the sphere was centred on the centre of mass of all particles, and the radius was defined as the distance to the furthest particles, $R = r_t$. At each iteration, the radius was decreased by $0.1\,R$ and the sphere was recentred on the centre of mass of all particles within this new radius. This process was repeated until there were fewer than 100 particles in the sphere. The value of $\vec{x}_{\rm cod}$ for the satellite was taken to be the centre of mass of all the particles within the final sphere. On the other hand, the velocity of the highest local density, $\vec{v}_{\rm cod}$, was calculated as the centre of mass velocity of all particles within the original sphere of radius $r_t$ centred on the peak density position.

Once the frame of the satellite was defined, the self-bound particles were identified. First, the energy of each particle was calculated in this frame (i.e. the particle positions and velocities were shifted by $\vec{x}_{\rm cod}$ and $\vec{v}_{\rm cod}$, respectively). Here, the total energy for each particle was a sum of their kinetic, $K_i$, and potential, $P_i$, energies, assuming a spherical potential (Drakos et al., 2022),

$$K_i = \frac{1}{2}M_p\,\|\vec{v}_i\|^2 \qquad\qquad P_i \approx -GM_p^2\left[\frac{N(<r_i)}{r_i} + \sum_{j,\,r_j>r_i}^{N}\frac{1}{r_j}\right] \tag{2.24}$$

where $r_i = \|\vec{x}_i\|$ is the distance of the $i^{\rm th}$ particle from the satellite's centre. It has been previously shown that the total energy calculation is insensitive to assuming a spherical

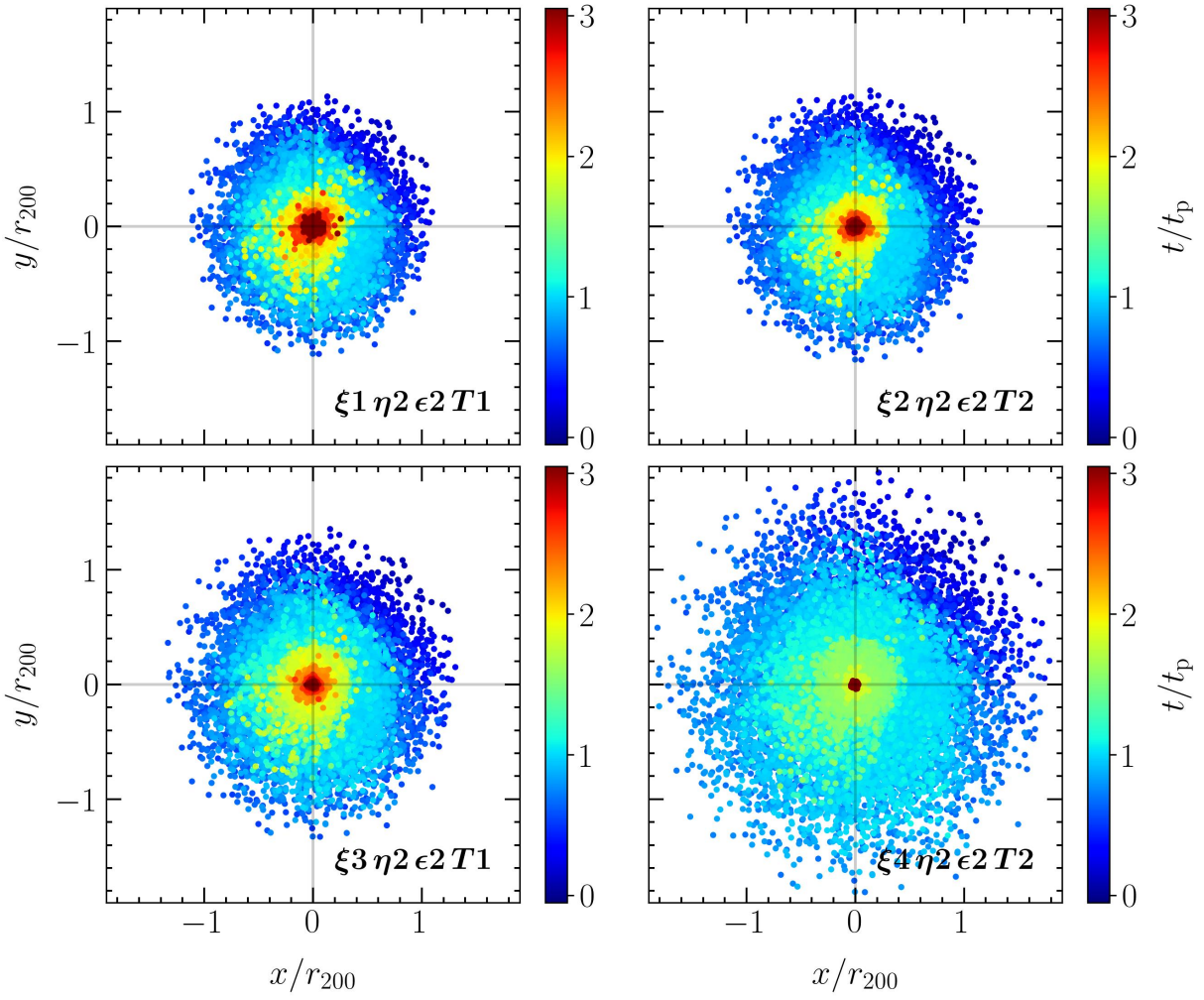



Figure 2.5: Initial spatial distribution of the satellite halo particles in the orbital plane. The colourbar depicts the time each individual particle first unbinds from the satellite, relative to the time to pericentre. The coordinates in these plots are shown relative to the virial radius of the central halo.

potential compared to calculating the potential using particles pairs (see Drakos et al., 2020, Appendix A). Particles that have negative total energy ($E_i = K_i + P_i < 0$) are considered to be self-bound, while all other particles (with $E_i > 0$) are removed from consideration. We iterate this process until the number of self-bound particles converges. The final subset of particles that remain are the particles that make up the bound satellite halo. The satellite mass is then simply the total mass of the self-bound particles, while the satellite halo's orbit is defined by the position of highest local density in each snapshot.

Fig. 2.5 shows the initial spatial distribution of the satellite halo particles coloured by the time the particles first unbind from the satellite. In the first snapshot, all satellite particles are considered self-bound. We find that particles are removed from the satellite in shells outwards to inwards. There is a preferential direction to how the particles are removed corresponding to the position of the central halo relative to the satellite.

It is important to note that at each timestep, only satellite particles that were bound in the previous snapshot are considered as part of the bound satellite in the next snapshot. In other words, particles that were previously unbound cannot become bound to the satellite again at a later time. Furthermore, when calculating the position and velocity of the satellite, $\vec{x}_{\rm cod}$ and $\vec{v}_{\rm cod}$, only the self-bound particles at a given time are considered. Once all the satellite particles are unbound, the orbit of the satellite becomes undefined. To avoid this, a minimum mass of 0.5% the initial satellite mass was set for the satellite. Once the satellite reached this mass, no additional particles were removed from the self-bound set in subsequent snapshots.

Finally, the position and velocity of the central halo were determined using the same method as above (i.e. the procedure for calculating $\vec{x}_{\rm cod}$ and $\vec{v}_{\rm cod}$), except in each snapshot we considered all central halo particles. Very few particles unbind from the central halo due to the influence of the satellite. This implies the mass of the central halo does not change from its initial mass during the merger. However, forces from the satellite cause the central halo to drift from its initial position. Since our orbital model assumes the host halo is stationary at the centre of the frame at all times, we need to shift the satellite's position and velocity when we measure its orbit in the simulation to account for this drift.

Fig. 2.6 demonstrates changes in the satellite halo as it orbits during the merger for a set of simulations. In the left column, we find that the major axis of the orbit precesses with time. The middle column depicts the radial separation between the satellite and central halos' positions of highest local density. We see that due to dynamical friction, the orbit of the satellite decays. Each subsequent apocentre of the orbit occurs closer to the host halo's centre. The satellite also experiences large amounts of mass loss. This is shown in the right column. We find that the satellite loses a significant fraction of its mass

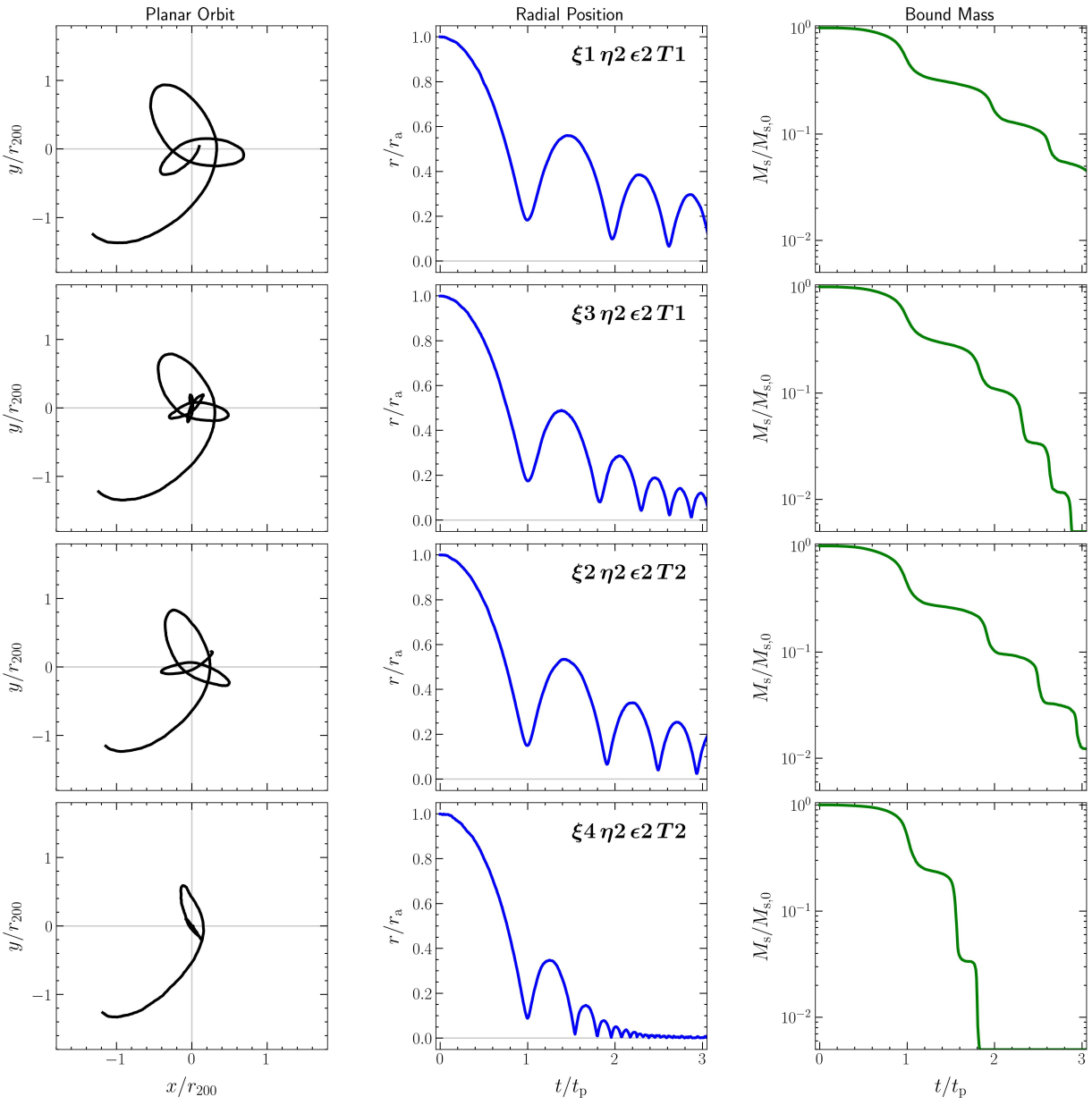



Figure 2.6: Orbital motion of the satellite around the central halo (left), satellite radial position (middle), and satellite bound mass (right) during the merger. The satellite's radial position and bound mass are scaled relative to its initial position and mass, respectively, while the satellite's orbit is scaled relative to the virial radius of the central halo. The timescale in these plots is shown relative to the time to pericentre.

at the first pericentric passage, with further mass loss occurring at later pericentres. Very little mass loss occurs at all other positions. In most cases, at least 90% of the satellite's particles are stripped by the central halo after only a few orbits.

Of the simulations shown in Fig. 2.6, $\xi 4\,\eta 2\,\epsilon 2\,T2$ has the most unique behaviour. Compared to the other simulations, the satellite's orbit becomes highly radial after the initial infall, the satellite loses its mass at the quickest rate, and the satellite merges with the host halo by the second orbit. These are all caused by the high mass ratio between the two halos. This simulation has a mass ratio that roughly corresponds to a 3:1 merger, while the other simulations have mass ratios of at least 8:1. Mergers with high $\xi$ have central and satellite halos with more equal masses. This causes the satellite to experience greater amounts of dynamical friction, leading to a more rapid orbital decay. In addition, the satellite passes closer to the host halo, resulting in increased mass loss.

### 2.3.2 Concentration and Scale Radius

The halos in our binary merger simulations were initially modeled using NFWT profiles. In cosmological simulations, dark matter halos exhibit a universal density profile regardless of mass or cosmological model (Navarro et al., 1996, 1997). Since the halos in these simulations undergo mergers, it implies that after the merger, the remnant halos should maintain the same general profile as their progenitors (i.e. the remnant profiles follow the same functional form as the progenitors, although the specific model parameters for the profiles may change). This has been shown to be the case in isolated systems (see e.g. Boylan-Kolchin & Ma, 2004; Aceves & Velázquez, 2006; Kazantzidis et al., 2006; McMillan et al., 2007; Vass et al., 2009; Drakos et al., 2019b), where the halo density profile was found to be largely robust to major mergers despite the relaxation that occurs. As a result, we fit NFWT profiles to the individual halos and the remnant system for each snapshot recorded. It is unclear how well profiles will be fit during the merger since this is when the system is most unrelaxed, but this is something we will explore.

To determine the NFWT parameters ($r_s$, $\rho_0$, $y_d$) of each halo and the remnant system, we fit the circular velocity profile using a $\chi^2$-minimization procedure. As opposed to using the density profile directly, fitting the circular velocity is less susceptible to noise (Vera-Ciro et al., 2013). We estimate the circular velocity profile by first taking the particles, shifting them into the frame of highest local density, and sorting them by radial position. Then, the particles are placed into logarithmically spaced bins. An equal number of particles is assigned to each bin. For the satellite halo, we use $N_i = 35$ particles per bin. This number is scaled by the inverse mass ratio, $\xi^{-1}$, for the central halo and remnant system. Finally,

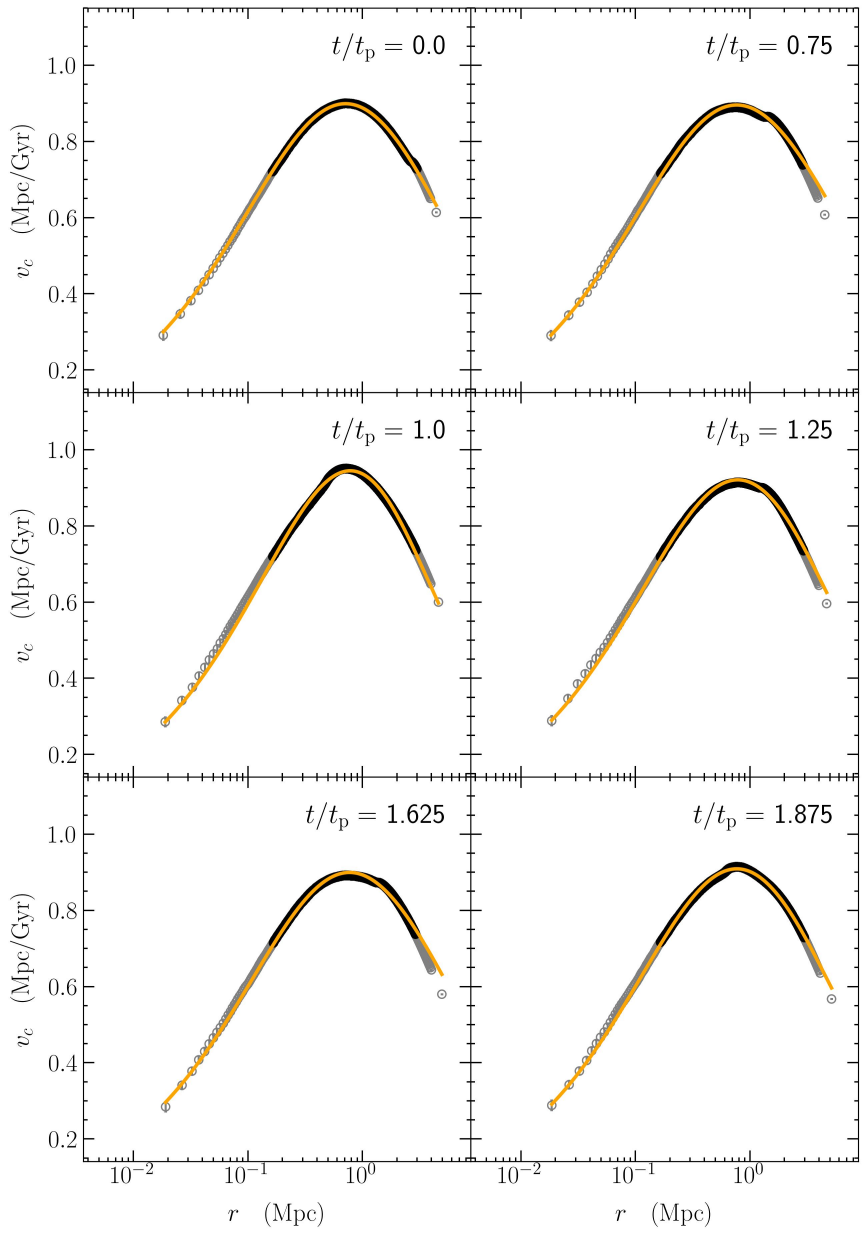



Figure 2.7: Remnant halo circular velocity profiles for the simulation shown in Fig. 2.4. The black points show the profile measured in the simulation (grey points excluded), while the orange line is the best-fit model. From top to bottom, left to right, each subplot depicts a different snapshot with increasing time from the start of the merger. These times are displayed in the top-right hand corner of each subpanel, relative to the time to pericentre.

as in Vera-Ciro et al. (2013, 2014), the profiles are fit by minimizing the residual,

$$\chi^2 = \frac{1}{N_{\rm bins}} \sum_{i=1}^{N_{\rm bins}} \frac{\left[\ln(v_c^2) - \ln(v_{c,i}^2)\right]^2}{2\left[\ln(\Delta v_{c,i}^2)\right]^2} \tag{2.25}$$

using the function `minimize` from the Python library LMFIT (Newville et al., 2016). In this expression, $N_{\rm bins}$ is the number of bins considered in our fit, $v_c$ is the circular velocity of the fitted profile at radius $r_i$, and $v_{c,i}$ is the circular velocity of the simulated halo at $r_i$. The circular velocity profile measured in the simulation is given by,

$$v_{c,i} = \sqrt{\frac{GM(<r_i)}{r_i}} \quad \text{where} \quad M(<r_i) = \sum_{j<i+1} M_p N_j \tag{2.26}$$

and $r_i = r_{u,i}$, the upper bin edge for the $i^{\rm th}$ radial bin. We use the upper bin edge since the circular velocity depends on the total mass of the particles. As in Balmès et al. (2014), the error in the circular velocity, $\Delta v_{c,i} = v_{c,i}/\sqrt{M(<r_i)/M_p}$, encodes the Poisson error since we are counting particles.

The fits were performed excluding the inner 5% and outer 5% of bins. In these ranges, we expect the circular velocity to poorly fit the model. The innermost radial bins are affected by random sampling of the particles. The profile in the outermost radial bins is no longer well represented by an NFWT profile due to low densities of particles (see Drakos et al., 2022, Section 3.1). The NFWT parameters that minimize Eq. 2.25 are said to be the best-fit parameters of the model to the data.

Fig. 2.7 plots the remnant system circular velocity (i.e. all particles) and its best-fit profiles for the first orbit of the merger in one of our simulations. We find that an NFWT profile is well fit to the circular velocity at all times shown. As the satellite orbits the central halo, we see its affect on the circular velocity as a slight enhancement in the profile. This is most pronounced at $t = t_p$, when the enhancement overlaps with the already existing peak in circular velocity. Despite this, an NFWT profile is still well fit.

The concentration of a halo quantifies the size of its central core relative to its outer envelope. How concentration is measured depends on the parameters used to calculate it. Here we consider a standard definition of concentration, $c = r_{\rm vir}/r_s$, where $r_{\rm vir}$ is the virial radius and $r_s$ is determined from the NFWT fit parameters. For halos in cosmological simulations, the virial radius describes the radius within which the system is in virial equilibrium. In practice, the virial radius is typically defined as the radius at which the mean density of the halo is some multiple of a reference density. However, this definition

only has a physical interpretation for systems that are accreting continuously from the surrounding background material. There is no clear physical analogue to this quantity in isolated simulations. As a result, we consider an analogous definition for $r_{\rm vir}$ in our isolated simulations using a different reference density,

$$\bar{\rho}_i(< r_{\rm vir}) = \rho_t \quad \text{where} \quad \rho_t = \frac{M(< r_{200})}{\frac{4\pi}{3} \times r_{200}^3} \tag{2.27}$$

and $r_{200}$ is the value of the halo's virial radius set in the initial conditions. When measuring $r_{\rm vir}$ for the remnant system, we use $r_{200}$ for the central halo. The quantity $\bar{\rho}_i$ is the average density of the halo within a radius $r_i$,

$$\bar{\rho}_i = \frac{M(< r_i)}{\frac{4\pi}{3} \times r_i^3} \tag{2.28}$$

Linear interpolation between the nearest values of $\bar{\rho}_i$ that bracket $\rho_t$ is used to find $r_{\rm vir}$. There are two additional parameters related to the virial radius that are sometimes used in structural property definitions. These are the virial mass, $M_{\rm vir} = M(< r_{\rm vir})$, the total mass within the virial radius, and the virial velocity, $v_{\rm vir} = \sqrt{GM_{\rm vir}/r_{\rm vir}}$, the circular velocity at the virial radius. Both of these quantities are used in one definition for the spin parameter (Bullock et al., 2001).

Figs. 2.8-2.9 depict how the NFWT parameters for the central halo and remnant system change during the merger for a set of simulations. We do not include results for the satellite halo since our modeling only requires its initial profile. In Fig. 2.8, we see that mergers lead to oscillations in scale radius for the whole remnant system. This behaviour is consistent with what is seen in cosmological simulations (Wang et al., 2020). At early times, the satellite has sufficient mass, so its direct position causes changes in structure since we are spherically averaging over an asymmetric system. Once the satellite loses a large fraction of its mass, the remnant's structural changes mirror the central halo. At this point, the satellite's motion itself has a smaller effect on the structural changes. The offset between the scale radius curves is caused by the position of the unbound satellite material.

The structure of the central halo responds to the motion of the satellite as it orbits. This effect is not seen in minor mergers since the perturbation caused by the satellite is too small to influence the central halo particles significantly. We find two types of responses for the central halo in Fig. 2.8: (1) $r_s$ gradually declines to a minimum value well before $t = t_p$ (e.g. $\xi 1\, \eta 2\, \epsilon 2\, T1$ and $\xi 3\, \eta 2\, \epsilon 2\, T1$), and (2) $r_s$ sharply drops to a minimum value slightly after $t = t_p$ (e.g. $\xi 2\, \eta 2\, \epsilon 2\, T2$ and $\xi 4\, \eta 2\, \epsilon 2\, T2$). For both types however we still find sharp oscillations at $t > t_p$. The type of central halo response in scale radius varies

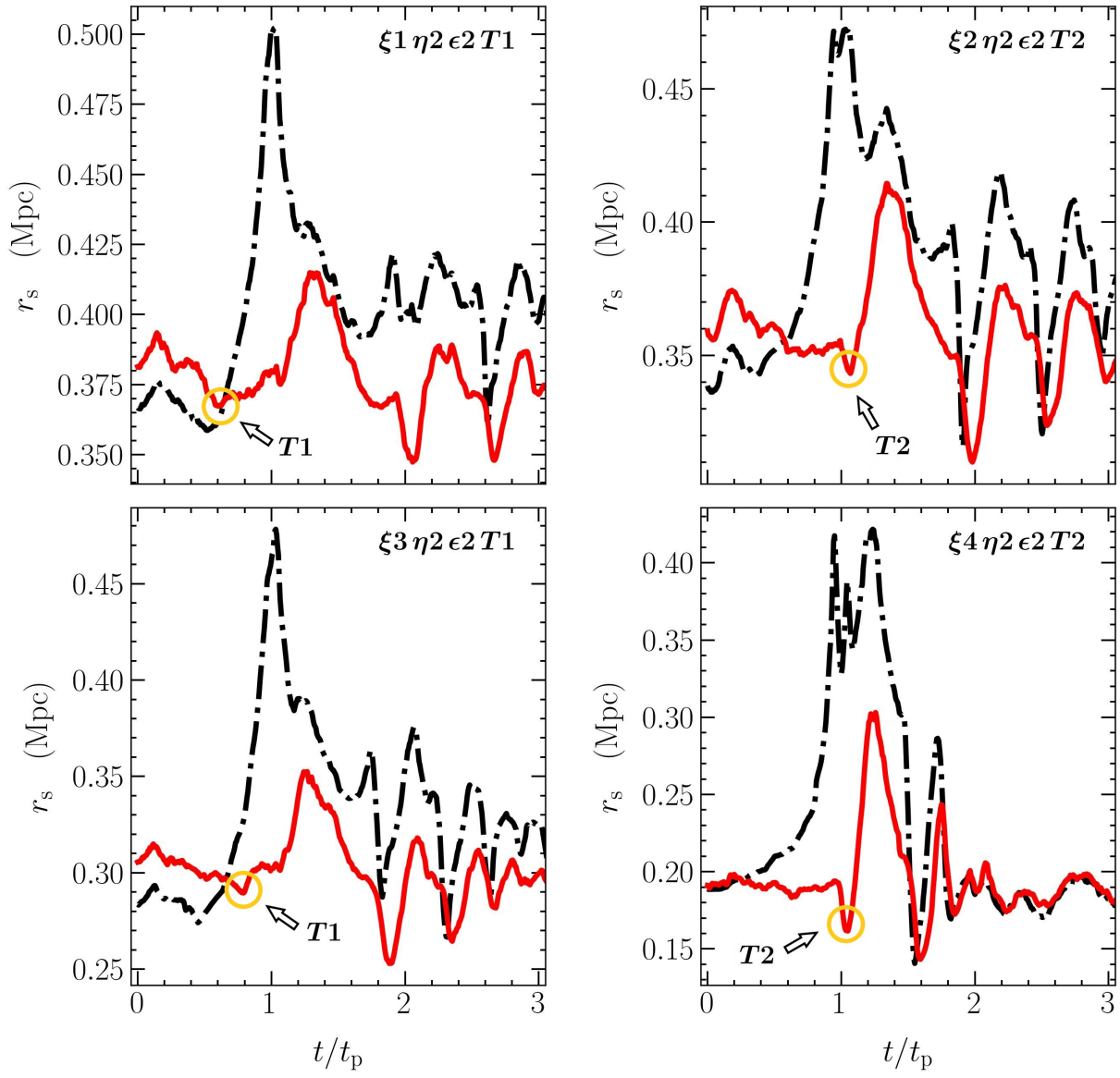



Figure 2.8: Scale radius for the central halo (red) and remnant system (black) during the merger. The gold circle highlights the minimum central halo scale radius prior to the first oscillation peak which is used to classify the type of central halo response. The timescale in these plots is shown relative to the time to pericentre.

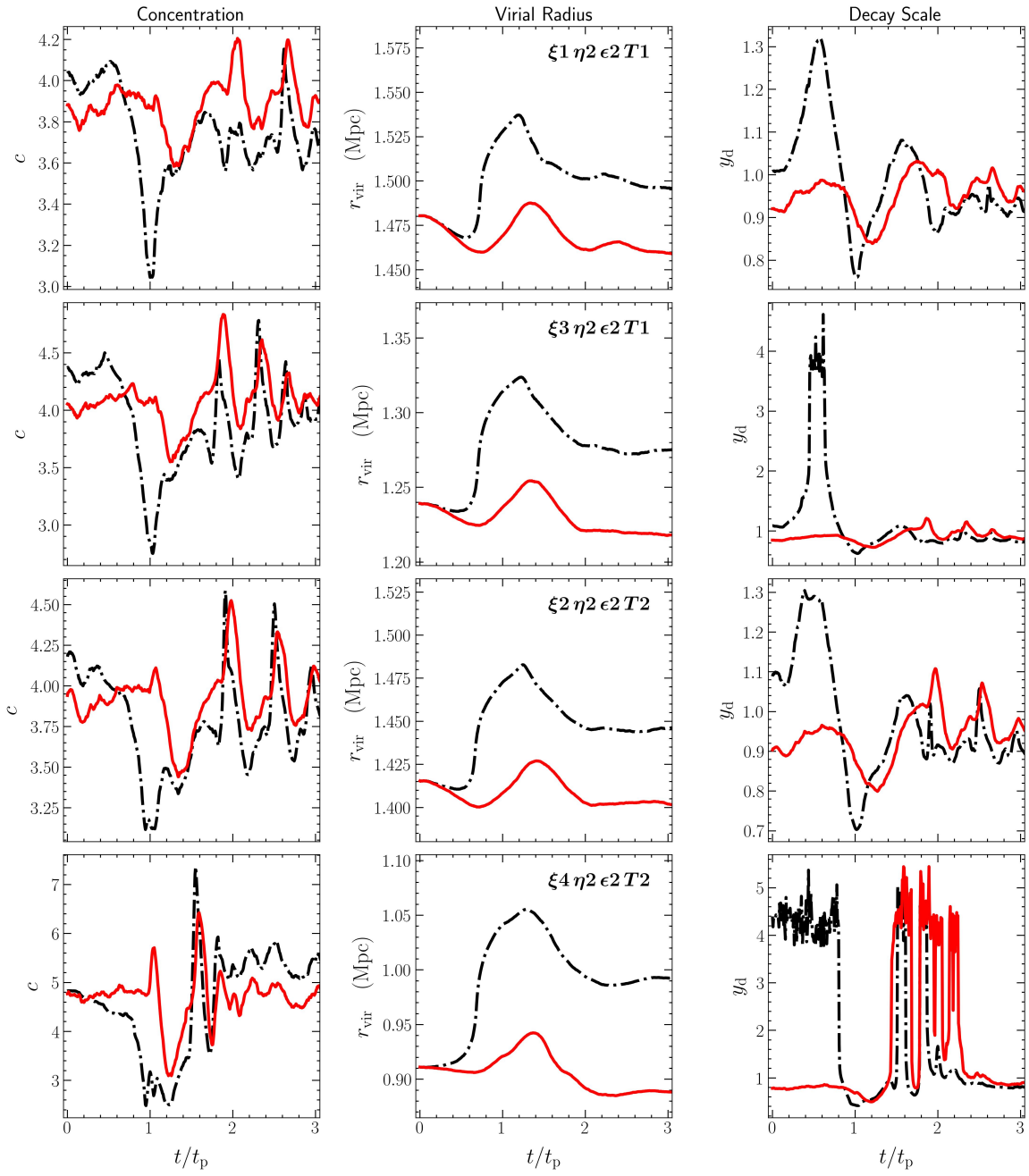



Figure 2.9: Concentration (left), virial radius (middle), and exponential truncation scale (right) for the central halo (red) and remnant system (black) during the merger. The timescale in these plots is shown relative to the time to pericentre.

primarily with circularity. Satellites on radial orbits, corresponding to mergers with low $\epsilon$, were able to produce a large enough compression on the central halo particles, leading to the sharp drop in scale radius at pericentre we see in type 2. High circularity mergers were unable to do this, as the satellite did not travel far enough into the core of the central halo's potential on its initial infall. The more gradual decrease in scale radius we see in type 1 results from an instability in the initial central halo profile (see Fig. A.1 for an illustration of this effect). These findings are discussed in more detail in Section 4.1 when we attempt to model the response.

Concentration is inversely proportional to scale radius. As a result, changes in concentration during the merger experience behaviour opposite to that which is shown in Fig. 2.8. For the central halo, its virial radius shrinks as the merger progresses. This implies the central halo expands and its density moves outwards to compensate. On the other hand, the virial radius grows for the remnant system. This is caused by the satellite moving inwards to within the original virial radius. Some of its unbound material is also placed within this radius. This increases the density within the initial virial radius, moving it outwards to compensate.

Finally, for the remnant system in most simulations, the scale radius does not initially decrease as the satellite falls towards pericentre. We would expect $r_s$ to drop since we have a dense satellite moving towards the centre of the system. The behaviour we do find is in fact the opposite, where $r_s$ is maximized at $t = t_p$. This is caused by the NFWT profile's truncation scale. At $t = t_p$, the truncation scale is minimized. Since the profile is exponentially truncating at a smaller radius, the scale radius needs to increase to compensate. In general, we find the truncation scale and scale radius are anti-correlated when fitting an NFWT profile to the circular velocity profile (see Fig. A.4 and its discussion). This effect also explains why the initial $r_s$ for the remnant system is smaller than that for the central halo. The remnant profile has a larger truncation scale causing the scale radius to move inwards in our fitting. We investigated fitting NFWT profiles using a constant $y_d$ and found a more pronounced decrease in scale radius at pericentre (see Appendix A.2 for details). This implies the increase in scale radius is not artificial, but rather is caused by the specific profile being fit. However, we did not use the constant $y_d$ fits since in general they were worse, the central halo median response was poorly constrained (i.e. more uncertainty in its form), and when trying to model the response, the model parameters ($A$, $t_{r_{s,c},\max}$) did not scale well with the initial conditions as opposed to the fits where $y_d$ was a free parameter.

### 2.3.3 Shape

The shape of a halo is related to its major, intermediate, and minor axis lengths denoted by $(a, b, c)$, respectively. Measured in the frame of highest local density, the relative axis lengths can be obtained directly by diagonalizing the second moment of the mass distribution tensor (Wong & Taylor, 2012),

$$\mathbf{T_M}^2 = M_p \sum_{i=1}^{N} \vec{x}_i \otimes \vec{x}_i \tag{2.29}$$

where here we are summing over the outer products of each coordinate position in the halo with itself for all particles. The three eigenvalues, $\lambda_i$, obtained from the diagonalization of $\mathbf{T_M}^2$ are directly related to the axis lengths,

$$\{a, b, c\} = \left\{ |\lambda_1|^{\frac{1}{2}}, |\lambda_2|^{\frac{1}{2}}, |\lambda_3|^{\frac{1}{2}} \right\} \tag{2.30}$$

where we assume that the axis lengths are relabelled so that $a > b > c$. An equivalent method to calculating the axis lengths involves finding the singular value decomposition (see e.g. Klema & Laub, 1980) of the coordinate matrix,

$$\mathbf{X} = \left[ \vec{x}_1^{\,T} \middle| \vec{x}_2^{\,T} \middle| \cdots \middle| \vec{x}_N^{\,T} \right] \tag{2.31}$$

If the singular values of $\mathbf{X}$ are denoted by $(s_1, s_2, s_3)$, then the axis lengths are given by,

$$\{a, b, c\} = \left\{ \frac{s_1}{\sqrt{N}}, \frac{s_2}{\sqrt{N}}, \frac{s_3}{\sqrt{N}} \right\} \tag{2.32}$$

since the singular values are sorted from largest to smallest by default. In practice, we calculate the relative axis lengths using singular value decomposition as opposed to eigenvalue decomposition due to its improved speed and stability (Klema & Laub, 1980).

The two main shape parameters for the halo are then related to the ratio of these axis lengths: $c/a$, $c/b$. Note that by definition, these shape parameters are bound between 0 and 1. Other versions of the shape parameters based on the major, intermediate, and minor axes lengths are defined in the literature as well (see e.g. Wong & Taylor, 2012; Lau et al., 2021). However, we do not consider these parameters since they are degenerate with the axis ratios $c/a$ and $c/b$. For example, in our simulations, the shape parameters elongation

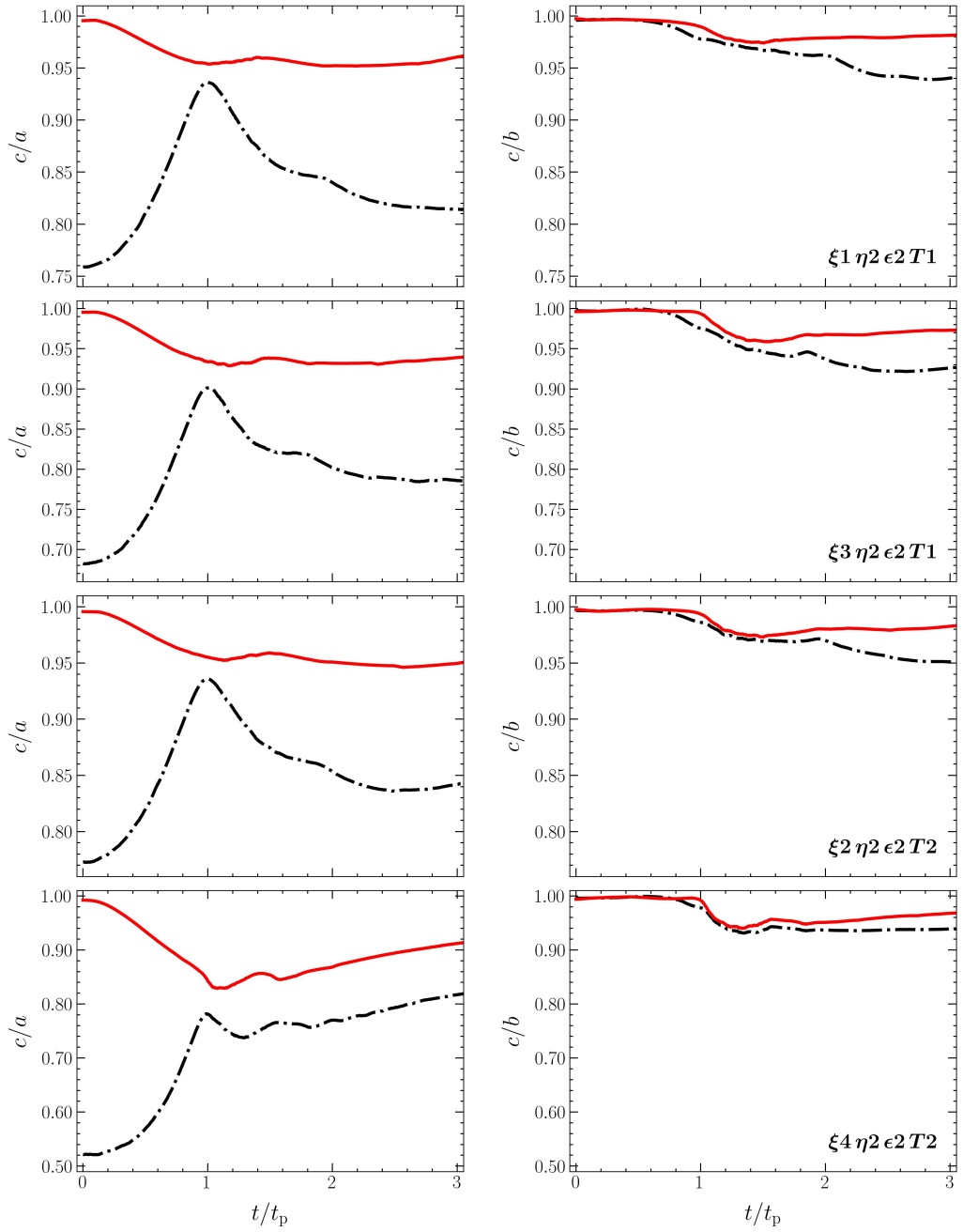



Figure 2.10: Minor-to-major axis ratio (left) and minor-to-intermediate axis ratio (right) for the central halo (red) and remnant system (black) during the merger. The timescale in these plots is shown relative to the time to pericentre.

and triaxiality have similar evolution to the axis ratios $c/a$ and $c/b$, respectively, although their values span a different range.

Fig. 2.10 illustrates how the shape parameters for the central halo and remnant system change during the merger for a set of simulations. For the remnant system, the minor-to-major axis ratio mostly traces the satellite's position during its orbit. It begins low since the satellite starts far from the central halo. As the satellite infalls, the value of $c/a$ increases until it reaches a maximum at pericentre. There it declines again as the satellite moves out towards apocentre. At late times, the motion of the satellite does not cause oscillations in $c/a$ since its mass is too low. The position of the unbound material sets the final value of $c/a$. The minor-to-intermediate axis ratio traces the off-major axis deviation. At $t = 0$, $c/b \sim 1$ since along the second axis the satellite and central halos are aligned. During the merger, the system only experiences small deviations along this axis, gradually growing with each orbit.

For the central halo, both the minor-to-major and minor-to-intermediate axis ratios start at $\sim 1$ due to the spherically symmetric nature of the NFWT profile. We find minimal changes in the shape parameters due to the merger. The most noticeable effects are seen just after the satellite reaches the first pericentre of its orbit. This indicates changes in the central halo's structure are slightly delayed with the satellite's position. Finally, larger mass ratios lead to the central halo becoming more ellipsoidal as seen in $\xi 4\,\eta 2\,\epsilon 2\,T2$.

### 2.3.4 Spin

Spin provides a measure for the amount of rotation in a system. It was originally defined using the energy of the system (Peebles, 1971),

$$\lambda_P = \frac{J\sqrt{|E|}}{GM^{5/2}} \qquad\qquad J = M_p \sum_i \|\vec{x}_i \times \vec{v}_i\| \tag{2.33}$$

where $E = K + P$ and $J$ are the total energy and angular momentum of the system, respectively. If we consider the remnant system, we would include both the satellite and central halo particles (i.e. $M = M_s + M_c$). Note that calculating $E$ and $J$ requires shifting particles into the frame of highest local density. Furthermore, the total kinetic

and potential energies of the system were calculated as described in Bett et al. (2010),

$$K = \frac{1}{2} M_p \sum_i \|\vec{v}_i\|^2 \tag{2.34}$$

$$P = \left(\frac{N^2 - N}{N_{\rm sel}^2 - N_{\rm sel}}\right)\left(\frac{-GM_p^2}{\varepsilon}\right)\sum_{i=1}^{N_{\rm sel}-1}\sum_{j=i+1}^{N_{\rm sel}} -W\left(\frac{\|\vec{x}_i - \vec{x}_j\|}{\varepsilon}\right) \tag{2.35}$$

where $N$ is the total number of particles, $N_{\rm sel}$ is the number of randomly selected particles used to approximate the entire distribution, and $\varepsilon$ is the softening length in the simulations. We calculate the potential using a subset of particles due to computational limitations. The same set of particles was selected for every snapshot in order to minimize noise in the measurement of $\lambda_P$ due to random sampling.

As in Drakos et al. (2019a), we set $N_{\rm sel} = 5000$ particles for the satellite halo. The number of particles picked for the central halo was scaled by the inverse mass ratio (i.e. $N_{\rm sel} = 5000\,\xi^{-1}$) to keep the fraction of particles sampled from each halo consistent. These choices were sufficient to calculate $P$ accurately. $W$ is the smoothing kernel used for force calculations in `GADGET-2` (Springel et al., 2001),

$$W(x) = \begin{cases} \frac{16}{3}x^2 - \frac{48}{5}x^4 + \frac{32}{5}x^5 - \frac{14}{5}, & 0 \le x < \frac{1}{2} \\ \frac{1}{15x} + \frac{32}{3}x^2 - 16x^3 + \frac{48}{5}x^4 - \frac{32}{15}x^5 - \frac{16}{5}, & \frac{1}{2} \le x < 1 \\ -\frac{1}{x}, & x \ge 1 \end{cases} \tag{2.36}$$

An alternative definition for the spin parameter used in the literature (see e.g. Macciò et al., 2007; Wong & Taylor, 2012) is proposed by Bullock et al. (2001) and is related to the virial parameters of a halo,

$$\lambda_B = \frac{J}{\sqrt{2} M_{\rm vir} r_{\rm vir} v_{\rm vir}} \tag{2.37}$$

This parameter is often preferred in the literature since it does not require calculating the full energy. However, due to the uncertain nature of the virial radius in isolated simulations, $\lambda_B$ may not be suitable in our case. This will be investigated. The parameters $\lambda_B$ and $\lambda_P$ are equivalent if the halo is virialized and follows an isothermal profile.

Fig. 2.11 presents how the spin parameters for the central halo and remnant system change during the merger for a set of simulations. In all simulations, curves for the Peebles and Bullock spin parameters have the same general shape with different absolute values. For the central halo, it initially has no net spin. The halo picks up spin as the satellite's

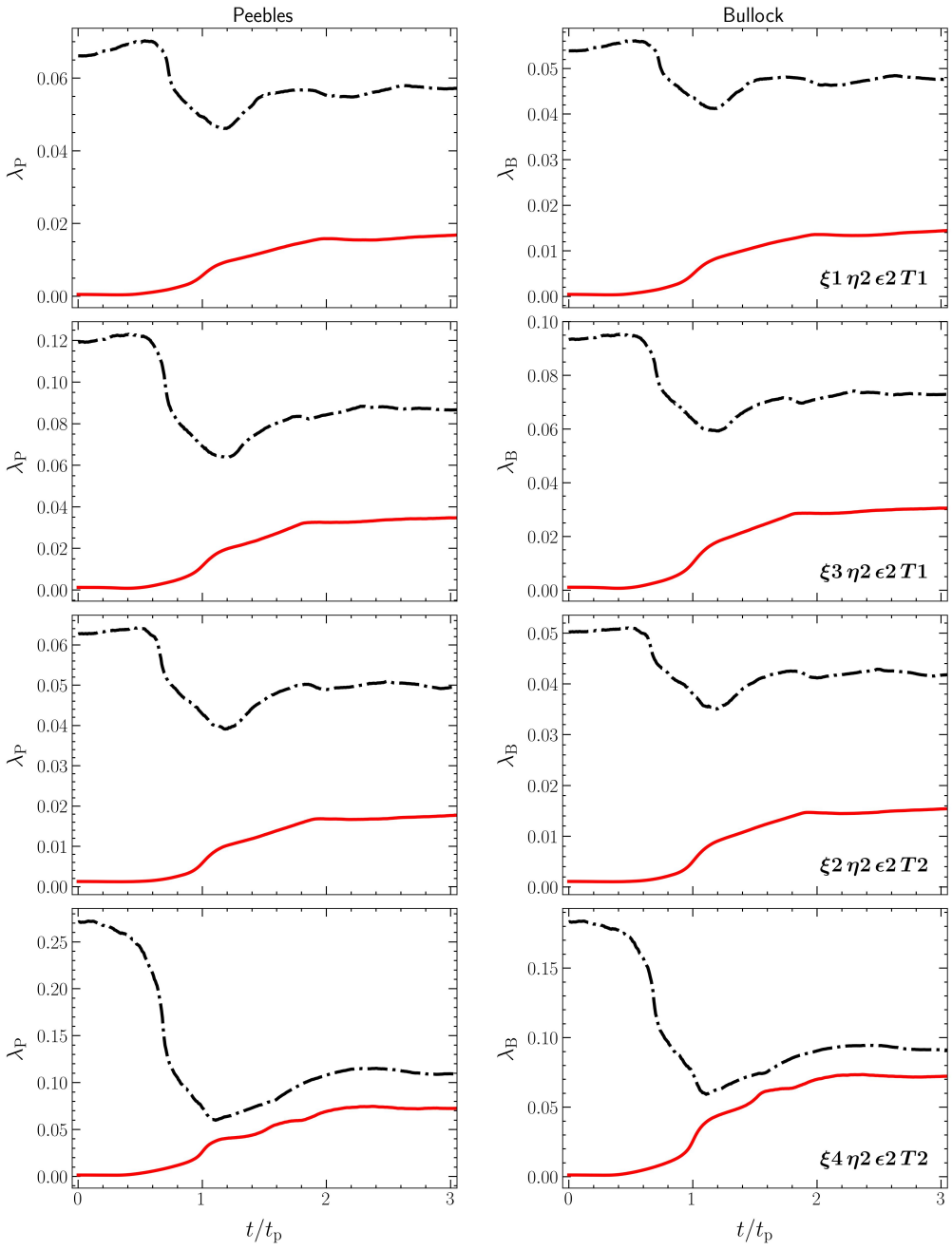



Figure 2.11: Peebles spin parameter (left) and Bullock spin parameter (right) for the central halo (red) and remnant system (black) during the merger. The timescale in these plots is shown relative to the time to pericentre.

angular momentum is transferred to it. The largest increases in spin occur as the satellite reaches a pericentre of the orbit.

For the remnant system, the initial spin quantifies the satellite's initial angular momentum. This sharply drops to a minimum just after the satellite first reaches pericentre, and only slightly increases as the merger progresses. This is caused by the satellite's orbital decay and mass loss. The amount of angular momentum lost by the satellite is not fully compensated by the gain in central halo spin, leading to a net decrease in the remnant's spin. Generally, the amount of spin lost by the remnant system scales with increasing mass ratio.

### 2.3.5 Asymmetry

Asymmetry, or centre of mass offset, is a measure of the distribution of mass in a system. It is defined as the distance between the centre of mass of the halo and the particle of highest local density, scaled by the virial radius of the halo,

$$x_{\rm off} = \frac{\|\vec{x}_{\rm com} - \vec{x}_{\rm cod}\|}{r_{\rm vir}} \tag{2.38}$$

This parameter is often used as a measure for the relaxedness, or dynamical state, of a system (see e.g. Neto et al., 2007; Ludlow et al., 2013). A halo might be considered dynamically relaxed if it satisfies $x_{\rm off} < 0.07$, although it must satisfy other criteria as well. Measures of relaxation provide insights into the merger state of a system, and can be used to quantify when the satellite and central halos have merged.

Fig. 2.12 shows the central halo's and remnant system's asymmetry during the merger for a set of simulations. For the central halo, asymmetry captures the sloshing motion of its particles in response to the satellite's orbit. Initially, the centre of mass and position of highest local density overlap. As the satellite merges, the central halo's $\vec{x}_{\rm cod}$ stays at the centre of the frame, but its $\vec{x}_{\rm com}$ moves in and out as its particles move in and out. This causes its asymmetry to peak when the satellite reaches apocentre.

For the remnant system, asymmetry captures the same behaviour as the $c/a$ shape parameter. At the beginning of the merger, the remnant's $\vec{x}_{\rm com}$ is shifted outwards due to the satellite's initial separation, while its $\vec{x}_{\rm cod}$ is at the centre of the frame. Its asymmetry is then minimized when the satellite first reaches pericentre and is maximized when the satellite moves back out to apocentre. The asymmetry settles to some value once the satellite loses most of its mass. The exact value is set by how the unbound mass is distributed in the system.

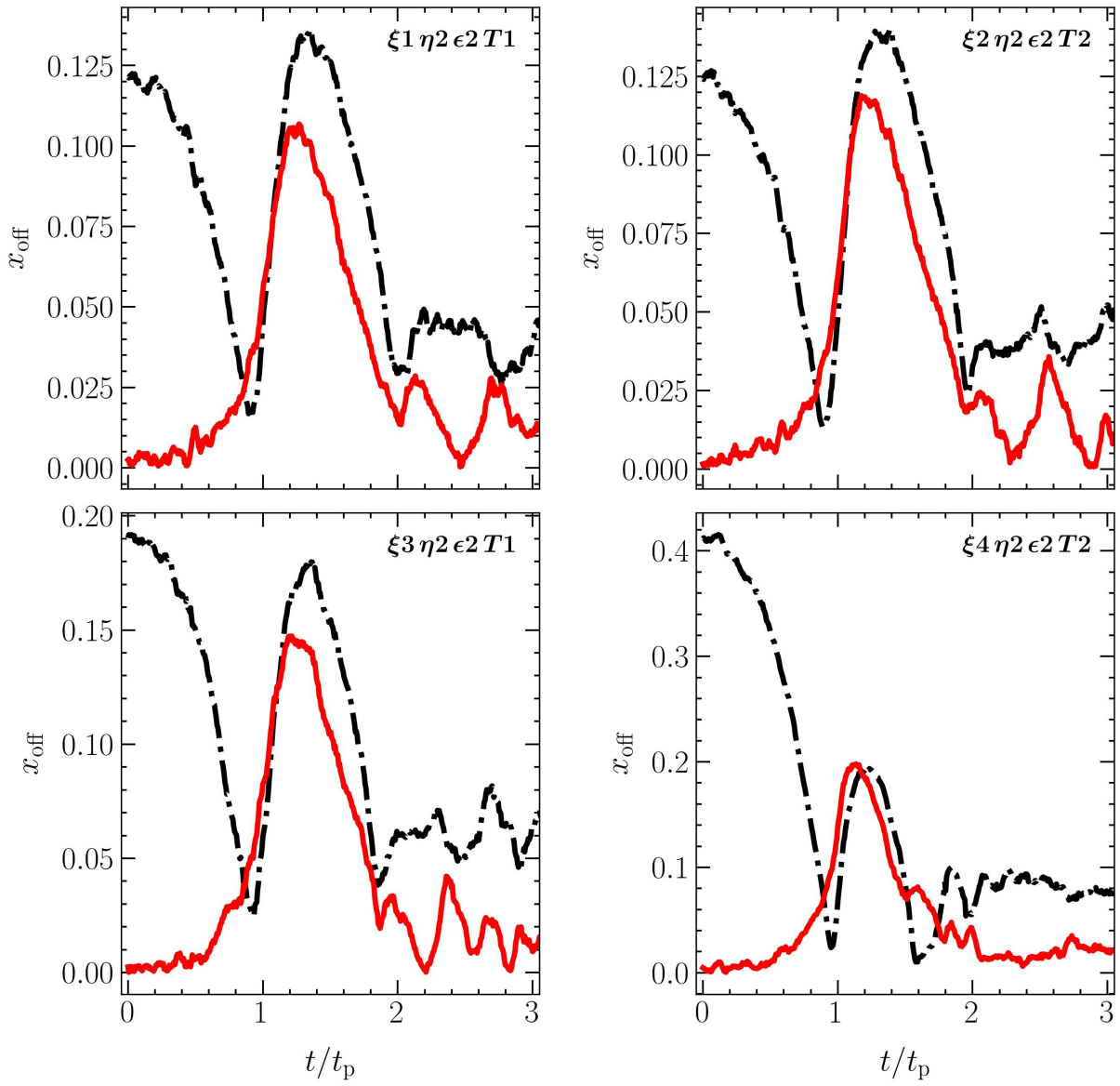



Figure 2.12: Asymmetry for the central halo (red) and remnant system (black) during the merger. The timescale in these plots is shown relative to the time to pericentre.

## 2.4 Fiducial Simulation Set

In building our model, we are primarily interested in replicating the median evolution of structural parameters during a merger. However, we also want to explore how well the model predicts structure for individual systems. Given the total number of simulations we have, it is not feasible to show predictions for every one of them. Instead, we define a subset of simulations, which represent typical mergers, to demonstrate our results.

Table 2.1 describes the initial conditions of the simulations in the fiducial set. These were selected using the distributions for mass ratio, relative energy, and circularity shown in Fig. 2.3. The relative energy and angular momentum parameters are degenerate with $v_r/v$ and $v/v_{200}$. While our simulations sampled the velocity ratios to setup the initial conditions, a majority of papers examine orbital energy and angular momentum as initial conditions instead. Moreover, the mass ratio, orbital energy, and angular momentum of the merger were used to model the satellite's orbit and mass loss. As a result, we choose the fiducial set using these parameters.

Our fiducial set consists of **16** simulations, eight for each type of central halo response. For a given response type, the eight simulations are selected using the divisions shown as orange-dotted lines in Fig. 2.3. These divisions represent percentiles of the distribution, and they separate it into groups. For mass ratio, there are four groups and the divisions depict the $25^{\text{th}}$-percentile, $50^{\text{th}}$-percentile, and $75^{\text{th}}$-percentile of the distribution. Similarly, for relative energy and circularity, there are three groups and the divisions split the distributions by the $33^{\text{rd}}$-percentile and $67^{\text{th}}$-percentile. The groups were numbered from lowest to highest percentile. Each simulation in the fiducial set only had one initial condition vary at a time. The other two initial conditions were sampled from their second groups since these are the most typical values of the distributions. If more than one simulation had initial conditions that satisfied our group selections, then the simulation added to our fiducial set was randomly selected. As previously stated, the names of the simulations given in Table 2.1 summarize the group choices and the type of central halo response. For example, the simulation labeled "$\xi 1\, \eta 2\, \epsilon 2\, T 1$" had a mass ratio in group 1, a relative energy in group 2, a circularity in group 2, and a type 1 central halo response.

| **Simulation** | $\boldsymbol{\xi}$ | $\boldsymbol{\eta}$ | $\boldsymbol{\epsilon}$ | $\boldsymbol{v_r/v}$ | $\boldsymbol{v/v_{200}}$ | $\boldsymbol{t_p}$ (Gyr) | $\boldsymbol{r_p}$ (Mpc) | **Type** |
|---|---|---|---|---|---|---|---|---|
| $\boldsymbol{\xi 1\,\eta 2\,\epsilon 2\,T1}$ | 0.0727 | 1.026 | 0.577 | −0.769 | 1.086 | 5.03 | 0.61 | 1 |
| $\xi 2\,\eta 2\,\epsilon 2\,T1$ | 0.0903 | 0.989 | 0.551 | −0.797 | 1.107 | 5.25 | 0.54 | 1 |
| $\boldsymbol{\xi 3\,\eta 2\,\epsilon 2\,T1}$ | 0.1241 | 1.062 | 0.583 | −0.765 | 1.061 | 4.86 | 0.53 | 1 |
| $\xi 4\,\eta 2\,\epsilon 2\,T1$ | 0.3030 | 1.027 | 0.559 | −0.805 | 1.131 | 5.19 | 0.42 | 1 |
| $\xi 2\,\eta 1\,\epsilon 2\,T1$ | 0.0928 | 0.568 | 0.571 | −0.733 | 1.345 | 10.6 | 0.77 | 1 |
| $\xi 2\,\eta 3\,\epsilon 3\,T1^{\dagger}$ | 0.0889 | 1.216 | 0.698 | −0.596 | 0.949 | 4.14 | 0.75 | 1 |
| $\xi 2\,\eta 1\,\epsilon 1\,T1^{\star}$ | 0.1082 | 0.527 | 0.381 | −0.883 | 1.394 | 11.1 | 0.43 | 1 |
| $\xi 2\,\eta 2\,\epsilon 3\,T1$ | 0.0731 | 1.195 | 0.635 | −0.688 | 0.965 | 4.16 | 0.66 | 1 |
| $\xi 1\,\eta 2\,\epsilon 2\,T2$ | 0.0613 | 1.164 | 0.476 | −0.842 | 0.993 | 4.22 | 0.46 | 2 |
| $\boldsymbol{\xi 2\,\eta 2\,\epsilon 2\,T2}$ | 0.0830 | 1.167 | 0.499 | −0.825 | 0.987 | 4.25 | 0.45 | 2 |
| $\xi 3\,\eta 2\,\epsilon 2\,T2$ | 0.1894 | 1.165 | 0.509 | −0.830 | 1.015 | 4.39 | 0.37 | 2 |
| $\boldsymbol{\xi 4\,\eta 2\,\epsilon 2\,T2}$ | 0.3119 | 1.131 | 0.447 | −0.879 | 1.055 | 4.52 | 0.29 | 2 |
| $\xi 2\,\eta 1\,\epsilon 1\,T2^{\dagger}$ | 0.1026 | 0.808 | 0.322 | −0.934 | 1.224 | 6.70 | 0.28 | 2 |
| $\xi 2\,\eta 3\,\epsilon 2\,T2$ | 0.0935 | 1.238 | 0.441 | −0.860 | 0.942 | 3.94 | 0.36 | 2 |
| $\xi 2\,\eta 2\,\epsilon 1\,T2$ | 0.1025 | 0.926 | 0.272 | −0.954 | 1.156 | 5.59 | 0.22 | 2 |
| $\xi 2\,\eta 3\,\epsilon 3\,T2^{\star}$ | 0.0823 | 1.356 | 0.594 | −0.685 | 0.847 | 3.51 | 0.54 | 2 |

$^{\star}$ No simulation satisfied our selection criteria when $\eta$ was sampled from group 2.

$^{\dagger}$ No simulation satisfied our selection criteria when $\epsilon$ was sampled from group 2.

Table 2.1: Summary of the initial conditions for the fiducial set. The columns list (1) the simulation name, (2) the mass ratio, (3) the relative energy, (4) the circularity, (5) the radial-to-total velocity ratio, (6) the total-to-virial velocity ratio, (7) the time to pericentre, (8) the pericentric passage distance, and (9) the class of central halo response. The simulations listed in bold are a subset of the fiducial set used for select plots. Note that the radial-to-total velocity ratio is negative since we require the satellite's radial velocity to point towards the central halo for them to merge.

# Chapter 3

# Orbital Evolution Model

## 3.1 Primary Components

The model for the orbital evolution of a satellite halo undergoing a merger around the position of highest local density of a central halo is built using Newtonian Mechanics. Our model includes two main physical processes, satellite mass loss and dynamical friction, as well as a correction factor associated with the frame the orbit is measured in. In our model, both the satellite and central halos are represented using NFWT profiles. Overall, the orbital model is completely described by the equations of motion of the satellite halo. Modeling the orbit of the satellite is one of the two components required for predicting structural changes in the remnant system during a major merger.

One thing to highlight is the orbital model considered in this chapter does not include how the structure of the central halo responds to the motion of the satellite as it mergers. That is, the profile of the central halo remains constant and its NFWT parameters remain unchanged. The effect of including a dynamic host halo on the trajectory of the satellite will be explored in Chapter 4. There it will be contrasted against the case where the effect is neglected.

### 3.1.1 Satellite Mass and Unbound Mass

The first component of the orbital model describes the mass loss the satellite experiences. Our measurements for the bound mass of the satellite in the simulations (see Fig. 2.6) indicate that the satellite loses mass as it orbits the central halo. Initially, all of the

satellite's mass is considered bound to it. As the satellite falls towards the central halo, mass is stripped from the satellite due to tidal forces and becomes unbound. The amount of mass that is removed corresponds to some fraction of the satellite mass located outside of its tidal radius, $M_{\rm out}$.

$$M_{\rm out} = M_s(r < r_t) - M_s(r < r_m) \tag{3.1}$$

where $r = \sqrt{x^2 + y^2 + z^2}$ is the radial position of the satellite along its orbit, $r_t$ is the satellite's truncation radius, and $r_m$ is the satellite's tidal radius. For a given timestep, if $M_{\rm out}$ is negative (the mass of the satellite increases), then we set $M_{\rm out} = 0$ so that the satellite's mass is only ever decreasing as in our simulations. While the mass of the satellite decreases, the amount of unbound material increases by the same amount. The rate of change in these quantities is given by,

$$\dot{M}_s = -\gamma\, M_{\rm out} \left(\frac{v}{r}\right) \qquad\qquad \dot{M}_{\rm ub} = +\gamma\, M_{\rm out} \left(\frac{v}{r}\right) \tag{3.2}$$

where $M_{\rm ub}$ is the unbound mass, $v = \sqrt{v_x^2 + v_y^2 + v_z^2}$ is the velocity of the satellite, and $\gamma$ is a scaling factor used to set the rate at which satellite mass becomes unbound over time. This mass loss formulation mirrors that in Taylor & Babul (2001) except in their analysis the procedure they use implies a value $\gamma = \sin(\theta)/(2\pi)$, where $\theta \in [0, \pi]$ is the instantaneous angle between $\vec{x}$ and $\vec{v}$. From Eq. 3.2, the rate at which mass is lost varies but is highest when the satellite passes pericentre on each orbit. This reflects the result we find in simulations and is encoded by the quantity $v/r$. Since we consider any material lost from the satellite as unbound, the mass of the central halo remains constant in our model. As with the simulations, the satellite was allowed to lose material until it reached a minimum mass of 0.5% the initial satellite mass, although in many cases the satellite never reached this mass by the end of the integration. This limit was imposed to prevent the integrator from diverging when calculating the orbit.

When integrating the orbit of the satellite, we consider a simple model for the unbound material. We assume that the unbound mass is distributed in spherical shells around the central halo. The material is placed instantaneously into these shells, with a radius corresponding to the satellite's position at the time it was removed from the satellite. Moreover, the material does not move from its position after placement. To ease computations, we created a lookup table corresponding to the radii of the shells and populated it with mass as it was unbound from the satellite.

Initially, we tried using a slightly different model for the unbound mass; the material was placed instantaneously at the location of the satellite at the time it was removed. The contribution of this mass to the force acting on the satellite was only considered at

subsequent timesteps and not during the step the mass was ejected. However, in this model, the force applied by the unbound mass on the satellite caused it to move onto a highly radial orbit until it became stationary instead of orbiting the central halo. The unbound material was located too close to the satellite after it was removed and the total contribution of all the unbound mass quickly balanced the force due to the host halo even after including a softening term. If the material were instead distributed in spherical shells, then the unbound mass would apply a force on the satellite only when it is located interior to the satellite's position. The unbound mass is placed instantaneously at the position of the satellite and thus does not apply a force on the satellite during its initial infall. It will only contribute to the total force after the satellite passes pericentre for the first time.

Our mass loss model requires calculating the tidal radius of the satellite at each point along its orbit. In this work, we define the tidal radius of the satellite, $r_m$, as the radius at which the tidal force from the central halo exceeds the self-gravity of the satellite. According to Binney & Tremaine (2008), tidal forces can be thought of as ascribing a limit to the density of a satellite. To see this, we start from the expression for the limiting (or tidal) radius derived by King (1962) used to estimate the stripping of stars in globular clusters as they orbit a galactic centre,

$$r_m = \left[ \frac{GM_s(< r_m)}{\Omega^2 - \frac{d^2\Phi_c}{dr^2}\Big|_{r_m}} \right]^{1/3} \tag{3.3}$$

where $\Phi_c$ is the potential of the host halo, $\Omega = \|\vec{v} \times \vec{x}\|/r^2$ is the instantaneous angular velocity of the satellite, and

$$\frac{d^2\Phi_c}{dr^2} = \frac{G}{r^2}\frac{dM_c(< r)}{dr} - \frac{2GM_c(< r)}{r^3} \tag{3.4}$$

We can rearrange Eq. 3.3 to convert it into a form relating mean densities.

$$\frac{M_s(< r_m)}{\frac{4}{3}\pi r_m^3} = \frac{1}{\frac{4}{3}\pi G}\left[\Omega^2 - \frac{d^2\Phi_c}{dr^2}\bigg|_{r_m}\right] \tag{3.5}$$

If we define $\Omega_c = \sqrt{GM_c(< r)/r^3}$ as the angular velocity of a circular orbit of radius $r$ around the central halo, we can rewrite Eq. 3.5 as,

$$\frac{M_s(< r_m)}{\frac{4}{3}\pi r_m^3} = \frac{1}{\frac{4}{3}\pi G}\left[\frac{\Omega^2}{\Omega_c^2} - \frac{1}{\Omega_c^2}\frac{d^2\Phi_c}{dr^2}\bigg|_{r_m}\right]\frac{GM_c(< r)}{r^3} \tag{3.6}$$

Finally, if we define $\bar{\rho}(< r) = 3M(< r)/(4\pi r^3)$ as the mean density of a halo within the radius $r$, Eq. 3.6 further simplifies to,

$$\overline{\rho_s}(< r_m) = \eta\, \overline{\rho_c}(< r) \quad \text{where} \quad \eta = \frac{\Omega^2}{\Omega_c^2} - \frac{1}{\Omega_c^2}\left.\frac{d^2\Phi_c}{dr^2}\right|_{r_m} \tag{3.7}$$

The quantities $\overline{\rho_s}$ and $\overline{\rho_c}$ are the mean densities of the satellite and host halo, respectively. Thus, we find that the tidal stripping condition is related to the densities of the halos, as expected.

The tidal radius proposed by King (1962) is only approximate and is based on two assumptions: (1) the orbit of the satellite is circular and (2) the distant-tide approximation can be used, which implies that the separation between the satellite and host halo is large compared to the size of the satellite. Depending on the model assumptions, different versions of $r_m$ can be derived and are used in the literature (see van den Bosch et al., 2018, for a discussion). For example, if the potential used in Eq. 3.7 were that of a point particle (i.e. $\Phi_c = -GM_c/r$), then we would obtain the well-known Jacobi limit with $\eta = 3$. Furthermore, if we were to neglect the centrifugal force as a result of the motion of the halos, we would obtain the Roche limit with $\eta = 2$.

Neither model assumption for the tidal radius expression we use holds for our problem: (1) the satellite is generally on an eccentric orbit and (2) the orbit's pericentre can be comparable to, or even smaller than, the size of the satellite. Despite this, it is common practice to apply a model of the form Eq. 3.7 by using instantaneous values for the satellite's orbit to calculate the instantaneous tidal radius (see e.g. Taylor & Babul, 2001; Zentner & Bullock, 2003; Peñarrubia & Benson, 2005). Others attempt a different approach and define an effective value for $\eta$ by averaging the instantaneous value of $\eta$ over each orbit (see e.g. Drakos et al., 2020, 2022). This is done in order to compensate for the different derivations of the tidal radius since the optimal definition of the tidal radius depends on the orbit in question (van den Bosch et al., 2018). In our case, we find that the more common approach of using an instantaneous tidal radius is sufficient for replicating the amount of satellite mass loss in the simulations. We solve for the tidal radius of the satellite by applying a root-finding method to Eq. 3.7 and update its value at each step along the orbit. The values of $\Omega$ and $\Omega_c$ were adjusted accordingly.

So far we have not described how the satellite's mass is lost from it. Does the internal structure of the satellite change or does something else happen? Fig. 3.1 depicts how the structure of the satellite changes with time for a subset of the fiducial simulations. Each column shows a different component of the radial density profile with all particles on the left, bound particles in the middle, and unbound particles on the right. Focusing on the

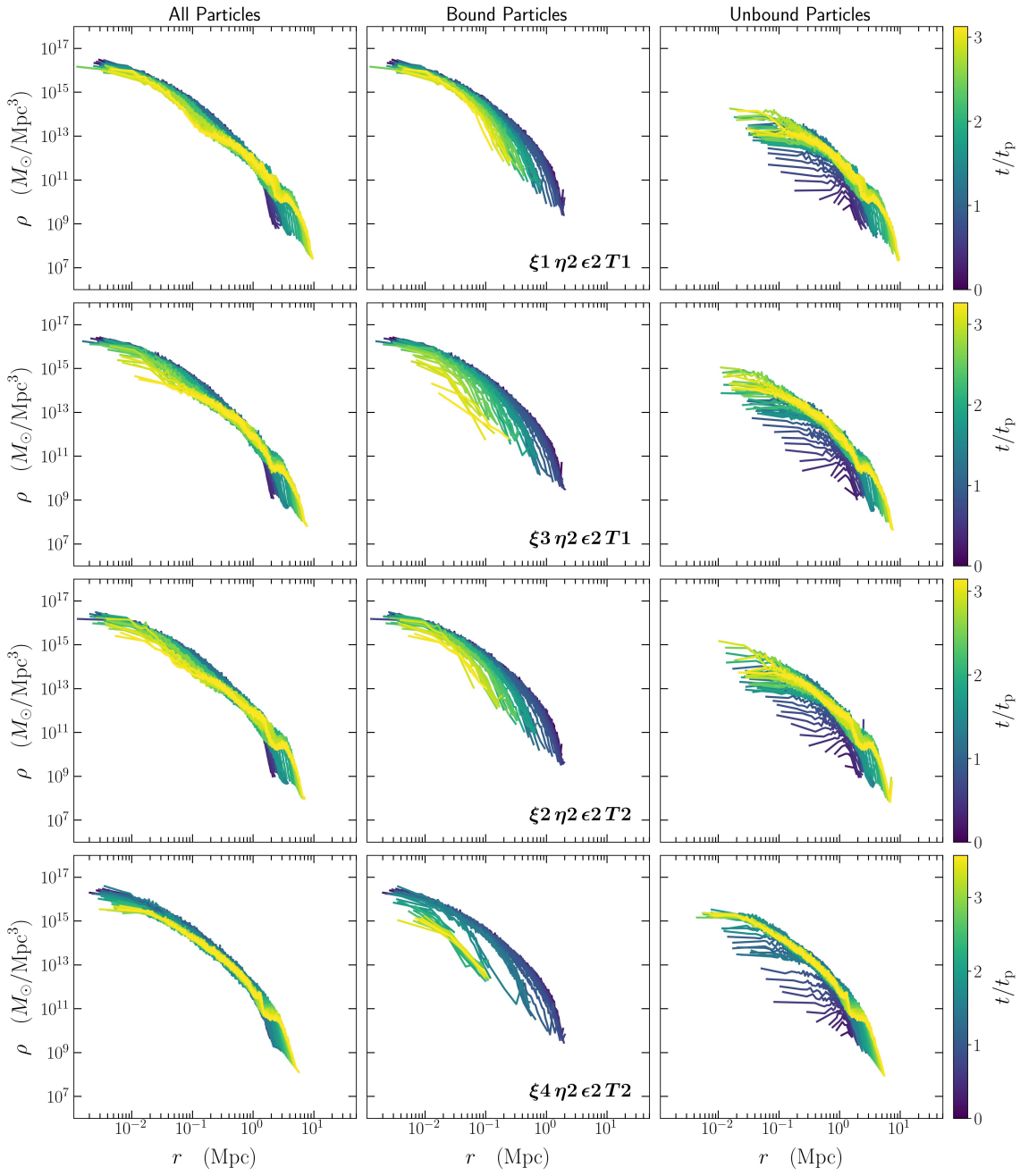



Figure 3.1: Density profiles of the satellite halo considering three components: all particles (left), bound particles (middle), and unbound particles (right). The colour of the profiles corresponds to the time from the start of the merger relative to the time to pericentre.

bound particles, the shape of the density profile is maintained with time. As the satellite loses mass, it is lost from the outer regions of the halo. This is further confirmed by looking at the unbound particles where the profiles are cored in the inner regions, implying less unbound material is found there (i.e. $\rho = M/V$ is constant and $V$ is decreasing, so $M$ must decrease proportionally). Thus, these profiles demonstrate how mass should be removed from the satellite in our model. At each timestep, the structural parameters ($r_s$, $\rho_0$, $y$) for the satellite are kept constant, while its truncation radius is adjusted to compensate for the amount of mass lost.

### 3.1.2 Dynamical Friction

The second component of the orbital model describes the dynamical friction force acting on the satellite as it orbits. For collisionless systems, dynamical friction quantifies the systematic transfer of energy from the motion of a moving body to the random motions of the background particles the body travels through. This force is caused by the background particles scattering into an overdense wake trailing the moving body and tugging back on it. Suppose we have a mass $M_s$ travelling through a background of particles with individual masses $m_a \ll M_s$ and a total mass $M_c \gg M_s$. Then, the deceleration of $M_s$ due to dynamical friction occurs at a rate (Chandrasekhar, 1943; Binney & Tremaine, 2008),

$$\dot{\vec{v}} = -16\pi^2 G^2 M_s m_a \ln(\Lambda) \left[ \int_0^v dv_a v_a^2 f(v_a) \right] \frac{\vec{v}}{v^3} \tag{3.8}$$

where $f(v_a)$ is the distribution function of the background particles and $\ln(\Lambda)$ is the Coulomb logarithm. Assuming the distribution function is Maxwellian (see e.g. Binney & Tremaine, 2008, Eq. 7.91), then the above expression simplifies to,

$$\dot{\vec{v}} = -\frac{4\pi G^2 M_s \rho_c \ln(\Lambda)}{v^3} \left[ \mathrm{erf}(X) - \frac{2X}{\sqrt{\pi}} e^{-X^2} \right] \vec{v} \tag{3.9}$$

where $\rho_c = \rho_c(r)$ is the density of the background particles at the position of $M_s$, `erf` is the error function, $X \equiv v/(\sqrt{2}\sigma_c)$, and $\sigma_c$ is the radial velocity dispersion of the background particles assuming an isotropic dispersion tensor (see e.g. Hernquist, 1993, Eq. 2.13),

$$\sigma_c = \frac{1}{\rho_c} \int_r^\infty \rho_c(r') \left. \frac{d\Phi_c}{dr} \right|_{r'} dr' \tag{3.10}$$

Eq. 3.9 is often referred to as Chandrasekhar's dynamical friction formula. The derivation of this formula assumes an idealized scenario; a massive particle moves through an

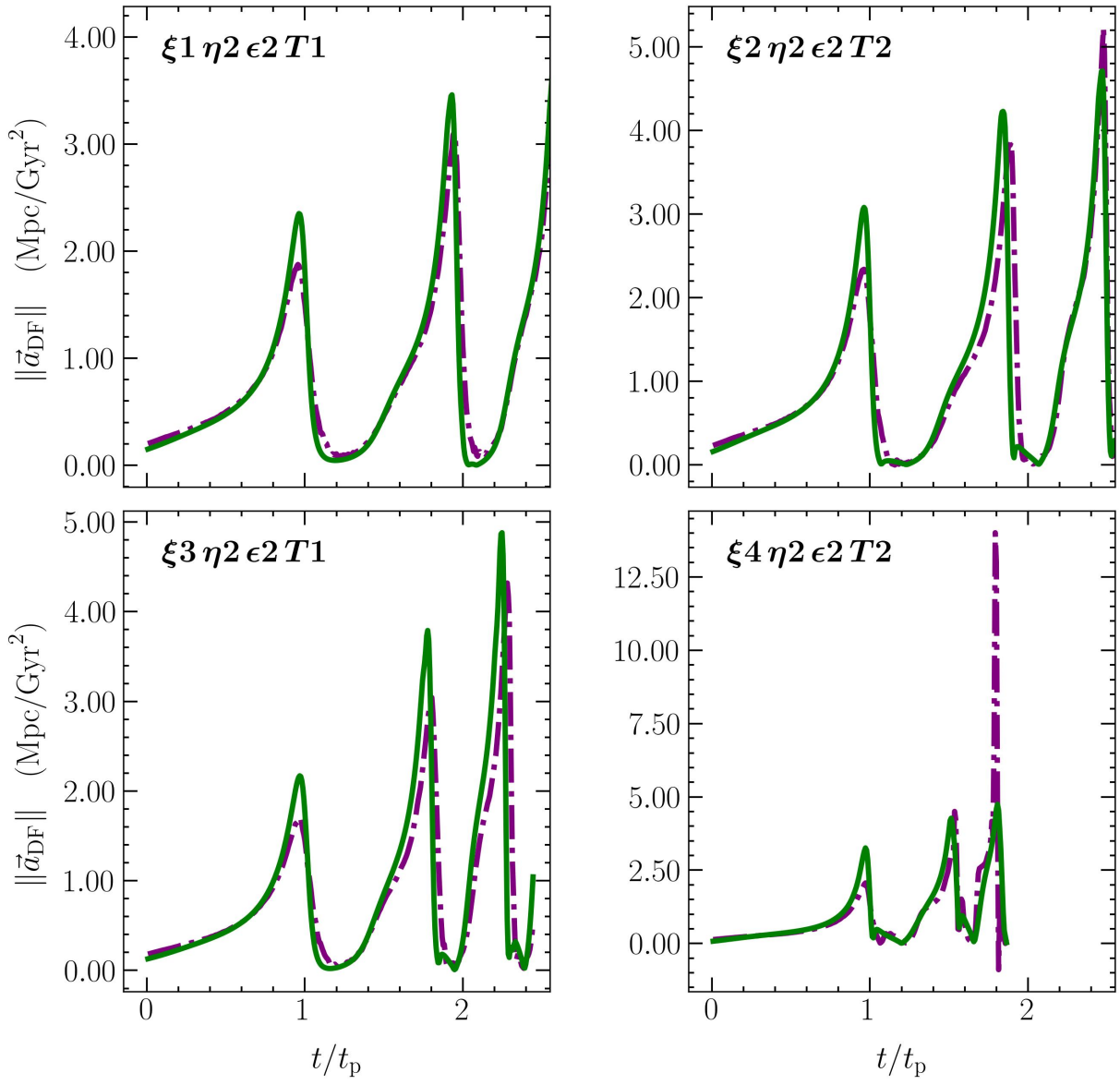



Figure 3.2: Measured dynamical friction deceleration in the simulations (purple) compared to the model (green) as the satellite orbits the central halo. The timescale in these plots is shown relative to the time to pericentre.

infinite, homogeneous background of much lighter particles with a characteristic form for the distribution function. In our case, the background particles are represented by the central halo which is finite in size. Furthermore, the satellite is an extended distribution with a mass similar to the background. As the satellite orbits, the background particle distribution will become anisotropic as it is disrupted by the satellite.

Nevertheless, many studies of satellite dynamics have shown Chandrasekhar's formula to be more widely applicable. These studies find that the formula provides a fairly accurate approximation to the drag force on an extended satellite within a finite system. Typically, one of two approaches is employed: (1) $\ln(\Lambda)$ is set as a constant but free parameter fit to $N$-body data (see e.g. Taylor & Babul, 2001; Benson et al., 2004; Peñarrubia et al., 2010), or (2) $\ln(\Lambda)$ is set by estimating the maximum and minimum impact parameters of the background particles contributing to its wake, and this value varies as the satellite orbits (see e.g. Hashimoto et al., 2003; Fujii et al., 2006; Fellhauer & Lin, 2007). In our case, we followed the first approach and left $\ln(\Lambda)$ as a free parameter. We tested using Eq. 3.8, the full expression for dynamical friction, to calculate the deceleration on the satellite by sampling particles from the central halo's distribution function (see Drakos et al., 2017, Appendix A for sampling velocities given a density profile). We found that this only marginally improved the accuracy of the satellite's orbit, while simultaneously significantly increasing the computation time required to integrate the orbit due to resampling particles at each timestep. Therefore, we used Eq. 3.9 to model the dynamical friction deceleration.

Fig. 3.2 illustrates the dynamical friction deceleration measured in the simulations compared to the model using Chandrasekhar's formula. Estimating dynamical friction in the simulations is tricky since the particles associated with the satellite continuously vary. Moreover, even the tidally stripped material in the vicinity of the satellite can contribute to the dynamical friction the bound core experiences (Fujii et al., 2006). To simplify our measurement, we calculate the total acceleration of the satellite's position of highest local density, $\vec{a}_{\rm cod}$, with respect to the central halo from its change in velocity at each timestep. We then subtract off the acceleration caused by a spherically symmetric background potential and call the remaining acceleration dynamical friction.

$$\vec{a}_{\rm df} = \vec{a}_{\rm cod} - \frac{d\Phi_c}{d\vec{x}} \tag{3.11}$$

$$\vec{a}_{\rm df} = \vec{a}_{\rm cod} + \frac{GM_c(<r)}{r^3}\vec{x} \tag{3.12}$$

In the simulations, we use the exact mass distribution of the central halo, while in the model, we assume it follows an NFWT distribution. Rather than calculate the dynamical

friction deceleration in the model directly from Chandrasekhar's formula, we use the same procedure as described above for consistency.

From the figure, we find that Chandrasekhar's formula replicates the total deceleration due to dynamical friction measured in the simulations well. The most significant difference we find is when the satellite reaches each pericentre of the orbit. At these points, the model predicts more deceleration compared to the simulations, resulting in pericentric passages occurring closer to the central halo in the model. Despite this difference, overall the model functions well regardless of the mass ratio between the halos. Even for simulations where the satellite and central halo masses are comparable (e.g. $\xi 4\,\eta 2\,\epsilon 2\,T2$ corresponding to a 3:1 merger), the drag force acting on the satellite is well modeled for several orbits before disagreeing. This disagreement is a relatively minor issue since the halos in high mass ratio mergers completely merge after a few orbits. Our result further demonstrates that properly tuning $\ln(\Lambda)$ allows Chandrasekhar's formula to be used in cases far from the idealized scenario.

### 3.1.3 Reduced Mass

In the default frame of the simulation, the satellite and central halo orbit about a common centre of mass. In our measurements, we have removed the motion of the central halo by subtracting off its position and velocity from the satellite's position and velocity. However, this process changes the frame the satellite is measured in. We want our model to use the same frame as the simulation measurements for consistency. By fixing the central halo's position at the origin of the frame, we need to apply a correction factor to the acceleration of the satellite in our model. How this works explicitly will be demonstrated in this section.

Suppose we have two bodies of masses $M_s$ and $M_c$ at the positions $\vec{x}_s$ and $\vec{x}_c$, respectively. The goal we have is to determine the trajectories of these masses given their initial positions and velocities. From Newton's second law, we find that the equations of motion for the two masses are,

$$\vec{F}_{sc}(\vec{x}_s, \vec{x}_c) = M_s\,\ddot{\vec{x}}_s \tag{3.13}$$

$$\vec{F}_{cs}(\vec{x}_s, \vec{x}_c) = M_c\,\ddot{\vec{x}}_c \tag{3.14}$$

where $\vec{F}_{sc}$ is the force on $M_s$ due to $M_c$ and $\vec{F}_{cs}$ is the force on $M_c$ due to $M_s$. We can translate our equations of motion into a single equation for the center of mass,

$$\vec{x}_{\text{com}} \equiv \frac{M_s\vec{x}_s + M_c\vec{x}_c}{M_s + M_c} = \frac{1}{M}\left(M_s\vec{x}_s + M_c\vec{x}_c\right) \tag{3.15}$$

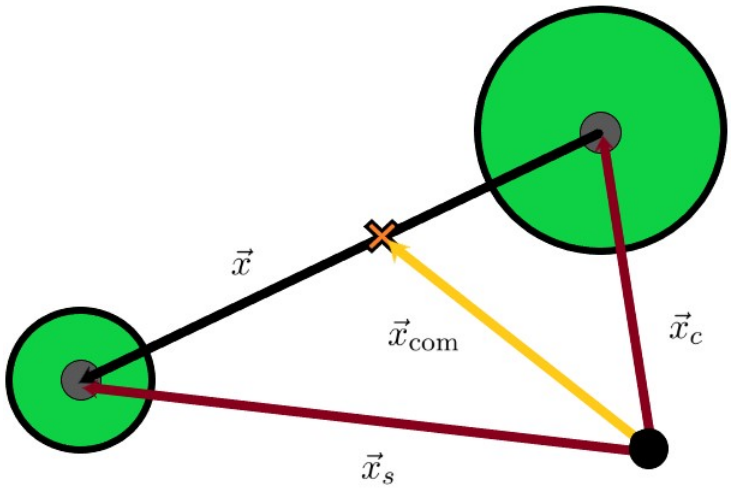



Figure 3.3: Diagram illustrating the two-body problem.

where we define the total mass of the system as $M = M_s + M_c$. Since the mass is time independent, this implies the acceleration of the center of mass is,

$$\ddot{\vec{x}}_{\text{com}} = \frac{1}{M}\left(M_s\ddot{\vec{x}}_s + M_c\ddot{\vec{x}}_c\right) \tag{3.16}$$

From Newton's third law, we know that $\vec{F}_{sc} = -\vec{F}_{cs}$. If we add our equations of motion together, we find that the acceleration of the center of mass is zero.

$$M\ddot{\vec{x}}_{\text{com}} = M_s\ddot{\vec{x}}_s + M_c\ddot{\vec{x}}_c = \vec{F}_{sc} + \vec{F}_{cs} = 0 \tag{3.17}$$

$$\ddot{\vec{x}}_{\text{com}} = 0 \tag{3.18}$$

Since we have two particles, we need two vectors to fully describe the system. We will define the separation vector between the two particles as $\vec{x} \equiv \vec{x}_s - \vec{x}_c$. If we take two derivatives, then the acceleration of the separation vector is,

$$\ddot{\vec{x}} = \ddot{\vec{x}}_s - \ddot{\vec{x}}_c = \left(\frac{\vec{F}_{sc}}{M_s} - \frac{\vec{F}_{cs}}{M_c}\right) = \left(\frac{1}{M_s} + \frac{1}{M_c}\right)\vec{F}_{sc} \tag{3.19}$$

The force between the two objects should only be a function of their radial separation and not their absolute positions $\vec{x}_s$ and $\vec{x}_c$, otherwise we would not have translational symmetry.

Thus, we can rewrite the expression above as,

$$\ddot{\vec{x}} = \left(\frac{M_s + M_c}{M_s M_c}\right) \vec{F}(\vec{x}) \tag{3.20}$$

$$\mu \ddot{\vec{x}} = \vec{F}(\vec{x}) \tag{3.21}$$

where we have defined the reduced mass $\mu \equiv (M_s M_c)/M$. For spherically symmetric mass distributions, the force is a central force and has the form $\vec{F}(\vec{x}) = -F(\vec{x})\vec{x}$, where we pick up a negative sign since the force is attractive. Finally, our equation of motion for the separation vector simplifies to,

$$\mu \ddot{\vec{x}} = -F(\vec{x})\vec{x} \tag{3.22}$$

We now have two equations of motion for our new coordinates given by Eqs. 3.18 and 3.22. Once we obtain expressions for $\vec{x}_{\rm com}(t)$ and $\vec{x}(t)$, we can find the trajectories of the particles in our original coordinate frame using the transformation,

$$\vec{x}_s(t) = \vec{x}_{\rm com}(t) + \frac{M_c}{M}\vec{x}(t) \tag{3.23}$$

$$\vec{x}_c(t) = \vec{x}_{\rm com}(t) - \frac{M_s}{M}\vec{x}(t) \tag{3.24}$$

The result of Eq. 3.22 demonstrates the origin of the correction factor on the acceleration of the satellite in our model equations of motion (see Eq. 3.30). Calculating the orbit of the satellite in the frame where the central halo's position of highest local density is motionless at the centre of the frame requires us to scale central forces by the reduced mass. In particular, this correction needs to be applied to the background potential and unbound mass terms. However, the value of the reduced mass we found above is not exactly correct since its derivation made several assumptions: (1) $M_s$ and $M_c$ are massive particles, (2) their masses are constant, and (3) they are the only particles in the system. In our case, $M_s$ and $M_c$ are extended distributions and we have unbound material accumulating in the system with time. To account for this, the correction factor we use is a modification to the reduced mass, $\mu' = B\mu$, where $B$ is a free parameter. Note that $\mu$ varies with time as the mass of the satellite changes.

## 3.2 Evaluating the Model

Given the components to the model described in Section 3.1, we can derive the equation of motion for the satellite as it orbits the central halo, which is stationary at the centre of

the frame.

$$\ddot{\vec{x}} = \vec{f}_c + \vec{f}_{\rm df} + \vec{f}_{\rm ub} \tag{3.25}$$

In this expression, $\vec{f}_c$ is the force per unit mass induced by the central halo, $\vec{f}_{\rm df}$ is the dynamical friction force exerted by the background of particles, and $\vec{f}_{\rm ub}$ is the force caused by the unbound material. The force induced by the central halo is related to its distribution of particles.

$$\vec{f}_c = -\vec{\nabla}\Phi_c \tag{3.26}$$

$$\vec{f}_c = -\frac{d\Phi_c}{dr}\hat{r} \tag{3.27}$$

$$\vec{f}_c = -\frac{GM_c(<r)}{r^3}\vec{x} \tag{3.28}$$

Here we obtain the last expression using the fact that the central halo is modeled by the spherically symmetric NFWT profile (see Eq. 1.9). We can obtain a similar expression for the force caused by the unbound material. Since the unbound mass is distributed in spherical shells around the centre of the host halo, we can use Newton's shell theorem to determine which shells apply a force on the satellite at a given time. This theorem states that for a spherically symmetric shell, no net gravitational force is exerted by the shell on any object inside the shell. In contrast, the force on any object outside the shell is equivalent to the force exerted by a point mass located at the centre of the shell with a mass equal to the total mass of the shell (see Binney & Tremaine, 2008, Chapter 2.2). Applying this theorem, the force exerted by the unbound mass on the satellite depends on the amount of material within the satellite's position,

$$\vec{f}_{\rm ub} = -G\left(\sum_{r>r_i} M_i\right)\frac{\vec{x}}{r^3} \tag{3.29}$$

where $M_i$ is the mass of the $i^{\rm th}$ shell located at $r_i$. Lastly, the dynamical friction force is given by Eq. 3.9. Putting our results together, we find that the equation of motion for the satellite is given by,

$$\ddot{\vec{x}} = -4\pi G^2 M_s \rho_c \ln(\Lambda)\left[\mathrm{erf}(X) - \frac{2X}{\sqrt{\pi}}e^{-X^2}\right]\frac{\vec{v}}{v^3} - \frac{G}{\mu'}\left(M_c(<r) + \sum_{r>r_i} M_i\right)\frac{\vec{x}}{r^3} \tag{3.30}$$

where we apply the reduced mass correction, $\mu'$, to the central potential and unbound mass terms as described in Section 3.1.3. We do not include this correction factor on the

component of the force associated with dynamical friction since the dynamical friction force is not a central force opposite to the separation vector, as required. This set of differential equations, along with Eq. 3.2, completely define our orbital and mass loss models.

Integrating the orbit to find the trajectory of the satellite and its mass loss as it merges with the central halo requires us to set the initial conditions to use in the model. In particular, our model requires choosing the initial position and velocity of the satellite relative to the host halo, the initial masses of the two halos, and their initial NFWT parameters ($r_s$, $\rho_0$, $y_d$, $r_t$). For a given simulation, the initial conditions we use are equivalent to those we generated in Section 2.2. Then, at each step along the trajectory the model operates as follows:

1. The truncation radius of the satellite and value of $\mu'$ are adjusted given the satellite's new mass after mass loss.
2. The quantities $\sigma_c$, $\Omega$, $\Omega_c$, and $\eta$ are adjusted given the satellite's new position and velocity.
3. The new tidal radius for the satellite, $r_m$, is calculated. This along with the satellite's truncation radius are used to find the amount of its mass located outside the tidal radius, $M_{\text{out}}$.
4. The model integrates to the next point along the trajectory. It outputs the position, velocity, and mass of the satellite, as well as the amount of unbound mass.
5. The unbound mass obtained in this step is placed at the previous position of the satellite. If adding more unbound material would cause the total unbound mass to exceed the initial satellite mass, then we ignore this step.

We solve the differential equations governing our model numerically using a Leapfrog method (see Appendix B.2 for how Leapfrog operates). We integrate the satellite's orbit up to a time equivalent to the last snapshot used in the simulations with a step size equal to the time between snapshots. This implies our model sampling mirrors that of the simulations. In principle, the integration time interval should be shorter than the snapshot resolution, but we found the snapshot time spacing to be sufficient to accurately determine the satellite's trajectory and calculate its mass loss. Finer sampling could be used if desired at the cost of longer evaluation times.

Finally, the orbital and mass loss models depend on three free parameters: (1) the mass loss scaling, $\gamma$, (2) the Coulomb logarithm, $\ln(\Lambda)$, and (3) the infall scaling, $B$. These

parameters were tuned by minimizing the difference between the model predictions and the simulation results. Specifically, our procedure comprised two steps. First, we adjusted the value of $B$ by comparing the model and simulation curves for the satellite's radial separation from the central halo up to the first pericentre. This parameter only affects the initial infall of the satellite, so we do not need to consider points outside this regime. During this phase, $\gamma$ and $\ln(\Lambda)$ are set to typical values.

Next, we found the best-fit values of $\gamma$ and $\ln(\Lambda)$ simultaneously by minimizing the difference between the model and simulation results for the satellite's radial separation and mass loss curves over the first three orbits of the merger. In particular, we minimized the residual,

$$\text{res} = \frac{1}{2}\sum_i \left[ \|\vec{x}(t_i)\| - \|\vec{x}_i\| \right]^2 + \frac{1}{2}\sum_i \ln\left[\frac{M_s(t_i)}{M_{s,i}}\right] \tag{3.31}$$

using the function `minimize` from the Python library LMFIT (Newville et al., 2016), similar to how we fit NFWT profiles in Section 2.3.2. In this expression, properties with bracketed $t_i$ refer to the model, while that with subscript $i$ refer to the simulation. The errors on the model parameters were estimated from the covariance matrix output from our least squares fitting. If necessary, we used $3^{\text{rd}}$-degree spline interpolation on the model predictions in both steps of the procedure above in order to evaluate the model at the same times as the simulation output for direct comparison.

Figs. 3.4-3.6 plot the orbit of the satellite, its radial separation from the central halo, and its mass loss, respectively, in a subset of the fiducial simulations. We compare this to our model for the first three orbits of the merger. The end of the third orbit corresponds to the time the satellite reaches apocentre for a third time in the simulations. Note that this version of the model does not include how the structure of the central halo responds to the motion of the satellite as it mergers. In Fig. 3.4, we find the orbit of the satellite in our model is well aligned with the simulation curve at most times except for the initial infall. In this regime, the model predicts a more radial infall to pericentre, although this effect is not seen for later orbits. Next, in Fig. 3.5, the satellite's radial separation from the central halo in our model is identical to the simulation result up to the second pericentre. Beyond this point, our model typically predicts the satellite will move to an apocentre position slightly further out than that in the simulations. This indicates that dynamical friction is being underestimated here, although only marginally.

Finally in Fig. 3.6, the mass loss curves agree over the first two orbits in most cases. For the third orbit, the satellite's mass can be either overestimated or underestimated in our model. Note that after the initial infall, the satellite does not experience mass loss between successive pericentres in our model. This results from changes in the truncation

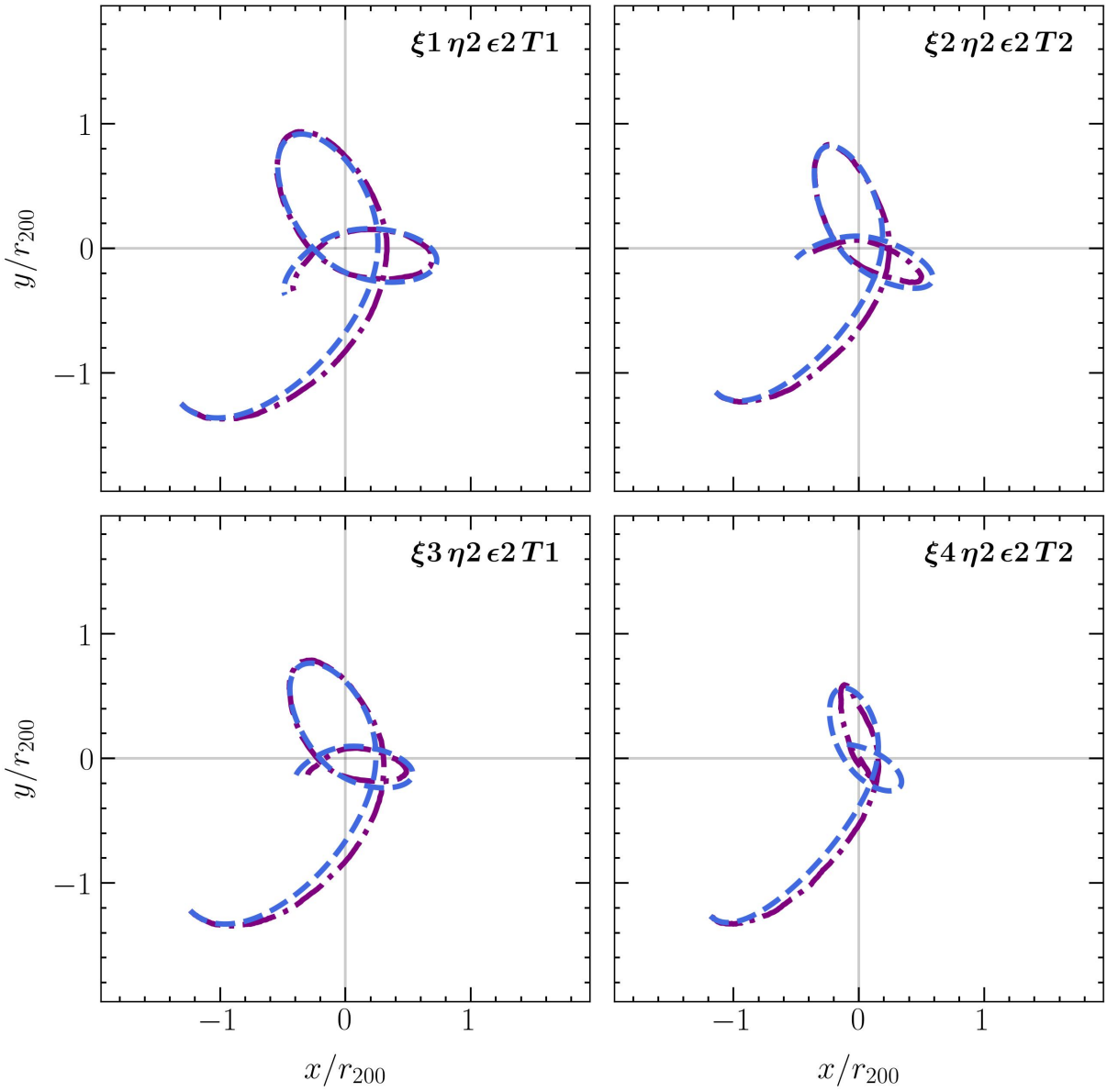



Figure 3.4: Measured motion of the satellite in the orbital plane in the simulations (purple, dashdot) compared to the model (blue, dashed) during the merger. The coordinates in these plots are shown relative to the virial radius of the central halo.

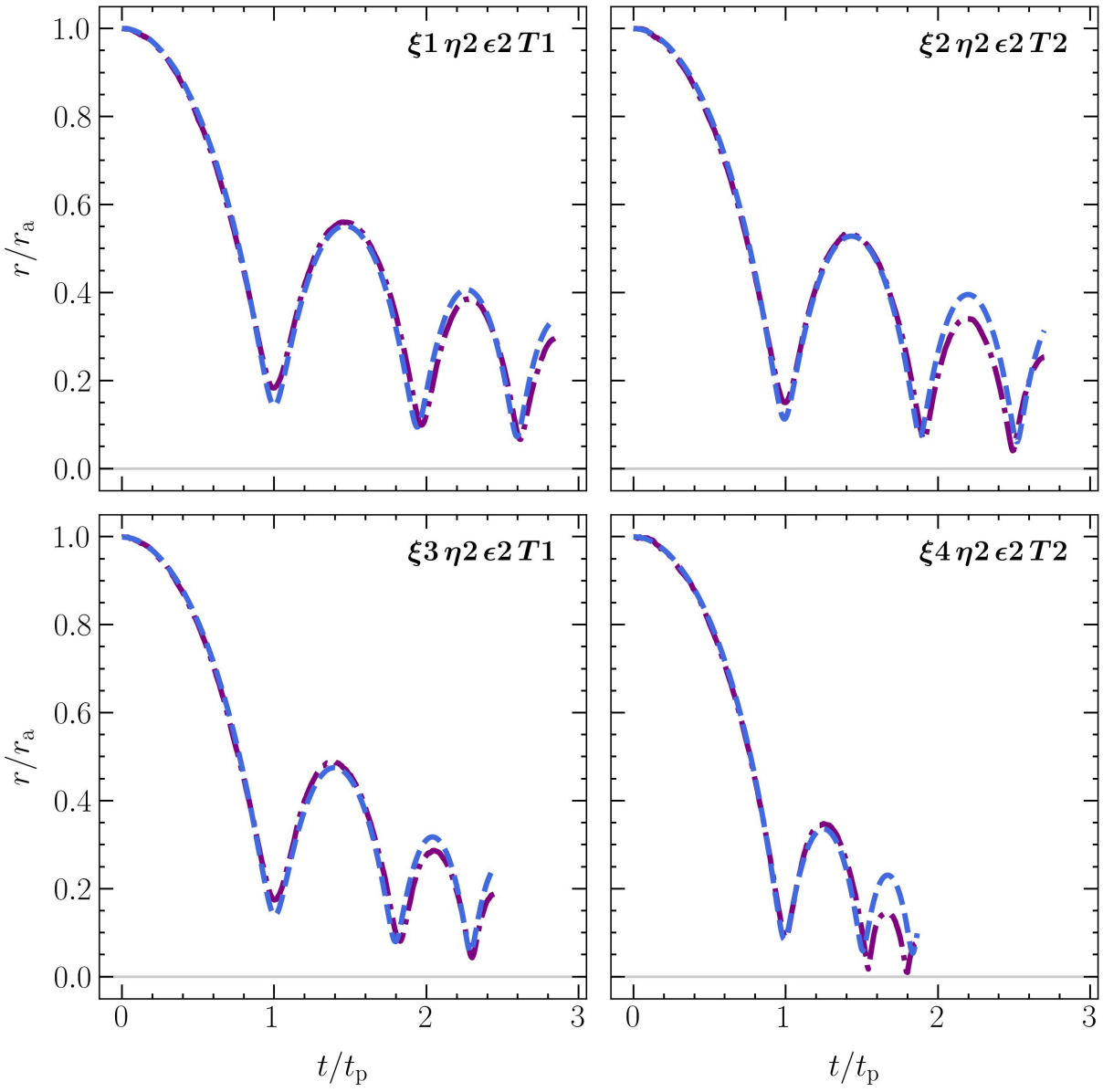



Figure 3.5: Measured radial separation between the satellite and central halos' positions of highest local density in the simulations (purple, dashdot) compared to the model (blue, dashed) during the merger. The timescale in these plots is shown relative to the time to pericentre.

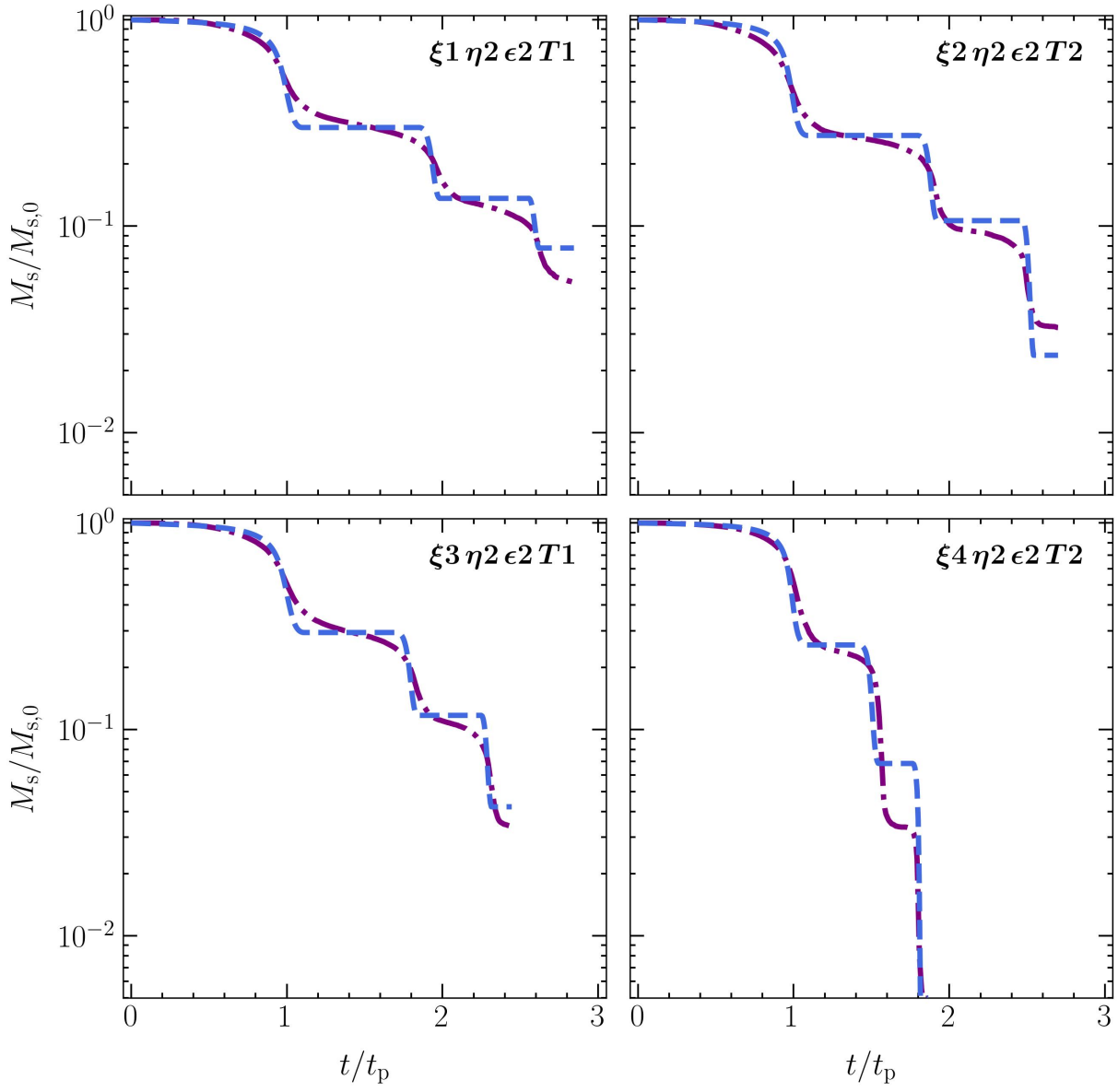



Figure 3.6: Measured satellite mass loss in the simulations (purple, dashdot) compared to the model (blue, dashed) during the merger. The timescale in these plots is shown relative to the time to pericentre.

radius of the satellite. As the satellite loses mass, its truncation radius becomes smaller and smaller to the point where it is less than the satellite's tidal radius at certain points along the orbit. Since all of the satellite's remaining mass is within the tidal radius, it cannot lose more material. This scenario mostly occurs when the satellite is near an apocentre.

Our model has the poorest agreement with the results of $\xi 4\,\eta 2\,\epsilon 2\,T2$, the simulation with the highest mass ratio merger in our fiducial set. We find the satellite's orbit, radial separation, and mass loss deviate moderately from that in the simulation after the second pericentre. This is caused by dynamical friction underestimating the deceleration on the satellite given the amount of mass loss it has experienced. More mass loss leads to less dynamical friction and subsequently, less orbital decay. However, the model accurately recreates the satellite's orbit and properties before the second pericentre. We find this is generally true for mergers with mass ratios of 5:1 and below. Since the primary structural oscillation we want to model in the remnant system occurs before this point, our orbital model should be sufficient even for high mass ratio mergers.

Overall, the orbital model works well at replicating the radial separation and mass of the satellite as it merges with the central halo for a few orbits. This is largely due to the model including many effects: the background potential, dynamical friction, mass loss, a reduced mass correction, and unbound material. However, how many of these components are truly necessary? If we were to neglect certain components, would the model still work as well as it does? Fig. 3.7 demonstrates the effect each model component has on the orbit of the satellite during the merger. The radial separation curves in the plot consider different combinations of model components. The specific combinations are described below.

- *Solid red line (BP)*: the model considers only the contribution to the force by the background potential. It does not include a mass loss model, reduced mass correction, or unbound material.
- *Solid teal line (BP, DF)*: the model considers both the contribution to the force by the background potential and dynamical friction. It does not include a mass loss model, reduced mass correction, or unbound material.
- *Dotted green line (BP, DF, ML)*: the model considers both the contribution to the force by the background potential and dynamical friction. It includes a mass loss model, but neglects the reduced mass correction and unbound material.
- *Dotted orange line (BP, DF, ML, FC)*: the model considers both the contribution to the force by the background potential and dynamical friction. It includes a mass loss model and the reduced mass correction, but neglects unbound material.

- *Dashed blue line (Standard Model)*: the model considers all contributions to the force by the background potential, dynamical friction, and unbound material. It includes a mass loss model and reduced mass correction. The model components are identical to our standard orbital model shown in Fig. 3.5.

- *Dash-dotted purple line (Simulation)*: this is the radial separation measured in the simulations and is identical to that shown in Fig. 3.5.

There are a couple notes to make regarding the modeling results shown in this figure. First, if the model included mass loss, we used the bound mass measured from the simulations (depicted in the right column of Fig. 2.6) and not that defined by Eq. 3.2. If we used our mass loss model directly, the mass loss curve would vary depending on which model components were included. In addition, if the model neglected unbound material, the satellite mass was instead transferred to the central halo by adjusting its characteristic density to compensate. In this case, we also needed to adjust the Coulomb logarithm used. This involved scaling the values of $\ln(\Lambda)$ used in the standard model by some factor. For the simulations shown in Fig. 3.7, the scaling factor varied between $1.05 - 1.48$, increasing with increasing mass ratio. If we did not change $\ln(\Lambda)$, the orbit for this model would move much further out after the initial infall compared to what we find in the standard model, and would poorly match the simulation result.

From Fig. 3.7, we find that including only the background potential leads to a static orbit for the satellite. After one orbit, the satellite goes back to its initial radial position. The effect of adding dynamical friction is to cause successive orbits to decay. The initial pericentric passage moves closer to the centre of the potential as well. However, without mass loss, the dynamical friction force causes the satellite to decelerate too much such that it cannot move back out after pericentre. This is similar to what we find in simulations if we were to represent the satellite using a single, massive particle (see Appendix A.4 for details). This issue can be fixed by adding mass loss. The satellite will continue to orbit after its initial decay, although it does so out of phase compared to the simulations. This phase difference is corrected for by including the reduced mass factor. Finally, we find there is no significant difference in the satellite's trajectory if we neglect unbound material provided the model parameters are tuned properly and the mass ratio is low. For high mass ratio mergers (e.g. $\xi 4\,\eta 2\,\epsilon 2\,T2$), the radial separation starts to deviate drastically from the target curve after the first orbit and soon becomes out of phase by a half-period, even when adjusting $\ln(\Lambda)$. In addition, the lower panels of Fig. 2.4 suggest that of the material that becomes unbound from the satellite, at least some of it cannot be directly transferred to the central halo. These two results demonstrate that we need to include some unbound material when modeling both the satellite's orbit and the remnant system.

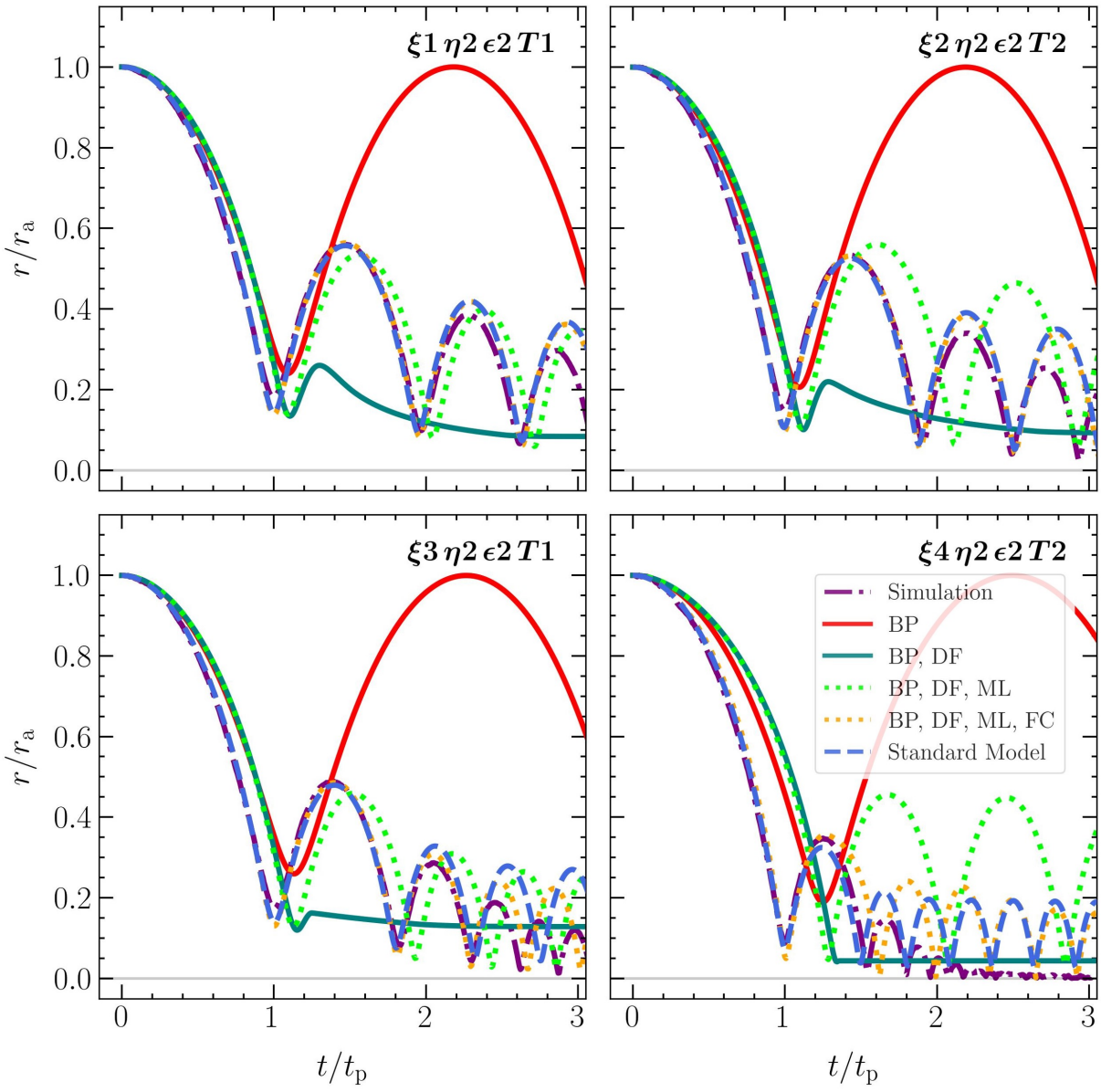



Figure 3.7: Modeled radial separation between the satellite and central halos' positions of highest local density during the merger. The timescale in these plots is shown relative to the time to pericentre. Each curve considers a model neglecting a certain combination of components. See the text for a detailed discussion.

## 3.3 Machine Learning to Predict Model Parameters

In the previous section, we showed that the satellite orbital and mass loss models are completely defined by Eqs. 3.30 and 3.2, respectively. These expressions depend on three free parameters: (1) the mass loss scaling, $\gamma$, (2) the Coulomb logarithm, $\ln(\Lambda)$, and (3) the infall scaling, $B$. The models shown in Figs. 3.4-3.6 calculated these parameters by minimizing the difference between the model predictions and the simulation results.

While this method works for tuning the model parameters, it relies on advance knowledge of the simulation output. The goal of our model is to bypass simulations. That is, we want the model to be self-contained, and predict the orbit and mass loss of the satellite from the initial conditions alone. Previous studies modeling satellite orbits using similar methods to our model consider the Coulomb logarithm to be the only free parameter (see e.g. Taylor & Babul, 2001; Benson et al., 2004). Moreover, their models use measurements in the two-body frame. Those that measure orbits in the reduced mass frame do not apply a correction to offset the effect of the satellite being an extended mass distribution that is losing material (see e.g. Colpi et al., 1999). As a result, we cannot apply the methods used in these studies to relate the model parameters to the initial conditions.

Fig. 3.8 illustrates all relationships between the model parameters and the initial conditions. We find that there is underlying structure in some of the relationships. For example, there appear to be correlations between ($\gamma$, $\epsilon$), ($\ln(\Lambda)$, $\xi$), and ($B$, $\eta$). However, these correlations tend to vary non-linearly and with significant scatter in the values of the model parameters. We tested relating the model parameters to other initial conditions (i.e. $v_r/v$, $v/v_{200}$, $t_p$, $r_p$, $r_a$, $x_c$) but we did not find these resulted in simpler patterns. Given the complexity of the relationships between the model parameters and the initial conditions, we unfortunately cannot relate them using simple formulae. Instead, we opt to train a machine learning model, specifically XGBoost, to predict the model parameters from the initial conditions.

XGBoost is an implementation of gradient-boosted decision trees, a set of machine learning methods used for classification and regression (Chen & Guestrin, 2016). Decision trees attempt to learn a set of rules from the data to try to predict target variables. Alone, tree methods can be unstable since small variations in the data can result in completely different trees being generated (Breiman et al., 1984). This problem is typically mitigated by weighting the predictions of a collection of trees, or a random forest. Random forests model target variables using simple weighted averaging of an ensemble of decision trees. The drawback to this technique is if the underlying models are weak, then the ensemble prediction will only be slightly stronger regardless of the number of trees in the ensemble (Breiman, 2001). The effect of gradient-boosting is to overcome this limitation by

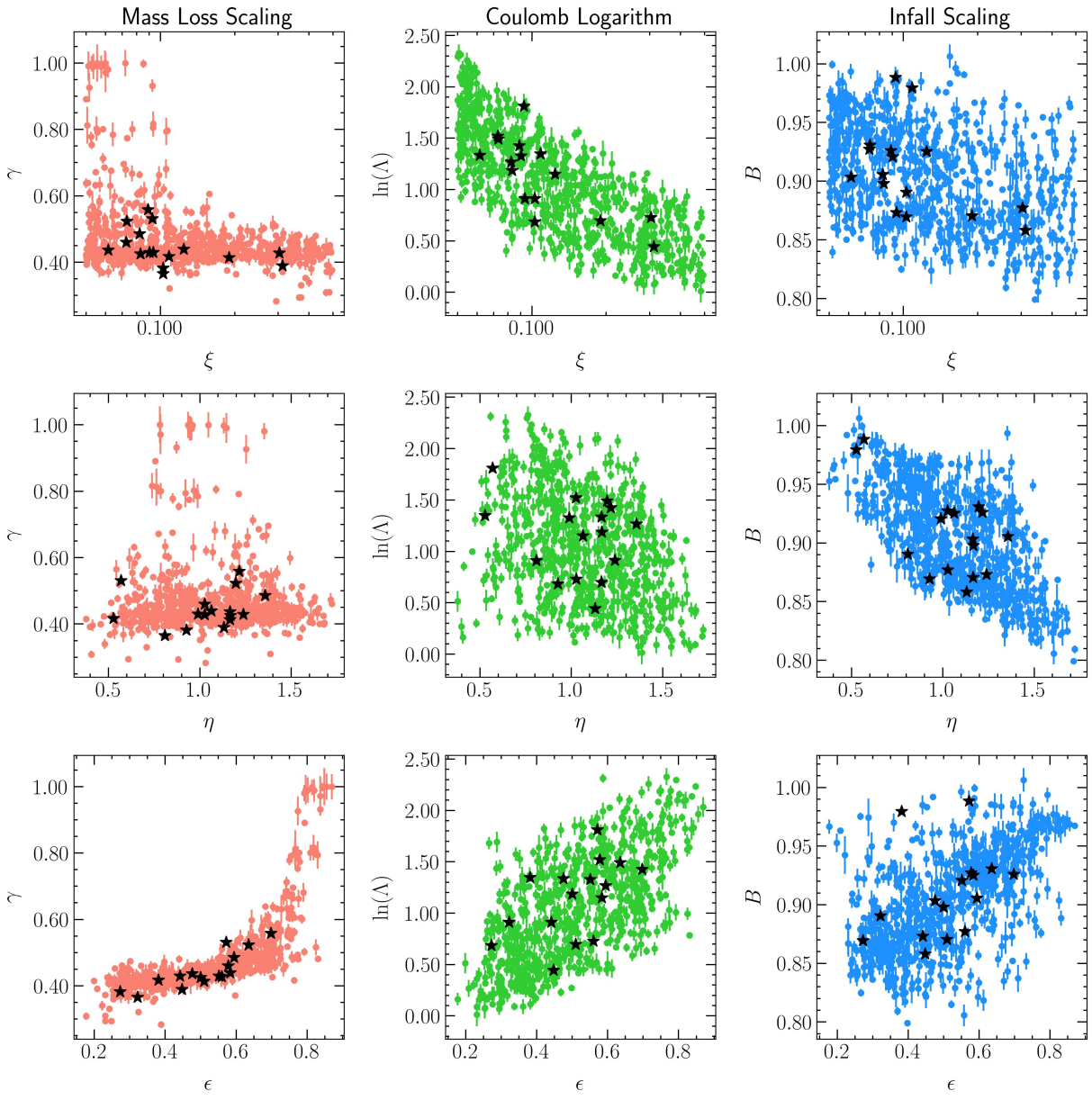



Figure 3.8: Model parameters tuned to the simulations as a function of the initial conditions. The red, green, and blue points show the parameters $\gamma$, $\ln(\Lambda)$, and $B$, respectively. The black stars depict their values for the fiducial simulations.

| XGBoost Hyperparameter | Explored Values | Optimal Values |
|---|---|---|
| **Learning Rate** | 0.002, 0.005, 0.01, 0.02, 0.05, 0.1, 0.2 | 0.02 |
| **Number of Estimators** | 500, 1000, 1500, 2000, 2500, 3000, 3500, 4000 | 2500 |
| **Subsample** | 0.05, 0.1, 0.15, 0.2, 0.25, 0.3, 0.4, 0.5 | 0.05 |

Table 3.1: Summary of the hyperparameters calibrated for training the XGBoost regression model. The columns list (1) the hyperparameter, (2) the values investigated for a given hyperparameter, and (3) their optimal values.

sequentially updating weaker base-models to minimize the error associated with the whole ensemble (Natekin & Knoll, 2013). Due to its speed, accuracy, and versatility, XGBoost has been used broadly in many scientific fields. In astronomy, applications include predicting the halo masses of galaxies (Calderon & Berlind, 2019), modeling the gas distributions in clusters (Machado Poletti Valle et al., 2021), and estimating the metallicities of stars (Andrae et al., 2023).

We train the XGBoost regression model using the initial conditions of the simulations ($\xi$, $\eta$, $\epsilon$) to predict the model parameters ($\gamma$, $\ln(\Lambda)$, $B$). The pipeline to do this involves several steps. First, we split the simulations into training and test datasets using the commonly applied 80-20 split, where 80% of the data is used for training, and the remaining 20% is used to validate the model. This is to prevent overfitting, a process where the model poorly predicts the target parameters when presented with new data not used in training. In total, there were 569 simulations in the training set and 160 simulations in the test set. All the fiducial simulations presented in this thesis were placed in the test set.

Next, we preprocessed the data using the function `RobustScaler` from the library scikit-learn (Pedregosa et al., 2011). This function standardizes the dataset by removing the median and scaling the data according to the interquartile range (IQR). XGBoost is highly sensitive to features at different scales and often biases towards using larger feature values as branches in its trees. Thus, preprocessing is used to transform all input features onto the same scale. The median and IQR were calculated for the training set, and these values were used to scale features in both it and the test set.

Finally, we tuned the hyperparameters used in XGBoost. These are parameters related to the learning process of the model and not the actual feature data. Hyperparameter optimization is essential in order to produce a model that accurately predicts the target

variables. In our case, there were three hyperparameters that needed to be optimized.

1. *Learning rate*: this controls the rate at which new trees are added to the model. Lower values reduce the rate at which trees are added, slowing the learning process to prevent overfitting.

2. *Number of estimators*: this sets the total number of trees fit during model training. While, larger values lead to more accurate models, they are more likely to be overfit.

3. *Subsample*: this controls the ratio of the training instances that occur once per boosting iteration. Setting it to 0.75 means 25% of the data is unused by a specific base-model during one iteration. The other 75% of the data is randomly sampled for creating the base tree. Lower values use smaller fractions of the training data, preventing overfitting.

XGBoost incorporates many other hyperparameters besides the ones we tuned above. All of these were set to their default values except we allowed the tree to have no limit on its depth. We perform a traditional grid search by considering every possible combination of the hyperparameters to find their optimal values. The accuracy of each model was assessed by calculating the root mean squared error (RMSE) between the predicted values of ($\gamma$, $\ln(\Lambda)$, $B$) and their values when calibrated directly from the simulations. We equally weight each orbital model parameter in this calculation. The best XGBoost model minimized the total RMSE of the simulations in the validation set.

Table 3.1 lists the values explored for each hyperparameter along with their optimal values. We found that properly calibrating the learning rate and number of estimators had the largest impact on improving model accuracy. The hyperparameter subsample only minimally contributed to reducing the RMSE. While general tuning was necessary, there were several combinations of hyperparameters that gave similar performance in estimating the orbital model parameters. This implies that the hyperparameters do not need to be fine-tuned to a precise value.

Fig. 3.9 presents predictions for the orbital model parameters from XGBoost compared to their values when calibrated directly from the simulations. The plot is split into the training and validation sets. Here we show how the model parameters vary with the initial conditions, although only for the relationships that had the tightest correlations in Fig. 3.8. The results demonstrate that our machine learning model works extremely well at replicating the values of $\ln(\Lambda)$ and $B$ from the initial conditions. For $\ln(\Lambda)$, its trend can be understood analytically given the Coulomb logarithm scales as $\ln(\xi^{-1})$ (see e.g. Binney

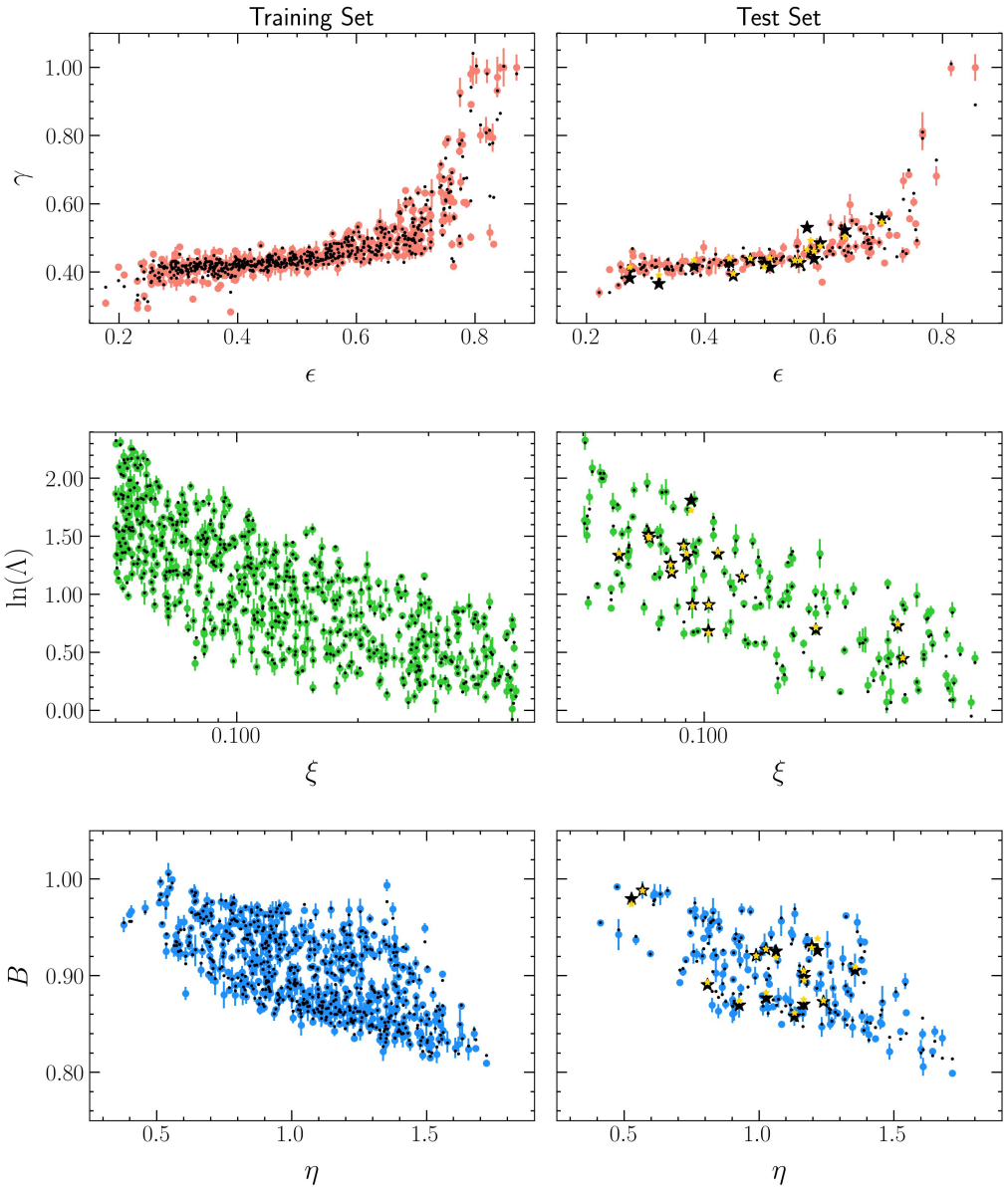



Figure 3.9: XGBoost model predictions as a function of the initial conditions for the training and test datasets. The red, green, and blue points show the parameters $\gamma$, $\ln(\Lambda)$, and $B$, respectively, calibrated directly from the simulations. The black stars depict their values for the fiducial simulations. On the other hand, the black points illustrate the model predictions from XGBoost, while the gold stars demonstrate these predictions for the fiducial simulations.

| Model Parameter | Training Set | Test Set | Combined Set |
|---|---|---|---|
| $\boldsymbol{\gamma}$ | 1.4 % | 2.6 % | 1.6 % |
| $\boldsymbol{\ln(\Lambda)}$ | 1.1 % | 2.5 % | 1.3 % |
| $\boldsymbol{B}$ | 0.21 % | 0.39 % | 0.23 % |

Table 3.2: Median percent difference between the XGBoost model predictions and the values of the parameters when calibrated directly from the simulations. The sets of simulations considered are the training set, the test set, and the total set consisting of all simulations.

& Tremaine, 2008, Eq. 8.1b). As a result, removing this effect from the machine learning architecture could be done in principle.

For the parameter $\gamma$, the model agrees with the value tuned to simulations so long as it falls along the primary, constant band. Outlier points beyond this range (at $\epsilon > 0.75$ in particular) have more considerable disagreement that is generally larger that the error on $\gamma$, although the effect of this on how well the orbital model functions is only moderate. Physically, these high $\gamma$ points are likely caused by additional heating on the satellite (acting for low $\xi$ mergers), enhancing mass loss. Note that the typical best-fit value of $\gamma$ we find for our orbital model is $\gamma \approx 0.4$. Taylor & Babul (2001) on the other hand, who use a very similar mass loss prescription, consider a maximum value for $\gamma = 1/(2\pi) \approx 0.16$ that is roughly 2.5 times smaller. This discrepancy is likely caused by their model including the effects of tidal heating which increases the mass loss rate. Thus, we would expect their model to have a smaller net $\gamma$.

For all parameters ($\gamma$, $\ln(\Lambda)$, $B$), we find that the XGBoost model performs slightly better for the training set than the test set. This is highlighted in Table 3.2, which shows the median percent difference in the orbital model parameters for different sets of simulations. We looked at the median value rather than the average since the underlying distributions were skewed towards lower percent difference. From these results, the median difference between the XGBoost model predictions and the values of the parameters when calibrated directly using the simulations is less than 3% for all sets of simulations considered. This showcases the utility of machine learning models given how well our model works in practice.

# Chapter 4

# Disruption of the Central Halo

## 4.1 Semi-analytic Model to Describe the Response

In Fig. 2.8, we found that at early times during the merger, the direct position of the satellite caused changes in the scale radius of the remnant system. However, once the satellite lost a large fraction of its mass by late times, the remnant's scale radius mirrored that of the central halo. This implies we need to include two components in our model for predicting the evolution of the remnant system's structure: (1) an orbital evolution model to trace the satellite's position and mass, and (2) a model to capture the response of the central halo particles to the motion of the satellite. In this chapter, we focus on the second component and construct a model for the central halo's response. To do this, we split the response of the central halo into its two types and measure the median response for each type. Then, we create scaling relations to transform the median response into the response for each individual system. Finally, we apply the model to determine to what extent including a dynamic host halo affects the trajectory of the satellite. We explore its affects on predictions for the remnant's structural parameters as well.

### 4.1.1 Classifying the Response Types

The central halo has two types of responses: (1) the scale radius gradually declines to a minimum value well before the first pericentre, and (2) the scale radius sharply drops to a minimum value slightly after the first pericentre. We need some method for classifying the responses from the initial conditions. Fig. 4.1 demonstrates we can cleanly separate

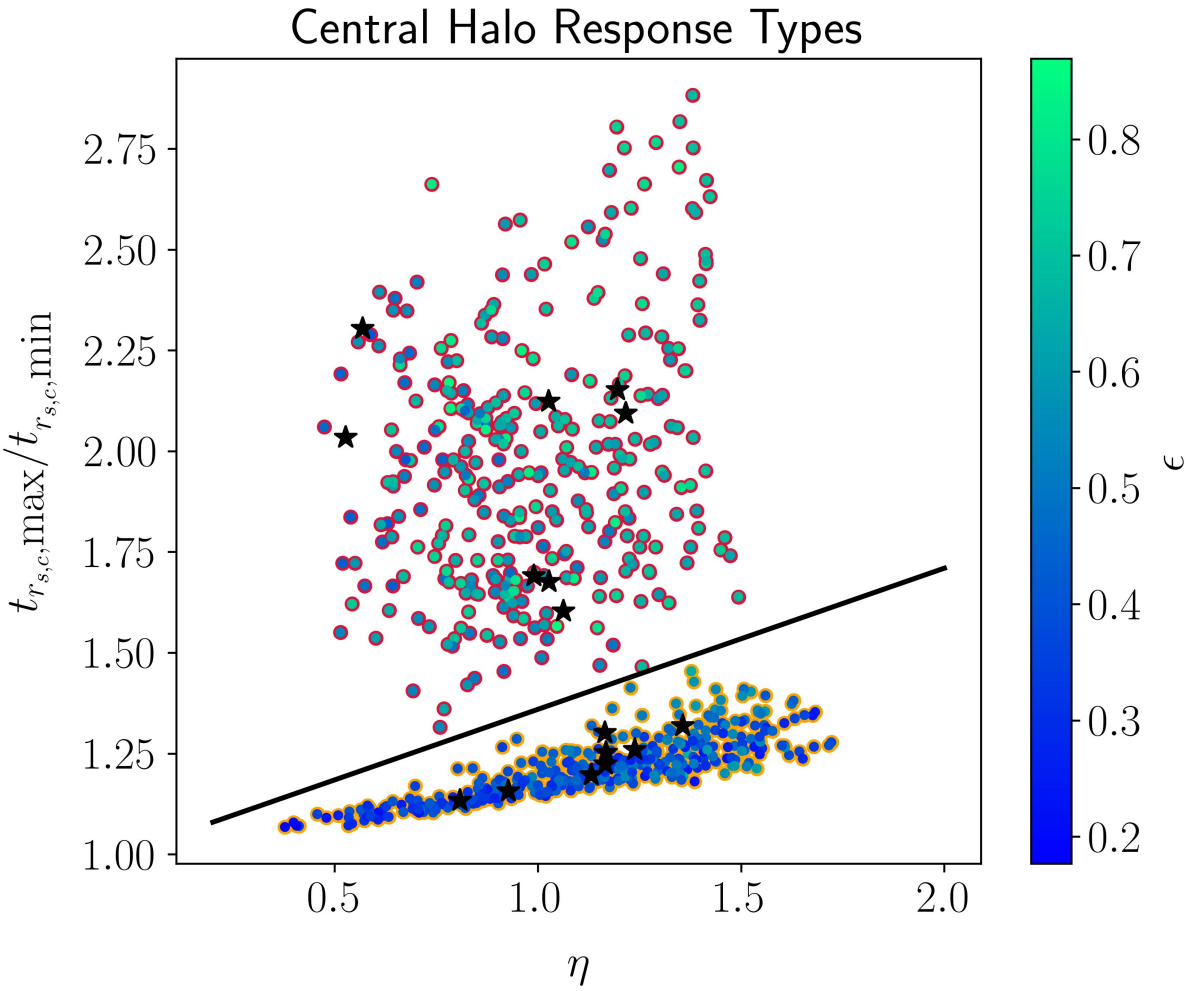



Figure 4.1: Classifying the central halo response into its two types using three parameters: (1) the relative energy, (2) the circularity, and (3) the maximum-to-minimum central halo scale radius time. The outline of each point describes their classification, with type 1 in crimson and type 2 in orange. The black line depicts the explicit separation between the response types, while the black stars illustrate the fiducial simulations.

the responses into their two types using the relative energy parameter and the maximum-to-minimum central halo scale radius time dubbed the time ratio, $t_{r_{s,c},\max}/t_{r_{s,c},\min}$, where $t_{r_{s,c},\max}$ is the time of the maximum value of the scale radius during its first oscillation and $t_{r_{s,c},\min}$ is the time of the minimum value of the scale radius before $t_{r_{s,c},\max}$. This separation into response types can also be made using one of ($\xi$, $\epsilon$, $r_p$) as the independent quantity, although the exact position to split them is not as clear when using one of these other initial conditions (see Appendix A.3 for details). In the plot, we find that type 1 responses are clustered into a broad group with larger time ratios, while type 2 responses are clustered into a tight group with smaller time ratios. Of the 729 simulations, 326 (44.7%) were type 1 and 403 (55.3%) were type 2. The explicit separation between the response types is depicted by the black line, which has the functional form,

$$t_{r_{s,c},\max}/t_{r_{s,c},\min} = 0.35\eta + 1.01 \tag{4.1}$$

The type of central halo response varies with circularity as well, although there is some overlap between the groups. This follows from the orbital dynamics during the merger. Satellites on radial orbits with low circularity compress the central halo particles significantly near pericentre leading to the sharp drop in scale radius and short time ratio we see in type 2 responses. On the other hand, satellites on tangential orbits with high circularity do not travel deep enough into the central halo's potential on their initial infall. Instead, for type 1 responses, the outer region of the central halo gradually expands and this slightly alters the truncation scale of the profile.

Meanwhile, the gradual drop in scale radius is dominated by an instability in the central halo's initial profile (see Fig. A.1 for an illustration of this effect). Therefore, it is not a physical effect caused by an interaction with the satellite unlike the primary oscillation after pericentre. The cross-over point where the initial drop in scale radius becomes physical (i.e. the type 1/2 separation) is $r_p \sim 2\, r_{s,c,0}$ or $t_{r_{s,c},\max}/t_{r_{s,c},\min} \approx 1.5$ (see the top-right panel of Fig. A.5). Regardless of if type 1 responses result from an instability, we still need to distinguish them from type 2 responses.

Eq. 4.1 provides a direct method to identify the type of central halo response for a given merger. However, the time ratio $t_{r_{s,c},\max}/t_{r_{s,c},\min}$ is a quantity that is generally not predictable from the initial conditions. We require advance knowledge of the simulation output to calculate it. While the value of $t_{r_{s,c},\max}$ roughly scales with the time the satellite reaches the first apocentre of the orbit, the value of $t_{r_{s,c},\min}$ is more complex as it depends on the response type. For type 2 responses, it usually coincides with the time of pericentric passage for the first orbit. Conversely, for type 1 responses, there does not exist a simple relationship to determine $t_{r_{s,c},\min}$. To overcome this problem, we employ a support vector

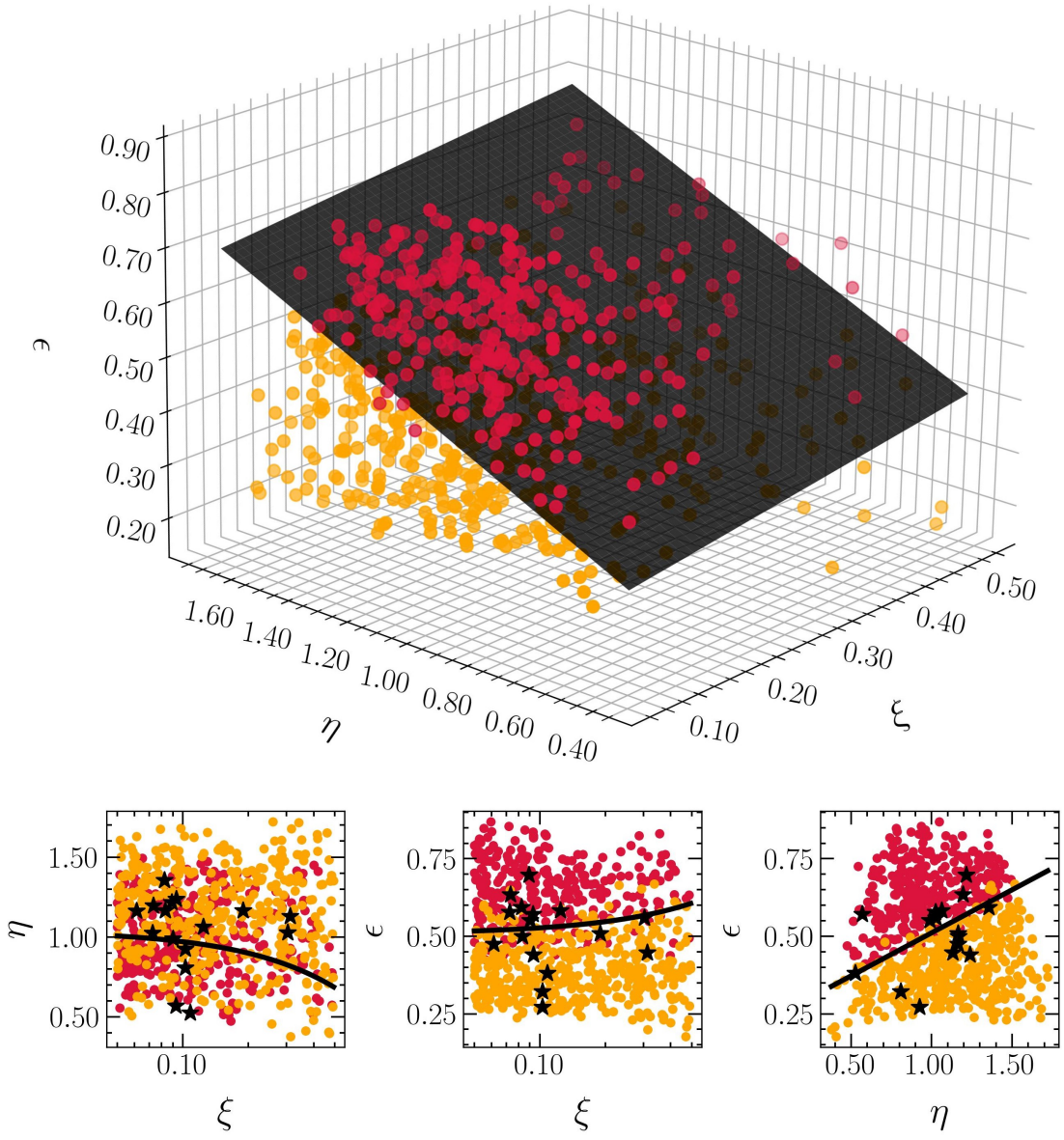



Figure 4.2: SVM derived plane used to predict the central halo response classification. Each point depicts the initial conditions of a given simulation coloured by their response type, with type 1 in crimson and type 2 in orange. In the bottom panels, the plane is projected into 2D for each pair of initial conditions, where the third parameter is evaluated using its median value. The black stars show the fiducial simulations.

machine to classify the central halo responses as accurately as possible solely from the initial conditions.

Support vector machines (SVMs) are a set of machine learning methods used for classification, regression, and outlier detection (Vapnik, 1995). As a classification tool, it attempts to fit some function, either a kernel or hyperplane, that maximizes the separation between the classes. For linearly separable data, a hyperplane is used, and the distance to the nearest point on each side of the plane is maximized. If the data is non-linear and non-separable, a kernel is built to map the data into some other space where the data is linearly separable by a hyperplane. The primary benefit of SVMs is their versatility given the numerous kernels that can be defined for mapping between spaces. Moreover, they are a multi-class classifier that operates well in many dimensional spaces and for small datasets as long as the classes are balanced.

In astronomy, SVMs have been employed to classify galaxy morphology (Huertas-Company et al., 2011) and supernovae types (Lochner et al., 2016) from photometry. While these works utilize SVMs for more complex tasks, our case involves the simplest possible problem, a two type classification. We train an SVM using the function `SVC` from the library SCIKIT-LEARN (Pedregosa et al., 2011) to predict the type of central halo response from the initial conditions. As before with XGBOOST (see Section 3.3), we split the simulations into training and test datasets, applying an 80-20 split. All the fiducial simulations were again placed in the test set. This time, we did not need to preprocess the target data. However, there were two hyperparameters that needed to be selected.

1. $C$: this is a regularization parameter that controls the error tolerance for non-separable data.

2. *Kernel*: this specifies the kernel type to use when mapping non-linear and non-separable data into a space where the data becomes linearly separable.

We chose to apply a linear kernel and found the optimal value for the regularization parameter that maximized the number of correctly identified response types in the test set was $C = 0.5$. All other hyperparameters used in `SVC` were set to their default values. Fig. 4.2 shows each combination of initial conditions ($\xi$, $\eta$, $\epsilon$) used in training the SVM. In the top panel, the plane derived by the SVM used to separate the classes is plotted in black. In the bottom panels, this plane is projected into 2D for each pair of initial conditions. For the third initial condition not included, it is evaluated at its median value considering all simulations. Since we used a linear kernel, we can explicitly state the equation of the

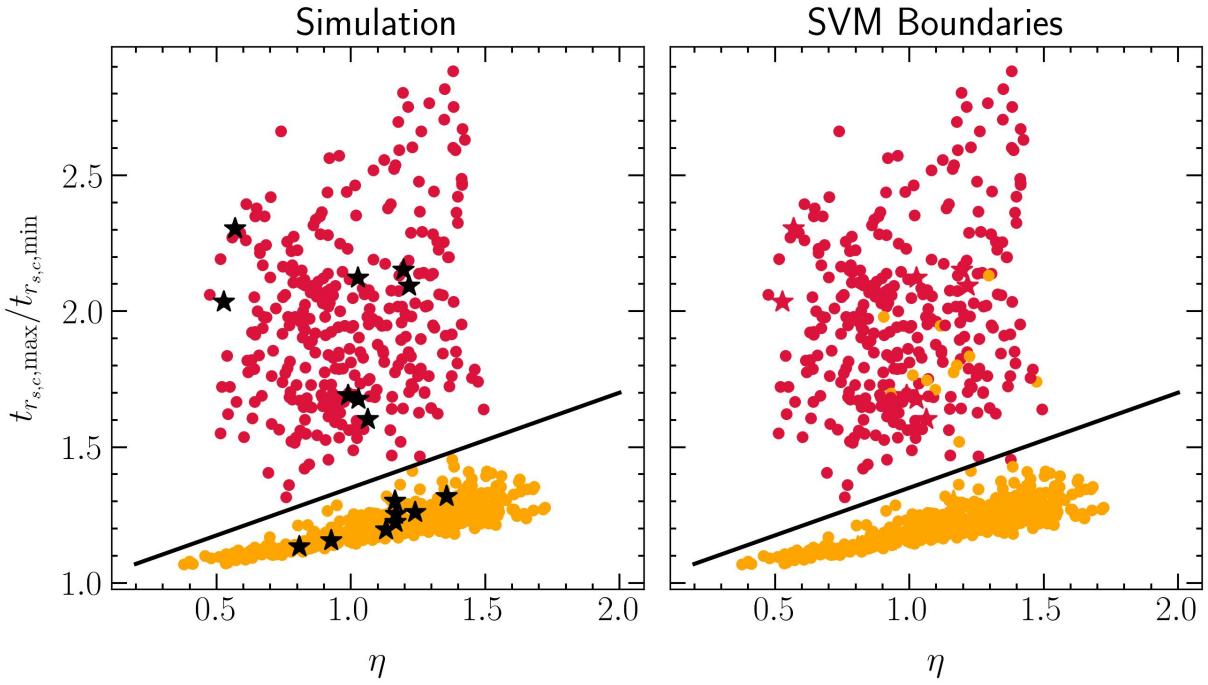



Figure 4.3: Comparing the central halo response types derived from the maximum-to-minimum central halo scale radius time measured in the simulations (left) to their predictions using the SVM derived plane (right). The colour of each point describes their classification, with type 1 in crimson and type 2 in orange. The black line depicts the explicit separation between the response types, while the black stars (left) and coloured stars (right) illustrate the fiducial simulations.

plane obtained by the SVM.

$$\text{type} = \begin{cases} 1, & \text{if} \quad 1.56\,\xi + 2.17\,\eta - 7.81\,\epsilon + 1.64 < 0 \\ 2, & \text{if} \quad 1.56\,\xi + 2.17\,\eta - 7.81\,\epsilon + 1.64 \geq 0 \end{cases} \tag{4.2}$$

Fig. 4.3 recreates Fig. 4.1 except the color of each point represents its classification. The central halo response type is determined directly from the simulations in the left panel, while it is obtained from Eq. 4.2 in the right panel. In both panels, we show the results of all simulations. Overall, we find the SVM classifies the responses very well. In total, the response types of 713/729 simulations were classified properly, including all the fiducial simulations, a 97.8% success rate. Of the remaining responses, 4/16 were misclassified as type 1, while 12/16 were misidentified as type 2. Thus, we find Eq. 4.2 has a slight

preference to mistake type 1 responses as type 2. In hindsight, using machine learning was not necessarily required in order to separate the responses into their two types given the decision surface (i.e. Eq. 4.2) is just a plane defined by a simple linear combination of the initial conditions. A different method to determine the weights on each initial condition could have been used instead. The advantage of SVMs is the different kernels that can be applied in the algorithm to transform the data. However, we found that more complex kernels did not improve our classification success rate.

### 4.1.2 Modeling the Central Halo Scale Radius

In the previous section, we were able to predict the response type from the initial conditions with high accuracy. Given this, we now need to construct a model for how the central halo scale radius evolves during the merger. Fig. 4.4 plots individual measurements of the central halo scale radius from every simulation separated into the two response types. Here we subtract off the quantity $\overline{r_{s,c,0}}$, the average value of the scale radius before $t = 0.5\,t_p$, from each curve and scale them by the amplitude of the primary oscillation, $A$, calculated as the difference between the maximum and minimum scale radii measured at $t_{r_{s,c},\max}$ and $t_{r_{s,c},\min}$, respectively. Furthermore, we adjust the timescale in order to get temporal overlap in the primary oscillation. While there is some variation, particularly at late times, it is clear that each curve follows a similar pattern once we separate them by response type.

As a result, we base our model for the central halo scale radius on the empirically measured median response, shown as the black curves. These are our baseline waveforms. The grey regions give the $1\sigma$ scatter in the median. We find that a majority of the variance in the median is after the satellite reaches pericentre for a second time. There is little scatter in the median around the primary oscillation and during the initial infall of the satellite. We tested using a simpler scaling for measuring the median response from the individual curves (i.e. scaling each curve as $r_{s,c}/r_{s,c,0}$, where $r_{s,c,0}$ is the initial value of the central halo scale radius) and found that this produced much larger error bars around the peak of the primary oscillation while simultaneously damping out its amplitude significantly. This was true for both response types. Therefore, the amplitude $A$ should be considered instead.

Given the empirically measured median response, $r_{s,c,\,\mathrm{med}}$, our model for the central halo response is then of the form,

$$r_{s,c}\left(\frac{t}{t_{r_{s,c},\max}}\right) = A \times r_{s,c,\,\mathrm{med}}\left(\frac{t}{t_{r_{s,c},\max}}\right) + r_{s,c,0} \tag{4.3}$$

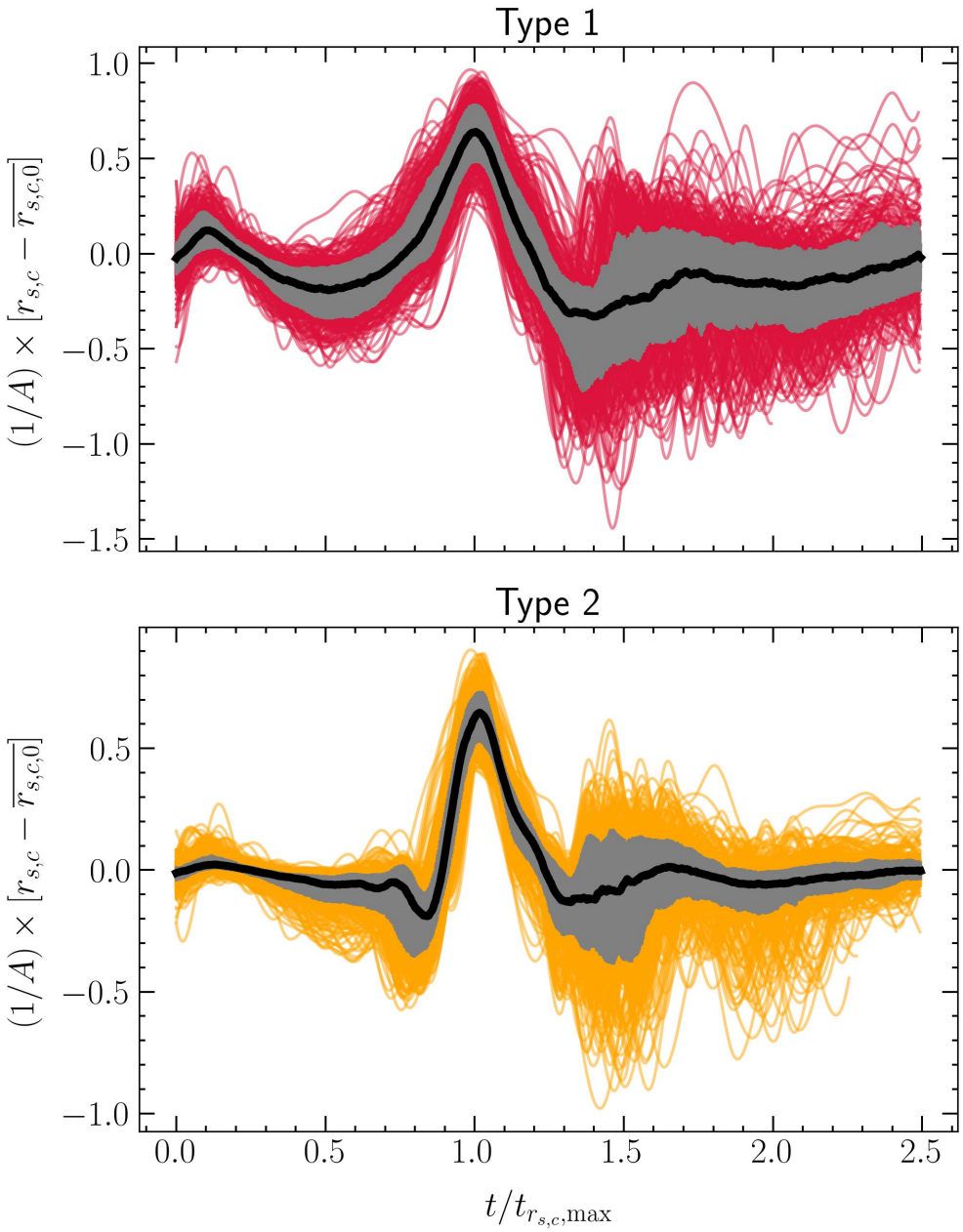



Figure 4.4: Stacked measurements of the central halo scale radius as a function of time in the simulations. Each line illustrates individual simulations separated by response type, with type 1 in crimson (top) and type 2 in orange (bottom). The black lines depict the median responses of each type, $r_{s,c,\mathrm{med}}$, while the grey regions show their $1\sigma$ scatter.

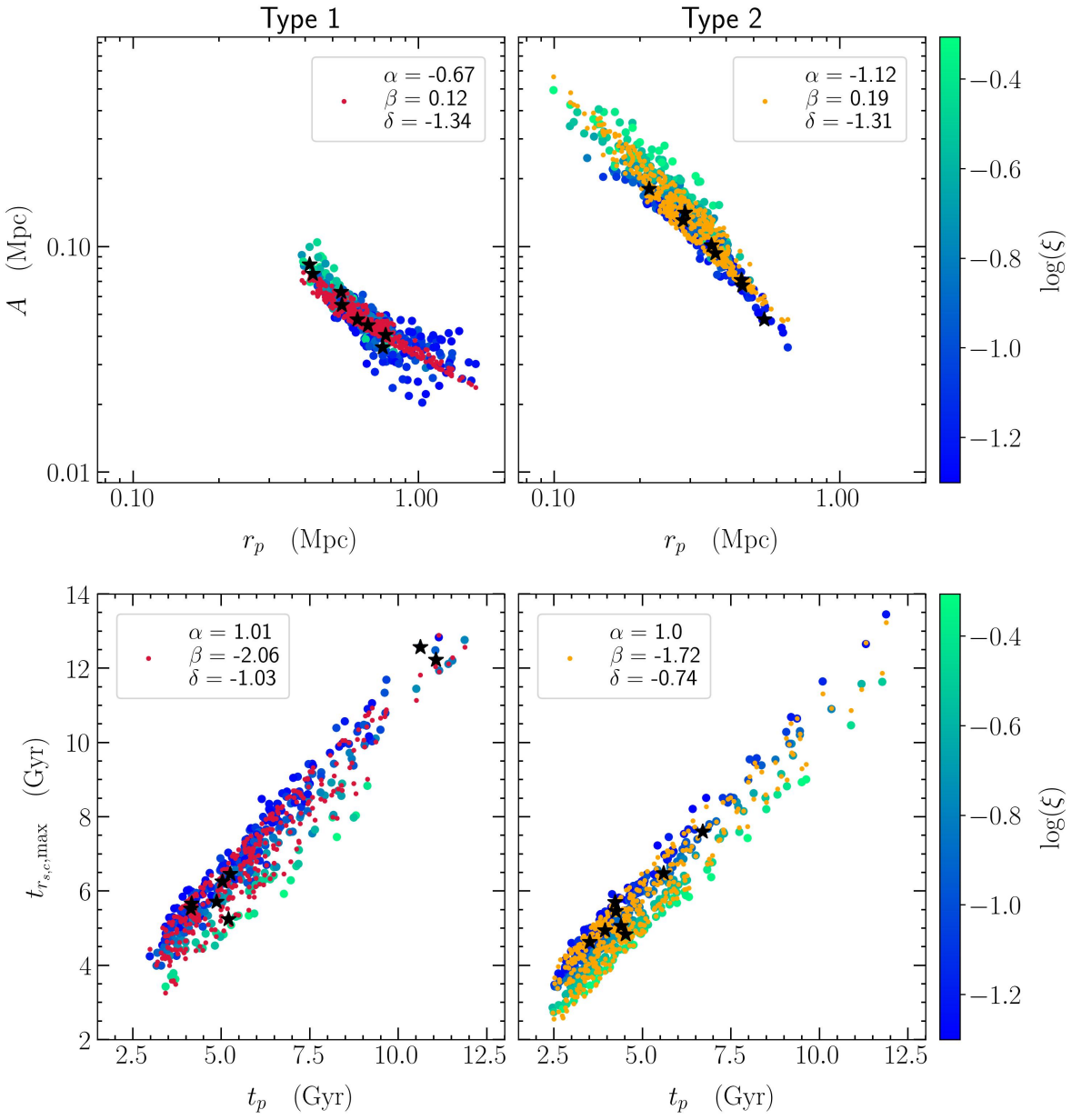



Figure 4.5: Predictions for the parameters $A$ (top) and $t_{r_{s,c},\max}$ (bottom) used in our central halo response model. The coloured, background points show their values measured directly from the simulations. The smaller, foreground points show their values predicted from the scaling relations, with type 1 in crimson (left) and type 2 in orange (right). The colourbar illustrates the mass ratio of the merger.

| Model Parameter | Type | $\boldsymbol{\alpha}$ | $\boldsymbol{\beta}$ | $\boldsymbol{\delta}$ |
|---|---|---|---|---|
| $\boldsymbol{A}$ | 1 | $-0.67 \pm 0.04$ | $0.12 \pm 0.02$ | $-1.34 \pm 0.02$ |
| | 2 | $-1.12 \pm 0.02$ | $0.19 \pm 0.01$ | $-1.31 \pm 0.02$ |
| $\boldsymbol{t_{r_{s,c},\max}}$ | 1 | $1.01 \pm 0.01$ | $-2.06 \pm 0.07$ | $-1.03 \pm 0.09$ |
| | 2 | $1.00 \pm 0.01$ | $-1.72 \pm 0.03$ | $-0.74 \pm 0.04$ |

Table 4.1: Central halo response model parameters used to scale the median $r_{s,c}$ evolution curve. Each type of central halo response, given in the second column, had different best-fit model parameters. The variables ($\alpha$, $\beta$, $\delta$) relate the model parameters to the initial conditions of the simulations. Their values are depicted in the labels of Fig. 4.5 as well.

where we use the initial value of the central halo scale radius rather than its average value since the median curves in Fig. 4.4 nearly start at zero. The response model parameters are best related to the initial conditions of the merger by,

$$\log(A) = \alpha \log(r_p) + \beta \log(\xi) + \delta \tag{4.4}$$

$$t_{r_{s,c},\max} = \alpha\, t_p + \beta \log(\xi) + \delta \tag{4.5}$$

where $t_p$ and $r_p$ are the time to pericentre and its position, respectively, for a static orbit in a spherically symmetric potential (see Appendix B.1 for details but note that we can convert from $\eta$ and $\epsilon$ to $t_p$ and $r_p$ since both sets of quantities depend on $E_{\rm orb}$ and $L_{\rm orb}$). We examined many initial conditions ($\xi$, $\eta$, $\epsilon$, $v_r/v$, $v/v_{200}$, $t_p$, $r_p$, $r_a$, $x_c$) when deriving these relations but ultimately found that $t_p$ and $r_p$ had the highest correlations with the model parameters, while $\xi$ varied perpendicular to this. The variables ($\alpha$, $\beta$, $\delta$) are scaling factors that relate the initial conditions to the response model parameters. Their best-fit values are shown in Table 4.1, where they differ for each model parameter and response type. These were obtained by minimizing the RMSE between the predicted values of ($A$, $t_{r_{s,c},\max}$) and their values measured directly from the simulations using the function `minimize` from the Python library LMFIT (Newville et al., 2016). The errors on the scaling factors were estimated from the covariance matrix output from our least squares fitting.

Fig. 4.5 compares predictions for the response model parameters to their values measured from the simulations. Note that the type 1 responses typically have lower oscillation amplitudes since pericentre after the initial infall is further out from the position of the central halo. From the plot, we find that the scaling relations accurately predict $t_{r_{s,c},\max}$ for both response types and $A$ for type 2 responses. However, the parameter $A$ is modeled

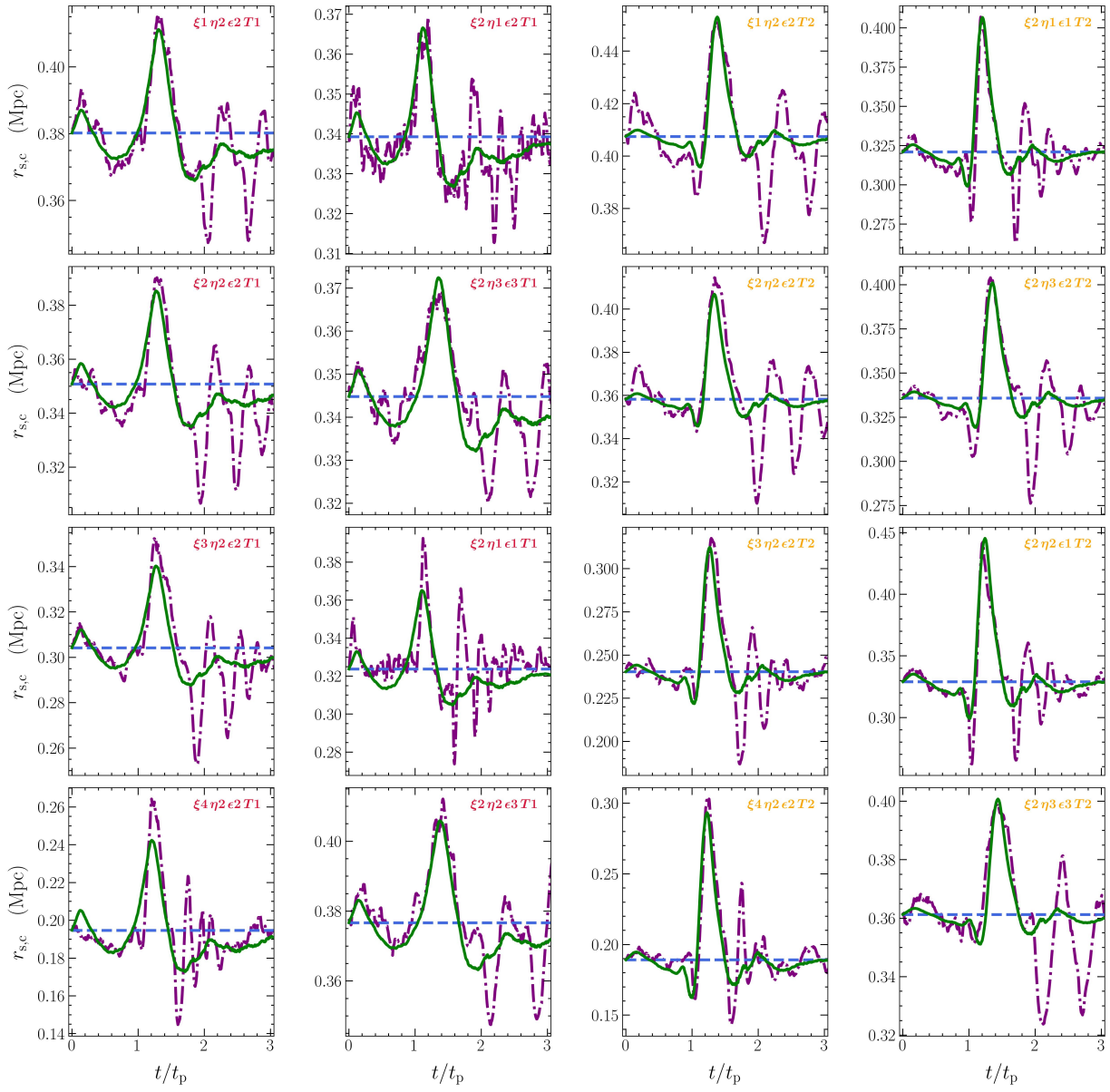



Figure 4.6: Measured central halo scale radius in the simulations (purple, dashdot) compared to models including (green, solid) or excluding (blue, dashed) the response of the central halo during the merger. In each subplot, the timescale is shown relative to the time to pericentre, while the label gives the simulation name and response type.

poorly for type 1 responses with large pericentric passage distances. Here, we were unable to capture the scatter in the amplitude since there is little perpendicular variation with mass ratio. We tested using a different definition for the amplitude (i.e. $A$ = the standard deviation of all scale radii measurements between $t_{r_{s,c},\min}$ and $t_{r_{s,c},\max}$) but found no improvement.

From the response model parameters and the median response, we can use Eq. 4.3 to model how the central halo scale radius evolves during individual mergers. Fig. 4.6 illustrates the model predictions for the fiducial simulations. For both response types, we find the model accurately recreates the simulation result up to the second pericentre of the orbit, although for a few type 1 responses the amplitude is marginally lower than expected. After this point, the model begins to fail since the median response the model is built from does not pick up the secondary oscillations in scale radius we find in the simulations. These later oscillations are damped out from the median behaviour when we centre it on $t_{r_{s,c},\max}$. In principle, we could try to capture the secondary oscillations in addition to the primary oscillation by measuring the median response for each orbit separately. Here, we would split the response curves into sub-orbits, centre them on the oscillation peaks, and stitch them back together to get the entire response. The drawback of doing this is it increases the number of model parameters (i.e. 2 extra parameters, an amplitude and a timescale, per orbit), and these new model parameters are not guaranteed to scale well with the initial conditions. Ultimately, modeling more than the primary oscillation in the central halo scale radius is largely unnecessary when trying to capture the median evolution of the remnant scale radius.

Lastly, in Fig. 4.6, we note that the central halo scale radius experiences an initial jump before it declines to a stable value. This is seen in both the model and most simulations, and is more pronounced in the type 1 responses. In the simulations, this is caused by collisional effects when generating the initial halos using ICICLE (see Appendix A.1 for a discussion). In other words, it is the result of an artificial change to the profile rather than a change brought about by a physical interaction with the satellite.

## 4.2 Orbital Model Predictions

In principle, incorporating a dynamic host halo into the orbital evolution model should impact the trajectory and mass loss of the satellite. To determine the extent of its effect, we consider the same orbital model as defined in Chapter 3, except at each step along the trajectory we update the value of the central halo scale radius using Eq. 4.3. Given its new scale radius, the characteristic density of the central halo is adjusted as well to keep the

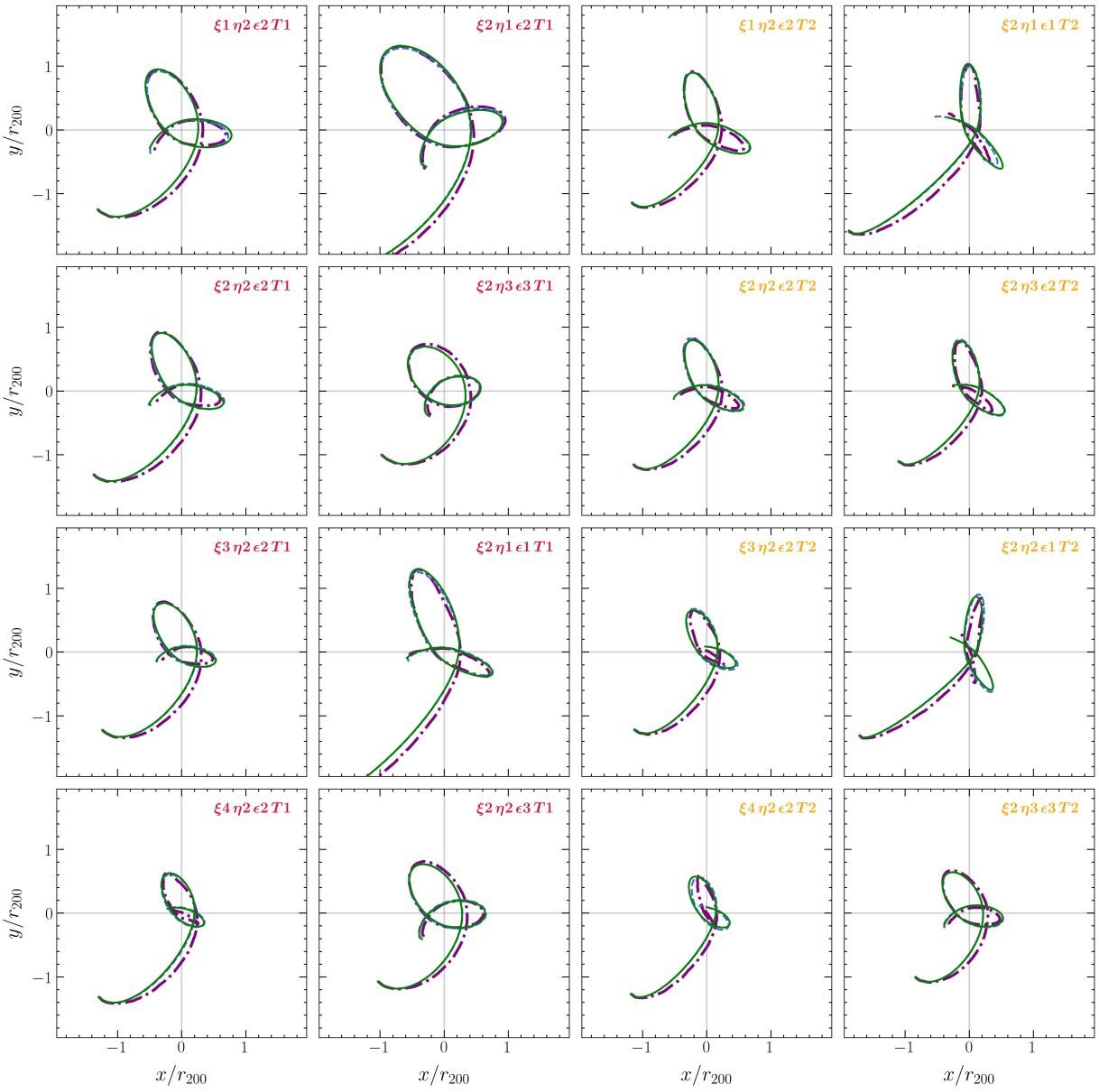



Figure 4.7: Measured motion of the satellite in the orbital plane in the simulations (purple, dashdot) compared to models including (green, solid) or excluding (blue, dashed) the response of the central halo during the merger. In each subplot, the coordinates are shown relative to the central halo virial radius, while the label gives the simulation name and response type.

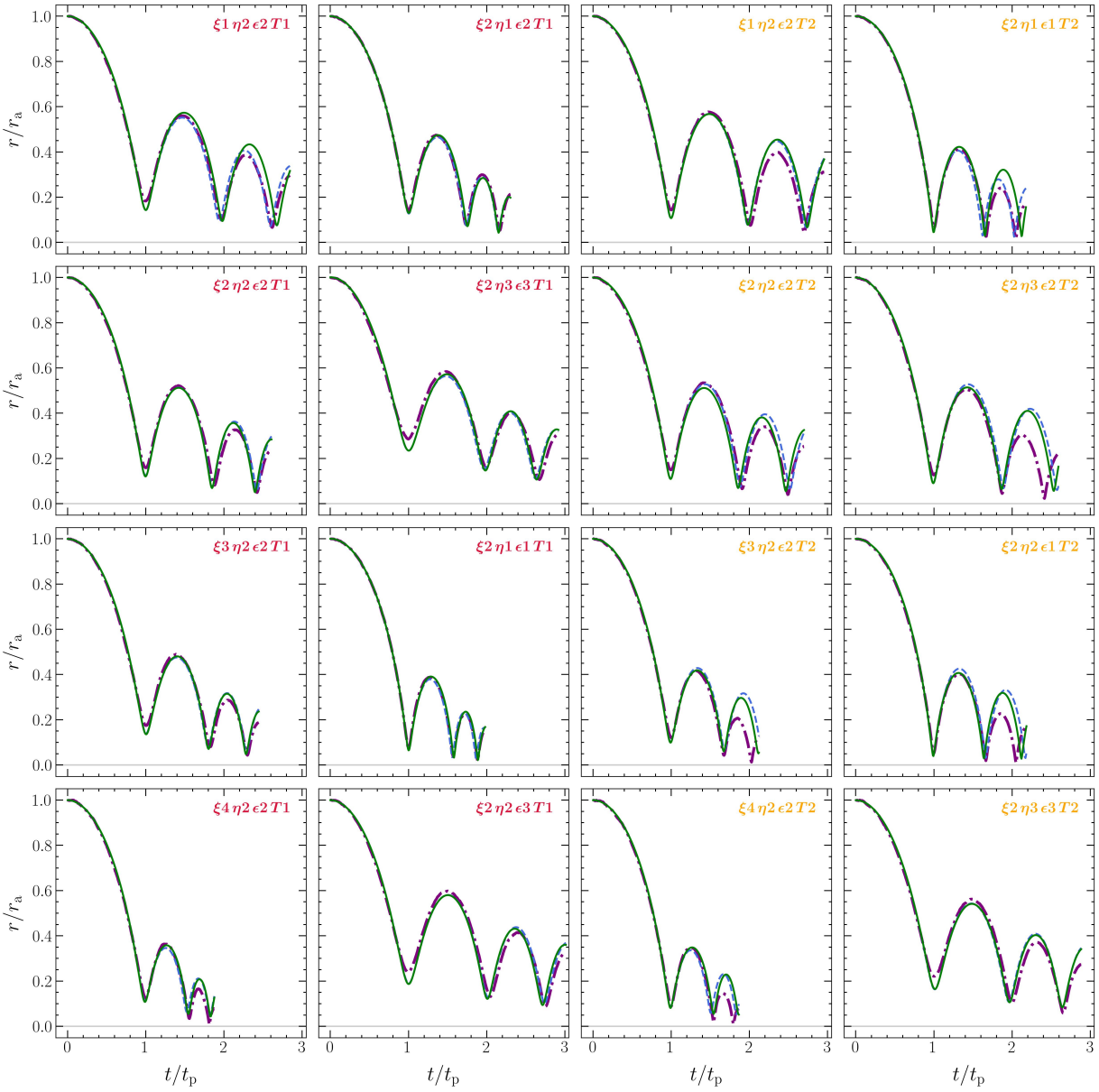



Figure 4.8: Measured radial separation between the satellite and central halos' positions of highest local density in the simulations (purple, dashdot) compared to models including (green, solid) or excluding (blue, dashed) the response of the central halo during the merger. In each subplot, the timescale is shown relative to the time to pericentre, while the label gives the simulation name and response type.

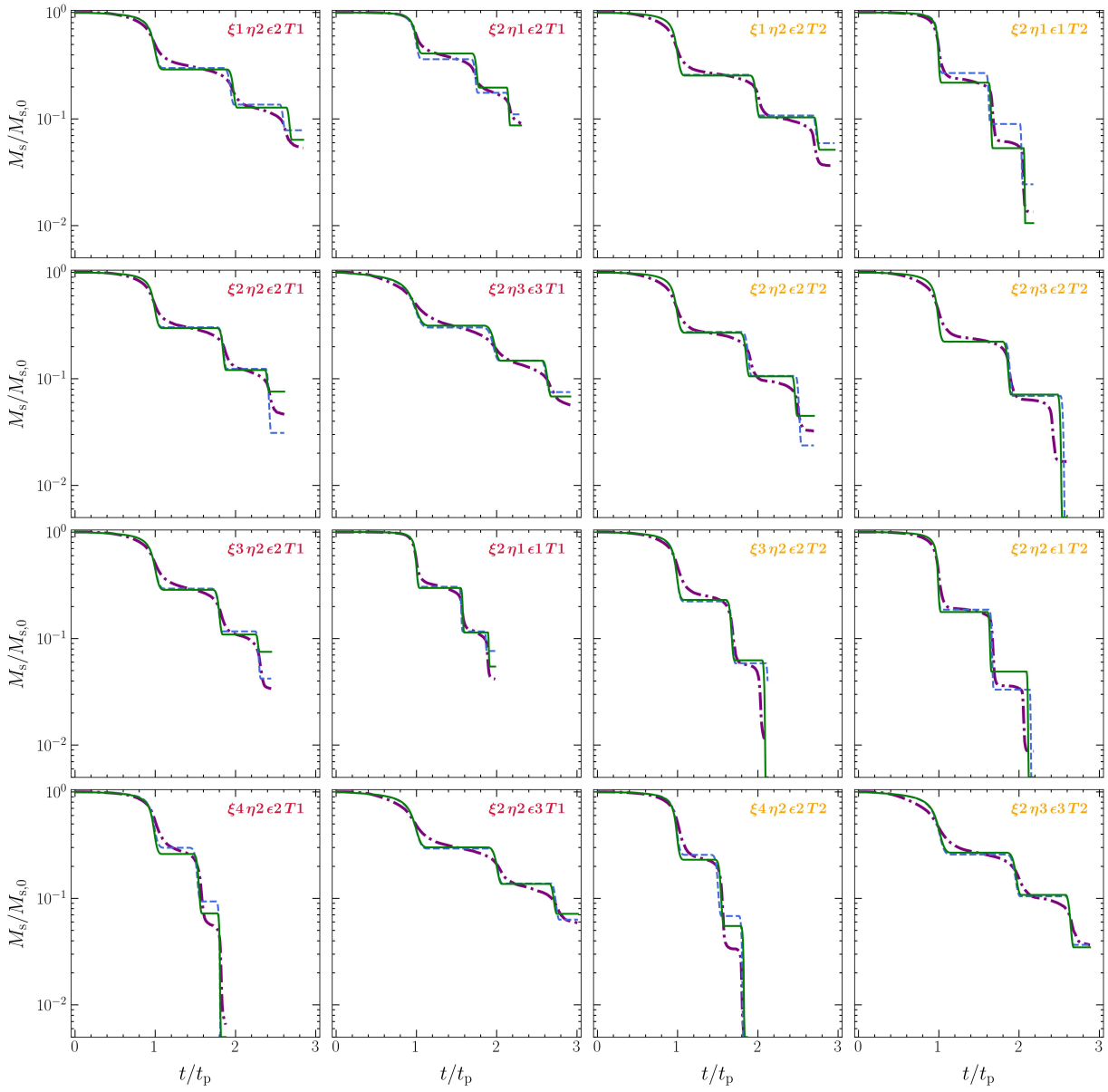



Figure 4.9: Measured satellite mass loss in the simulations (purple, dashdot) compared to models including (green, solid) or excluding (blue, dashed) the response of the central halo during the merger. In each subplot, the timescale is shown relative to the time to pericentre, while the label gives the simulation name and response type.

total mass within the truncation radius consistent with its initial mass. Since the median response curve used to model changes in the central halo scale radius is discretely sampled (i.e. a time sampling equivalent to the time of the simulation snapshots), linear interpolation is utilized to predict the value of the central halo scale radius at times in between our sampling, if required. Additionally, compared to the orbital model described in Chapter 3, this version determines the central halo response type using Eq. 4.2 and it employs model parameters ($\gamma$, $\ln(\Lambda)$, $B$) predicted from XGBoost as opposed to calibrating them from the simulations (see Section 3.3).

Figs. 4.7-4.9 show the orbit of the satellite, its radial separation from the central halo, and its mass loss, respectively, for the fiducial simulations. As in Chapter 3, we include measurements for the first three orbits of the merger, ending at the time the satellite reaches the third apocentre of its orbit. In the plots, a solid green line illustrates a model that incorporates the response of the central halo, while a dashed blue line depicts that neglecting it. In Fig. 4.7, we find that including the central halo response does not affect the planar orbit of the satellite. The model still predicts a more radial initial infall to pericentre compared to the simulations.

In Figs. 4.8 and 4.9, predictions for the satellite's radial separation and mass loss are either equivalent or marginally improved when adding the central halo response to the orbital model compared to when it is excluded. For mass loss, typically agreement with the simulations is enhanced during the third orbit after 90% or more of the satellite's mass has already become unbound. The mass loss before this point is largely unaffected. $\xi 2\,\eta 2\,\epsilon 1\,T2$ is the only simulation in our fiducial set where the mass loss model is worse when including the central halo response. This is caused by a 10.1% difference in the value of $\gamma$ from XGBoost compared to its best-fit value calibrated to the simulation directly. In contrast, the median percent difference in this parameter is 1.6% (see Table 3.2). This explains the poor mass loss agreement we find, since $\gamma$ is poorly estimated, even though the orbit is well modeled.

Lastly, as a result of better mass loss predictions, some simulations (e.g. $\xi 1\,\eta 2\,\epsilon 2\,T1$ and $\xi 2\,\eta 1\,\epsilon 1\,T2$) appear to exhibit less orbital decay than expected when including the response of the central halo. This occurs during the second orbit when the satellite is moving from pericentre to apocentre. During this period, the satellite loses more mass as opposed to the model neglecting the response, resulting in less dynamical friction acting on it and an orbit that is further out. Overall, we conclude that incorporating the central halo response has little impact on the orbital evolution of the satellite and its mass loss.

## 4.3 Remnant System Structural Property Predictions

Putting together predictions for the orbital evolution of the satellite and the central halo response, we can model the remnant system structural properties during and after the merger. From the orbital evolution model, we obtain the satellite's position, velocity, and mass, as well as the amount of unbound material at each step along its trajectory. On the other hand, the central halo response model describes how its profile changes with time. To predict structural properties of the remnant system at any given time, we implement the following procedure:

1. The truncation radius of the satellite is adjusted given its mass from the orbital evolution model.

2. The central halo scale radius is updated given its value from the central halo response model. Its characteristic density is then adjusted as well so that the total mass within the truncation radius is consistent with its initial mass.

3. Particle realizations of the satellite and central halos are generated using rejection sampling given their current NFWT parameters (see Appendix B.3 for details on this process). The satellite is then moved to its position output from the orbital evolution model, while the central halo remains at the centre of the frame.

4. A particle realization of the unbound mass is placed into a spherical shell around the central halo. The shell's radius corresponds to the satellite's position at the time it was removed. The particles in the shell are given a 3D position by way of random angles (see Eqs. B.39 and B.40). Note that only the particles that unbind at the current time are generated. For particles that became unbound at an earlier time, their positions are stored for later use. Once it is placed, the material does not move from its original position.

This method for modifying each halo's parameters and placing the unbound mass is consistent with that employed in the orbital evolution model. In addition, using particle realizations for the halos is ideal since it allows us to measure the remnant system structural properties in the model identically to the simulations. In principle, we could instead use a 3D grid to represent the mass distribution of the remnant system from its components. However, we found that doing this significantly increases the time required to compute the mass distribution given the fine resolution we need in the interior of each halo. For consistency, we set the mass of each sampled particle, $M_p$, to the value used in

the simulations. As a result, the number of particles used to represent the halos in our model is similar as well.

Rather than generate particles for the halos in our model using ICICLE, we instead chose to implement rejection sampling. There were two primary reasons for this. First, ICICLE operates notably slower than rejection sampling since it produces particle velocities in addition to their positions. Compounding this, we cannot set the exact number of particles to sample in ICICLE due to how it truncates profiles (see Section 2.2.1 for a discussion). To create a halo with a mass accurate to within 1%, in general, we need to iteratively resample the halo $\sim 10$ times while varying the input number of untruncated particles. The combination of these effects makes ICICLE prohibitively slow, and thus unsuited for our model given that we need to generate new halos at each timestep. Rejection sampling overcomes both of these obstacles as we can select the exact number of particles to sample and it operates significantly faster than ICICLE (i.e. $\sim$ 200x faster for a typical profile).

In our model, the remnant structural properties can be measured in $3-5$ minutes assuming we use the standard number of timesteps to evaluate the satellite's trajectory (see Section 3.2). The orbital model itself can be evaluated within 10 seconds as well. On the other hand, running the merger simulation and analyzing it to extract the remnant properties takes $40-80$ minutes depending on the total number of particles in the system. Overall, we expect the model to generate these properties $\sim 8-25$x faster than the architecture required to simulate the merger directly. This can be increased further given the simulation runs in parallel whereas the model only uses a single core.

One difference from the orbital evolution model is that not all the mass lost from the satellite turns into unbound material when modeling the remnant system. The reason for this is demonstrated in Fig. 4.10. Here we show how predictions for the remnant system scale radius change depending on the fraction of unbound material that is transferred to the central halo. In the plot, a transferred $M_{\rm ub}$ fraction of 50% indicates that 50% of the unbound material is instead moved to the central halo.

In Fig. 4.10, we find the predicted evolution of the remnant scale radius varies drastically depending on the value of the transferred $M_{\rm ub}$ fraction, particularly after the initial infall to pericentre. The transferred $M_{\rm ub}$ fractions that result in the best match between the model and simulation remnant scale radii are 75% for type 1 responses and 90% for type 2 responses. These are the values we ultimately use when modeling the remnant system structural parameters. Since a fraction of the unbound material is transferred to the central halo, its characteristic density is adjusted to account for this increase in mass. Thus, the material is essentially distributed throughout the central halo.

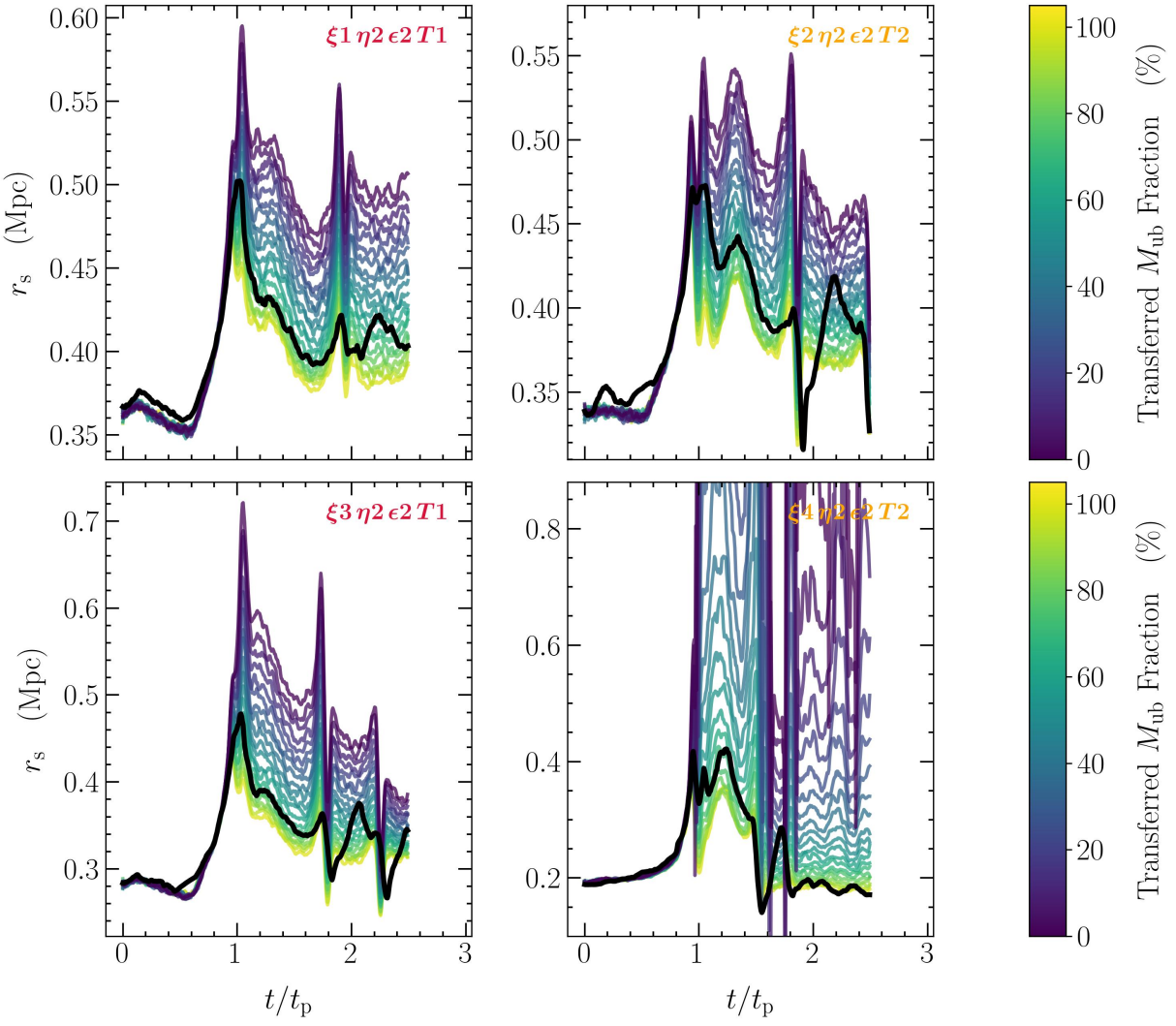



Figure 4.10: Examining how predictions for the remnant system scale radius change depending on the fraction of unbound material that is transferred to the central halo, depicted by the colourbar. In each subplot, the black lines give the simulation measurement for the scale radius. The simulations and their response types are labeled in the top-right corners.

Unfortunately, to predict the remnant system scale radius as accurately as possible, we must make this concession. If we try to use these values for the transferred $M_{\rm ub}$ fraction in the orbital model (i.e. material is moved to the central halo when evaluating the satellite's orbit), then we cannot reproduce the radial separation or mass loss curves for high mass ratio mergers, even when adjusting the model parameters. If we neglect unbound material entirely, then the remnant system NFWT parameters are poorly modeled in the median case, specifically after the satellite first reaches pericentre. Our tests indicate there is no consistent configuration of the model that works perfectly if the unbound mass is distributed in spherical shells. In Section 4.3.2, we will propose a different unbound mass model and examine its effects on predictions for the remnant system structural properties.

### 4.3.1 Concentration and Scale Radius

From the particle realizations of the remnant system at each timestep in the model, we predict the evolution of its scale radius and concentration during the merger. To do this, we apply the same method for measuring these properties as in the simulations (see Section 2.3.2 for details). The only difference to this procedure is the radial bins we consider when fitting NFWT profiles from the circular velocity. For consistency, at each point along the orbit, we use inner and outer bins with radii identical to the limits used to find the best-fit NFWT parameters in the simulations.

Figs. 4.11 and 4.12 depict changes in the remnant system scale radius and concentration, respectively, for the fiducial simulations. As with predictions for the satellite's properties, we compute these parameters for the first three orbits of the merger. In the plots, models including the central halo response are shown as solid green lines, while models excluding it are illustrated by dashed blue lines. Note that the results of both models were smoothed using the function `savgol_filter` (Savitzky & Golay, 1964) from the Python library SciPy (Virtanen et al., 2020). Since our random sampling of the halos changes at each timestep, the model predictions for the parameters contained some minor artificial noise. Increasing the number of particles used to represent the halos would cause this noise to disappear, at the cost of computational speed.

In Fig. 4.11, when including the central halo response, we generally find the remnant scale radius is well modeled for type 1 responses over the first two orbits until the satellite reaches apocentre for a second time. For type 2 responses, this agreement is typically limited to just the initial infall to pericentre. At pericentre, the model predicts a sharp drop in scale radius which is not exhibited in the simulations. This is caused by the model solely reducing the satellite's truncation radius as it loses mass as opposed to reducing

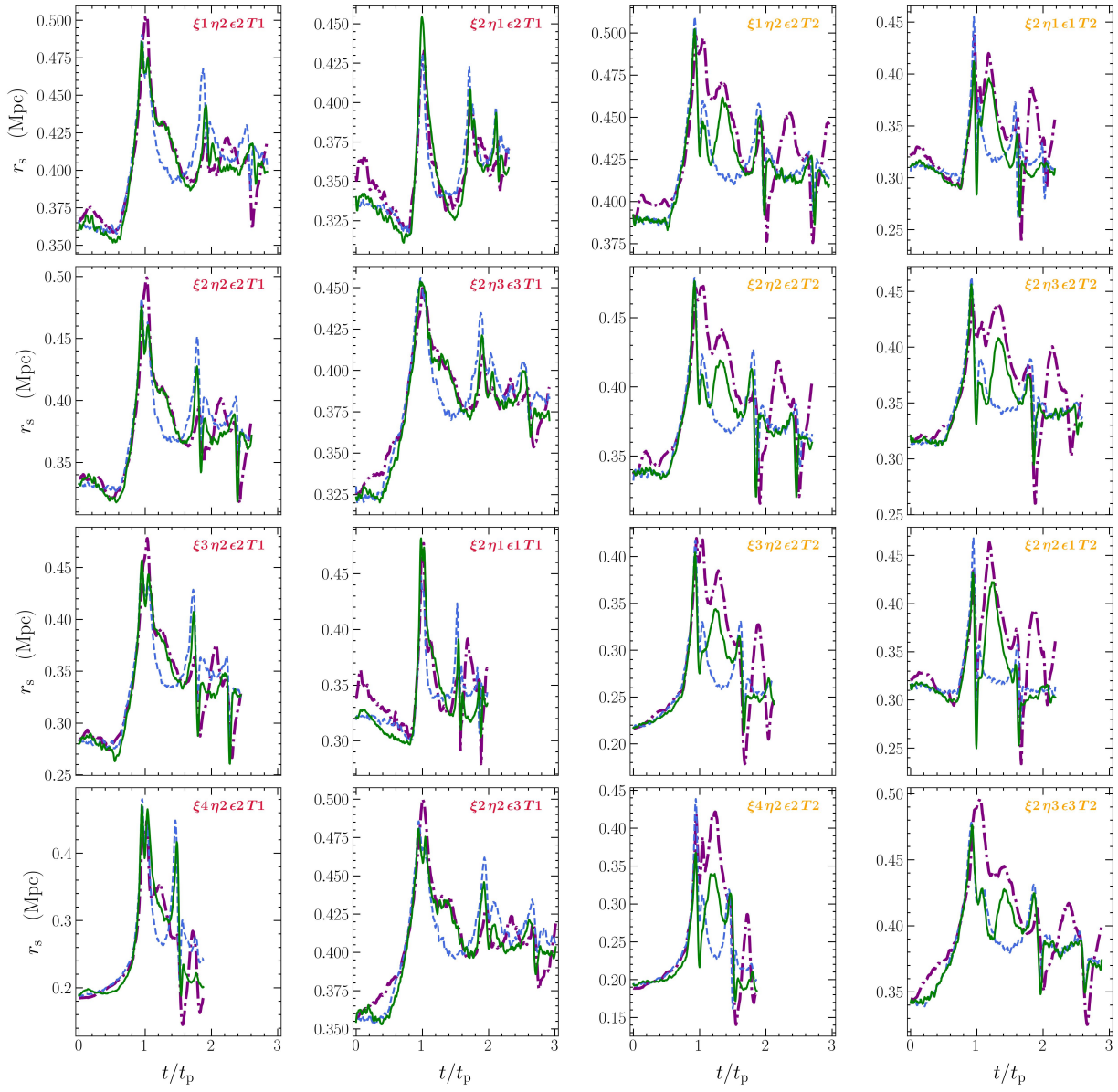



Figure 4.11: Measured remnant system scale radius in the simulations (purple, dashdot) compared to models including (green, solid) or excluding (blue, dashed) the response of the central halo during the merger. In each subplot, the timescale is shown relative to the time to pericentre, while the label gives the simulation name and response type.

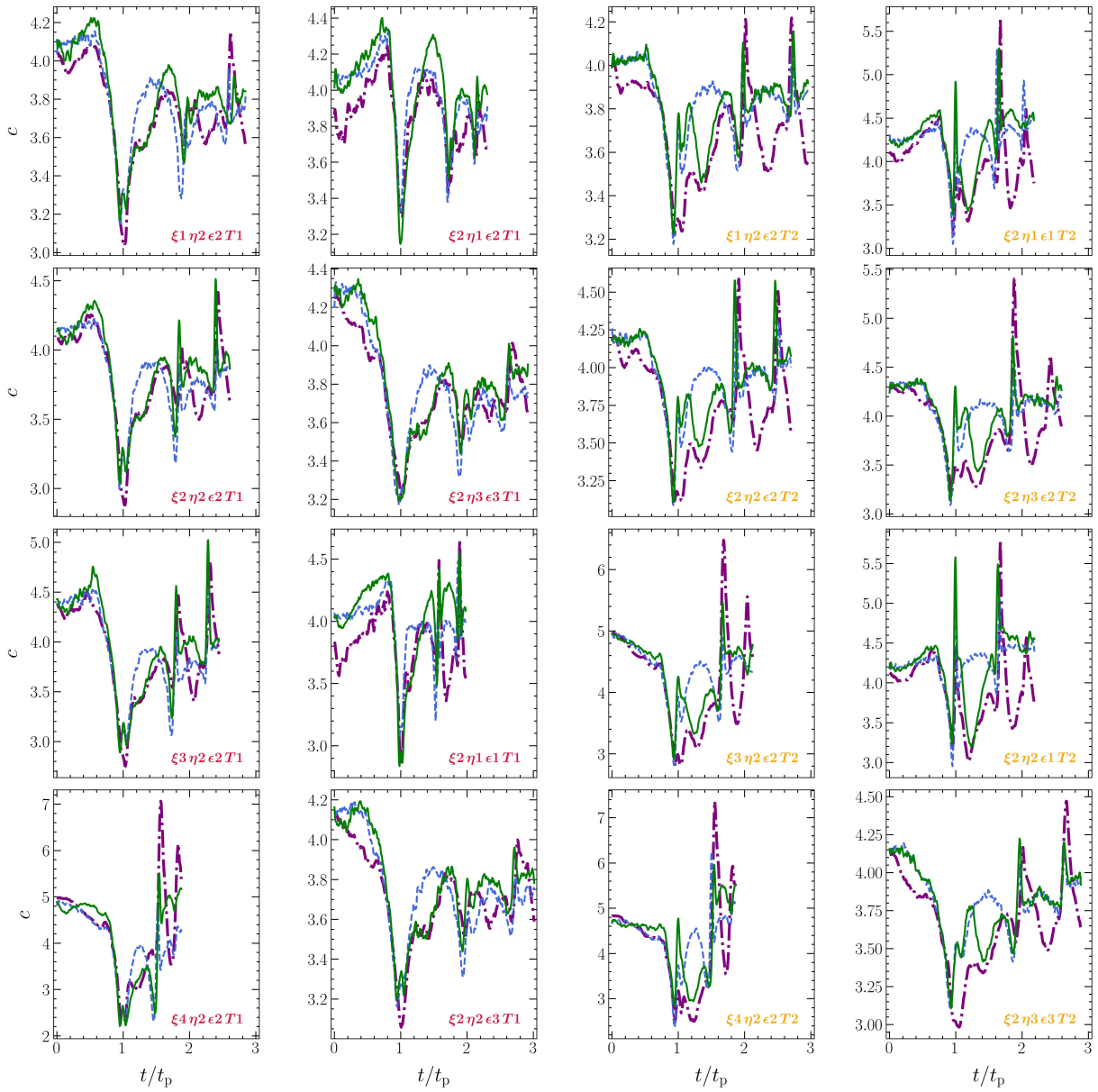



Figure 4.12: Measured remnant system concentration in the simulations (purple, dashdot) compared to models including (green, solid) or excluding (blue, dashed) the response of the central halo during the merger. In each subplot, the timescale is shown relative to the time to pericentre, while the label gives the simulation name and response type.

its characteristic density as well, resulting in a more compact satellite than found in the simulations. Thus, the direct position of the satellite has a larger effect on the measured scale radius as it moves in and out of the potential. Energy-based truncation models for the satellite (see e.g. Drakos et al., 2017, 2020) may be able to correct this. After pericentre, the scale radius is usually slightly underestimated until the end of the second orbit due to unbound material being deposited too close to the centre of the system.

For both response types, sharply truncating the satellite's profile as it loses mass results in its position having a more dramatic effect on the modeled scale radius at late times as opposed to direct changes in the central halo's profile. This is evident by the shorter duration of the oscillations in scale radius compared to what is found in the simulations. The primary consequence of neglecting the response of the central halo is that the remnant scale radius does not increase when moving back out to apocentre during the first orbit, as expected. On the timescale shown, this occurs at times $t = 1.2 - 1.6\ t_p$ for most simulations. Beyond this, there are no other major differences. In Fig. 4.12, concentration evolves with behaviour similar but opposite to the scale radius, implying the virial radius changes minimally in our model.

For several mergers (e.g. $\xi 2\,\eta 1\,\epsilon 2\,T1$, $\xi 2\,\eta 1\,\epsilon 1\,T1$, and $\xi 1\,\eta 2\,\epsilon 2\,T2$), the initial value of the remnant scale radius in the model does not align with that in the simulations. This results from using rejection sampling to create halos in our model. The drawback to rejection sampling, as opposed to generating profiles with ICICLE, is that the profiles it creates are slightly different than those in the simulations (see Fig. B.4). The halos generated by ICICLE are more compact (i.e. more mass at smaller radii) than those in our model. This occurs since the truncation procedure ICICLE uses diverges from the NFWT profile at large radii. This causes the initial scale radius to be larger in simulations where the initial separation between the satellite and central halo is small such that the presence of the satellite has an impact on the initial remnant properties. The effect disappears after the satellite has lost a large fraction of its mass during infall and the central halo profile dominates. This follows given the individual halos from ICICLE and rejection sampling agree in the interior of the profile where the scale radius is measured. For concentration, since the initial virial radii in the model and simulation are the same, we find a result consistent with the scale radius.

Finally, in building our model, we are interested in replicating the median evolution of structural parameters during mergers. Fig. 4.13 showcases changes in the median remnant system scale radius and concentration in the simulations compared to our models. Here, the parameters are scaled by their initial values as was done in Wang et al. (2020). The coloured regions illustrate the $1\sigma$ scatter in the median for the full model that includes the central halo response (i.e. the solid green lines).

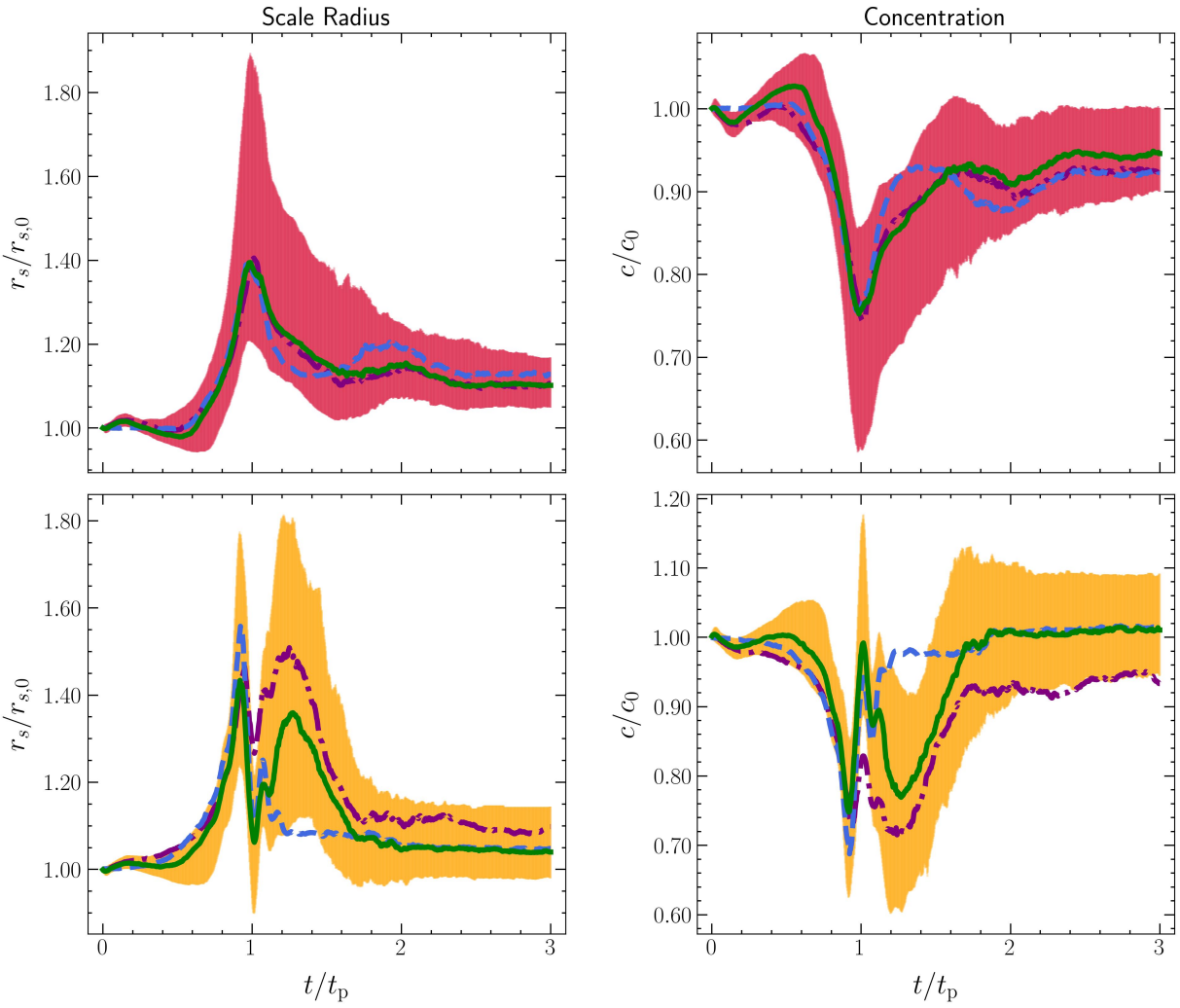



Figure 4.13: Median remnant system scale radius (left) and concentration (right) in the simulations (purple, dashdot) compared to models including (green, solid) or excluding (blue, dashed) the response of the central halo during the merger. The coloured regions depict the $1\sigma$ scatter in the median for the model including the central halo response, with type 1 in crimson (top) and type 2 in orange (bottom).

Considering our earlier results in Section 4.2, each model predicts slightly different orbital evolution and mass loss for the satellite given the different components included and model parameters used. In principle, this would alter the measured remnant properties because the satellite would behave in a inconsistent manner. To overcome this, we use the same satellite trajectory and mass loss (i.e. from the full model) in both models to predict the remnant properties when measuring the median response. Thus, the only difference between the model curves shown is whether or not the central halo response model is included.

From the plot, we find the remnant scale radius is well modeled at all times for type 1 responses. For type 2 responses, the simulation and model curves exhibit the same behaviour after $t = t_p$, although there is an offset between the two. As discussed previously, this is partially caused by the model using a more compact satellite, but it is also a result of the model placing unbound material too close to the centre of the system, reducing the scale radius. For concentration, its median evolution is similar to the scale radius except at late times, where we find a larger difference between the simulation and model measurements irrespective of the response type. This again implies that too much of the satellite's material is placed in the inner region of the system, increasing the virial radius and moving it outwards. Regardless, the simulation concentration still falls within the $1\sigma$ scatter of the model.

As with the individual mergers, the net effect of excluding the central halo response from our model is that the median remnant scale radius curve stagnates when the satellite moves back out to apocentre during the first orbit. This is seen in both response types, but is more pronounced for type 2. Overall, we conclude that incorporating the central halo response in our model is required in order to replicate how the remnant system's structure evolves after the satellite's initial infall to pericentre.

### 4.3.2 Other Parameters

While the focus of our model is to accurately predict the remnant system scale radius and concentration, because we generate particle realizations of the system, we can test how well the model performs for other parameters, specifically shape and asymmetry. To do this, we apply the same method for measuring these properties as in the simulations with no differences (see Sections 2.3.3 and 2.3.5 for details). In our analysis, we neglect the spin parameter since the individual particles produced in the model do not have velocities. Moreover, even if we were able to sample velocities for the particles using a technique similar to ICICLE, the remnant system spin would be poorly modeled by default since

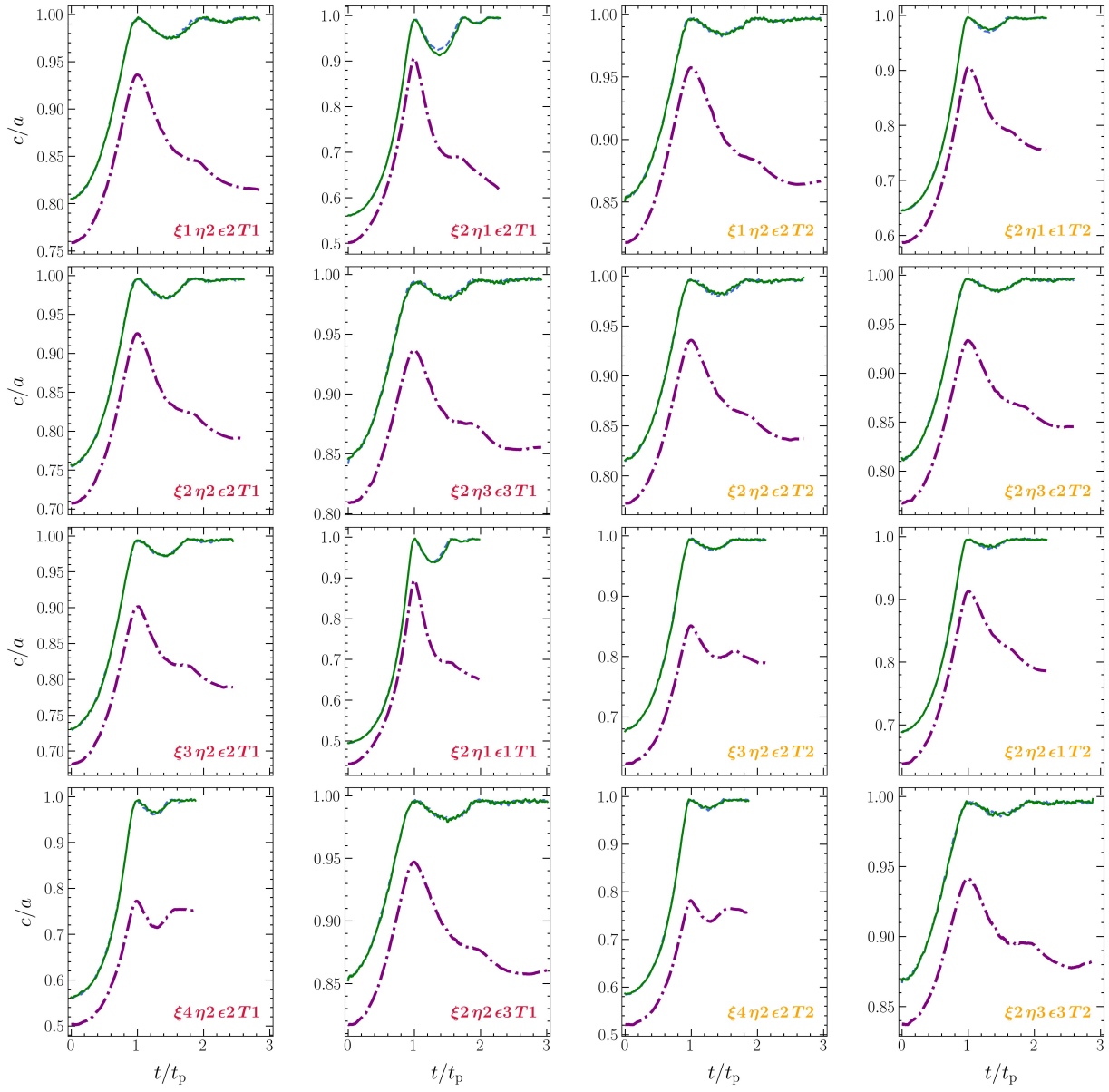



Figure 4.14: Measured remnant system minor-to-major axis ratio in the simulations (purple, dashdot) compared to models including (green, solid) or excluding (blue, dashed) the response of the central halo during the merger. In each subplot, the timescale is shown relative to the time to pericentre, while the label gives the simulation name and response type.

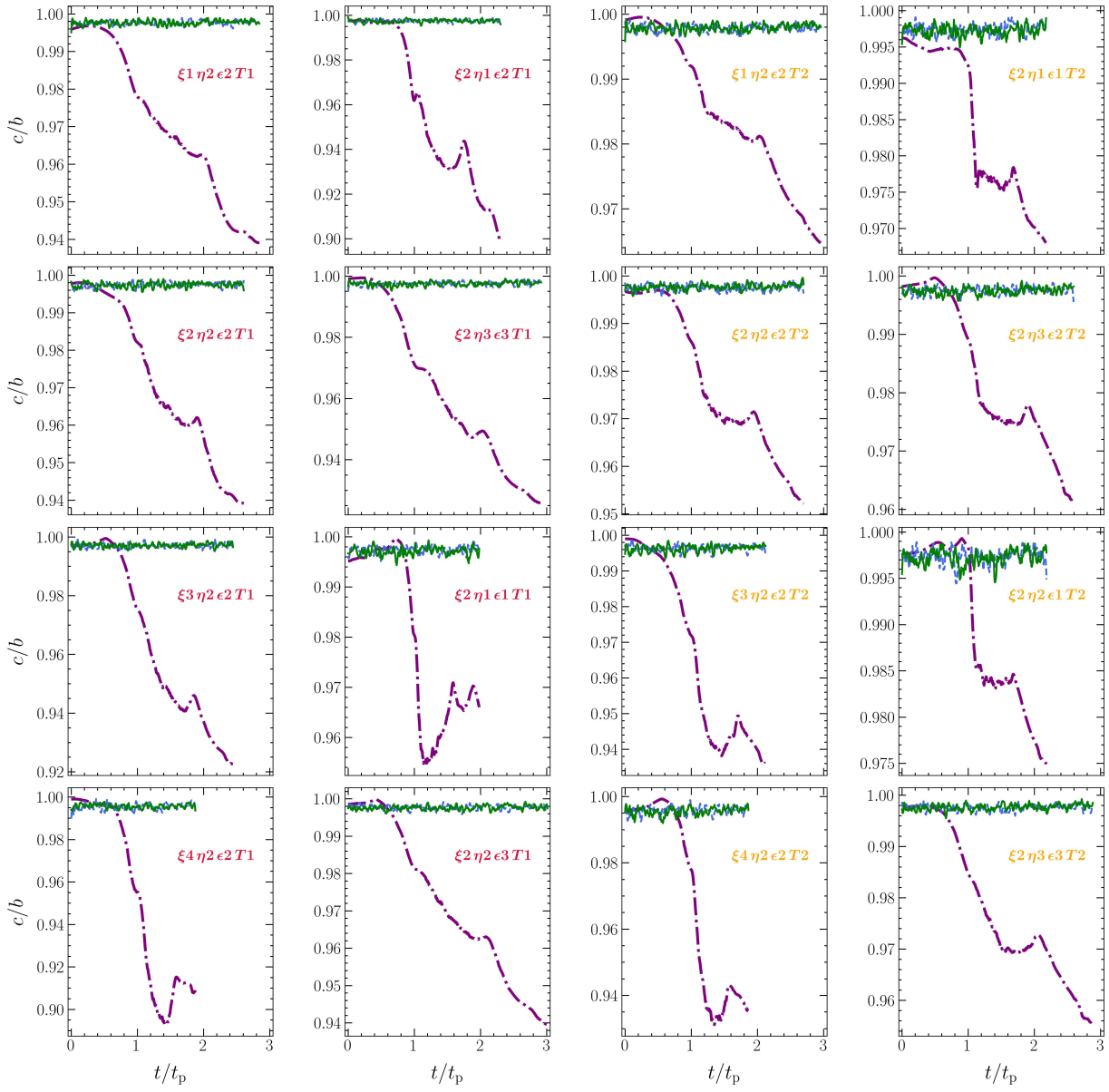



Figure 4.15: Measured remnant system minor-to-intermediate axis ratio in the simulations (purple, dashdot) compared to models including (green, solid) or excluding (blue, dashed) the response of the central halo during the merger. In each subplot, the timescale is shown relative to the time to pericentre, while the label gives the simulation name and response type.

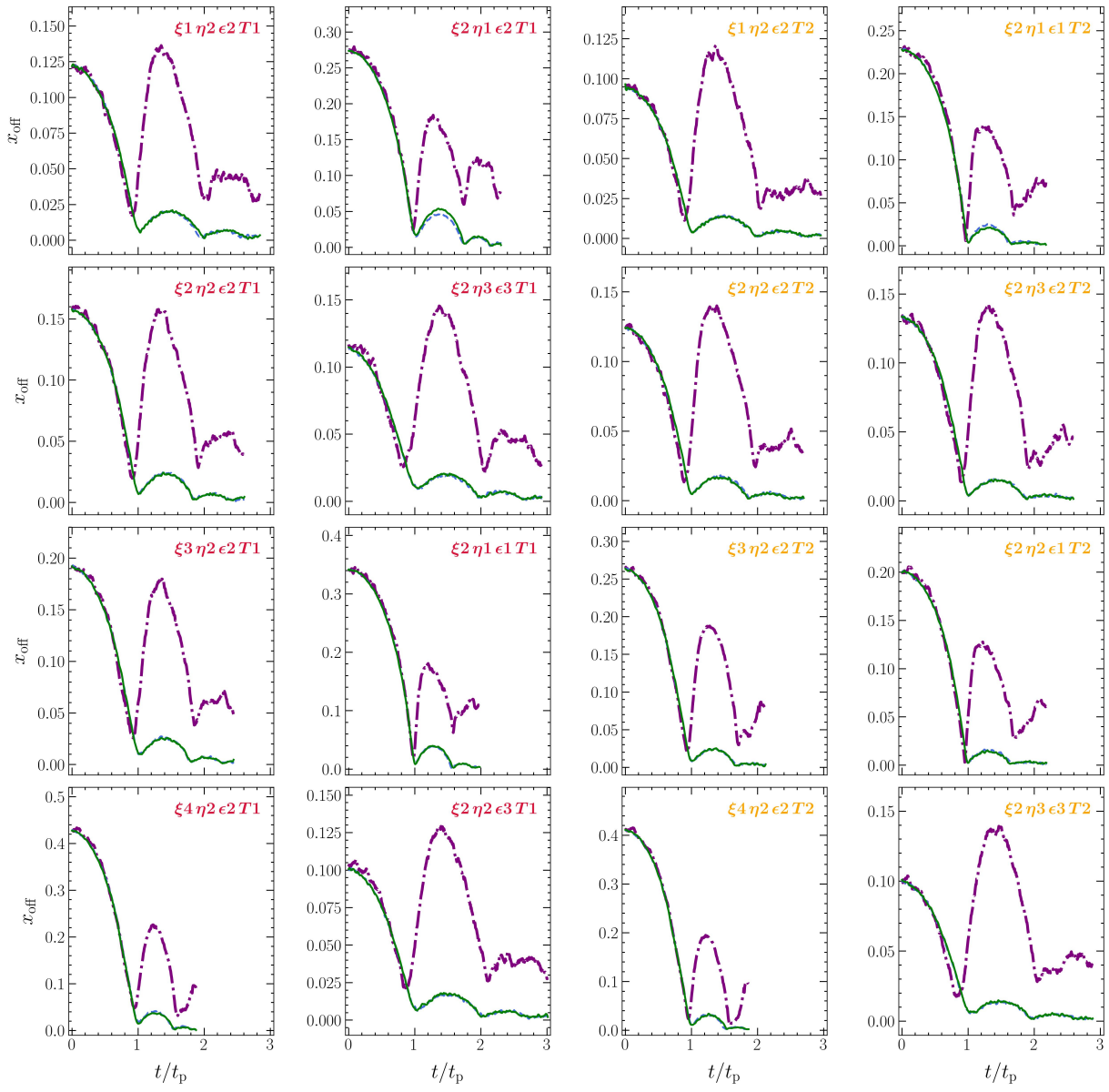



Figure 4.16: Measured remnant system asymmetry in the simulations (purple, dashdot) compared to models including (green, solid) or excluding (blue, dashed) the response of the central halo during the merger. In each subplot, the timescale is shown relative to the time to pericentre, while the label gives the simulation name and response type.

the particles themselves do not interact with each other. Our model continuously resamples new particles at each timestep so no angular momentum is ever transferred to the central halo, as expected (see Fig. 2.11). Thus, the spin of the system would simply drop as the satellite loses mass and its orbit decays.

Figs. 4.14-4.16 demonstrate how the remnant system shape and asymmetry parameters evolve for the fiducial simulations. In these plots, we find little difference in the model predictions when including or excluding the central halo response. There is only a very minor affect on asymmetry at apocentre for low $\eta$ mergers (e.g. $\xi 2\,\eta 1\,\epsilon 2\,T1$ and $\xi 2\,\eta 1\,\epsilon 1\,T2$). Compared to the simulations, the model poorly replicates the parameters at most times except for the minor-to-major axis ratio and asymmetry during the satellite's initial infall, although the shape parameter has a systematic offset. As with scale radius, this offset is caused by the material in the halos in our model being more spread out, leading to an increase in the minor-to-major axis ratio.

For the parameters shown, the model heavily disagrees with the simulation measurements primarily because every component of the remnant system is spherically symmetric. The satellite, central halo, and unbound mass all exhibit spherical symmetry. The shape parameters, in essence, quantify the sphericity of a system. Axis ratios equal to 1 indicate the system resembles a perfect sphere. Similarly, asymmetry is a measure of the difference between the centre of mass and the position of highest local density. Spherically symmetric systems will have asymmetries equal to 0. In our model, the central halo profile dominates changes in the remnant system once the satellite has lost a large fraction of its mass. This occurs during the first pericentric passage of the satellite. After this point, the satellite's motion will have little effect on perturbing the remnant system from a spherical profile, which is why we obtain near spherical measurements of the parameters. This also explains why including the central halo response in our model does not affect predictions since it is a spherical process as well. In contrast, the median remnant scale radius and concentration can be modeled accurately since these parameters are based on fits to radial profiles.

Clearly, we need to implement some type of asymmetry into the system in order to properly model these other parameters for the remnant system. Will using an asymmetric unbound mass distribution fix this? In the following, we propose a different, more complex model for the unbound material when measuring the remnant system structural properties. We assume that the unbound mass is uniformly placed into "pseudo-ellipsoids" aligned with the instantaneous separation vector between the satellite and central halo, and located between apocentre and pericentre of a static orbit. By "pseudo-ellipsoid" we mean that our particle realization of the unbound mass follows the equation of an ellipse,

$$\frac{x^2}{a^2} + \frac{y^2}{b^2} = 1 \tag{4.6}$$

in the plane of the orbit (which coincides with the $xy$-plane for our simulations), while the off-plane coordinate is randomly sampled from an NFWT profile (i.e. the $z$-coordinate in Eq. B.40) assuming its model parameters ($r_s$, $\rho_0$, $y$, $r_t$) are that of the satellite's initial profile. In the above expression, $a$ and $b$ are the semi-major and semi-minor axes of an ellipse, respectively, centred at the origin. Furthermore, the width and height of the ellipse are given by $2a$ and $2b$, respectively.

We select this particular form for the unbound material because an ellipsoid is the simplest triaxial shape obtained by deforming a sphere. The major axis of the ellipse rotates with the orbit of the satellite since there is a preferential direction to how the unbound mass is removed; it is stripped parallel to the satellite's trajectory. The material itself should be distributed in the plane of the orbit, while its off-plane vertical structure should on average be maintained and equivalent to the satellite's initial off-plane distribution.

In our model, the ellipse parameters are related to the apocentre and pericentre positions of the orbit assuming the initial central halo profile is static (see Appendix B.1),

$$a = \frac{r_p + r_a}{2} \qquad\qquad b = \sqrt{r_p\, r_a} \tag{4.7}$$

Here, we use the Keplerian definition for the eccentricity (see e.g. Binney & Tremaine, 2008, Section 3.1) to derive the semi-minor axis. This value is only approximate as it assumes the orbit is closed, while for an NFWT profile bound orbits are open. Nevertheless, we find it is acceptable for calculating the height of the ellipse. The ellipse parameters are kept constant throughout the merger.

At each timestep, we uniformly sample particles in the ellipse using the algorithm described in Section 3.29 of Fishman (1996) for generating points in a hyperellipse. The algorithm functions by uniformly sampling points in an hypersphere and applying a linear transformation to map the points onto a hyperellipse with dimension $d = 2$. Since the uniform distribution is invariant under a linear transformation, the points in the hyperellipse are also uniformly distributed. The ellipse the particles are sampled from will have its major axis aligned with the $x$-axis and its centre at the origin. Next, we shift the particles by an amount $\Delta x = a - r_p$, such that the left edge of the ellipse is aligned with the pericentre position. Finally, we rotate the particles to account for the satellite's position,

$$\mathbf{X_{ub}} = \mathbf{R}(\theta)\, \mathbf{X_{ub}} \tag{4.8}$$

$$\mathbf{X_{ub}} = \begin{bmatrix} \cos(\theta) & -\sin(\theta) \\ \sin(\theta) & \cos(\theta) \end{bmatrix} \left[\begin{array}{c|c|c|c} & & & \\ \vec{x}^{\,T}_{\mathrm{ub},1} & \vec{x}^{\,T}_{\mathrm{ub},2} & \cdots & \vec{x}^{\,T}_{\mathrm{ub},n} \\ & & & \end{array}\right] \tag{4.9}$$

where $\vec{x}_{\mathrm{ub},i} = (x_{\mathrm{ub},i}, y_{\mathrm{ub},i})$ is the 2D position of the $i^{\mathrm{th}}$ randomly generated particle in the ellipse, $\theta = \tan^{-1}(y/x)$ is the angle of the instantaneous separation vector between the satellite and central halo measured counterclockwise from the $x$-axis, and $n$ is the number of particles created during the current timestep. Note that as with the spherical unbound mass model, we only consider the unbound material produced at the current time. Particles that became unbound at an earlier time have their positions stored for later use. Once the material is placed it does not move from its position.

Fig. 4.17 exhibits the effect of the ellipsoidal unbound mass model on measurements for the remnant system shape and asymmetry parameters. For low mass ratio mergers, we find the minor-to-intermediate axis ratio has moderate agreement with the simulation result up to the second pericentre where $t \approx 2\,t_p$. The asymmetry matches at late times as well. Outside of these improvements, the model still heavily disagrees with the simulations for these other parameters. In Fig. 4.18, we examine how the remnant system scale radius is affected by the new unbound mass model. For type 1 responses, there is no difference in the predictions. However, for type 2 responses, the ellipsoidal model better matches the simulation result after the first pericentre compared to the spherical model. This is caused by the unbound material being distributed more uniformly and further from the centre of the system, increasing the scale radius. We tested and found this to be consistent across all the fiducial simulations. Thus, this model might be preferred for predicting the median evolution of the remnant concentration and scale radius.

On the other hand, there is no simple way to implement this type of unbound mass distribution into the orbital evolution model. While the unbound material can be placed concurrently with the evolution of the satellite in the model, estimating the force induced by this mass is another matter entirely. There is no simple analytic form for our pseudo-ellipsoids and even if this did exist, the orientation of the ellipse changes at each timestep, further complicating the force calculation. Our tests have shown that the alignment of the ellipse must change with the satellite's position in order to obtain any improvement in the remnant scale radius predictions for type 2 responses. Moreover, for high mass ratio mergers, the satellite cannot be modeled properly beyond the first orbit if the contribution to the total force by the unbound material is neglected (see Fig. 3.7 and its discussion).

Overall, neither unbound mass model can accurately describe the distribution of the unbound material in the simulations. However, this may not be the dominant process affecting predictions for the other remnant parameters. Currently, for the first few orbits, the full model captures the radial evolution of the central halo as well as the orbit and mass loss of the satellite given their agreement with the simulation measurements. The only other components that could differ are the non-spheroidal shape of the central halo as it is perturbed by the satellite, and the unbound mass distribution. To what extent

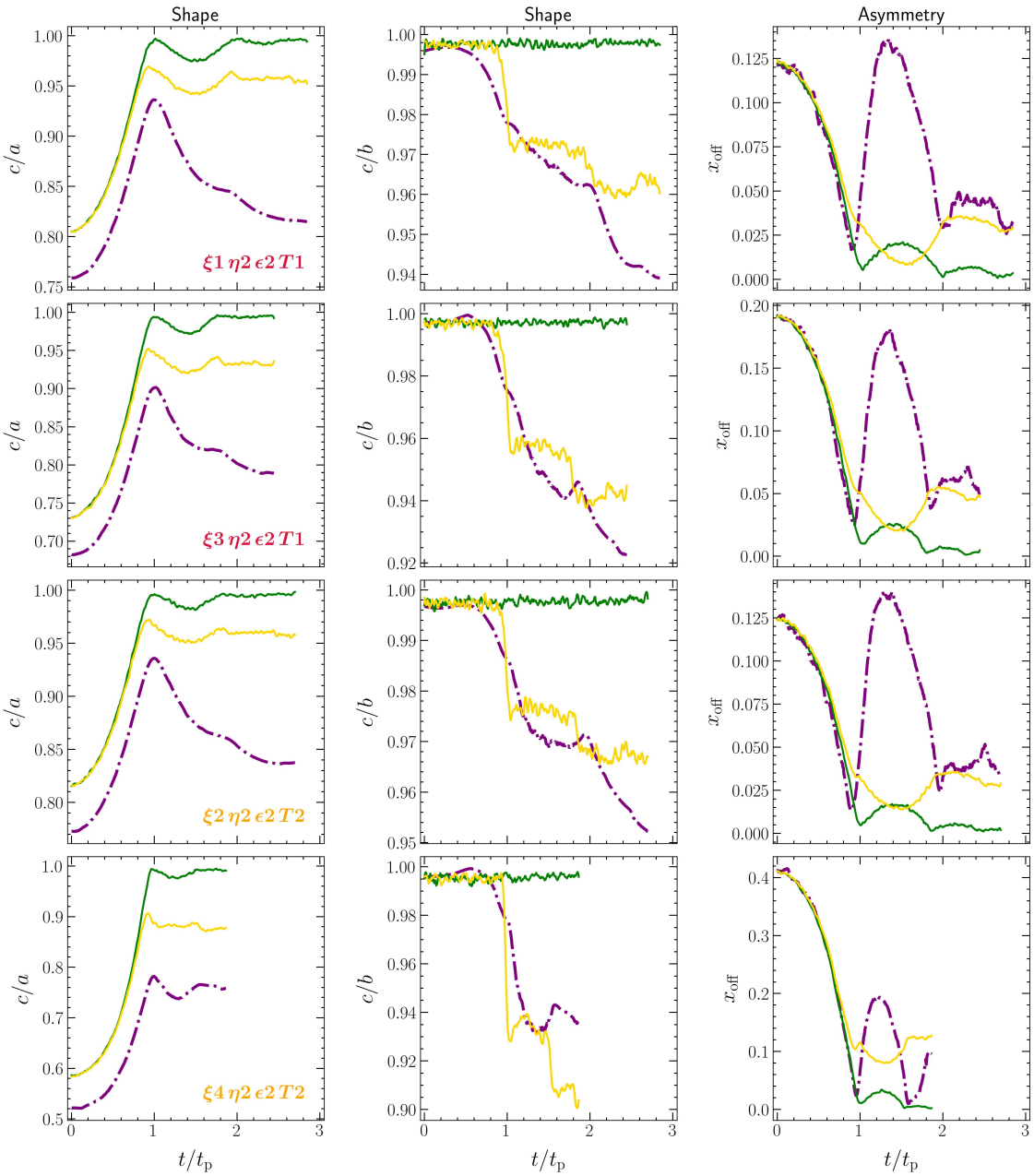



Figure 4.17: Measured remnant system shape parameters (left, middle) and asymmetry (right) in the simulations (purple, dashdot) compared to models incorporating spherical (green, solid) or ellipsoidal (gold, solid) unbound mass distributions. Each row depicts a different simulation, with their name and response type labeled accordingly.

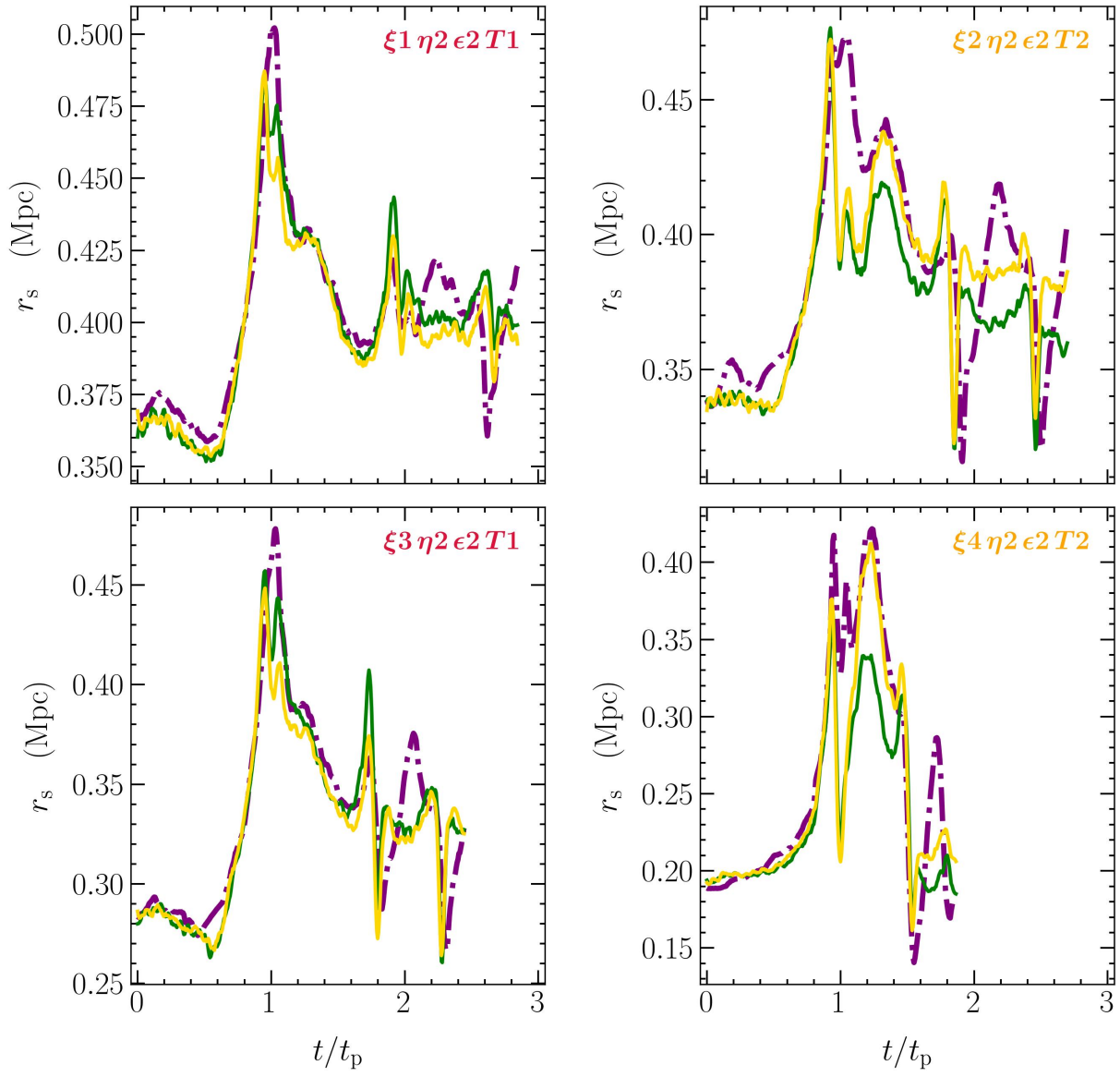



Figure 4.18: Measured remnant system scale radius in the simulations (purple, dashdot) compared to models incorporating spherical (green, solid) or ellipsoidal (gold, solid) unbound mass distributions. The simulations and their response types are labeled in the top-right corners.

do these components affect the remnant shape and asymmetry parameters? Fig. 4.19 attempts to quantify the importance of each component on replicating the other remnant parameters. Here, we examine high and low mass ratio mergers of both response types. Each curve in the plot considers a different model or simulation result.

- *Solid green line*: the default model that includes the central halo response and places the unbound mass in spherical shells.
- *Solid gold line*: the alternative model that includes the central halo response and places the unbound mass in pseudo-ellipsoids.
- *Dash-dotted purple line*: the default simulation result that includes all particles (bound satellite, central halo, and unbound material) when measuring the remnant system properties.
- *Dotted blue line*: an alternative simulation result that includes the bound satellite and central halo particles, but neglects the unbound material when measuring the remnant system properties. In this scenario, the unbound particles disappear during the merger.
- *Dotted red line*: an alternative simulation result that includes all particles (bound satellite, central halo, and unbound material), but the central halo is always represented by its initial profile when measuring the remnant system properties. In this scenario, the central halo particles are static during the merger. Note that this implies the radial evolution of the central halo (i.e. its change in scale radius) is also excluded from the results. Nonetheless, incorporating this would have little impact on the remnant properties (see the modeling in Figs. 4.14-4.16).

For the alternative simulation results, the difference between the dotted curves and the default simulation result demonstrates the importance of the excluded component when modeling a given remnant system property. That is to say, variations between the blue and purple curves highlight the effect of having an accurate unbound mass model, while differences between the red and purple curves showcase this but for an asymmetric central halo. In the plot, we find the remnant system minor-to-major axis ratio is most affected by the unbound material after pericentre for low mass ratio mergers. For high mass ratio mergers, accurately modeling both the unbound mass and the central halo asymmetry are of equal importance during this time. Next, the remnant system minor-to-intermediate axis ratio primarily differs with the central halo asphericity except for at late times. Finally, the asymmetry parameter requires a proper description of the central halo's profile to obtain

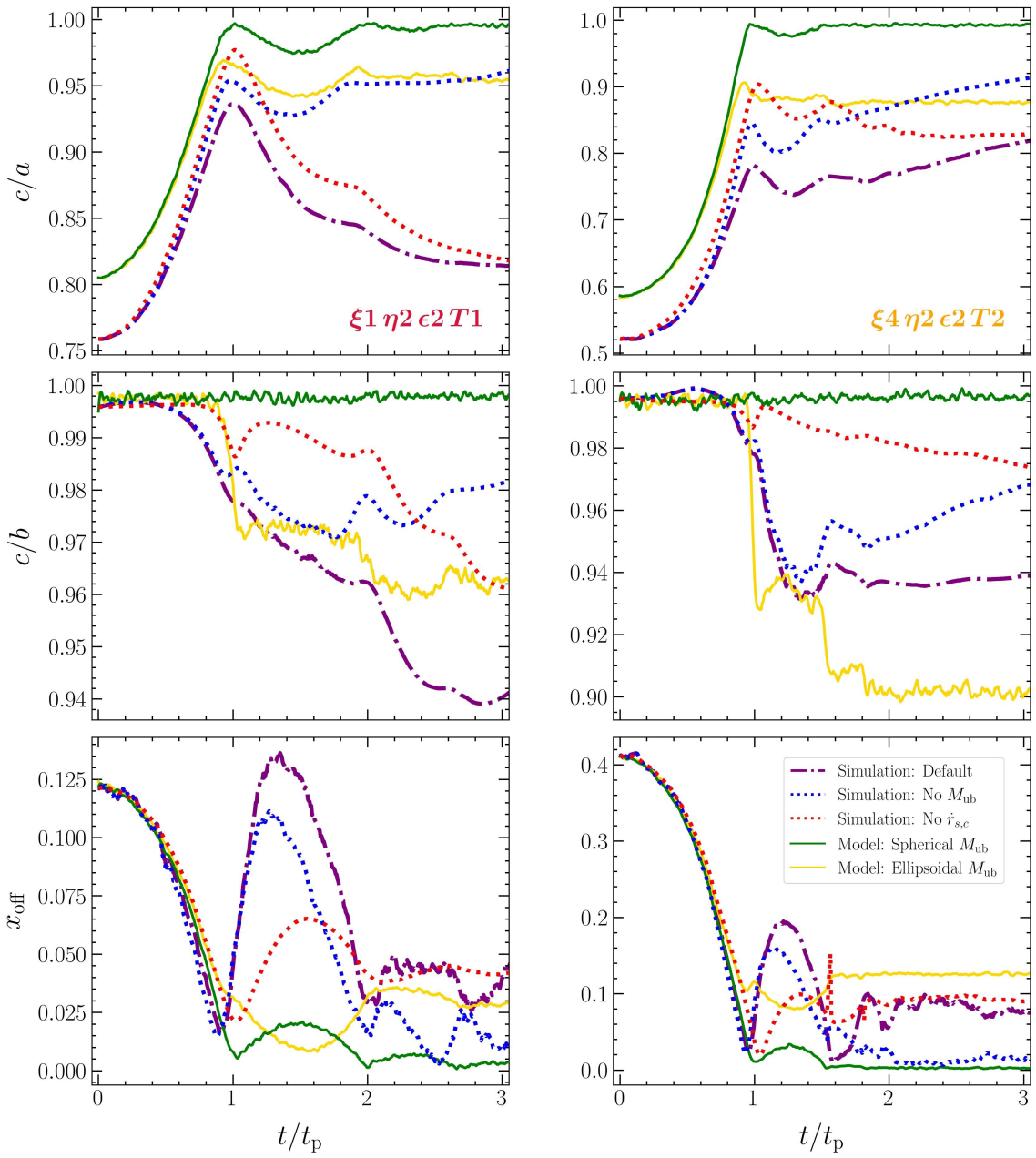



Figure 4.19: Remnant system shape parameters (top, middle) and asymmetry (bottom) during the merger. Each curve either considers a simulation neglecting a certain component from it or a model with a different unbound mass distribution. See the text for a detailed discussion.

good predictions after the initial infall of the satellite until the end of the second orbit. After this point, the unbound mass distribution predominately sets the asymmetry.

Ultimately, we conclude that models for any parameter related to the 3D shape of the remnant system ($c/a$, $c/b$, $x_{\rm off}$) during a merger must incorporate accurate descriptions of both the unbound mass and the central halo's triaxiality. While quantifying the distribution of the unbound material is difficult since most subhalo models neglect it, formulations of aspheric NFW profiles have been proposed (see e.g. Jing & Suto, 2002; Buote & Humphrey, 2012). Typically these are ellipsoidal models derived through a simple modification to the spherical NFW profile. As such, an analytic form to the potential associated with the profile exists, allowing it to be easily implemented into an orbital evolution model. On the other hand, modifying the profile in this way adds additional model parameters that need to be predicted.

# Chapter 5

# Conclusion

## 5.1 Summary of the Thesis

In this thesis, we presented a model for how structure evolves in remnant systems due to binary mergers. This model incorporated changes to the central halo's potential as it responds to the motion of the satellite. Our goal was to study the impact of a dynamic central halo on satellite orbits and determine the effect of mergers on remnant structural parameters in hopes of predicting the properties of unrelaxed halos as a function of merger phase. Clusters and their structural properties can be used as tools to constrain $\Omega_m$ and $\sigma_8$, potentially helping to solve the $S_8$ tension. However, measurements of their parameters vary greatly during active mergers provided the mass ratio between the two merging components is sufficiently large. Since mergers happen frequently, it is therefore important to accurately model this variation in order to get meaningful values for cluster halo properties to improve cosmological constraints.

In Chapter 2, we described the initial conditions used in the simulations. These were cosmologically motivated with the mass ratio sampled from the Fakhouri & Ma (2008) merger rate and the orbital properties sampled from the Jiang et al. (2015) distributions. Then, we measured properties of the satellite, central halo, and remnant system in the simulations. These included the NFWT parameters of each halo as well as their shape, spin, and asymmetry. In all simulations, we found that the central halo's profile experienced oscillations, and these could be grouped into two types based on the initial response: (1) $r_s$ gradually declined to a minimum value sometime before first pericentre and (2) $r_s$ sharply dropped to a minimum value just after first pericentre. After the merger, the central halo became slightly prolate (but still largely spherical) and it gained spin from interactions with

the satellite. For the remnant, its scale radius exhibited similar oscillations. Moreover, we found that in general, its shape became moderately prolate and it had lost spin post merger.

Next in Chapter 3, we introduced an orbital evolution model used to trace the satellite's position and quantify its mass loss. The model we built consisted of three components: dynamical friction, mass loss, and a reduced mass correction. Typically, we found the orbit was well aligned and the radial separation agreed with the simulation result up to the second pericentre. In contrast, our mass loss predictions for high mass ratio mergers (i.e. 5:1 and below) moderately deviated from the simulation curves after this point. Additionally, in this chapter we trained an XGBoost model to determine the orbital model parameters ($\gamma$, $\ln(\Lambda)$, $B$) solely from the initial conditions. Our results demonstrated that the model works extremely well given the median difference between the model output and the values of the orbital parameters calibrated directly to the simulations was less than 2% in the combined set.

Finally in Chapter 4, we proposed a semi-analytic model to capture the response of the central halo during the merger. To do this, we used an SVM to derive an expression to separate the responses into their two types from the initial conditions. We found the SVM derived plane could predict the type of response with 98% accuracy. Then, we modeled the central halo scale radius using two parameters, $A$ and $t_{r_{s,c},\max}$, by scaling the empirically measured median response. Given the response model, we explored the extent to which incorporating this process affected the satellite trajectory and remnant system properties. Overall, our findings suggest that adding the central halo response has little impact on the orbital evolution of the satellite and its mass loss. In contrast, the central halo response must be included in our model in order to accurately predict how the remnant's structure evolves after the satellite's initial infall to pericentre. In particular, the model works well at replicating the remnant scale radius and concentration, especially in the median case, although an ellipsoidal unbound mass model may work better for type 2 responses. On the other hand, the model performs poorly for parameters related to the 3D shape of the remnant since we neglected the asphericity of the central halo.

## 5.2 Discussion

Models for the structural properties of remnants during major mergers have not been previously considered in the literature, thus we cannot compare how our model performs to other works. Instead, we will focus on the parameters we measure directly from the simulations as these have been studied in both isolated and cosmological settings before. Drakos et al. (2019a,b) analyzed the long-term effects of binary, equal-mass mergers on the structure

of remnants in isolated simulations. They found that the final shape of the remnant was determined by the orbital parameters of the merger. The orbital energy correlated with $c/a$ and the angular momentum controlled $c/b$. In general, lower energy mergers produced more elongated remnants, while high spin mergers created oblate, disky remnants that became increasingly more prolate (cigar-shaped) as the angular momentum of the system decreased. The shape of the remnant aligned with the direction of the merger as well. In terms of the remnant's profile, they found that the scale radius typically increased after mergers, whereas concentration had more complex behaviour. Energetic mergers increased the final concentration, while low energy mergers decreased it. Furthermore, low energy mergers resulted in mass moving inwards creating more compact halos.

In Fig. 5.1, we showcase the final or net change in the properties of remnants in our isolated simulations as functions of the initial condition that had the most correlation. Concentration, scale radius, and spin are all scaled to their initial values because these parameters are directly related to the sampled initial conditions. For example, the initial concentration follows a power-law as it is calculated from the sampled mass ratio of the merger. Thus, we want to remove this dependence when examining the final remnant concentration. The parameters in the top row are plotted against relative energy to directly compare our results to Drakos et al. (2019b). In the middle and bottom rows, we did not vary the colour of each point since these parameters exhibited no defining trends with the other initial conditions.

From the plot, we find the same result as Drakos et al. (2019a) for the shape parameters, where $c/a$ and $c/b$ are best related to the relative energy and circularity, respectively. However, since we consider lower mass ratios, $c/b$ is typically higher and more spherical than what they find. In our simulations, the net change in remnant spin has a tight relationship with mass ratio and exhibits little scatter due to the other initial conditions. Similarly, asymmetry primarily varies with relative energy, and energetic mergers create remnants with less offset. On the other hand, concentration follows a different pattern compared to that in Drakos et al. (2019b). Our mergers generally made less concentrated remnants regardless of orbital energy, although some orbits with high energy and large mass ratio did increase the remnant's concentration. For scale radius, our results have more agreement as we find that halos are usually more extended after mergers. While this may be the case, the overall change in concentration and scale radius is usually smaller (i.e. $< 30\%$ effect) suggesting it is quite difficult to change the structure of the remnant system through major mergers. This is true even in the case of 1:1 mergers studied in Drakos et al. (2019b).

Major mergers also cause short-term, transitory effects on the remnant system. Wang et al. (2020, 2023) investigated these effects in cosmological simulations for halos with

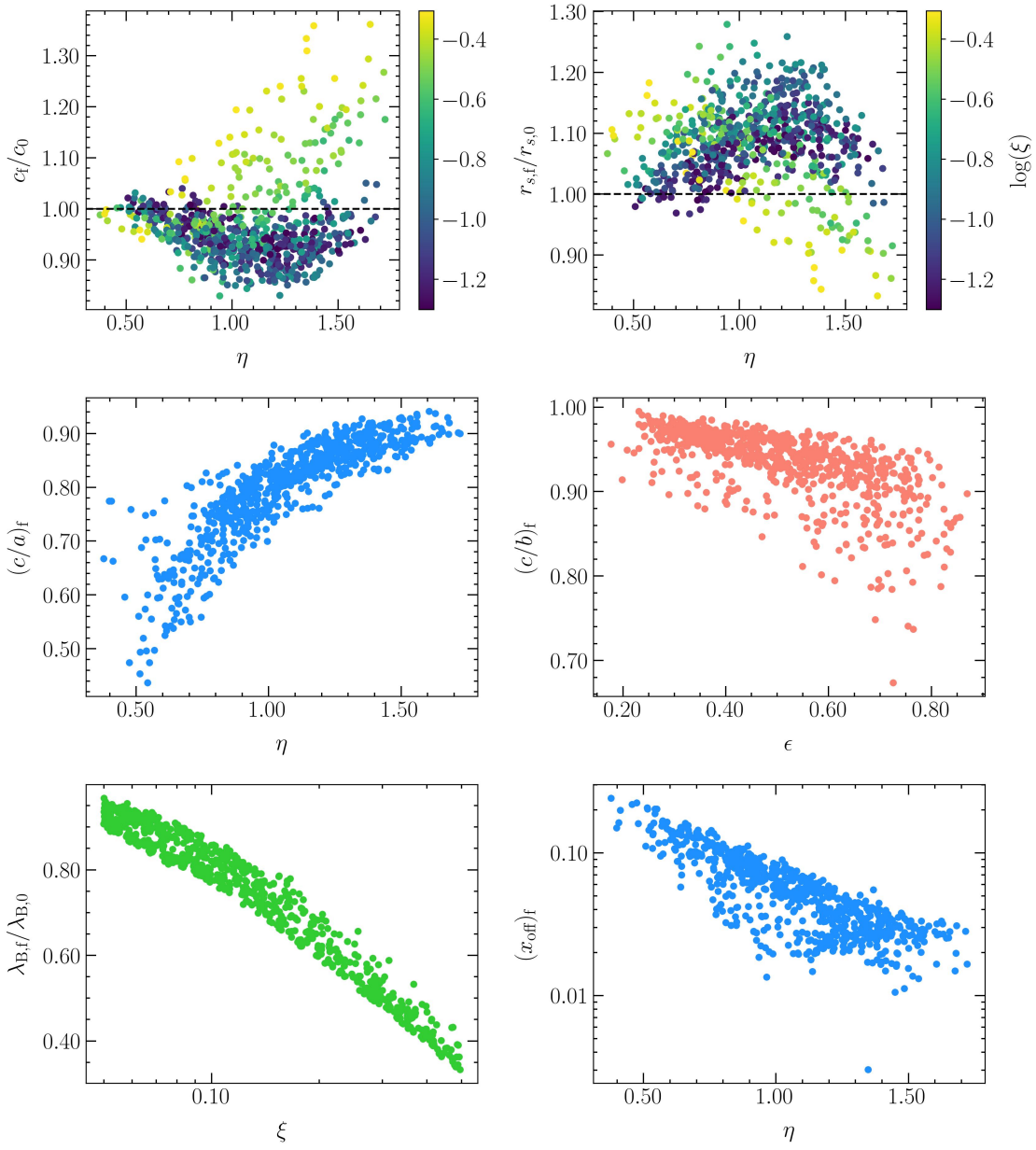



Figure 5.1: Final value or net change in the remnant system concentration (top-left), scale radius (top-right), shape parameters (middle), spin (bottom-left), and asymmetry (bottom-right), after the merger as measured in the simulations. Each point represents a different simulation and their colours (in the bottom two rows) correspond to the initial condition shown on the $x$-axis with $\xi$, $\eta$, and $\epsilon$ in green, blue, and red, respectively.

host masses between $10^{12} - 10^{14} h^{-1} M_{\odot}$. They found major mergers produce oscillations in many remnant structural properties including concentration, shape, spin, and asymmetry regardless of the host halo mass. These oscillations last for $1 - 2$ orbits and the oscillation amplitude increases with higher mass ratios. In the median case, the host halo's minor-to-major axis ratio, spin, and asymmetry marginally decrease after the merger, while its concentration slightly increases. In contrast, all of these parameters fluctuate significantly during the merger. For instance, concentration can vary by up to double its initial value as the satellite travels to first pericentre. Similarly, asymmetry can drop by $\sim 33\%$ over the same period of time.

In our isolated simulations, we find the same general trends in the evolution of the remnant properties during a merger. This can be seen by comparing Figs. 2.8-2.12 in this thesis to Fig. 4 in Wang et al. (2020) and Fig. 5 in Wang et al. (2023). Note that these plots consider the median case. Since the behaviour we find is quite similar, we will instead focus on differences between our results. First, the minor-to-major axis ratios we find in our simulations are initially higher than that typically found in Wang et al. (2023). This stems from the host halos in cosmological simulations having already undergone many minor mergers, distorting their shapes from perfectly spherical before the major merger.

Next, concentration can have opposite evolution to what is expected in cosmological simulations depending on the central halo response type (see Fig. 4.13 for the median response). From the orbital motion of the satellite, we would expect concentration to maximize at first pericentre. We find this does occur for type 2 responses. Given the orbits are more radial, the satellite can penetrate further into the core of the host halo. However, the amplitude of the oscillation in our simulations is reduced compared to Wang et al. (2020) since the truncation scale absorbs some of the profile change. Conversely, concentration does not increase at all at first pericentre for type 1 responses since the orbits are more circular, so only the outer profile of the remnant is affected. Fortunately, this issue where the truncation scale masks changes to the remnant concentration should not occur in cosmological simulations given the standard NFW profile can be used to model halos.

### 5.2.1 Potential Applications

In this section, we describe possible use cases for the model presented in this thesis that are relevant to our goals. Note that these applications do not represent an exhaustive list.

1. *Producing Statistics of Halo Properties*: In its current state, the model generally works well at replicating satellite mass loss, as well as the remnant system scale radius

and concentration, for the first couple of orbits during a major merger. Therefore, the model could be used as a computationally inexpensive way to generate predictions for halo properties at any phase of the merger solely from the initial conditions. Subhalo orbits have been studied extensively (see Section 2.2.3 for a list), and these works would form a basis for the initial conditions. We could then study how the distributions of these properties vary as a function of merger phase. One practical issue would be linking our predictions to real observables given projection effects. A solution to this is through mock observations. These are simulations meant to mimic observations of a particular survey (see e.g. Smith et al., 2017; Euclid Collaboration et al., 2024), which would in principle allow us to accurately map between simulation based properties and observables.

2. *Correlating Halo Properties*: As we previously discussed, the model typically works well at replicating the remnant system concentration for both individual systems and in the median case. Given halo properties are not independent, we can use predictions for concentration to gain insights into other structural parameters. This is demonstrated in Fig. 5.2, where we plot the anisotropic properties of halos for a set of simulations. The colourbar shows the concentration of the remnant relative to its initial concentration at the time these other properties are measured. We find there are some distinct correlations between concentration and the other structural parameters. These occur when the satellite first passes pericentre and the change in concentration maximizes. At this time, the minor-to-major axis ratio peaks, while the spin and asymmetry parameters minimize. Unfortunately, this is the only phase of the orbit where these relationships exist and are distinct enough to be noticeable.

3. *Controlling for Dynamical State*: At several points during the satellite's first orbit, the remnant concentration can describe the dynamical state of the system. In Fig. 5.3, we compare the maximum change in the remnant's concentration during the merger, $\Delta c = c_{\rm max} - c_0$, to its overall change. This maximum deviation usually occurred at first pericentre in our simulations, although concentration reaches an extreme value at turnaround (i.e. the first apocentre) as well. We find mergers lead to a characteristic enhancement in concentration that varies with mass ratio,

$$\frac{|\Delta c|}{c_0} = \alpha \log(\xi) + \delta \tag{5.1}$$

where $\alpha = 0.538$ and $\delta = 0.821$ are the best-fit parameters. This enhancement is much larger than the overall change in concentration after the merger. These results highlight that concentration can be used for sample selection. For example, we could

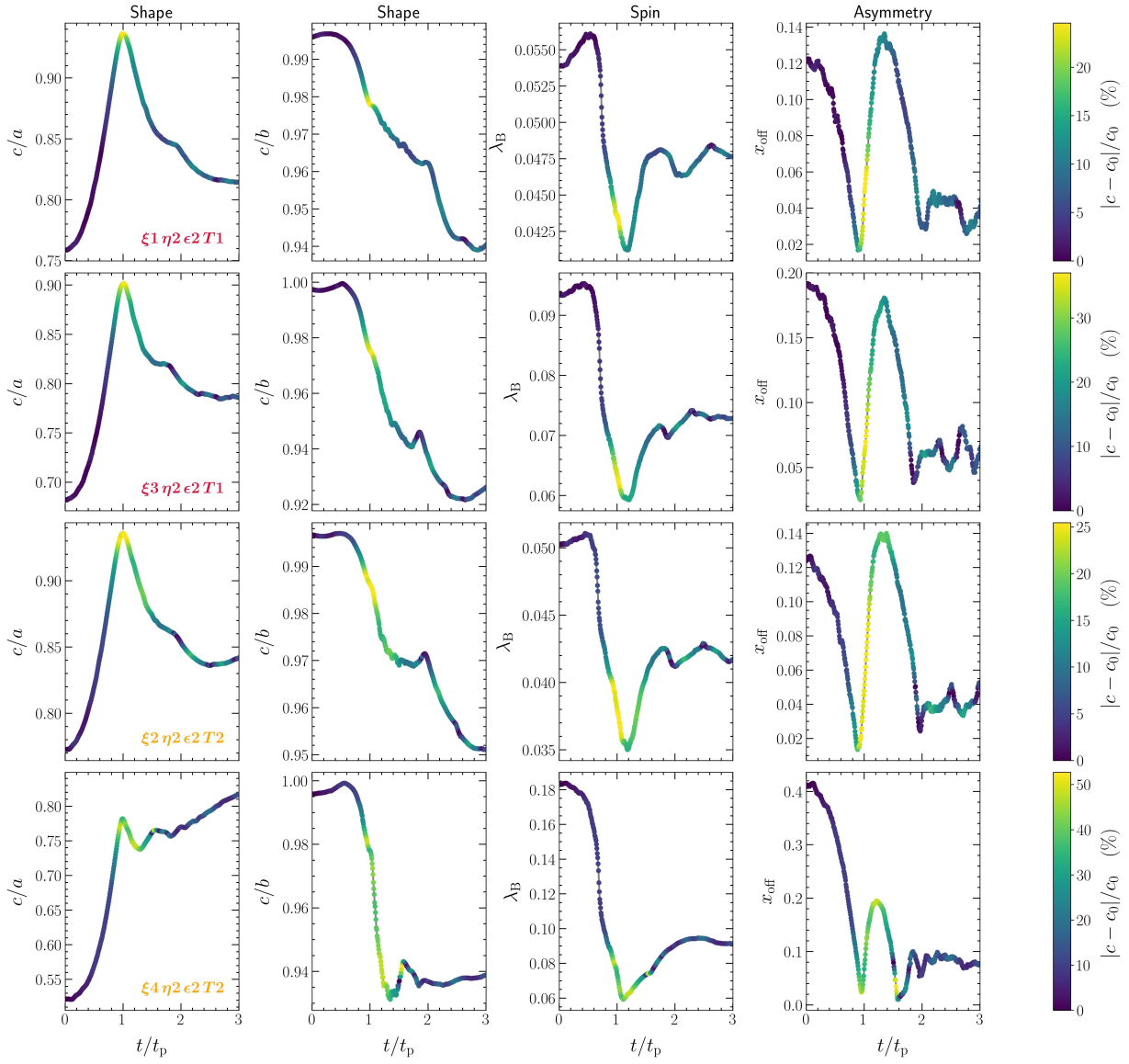



Figure 5.2: Minor-to-major axis ratio (left), minor-to-intermediate axis ratio (middle-left), spin (middle-right), and asymmetry (right) for the remnant system during the merger as measured in the simulations. The colourbar illustrates the corresponding concentration of the remnant system relative to its initial value. The simulations and their response types are labeled in the left subplots.

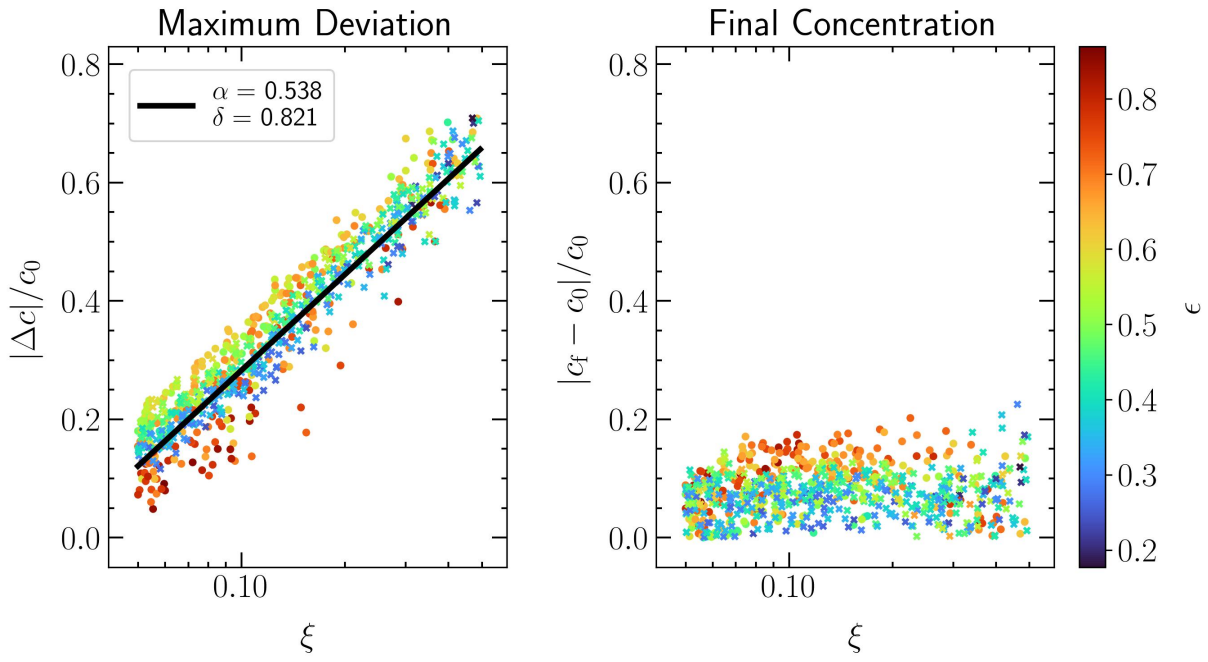



Figure 5.3: Comparing the maximum change in the remnant system concentration during the merger (left) against its overall change after the satellite merges with the central halo (right) as measured in the simulations. Each point represents a different simulation. Their colours correspond to the circularity of the merger and their markers describe the central halo response type, with type 1 as circles and type 2 as crosses. The black line depicts the best-fit to the maximum deviation distribution.

use the $c-M$ relation to get an idea of the expected concentration of a cluster halo given its mass. Then, if we measure a concentration that is far from its expected value, this would be an indication that a recent merger has taken place. Thus, we could filter these clusters from our sample, controlling for dynamical state. From Eq. 5.1, we could also identify the mass ratio of the merger that took place. However, this type of analysis is limited by the fact that large deviations in concentration only occur at certain points along the satellite's orbit. Moreover, individual cluster concentration observations can be imprecise with large uncertainties (see e.g. Groener et al., 2016; Biviano et al., 2017; Shan et al., 2017), which would make it difficult to determine if a merger occurred from the concentration alone if the scatter in its value is larger than the actual enhancement. New surveys will provide better signal-to-noise on individual detections of clusters, leading to tighter constraints.

### 5.2.2 Issues and Shortcomings

While the model presented in this thesis has its successes, it also has limitations and these should not be overlooked. Furthermore, our model has several shortcomings that will need to be addressed in the future. These are highlighted in this section.

1. *Simplifications*: At the moment, our orbital model neglects two additional effects: tidal heating and dynamical self-friction. The former accelerates mass loss which could improve predictions for the satellite's mass after the second orbit where it is usually underestimated. The latter should enhance the amount of orbital decay at late times, which is currently underestimated as well in our model. Dynamical self-friction is the process by which tidally stripped material in the vicinity of the satellite can torque the remaining bound particles, accelerating the decay in its orbital angular momentum (Fujii et al., 2006; Fellhauer & Lin, 2007). In idealized simulations of subhalo orbits, Miller et al. (2020) found that self-friction typically only contributes at the 10% level, but the effect is amplified further for radial orbits and higher mass ratio mergers. Properly incorporating self-friction would require a more accurate model for the unbound material and for dynamical friction to be described using linear response theory (see e.g. Weinberg, 1986, 1989). Fujii et al. (2006) propose a method for calculating the contribution of unbound particles in enhancing dynamical friction. Other techniques include using action-angle variables to trace the phase-space evolution of the unbound mass (see e.g. Binney & Tremaine, 2008, Section 8.3.3; Vasiliev, 2018). Regardless, a better unbound mass model would improve remnant property predictions as well.

2. *Central Halo Response Model*: The issue with the central halo response model is that it is not physically motivated, but instead based on the empirically measured median scale radius in our simulations. As a result, it is difficult to gauge how well it will translate to more realistic mergers in cosmological simulations. In the short-term, a functional form for the median response could be obtained through symbolic regression techniques (see e.g. PySR in Cranmer 2023 and ESR in Bartlett et al. 2024). The exact form may be complex, but in general it should be an oscillatory function with a decay in the amplitude. Note that in cosmological simulations, Wang et al. (2020) found that the remnant concentration oscillated in a simpler manner, and it seemed to be well correlated with the position of the satellite. We would then expect the central halo response to be slightly delayed with this.

3. *Baryonic Effects*: A major uncertainty in our model is the net effect of baryons on satellite orbits and the host halo structure. Baryonic processes can alter the halo

density profile. Adiabatic contraction can cause the dark matter halo to contract in response to the gas condensing towards its centre as it radiates away energy, increasing concentration (Gnedin et al., 2004). On the other hand, gas outflows through stellar or Active Galactic Nuclei (AGN) feedback can decrease the central potential, expanding the halo and reducing concentration (Macciò et al., 2012). This process may make halos more spherical as well given the gas carries away angular momentum from the system with it (Butsky et al., 2016). However, baryonic effects are expected to be largest on galaxy-scale halos. On cluster scales, only $\sim 10\%$ of the total mass of the cluster is composed of stellar material or gas (see e.g. Section 1.2). This leads to more minor changes in the remnant's structure. For instance, Debackere et al. (2021) find a 10% increase in estimates of the scale radius at masses $\sim 10^{14}h^{-1}M_{\odot}$ when including baryons (see their Fig. 6). This bias drops as mass increases. Similarly, cluster halo shapes are largely unaffected by baryons as they remain quite triaxial (see e.g. Lee et al., 2018; Sereno et al., 2018). Lastly, the presence of baryons contributes negligibly to the dynamical friction on satellites, where merging timescales are less than 10% faster (Boylan-Kolchin et al., 2008).

The effects of baryons on the structural properties measured for the remnant in our simulations should be similar to that described above. The remnant shapes should be largely unaffected, while the concentrations of the individual halos should decrease. As a consequence, the material in the overall remnant will be more broadly distributed, reducing the oscillation amplitude. Finally, quicker mergers caused by an enhancement in dynamical friction will result in an earlier oscillation timescale.

More work is required to properly address the impact of baryonic effects on halo structure during mergers. For example, if baryonic processes cause a net shift in concentration, this would be easy to calibrate in our model. Conversely, more complex changes would likely require redoing our analysis using full hydrodynamical simulations. Current and future cosmological simulations of this type include EAGLE (Schaye et al., 2014), IllustrisTNG (Vogelsberger et al., 2014), MillenniumTNG (Pakmor et al., 2023), and FLAMINGOs (Schaye et al., 2023). For our purposes, we would need the simulation to have sufficient time resolution to accurately track satellite orbits and to resolve changes in the host halo's structure during mergers. Moreover, we would need sufficient numbers of cluster-sized halos to be undergoing major mergers in order to model the response based on the initial conditions of the orbits. One issue with these simulations is that there is no single way of implementing baryonic physics, and the exact prescriptions employed often vary between simulations. This presents a problem given changes to the internal structure of halos will depend on this physics, so this will need to be explored as well.

## 5.3 Future Work

A simple modification to this work would be to test how adjusting the initial conditions we use affects the measured structural properties for the satellite, central halo, and remnant system. Our initial conditions had two free parameters, the satellite mass and the number of particles composing it. What if we instead considered mergers that create galaxy-scale or group-scale remnants? Preliminary results suggest that the properties we measure for the satellite and remnant system are largely independent of the choice of satellite mass with a few minor differences, provided the other initial conditions for the merger are unchanged (see Appendix A.5 for details). This is encouraging to see and perhaps indicates the response is universal. In addition to changing the satellite mass, we could also try examining a different redshift. Originally, we were interested in studying clusters at the present-day since most observations of them have been made at low redshift. At higher redshifts, halo concentration decreases (see e.g. Ludlow et al., 2014; Diemer & Joyce, 2019) which should lead to smaller oscillation amplitudes for the remnant structural properties when considering mergers with group scale satellite masses and the same mass ratio.

In the future, we would like to explore the effects of major mergers on halo properties in cosmological simulations. Currently, our simulations study the simplest possible case, the merger between two isolated, spherically symmetric components. We started with this since the structure of halos in cosmological simulations is affected by many processes. Multiple mergers, an expanding background, smooth accretion, and pseudo-evolution all influence halo properties. Furthermore, the presence of other subhalos in clusters will alter the satellite's orbit. Thus, in isolated simulations, we can study the baseline effect of mergers without these complications. Additionally, major mergers between cluster-sized halos are relatively rare, even at the present-day, and accurately measuring the initial conditions of the merger can be difficult in these simulations.

However, there is precedent for studying major mergers in cosmological simulations. Wang et al. (2020, 2023) do this by selecting samples of halos that undergo a single major merger at the same epoch, regardless of their mass. These halos must be hosts at the present-day and at the time of the merger. They then measure the structural property of interest as a function of time during the merger. Finally, they scale the structural property by its initial value, set the timescale in units of dynamical time (i.e. the time required to cross an equilibrium dynamical system), and stack all the individual measurements to find the median response. In our case, we would only want to consider cluster-scale halos with relatively quiescent merger histories given 10:1 mergers can still cause fluctuations in structural properties. On top of this, we may require better time resolution than that used in their simulations in order to accurately track satellite orbits for modeling purposes.

Unfortunately, it is unlikely our model can be directly applied to cosmological simulations in its current state. Because we use NFWT profiles to model our halos, part of the scale radius response is absorbed by the truncation scale. This parameter was necessary since our halos are isolated and there is no background. However, in cosmological simulations, we do have an evolving background, and halos can be modeled using the standard NFW profile. Without the truncation scale, it is likely that both the central halo and remnant system scale radii correlate well with the satellite's position as it orbits. Nevertheless, this thesis provides a framework for analyzing the response of halo properties to mergers and it establishes what components are important to model this.

# References


Abazajian K., et al., 2019, CMB-S4 Science Case, Reference Design, and Project Plan (arXiv:1907.04473)

Abdalla E., et al., 2022, Journal of High Energy Astrophysics, 34, 49

Aceves H., Velázquez H., 2006, Revista Mexicana de Astronomía y Astrofísica, 42, 41

Akeson R., et al., 2019, The Wide Field Infrared Survey Telescope: 100 Hubbles for the 2020s (arXiv:1902.05569)

Allen S. W., Evrard A. E., Mantz A. B., 2011, Annual Review of Astronomy and Astrophysics, 49, 409

Allgood B., Flores R. A., Primack J. R., Kravtsov A. V., Wechsler R. H., Faltenbacher A., Bullock J. S., 2006, Monthly Notices of the Royal Astronomical Society, 367, 1781

Amoura Y., Drakos N. E., Berrouet A., Taylor J. E., 2021, Monthly Notices of the Royal Astronomical Society, 508, 100

Amoura Y., Drakos N. E., Berrouet A., Taylor J. E., 2023, Monthly Notices of the Royal Astronomical Society, 527, 3459

Andrae R., Rix H.-W., Chandra V., 2023, The Astrophysical Journal Supplement Series, 267, A8

Astier P., et al., 2006, Astronomy & Astrophysics, 447, 31

Balmès I., Rasera Y., Corasaniti P. S., Alimi J. M., 2014, Monthly Notices of the Royal Astronomical Society, 437, 2328

Bartelmann M., 2010, Classical and Quantum Gravity, 27, 233001

Bartlett D. J., Desmond H., Ferreira P. G., 2024, IEEE Transactions on Evolutionary Computation, 28, 950

Benson A. J., 2005, Monthly Notices of the Royal Astronomical Society, 358, 551

Benson A. J., Lacey C. G., Frenk C. S., Baugh C. M., Cole S., 2004, Monthly Notices of the Royal Astronomical Society, 351, 1215

Bett P., Eke V., Frenk C. S., Jenkins A., Helly J., Navarro J., 2007, Monthly Notices of the Royal Astronomical Society, 376, 215

Bett P., Eke V., Frenk C. S., Jenkins A., Okamoto T., 2010, Monthly Notices of the Royal Astronomical Society, 404, 1137

Binney J., Tremaine S., 2008, Galactic Dynamics: Second Edition. Princeton University Press, http://www.jstor.org/stable/j.ctvc778ff

Biviano A., et al., 2017, Astronomy & Astrophysics, 607, A81

Blumenthal G. R., Faber S. M., Primack J. R., Rees M. J., 1984, Nature, 311, 517

Bode P., Ostriker J. P., Xu G., 2000, The Astrophysical Journal Supplement Series, 128, 561

Bond J. R., Kofman L., Pogosyan D., 1996, Nature, 380, 603

Boylan-Kolchin M., Ma C.-P., 2004, Monthly Notices of the Royal Astronomical Society, 349, 1117

Boylan-Kolchin M., Ma C.-P., Quataert E., 2008, Monthly Notices of the Royal Astronomical Society, 383, 93

Bradač M., et al., 2006, The Astrophysical Journal, 652, 937

Breiman L., 2001, Machine Learning, 45, 5

Breiman L., Friedman J., Stone C., Olshen R., 1984, Classification and Regression Trees. Taylor & Francis, https://books.google.ca/books?id=8k1DvQEACAAJ

Bryan G. L., Norman M. L., 1998, The Astrophysical Journal, 495, 80

Bullock J. S., Boylan-Kolchin M., 2017, Annual Review of Astronomy and Astrophysics, 55, 343

Bullock J. S., Kolatt T. S., Sigad Y., Somerville R. S., Kravtsov A. V., Klypin A. A., Primack J. R., Dekel A., 2001, Monthly Notices of the Royal Astronomical Society, 321, 559

Buote D. A., Humphrey P. J., 2012, Monthly Notices of the Royal Astronomical Society, 421, 1399

Burden R., Faires J., 2010, Numerical Analysis. Cengage Learning, https://books.google.ca/books?id=zXnSxY9G2JgC

Butsky I., et al., 2016, Monthly Notices of the Royal Astronomical Society, 462, 663

CCAT-Prime Collaboration et al., 2023, The Astrophysical Journal Supplement Series, 264, A7

CHEX-MATE Collaboration et al., 2021, Astronomy & Astrophysics, 650, A104

Calderon V. F., Berlind A. A., 2019, Monthly Notices of the Royal Astronomical Society, 490, 2367

Carroll S. M., 2001, Living Reviews in Relativity, 4, A1

Castignani G., Benoist C., 2016, Astronomy & Astrophysics, 595, A111

Chambers K., Unions Team Including Pan-Starrs Team, CFIS Team, 2020, in American Astronomical Society Meeting Abstracts #235. p. 154.04, https://aas.org/sites/default/files/2020-01/AAS235-Meeting-Abstracts.pdf

Chandrasekhar S., 1943, The Astrophysical Journal, 97, 255

Chen T., Guestrin C., 2016, in Proceedings of the 22nd ACM SIGKDD International Conference on Knowledge Discovery and Data Mining. https://dl.acm.org/doi/10.1145/2939672.2939785

Clowe D., Gonzalez A., Markevitch M., 2004, The Astrophysical Journal, 604, 596

Clowe D., Bradač M., Gonzalez A. H., Markevitch M., Randall S. W., Jones C., Zaritsky D., 2006, The Astrophysical Journal, 648, L109

Coe D., 2010, Dark Matter Halo Mass Profiles (arXiv:1005.0411)

Coe D., et al., 2012, The Astrophysical Journal, 757, A22

Colpi M., Mayer L., Governato F., 1999, The Astrophysical Journal, 525, 720

Copeland E. J., Sami M., Tsujikawa S., 2006, International Journal of Modern Physics D, 15, 1753

Cox T. J., Jonsson P., Somerville R. S., Primack J. R., Dekel A., 2008, Monthly Notices of the Royal Astronomical Society, 384, 386

Cranmer M., 2023, Interpretable Machine Learning for Science with PySR and SymbolicRegression.jl (arXiv:2305.01582)

Cyburt R. H., Fields B. D., Olive K. A., Yeh T.-H., 2016, Reviews of Modern Physics, 88, 015004

De Luca F., De Petris M., Yepes G., Cui W., Knebe A., Rasia E., 2021, Monthly Notices of the Royal Astronomical Society, 504, 5383

Debackere S. N. B., Schaye J., Hoekstra H., 2021, Monthly Notices of the Royal Astronomical Society, 505, 593

de Jong J. T. A., Verdoes Kleijn G. A., Kuijken K. H., Valentijn E. A., 2013, Experimental Astronomy, 35, 25

Diemer B., 2018, The Astrophysical Journal Supplement Series, 239, A35

Diemer B., Joyce M., 2019, The Astrophysical Journal, 871, A168

Diemer B., More S., Kravtsov A. V., 2013, The Astrophysical Journal, 766, A25

Drakos N. E., Taylor J. E., Benson A. J., 2017, Monthly Notices of the Royal Astronomical Society, 468, 2345

Drakos N. E., Taylor J. E., Berrouet A., Robotham A. S. G., Power C., 2019a, Monthly Notices of the Royal Astronomical Society, 487, 993

Drakos N. E., Taylor J. E., Berrouet A., Robotham A. S. G., Power C., 2019b, Monthly Notices of the Royal Astronomical Society, 487, 1008

Drakos N. E., Taylor J. E., Benson A. J., 2020, Monthly Notices of the Royal Astronomical Society, 494, 378

Drakos N. E., Taylor J. E., Benson A. J., 2022, Monthly Notices of the Royal Astronomical Society, 516, 106

Dutton A. A., Macciò A. V., 2014, Monthly Notices of the Royal Astronomical Society, 441, 3359

Einasto J., 1965, Trudy Astrofizicheskogo Instituta Alma-Ata, 5, 87

Euclid Collaboration et al., 2024, Euclid. V. The Flagship Galaxy Mock Catalogue: A Comprehensive Simulation for the Euclid Mission (arXiv:2405.13495)

Fakhouri O., Ma C.-P., 2008, Monthly Notices of the Royal Astronomical Society, 386, 577

Fellhauer M., Lin D. N. C., 2007, Monthly Notices of the Royal Astronomical Society, 375, 604

Fishman G. S., 1996, Monte Carlo: Concepts, Algorithms and Applications. Springer Verlag, https://doi.org/10.1007/978-1-4757-2553-7

Fujii M., Funato Y., Makino J., 2006, Publications of the Astronomical Society of Japan, 58, 743

Ghigna S., Moore B., Governato F., Lake G., Quinn T., Stadel J., 1998, Monthly Notices of the Royal Astronomical Society, 300, 146

Gnedin O. Y., Ostriker J. P., 1999, The Astrophysical Journal, 513, 626

Gnedin O. Y., Kravtsov A. V., Klypin A. A., Nagai D., 2004, The Astrophysical Journal, 616, 16

Groener A. M., Goldberg D. M., Sereno M., 2016, Monthly Notices of the Royal Astronomical Society, 455, 892

Gunn J. E., Gott J. R., 1972, The Astrophysical Journal, 176, 1

Haggar R., Kuchner U., Gray M. E., Pearce F. R., Knebe A., Yepes G., Cui W., 2022, Monthly Notices of the Royal Astronomical Society, 518, 1316

Haggar R., et al., 2024, Monthly Notices of the Royal Astronomical Society, 532, 1031

Hashimoto Y., Funato Y., Makino J., 2003, The Astrophysical Journal, 582, 196

Hayashi E., Navarro J. F., Taylor J. E., Stadel J., Quinn T., 2003, The Astrophysical Journal, 584, 541

Hernquist L., 1993, The Astrophysical Journal Supplement Series, 86, 389

Hoekstra H., Herbonnet R., Muzzin A., Babul A., Mahdavi A., Viola M., Cacciato M., 2015, Monthly Notices of the Royal Astronomical Society, 449, 685

Hopkins P. F., et al., 2009, Monthly Notices of the Royal Astronomical Society, 397, 802

Huchra J. P., Geller M. J., 1982, The Astrophysical Journal, 257, 423

Huertas-Company M., Aguerri J. A. L., Bernardi M., Mei S., Sánchez Almeida J., 2011, Astronomy and Astrophysics, 525, A157

Jiang L., Cole S., Sawala T., Frenk C. S., 2015, Monthly Notices of the Royal Astronomical Society, 448, 1674

Jing Y. P., Suto Y., 2002, The Astrophysical Journal, 574, 538

Joudaki S., et al., 2017, Monthly Notices of the Royal Astronomical Society, 474, 4894

Kauffmann G., White S. D. M., Heckman T. M., Ménard B., Brinchmann J., Charlot S., Tremonti C., Brinkmann J., 2004, Monthly Notices of the Royal Astronomical Society, 353, 713

Kazantzidis S., Magorrian J., Moore B., 2004, The Astrophysical Journal, 601, 37

Kazantzidis S., Zentner A. R., Kravtsov A. V., 2006, The Astrophysical Journal, 641, 647

King I., 1962, Astronomical Journal, 67, 471

Klema V., Laub A., 1980, IEEE Transactions on Automatic Control, 25, 164

Klypin A. A., Trujillo-Gomez S., Primack J., 2011, The Astrophysical Journal, 740, A102

Klypin A. A., Yepes G., Gottlöber S., Prada F., Heß S., 2016, Monthly Notices of the Royal Astronomical Society, 457, 4340

Knebe A., et al., 2011, Monthly Notices of the Royal Astronomical Society, 415, 2293

Kravtsov A. V., Borgani S., 2012, Annual Review of Astronomy and Astrophysics, 50, 353

LSST Dark Energy Science Collaboration et al., 2021, The Astrophysical Journal Supplement Series, 253, A31

Lacey C., Cole S., 1993, Monthly Notices of the Royal Astronomical Society, 262, 627

Lacey C., Cole S., 1994, Monthly Notices of the Royal Astronomical Society, 271, 676

Lau E. T., Hearin A. P., Nagai D., Cappelluti N., 2021, Monthly Notices of the Royal Astronomical Society, 500, 1029

Leauthaud A., et al., 2012, The Astrophysical Journal, 744, A159

Lee B. E., Le Brun A. M. C., Haq M. E., Deering N. J., King L. J., Applegate D., McCarthy I. G., 2018, Monthly Notices of the Royal Astronomical Society, 479, 890

Lochner M., McEwen J. D., Peiris H. V., Lahav O., Winter M. K., 2016, The Astrophysical Journal Supplement Series, 225, A31

Ludlow A. D., Navarro J. F., Li M., Angulo R. E., Boylan-Kolchin M., Bett P. E., 2012, Monthly Notices of the Royal Astronomical Society, 427, 1322

Ludlow A. D., et al., 2013, Monthly Notices of the Royal Astronomical Society, 432, 1103

Ludlow A. D., Navarro J. F., Angulo R. E., Boylan-Kolchin M., Springel V., Frenk C., White S. D. M., 2014, Monthly Notices of the Royal Astronomical Society, 441, 378

Macciò A. V., Dutton A. A., van den Bosch F. C., Moore B., Potter D., Stadel J., 2007, Monthly Notices of the Royal Astronomical Society, 378, 55

Macciò A. V., Dutton A. A., van den Bosch F. C., 2008, Monthly Notices of the Royal Astronomical Society, 391, 1940

Macciò A. V., Stinson G., Brook C. B., Wadsley J., Couchman H. M. P., Shen S., Gibson B. K., Quinn T., 2012, The Astrophysical Journal Letters, 744, L9

Machado Poletti Valle L. F., Avestruz C., Barnes D. J., Farahi A., Lau E. T., Nagai D., 2021, Monthly Notices of the Royal Astronomical Society, 507, 1468

Mahdavi A., Hoekstra H., Babul A., Bildfell C., Jeltema T., Henry J. P., 2013, The Astrophysical Journal, 767, A116

Markevitch M., Gonzalez A. H., Clowe D., Vikhlinin A., Forman W., Jones C., Murray S., Tucker W., 2004, The Astrophysical Journal, 606, 819

Mastropietro C., Burkert A., 2008, Monthly Notices of the Royal Astronomical Society, 389, 967

McMillan P. J., Athanassoula E., Dehnen W., 2007, Monthly Notices of the Royal Astronomical Society, 376, 1261

Merloni A., et al., 2012, eROSITA Science Book: Mapping the Structure of the Energetic Universe (arXiv:1209.3114)

Miller T. B., van den Bosch F. C., Green S. B., Ogiya G., 2020, Monthly Notices of the Royal Astronomical Society, 495, 4496

Mo H., van den Bosch F. C., White S., 2010, Galaxy Formation and Evolution. Cambridge University Press, https://doi.org/10.1017/CBO9780511807244

Moore B., Katz N., Lake G., Dressler A., Oemler A., 1996, Nature, 379, 613

Moore B., Governato F., Quinn T., Stadel J., Lake G., 1998, The Astrophysical Journal, 499, L5

More S., Kravtsov A. V., Dalal N., Gottlöber S., 2011, The Astrophysical Journal Supplement Series, 195, A4

Myers S. T., Baker J. E., Readhead A. C. S., Leitch E. M., Herbig T., 1997, The Astrophysical Journal, 485, 1

Nagai D., Vikhlinin A., Kravtsov A. V., 2007, The Astrophysical Journal, 655, 98

Natekin A., Knoll A., 2013, Frontiers in Neurorobotics, 7, A21

Navarro J. F., Frenk C. S., White S. D. M., 1996, The Astrophysical Journal, 462, 563

Navarro J. F., Frenk C. S., White S. D. M., 1997, The Astrophysical Journal, 490, 493

Navarro J. F., et al., 2010, Monthly Notices of the Royal Astronomical Society, 402, 21

Neto A. F., et al., 2007, Monthly Notices of the Royal Astronomical Society, 381, 1450

Newman M., 2013, Computational Physics. CreateSpace Independent Publishing Platform, https://books.google.ca/books?id=SS6uNAEACAAJ

Newville M., Stensitzki T., Allen D. B., Rawlik M., Ingargiola A., Nelson A., 2016, Lmfit: Non-Linear Least-Square Minimization and Curve-Fitting for Python, https://ascl.net/1606.014

Ostriker J. P., Steinhardt P. J., 1995, Nature, 377, 600

Pakmor R., et al., 2023, Monthly Notices of the Royal Astronomical Society, 524, 2539

Peacock J. A., 1999, Cosmological Physics. Cambridge University Press, https://books.google.ca/books?id=t8O-yylU0j0C

Pedregosa F., et al., 2011, Scikit-learn: Machine Learning in Python, http://jmlr.org/papers/v12/pedregosa11a.html

Peebles P., 1971, Physical Cosmology. Princeton University Press, https://www.jstor.org/stable/j.ctt13x0w7r

Peñarrubia J., Benson A. J., 2005, Monthly Notices of the Royal Astronomical Society, 364, 977

Peñarrubia J., Benson A. J., Walker M. G., Gilmore G., McConnachie A. W., Mayer L., 2010, Monthly Notices of the Royal Astronomical Society, 406, 1290

Peng Y.-J., et al., 2010, The Astrophysical Journal, 721, 193

Perivolaropoulos L., Skara F., 2022, New Astronomy Reviews, 95, 101659

Planck Collaboration et al., 2020, Astronomy & Astrophysics, 641, A6

Postman M., et al., 2012, The Astrophysical Journal Supplement Series, 199, A25

Power C., Knebe A., Knollmann S. R., 2011, Monthly Notices of the Royal Astronomical Society, 419, 1576

Prada F., Klypin A. A., Cuesta A. J., Betancort-Rijo J. E., Primack J., 2012, Monthly Notices of the Royal Astronomical Society, 423, 3018

Press W. H., Schechter P., 1974, The Astrophysical Journal, 187, 425

Reid B. A., et al., 2010, Monthly Notices of the Royal Astronomical Society, 404, 60

Richardson T. R. G., Corasaniti P.-S., 2022, Monthly Notices of the Royal Astronomical Society, 513, 4951

Robotham A. S. G., Howlett C., 2018, A Short Research Note on Calculating Exact Distribution Functions and Random Sampling for the 3D NFW Profile (arXiv:1805.09550)

Rubin V. C., Ford W. Kent J., 1970, The Astrophysical Journal, 159, 379

Sánchez-Conde M. A., Prada F., 2014, Monthly Notices of the Royal Astronomical Society, 442, 2271

Sartoris B., et al., 2016, Monthly Notices of the Royal Astronomical Society, 459, 1764

Savitzky A., Golay M. J. E., 1964, Analytical Chemistry, 36, 1627

Schaye J., et al., 2014, Monthly Notices of the Royal Astronomical Society, 446, 521

Schaye J., et al., 2023, Monthly Notices of the Royal Astronomical Society, 526, 4978

Sehgal N., Bode P., Das S., Hernandez-Monteagudo C., Huffenberger K., Lin Y.-T., Ostriker J. P., Trac H., 2010, The Astrophysical Journal, 709, 920

Sereno M., Umetsu K., Ettori S., Sayers J., Chiu I. N., Meneghetti M., Vega-Ferrero J., Zitrin A., 2018, The Astrophysical Journal Letters, 860, L4

Shan H., et al., 2017, The Astrophysical Journal, 840, A104

Sheth R. K., Tormen G., 2002, Monthly Notices of the Royal Astronomical Society, 329, 61

Smith A., Cole S., Baugh C., Zheng Z., Angulo R., Norberg P., Zehavi I., 2017, Monthly Notices of the Royal Astronomical Society, 470, 4646

Spergel D. N., et al., 2007, The Astrophysical Journal Supplement Series, 170, 377

Spinnato P. F., Fellhauer M., Portegies Zwart S. F., 2003, Monthly Notices of the Royal Astronomical Society, 344, 22

Springel V., 2005, Monthly Notices of the Royal Astronomical Society, 364, 1105

Springel V., Yoshida N., White S. D., 2001, New Astronomy, 6, 79

Springel V., Frenk C. S., White S. D. M., 2006, Nature, 440, 1137

Sunyaev R. A., Zeldovich Y. B., 1972, Comments on Astrophysics and Space Physics, 4, 173

Taylor J. E., Babul A., 2001, The Astrophysical Journal, 559, 716

Tinker J., Kravtsov A. V., Klypin A., Abazajian K., Warren M., Yepes G., Gottlöber S., Holz D. E., 2008, The Astrophysical Journal, 688, 709

Tormen G., Bouchet F. R., White S. D. M., 1997, Monthly Notices of the Royal Astronomical Society, 286, 865

Tormen G., Diaferio A., Syer D., 1998, Monthly Notices of the Royal Astronomical Society, 299, 728

van Kampen E., 2000, Overmerging in N-body simulations (arXiv:astro-ph/0002027)

van den Bosch F. C., Lewis G. F., Lake G., Stadel J., 1999, The Astrophysical Journal, 515, 50

van den Bosch F. C., Ogiya G., Hahn O., Burkert A., 2018, Monthly Notices of the Royal Astronomical Society, 474, 3043

van der Burg R. F. J., et al., 2020, Astronomy & Astrophysics, 638, A112

Vapnik V. N., 1995, The Nature of Statistical Learning Theory. Springer-Verlag, http://dx.doi.org/10.1007/978-1-4757-2440-0

Vasiliev E., 2018, Monthly Notices of the Royal Astronomical Society, 482, 1525

Vass I. M., Kazantzidis S., Valluri M., Kravtsov A. V., 2009, The Astrophysical Journal, 698, 1813

Vera-Ciro C. A., Helmi A., Starkenburg E., Breddels M. A., 2013, Monthly Notices of the Royal Astronomical Society, 428, 1696

Vera-Ciro C. A., Sales L. V., Helmi A., Navarro J. F., 2014, Monthly Notices of the Royal Astronomical Society, 439, 2863

Vikhlinin A., Kravtsov A., Forman W., Jones C., Markevitch M., Murray S. S., Van Speybroeck L., 2006, The Astrophysical Journal, 640, 691

Virtanen P., et al., 2020, Nature Methods, 17, 261

Vogelsberger M., et al., 2014, Monthly Notices of the Royal Astronomical Society, 444, 1518

Wahde M., Donner K. J., 1996, Astronomy and Astrophysics, 312, 431

Wang K., Mao Y.-Y., Zentner A. R., Lange J. U., van den Bosch F. C., Wechsler R. H., 2020, Monthly Notices of the Royal Astronomical Society, 498, 4450

Wang K., Mansfield P., Anbajagane D., Avestruz C., 2023, Merger Response of Halo Anisotropy Properties (arXiv:2311.08664)

Wechsler R. H., Bullock J. S., Primack J. R., Kravtsov A. V., Dekel A., 2002, The Astrophysical Journal, 568, 52

Weinberg M. D., 1986, The Astrophysical Journal, 300, 93

Weinberg M. D., 1989, Monthly Notices of the Royal Astronomical Society, 239, 549

Wetzel A. R., 2011, Monthly Notices of the Royal Astronomical Society, 412, 49

White M., 2001, Astronomy & Astrophysics, 367, 27

Wong A. W. C., Taylor J. E., 2012, The Astrophysical Journal, 757, A102

XRISM Science Team 2020, Science with the X-ray Imaging and Spectroscopy Mission (XRISM) (arXiv:2003.04962)

Zentner A. R., Bullock J. S., 2003, The Astrophysical Journal, 598, 49

Zhang J., Fakhouri O., Ma C.-P., 2008, Monthly Notices of the Royal Astronomical Society, 389, 1521

Zwicky F., 1933, Helvetica Physica Acta, 6, 110

# APPENDICES

# Appendix A

# Supplemental Simulation Results

## A.1 Evolving the Central Halo in Isolation

In Section 2.3.2, we found that the motion of the satellite as it orbits produces a response in the structure of the central halo. However, it is unclear whether or not any of this change in structure is attributed to self-interactions between the particles in the halo itself. To test this, we evolve the central halo in the absence of a satellite. We use the same initial profile for the central halo as in the full merger simulations where a satellite is present. In this way, we can test the stability of the initial conditions generated using ICICLE.

Fig. A.1 examines how the scale radius of the central halo changes when evolved in isolation compared to when it is in the presence of a satellite, for a set of simulations. For both types of central halo responses, we find there is an initial jump in scale radius before it declines to a stable value, except for the high mass ratio merger $\xi 4\,\eta 2\,\epsilon 2\,T2$ where the response is extremely stable at all times. This effect is most pronounced for type 1 responses of low mass ratio (e.g. $\xi 1\,\eta 2\,\epsilon 2\,T1$). This result is similar to that discussed in Drakos et al. (2017), where the authors showed the innermost region of the profile created by ICICLE evolves at early times due to a collisional effect from finite resolution. Other methods for sampling particles and their velocities from a given density profile generally suffer from the same limitation in which the centre of the system is unstable (see e.g. Kazantzidis et al., 2004). However, in our case, the timescale of the effect is short and the halo profile stabilizes before the primary oscillation in scale radius occurs. The initial change in scale radius is relatively small compared to the oscillation amplitude as well. This implies the response of the central halo particles is largely unaffected by particle-particle interactions within the halo.

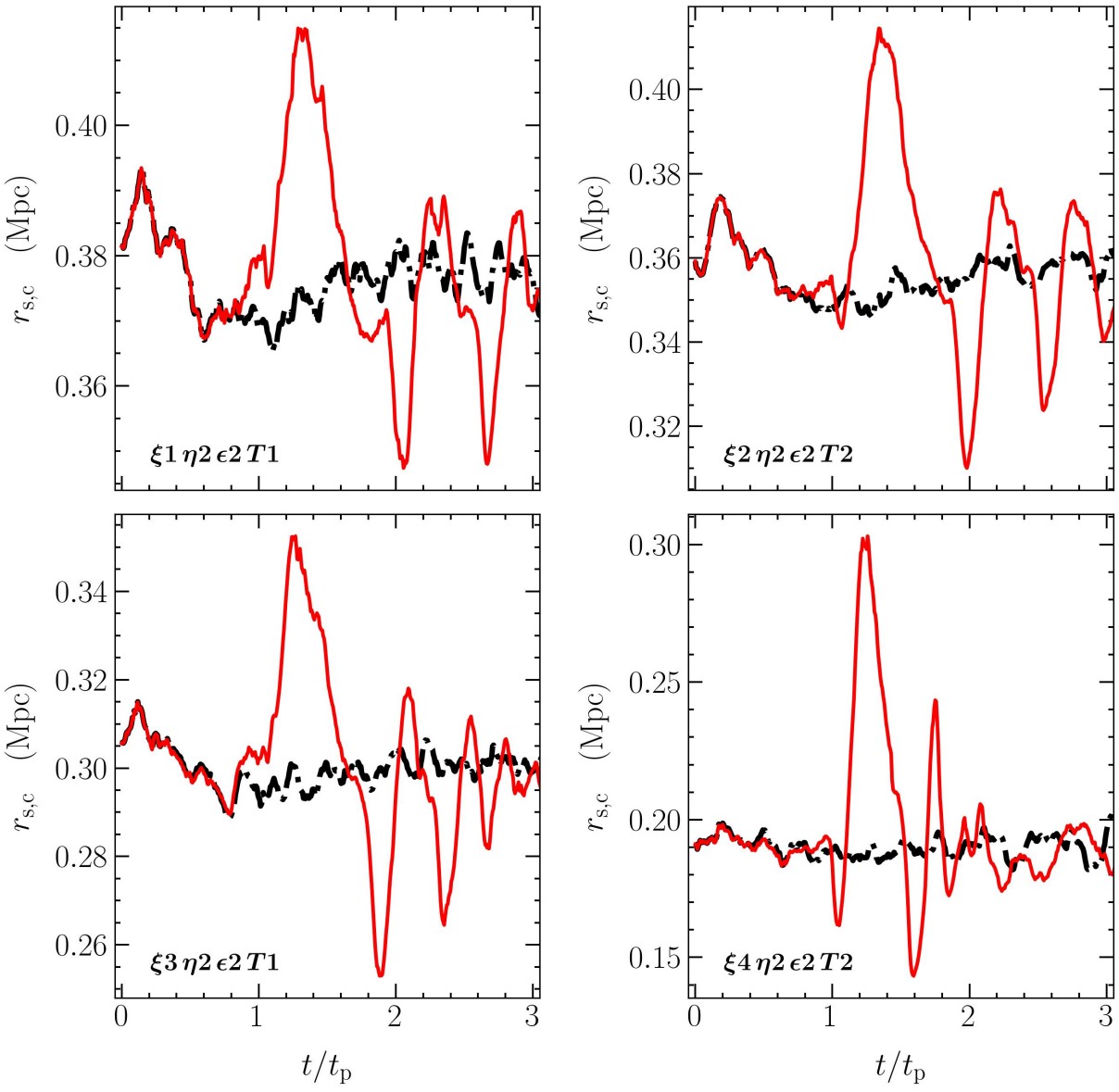



Figure A.1: Testing the stability of the particle distributions generated by ICICLE. The lines depict the change in central halo scale radius with time when the halo is evolved in isolation (black, dashdot) compared to when it merges with the satellite (red, solid).

## A.2 Fitting NFWT Parameters Using a Fixed Truncation Scale $y_d$

When we fit an NFWT profile to the remnant system in each snapshot of a given simulation, we let all of its parameters ($r_s$, $\rho_0$, $y_d$) be free parameters by default. In Section 2.3.2, we found this led to an anti-correlation between the best-fit values for the scale radius and truncation scale. If the profile exponentially truncates at a smaller radius, the scale radius needs to increase to compensate. This effect is demonstrated further below and it causes the remnant scale radius to maximize at pericentre after the initial infall since the truncation scale drops instead. In general, we would expect the opposite behaviour, where the scale radius declines to a minimum value at pericentre, since we have a dense satellite moving towards the centre of the system. However, incorporating a truncation scale into the profile complicates the result.

The standard NFW profile ($r_s$, $\rho_0$) does not include a truncation scale as one of its parameters. If we were to remove the impact of this parameter from our NFWT fits, would we recover the behaviour we expect when considering the satellite's dynamics? Fig. A.2 illustrates the best-fit NFWT parameters for the remnant system when the truncation scale is a free parameter compared to when it is a fixed parameter. In the fixed parameter case, we set the value of $y_d$ to its initial value when it was allowed to be a free parameter. We find that using a constant truncation scale leads to the scale radius following its expected behaviour. During the initial infall, the scale radius slowly rises as the satellite's mass starts to make an impact on the outer edges of the remnant system's density profile. As the satellite moves further into the centre of the potential, the scale radius drops until it reaches a minimum value at pericentre. Finally, the satellite travels back out towards apocentre leading to an increase in the scale radius once again. Our results demonstrate that using a fixed truncation scale in the NFWT fits causes the change in the remnant's scale radius to be largely correlated with the position of the satellite during the merger.

On the other hand, the evolution of the virial radius during the merger is independent of the truncation scale. This is because its definition uses the particles from the simulation itself, which is independent of the profile being fit. This implies differences in concentration between the free and fixed truncation scale cases are solely due to differences in the scale radius. While the results for the remnant system's NFWT parameters are more in line with our expectations if the truncation scale is set to a fixed value, we did not use these fits in our analysis. As stated in the main text, we found the central halo median response had worse constraints and its model parameters scaled poorly with the initial conditions when fitting profiles using a fixed truncation scale.

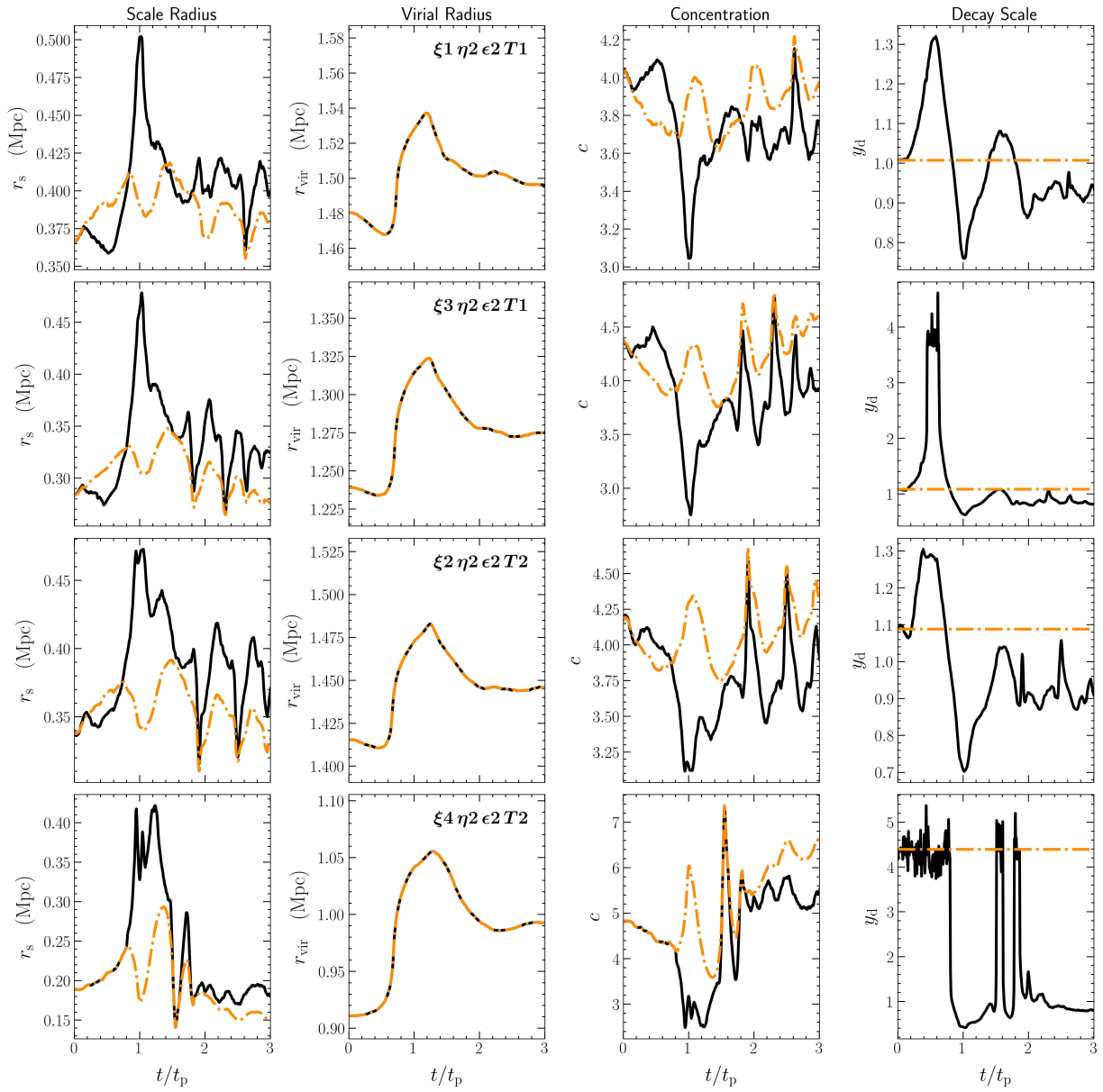



Figure A.2: Scale radius (left), virial radius (middle-left), concentration (middle-right), and exponential truncation scale (right) for the remnant system during the merger. The lines depict the best-fit NFWT parameters when $y_d$ is a free parameter (black, solid) compared to when it is a fixed parameter (orange, dashdot).

In our default procedure, we measure the concentration of each halo and the remnant system directly from the scale radius by finding the NFWT profile that is best-fit to the circular velocity profile. However, concentration can also be determined indirectly from other properties, such as the peak circular velocity, $v_{\rm peak}$ (see e.g. Prada et al., 2012; Klypin et al., 2016). The ratio of the maximum circular velocity to the virial velocity, $v_{\rm peak}/v_{\rm vir}$, can be used as a profile-independent measure of halo concentration since the larger the ratio, the higher the halo concentration is irrespective of any particular analytic description for the profile. This may be preferred for the remnant system given the presence of the satellite causes it to diverge from an NFWT profile. Klypin et al. (2016) describe how the ratio $v_{\rm peak}/v_{\rm vir}$ can be related to the standard NFW concentration in the following way,

$$\left(\frac{v_{\rm peak}}{v_{\rm vir}}\right)^2 = \frac{c}{x_{\rm max}}\frac{f(x_{\rm max})}{f(c)} \tag{A.1}$$

where $x_{\rm max} = 2.163$ and $f(x) = \ln(1+x) - x/(1+x)$ is the NFW mass profile. This is an implicit equation for $c$ that can be solved using root-finding algorithms. The concentration can then be converted to the scale radius if the virial radius is known using $r_s = r_{\rm vir}/c$.

Fig. A.3 compares the remnant system scale radius estimated using Eq. A.1 to that obtained from the best-fit NFWT profiles when considering $y_d$ to be a free parameter or a fixed parameter. For the set of simulations shown, we find there is a systematic offset between the scale radius calculated using $v_{\rm peak}/v_{\rm vir}$ and that from the NFWT fits, likely due to $f(x)$ in Eq. A.1 assuming an NFW profile rather than an NFWT profile. Despite this, we find the scale radius determined from $v_{\rm peak}/v_{\rm vir}$ follows a similar trend to that of the fixed truncation scale curve, although the oscillations are much larger.

Overall, measuring concentration using the peak circular velocity may be more suitable for our simulations since when fitting NFWT profiles, the truncation scale masks the evolution of the scale radius expected from the physical motion of the satellite. This is shown in Fig. A.4, where we plot for an example simulation how the remnant scale radius and truncation scale change depending on if $y_d$ is a free or fixed parameter. The blue lines illustrate their initial values which are the same regardless of whether or not we fit $y_d$. The main comparison is between the middle and right panels. In the free $y_d$ case, the truncation scale moves from a value that is larger than its initial value to one that is smaller. At the same time, the scale radius has the opposite behaviour moving from a small value to a larger one even though we would expect it to minimize around $t_p$ based on the position of the satellite. In the fixed $y_d$ case, we do find the expected behaviour as the scale radius gets smaller during this period, although only slightly. Thus, the truncation scale has a direct effect on the scale radius when it is left as a free parameter in our profile fitting.

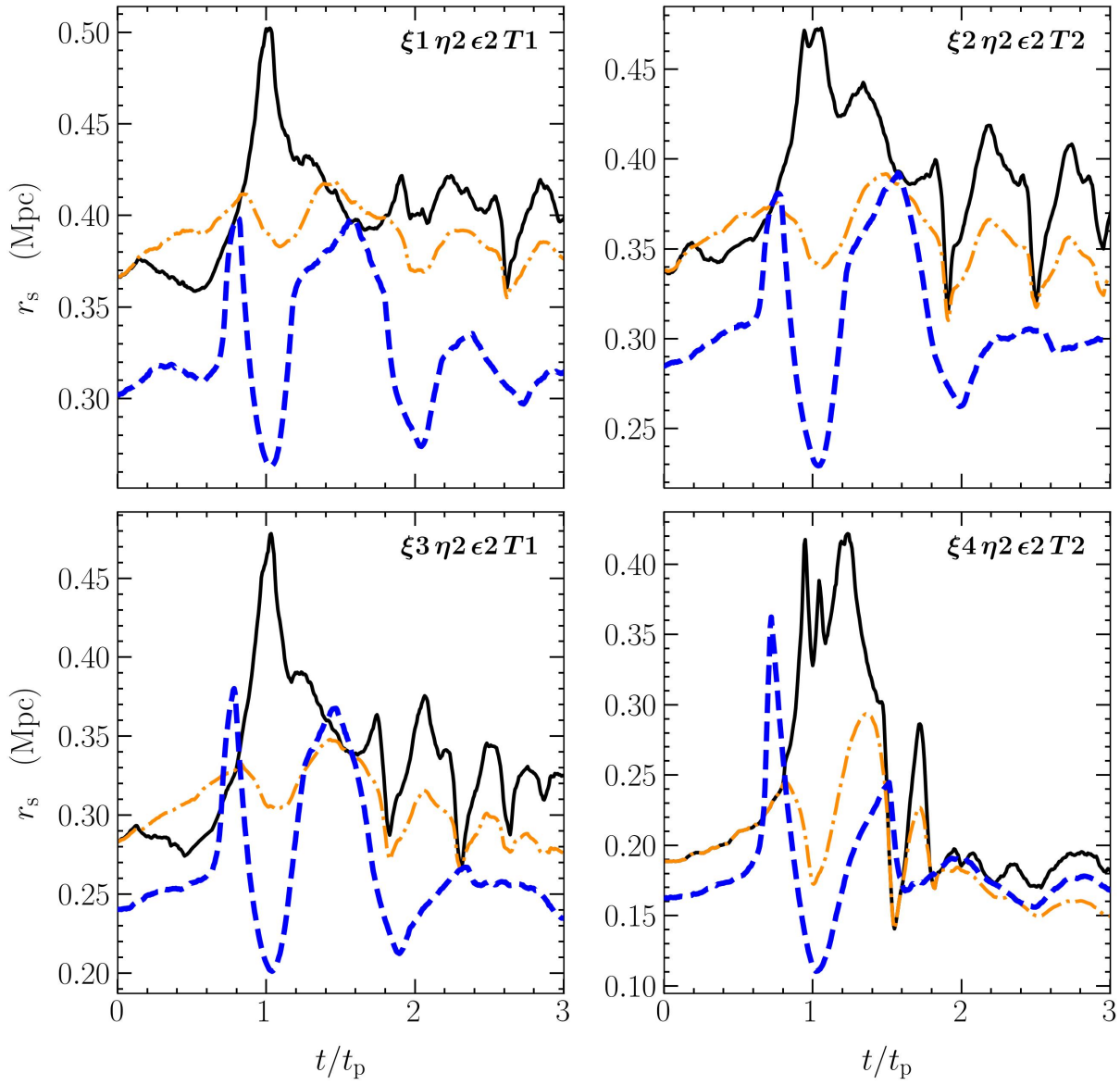



Figure A.3: Scale radius for the remnant system during the merger estimated using the peak circular velocity (blue, dashed). The other lines correspond to the scale radii extracted from the best-fit NFWT profiles when considering $y_d$ to be a free parameter (black, solid) or a fixed parameter (orange, dashdot).

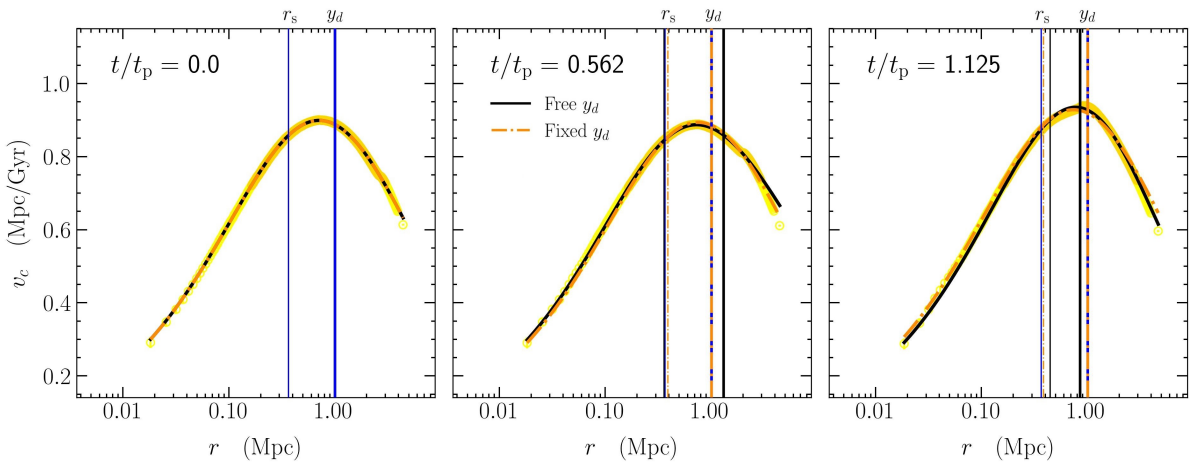



Figure A.4: Remnant halo circular velocity profiles for the simulation $\xi 1\,\eta 2\,\epsilon 2\,T1$. The gold points show the profile measured in the simulation (yellow points excluded), while the lines depict the best-fit model when $y_d$ is a free parameter (black, solid) compared to when it is a fixed parameter (orange, dashdot). The corresponding vertical lines plot the fitted values of the scale radius (thin) and truncation scale (thick) at the time displayed in the top-left hand corner of each subpanel, while the blue lines are their initial values.

## A.3 Investigating the Central Halo Response Type Separation Using Other Initial Conditions

In Section 4.1.1, we determined that the two central halo response types could be classified using the relative energy parameter and the time ratio between the maximum-to-minimum central halo scale radius time. The time ratio seems to be necessary for splitting the response types. However, the relative energy is one of several initial conditions we could consider. If we were to use a different initial condition as the independent quantity, could we distinguish the response types with equal success? Fig. A.5 depicts the time ratio, $t_{r_{s,c},\max}/t_{r_{s,c},\min}$, as a function of other initial conditions we use in the simulations. The colour of each point in the plot shows the response type obtained from Eq. 4.1, our original classification scheme. We find there is a discernible separation between the response types when using other initial conditions ($r_p$, $\xi$, $\epsilon$), although the exact position of the split is not as clear. For example, type 2 responses track well with pericentre but not completely (i.e. most type 2 are at $r_p < r_{s,c,0}$ but not all). While classifying the responses using $\eta$ is not unique given we would obtain a similar result if we considered a different initial condition as our independent variable, it has the most noticeable break to make the split.

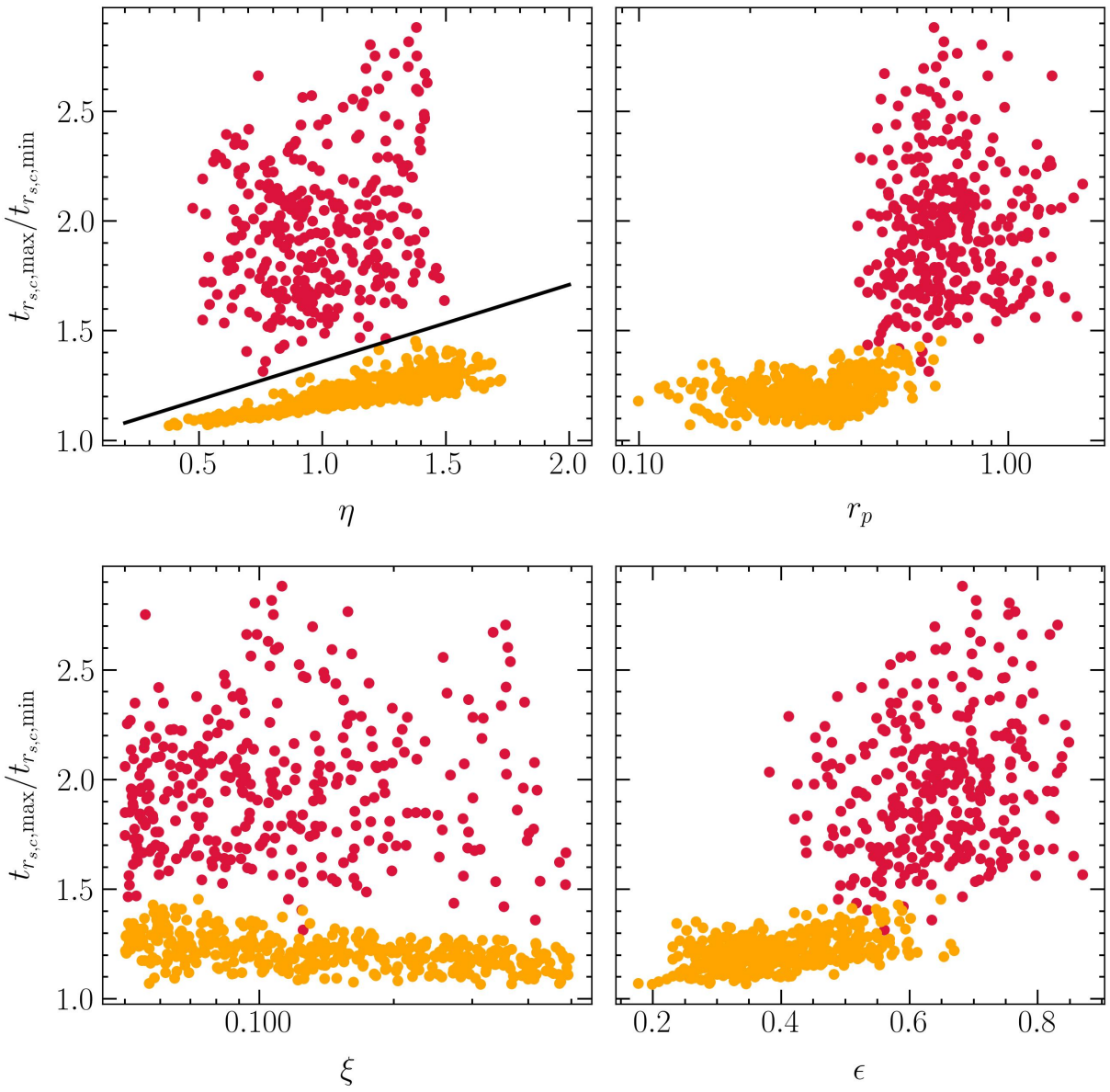



Figure A.5: Investigating if the central halo response classification can be made using other initial conditions. The color of each point shows the original classification obtained from the time ratio-relative energy separation (black line), with type 1 in crimson and type 2 in orange. From top to bottom, left to right, the initial conditions depicted in each subplot are as follows: (1) the relative energy, (2) the pericentric passage distance, (3) the mass ratio, and (4) the circularity.

## A.4 Measuring Orbits for a Point Mass Satellite with Various Mass Resolutions

In this section, we explore how the mass resolution of a point mass satellite affects its orbit in an $N$-body simulation. We compare this to our standard simulation where the satellite is represented using many particles as opposed to a single particle. Fig. A.6 demonstrates the effect of mass resolution on the orbit of the satellite measured for a set of simulations. The dotted and dashed horizontal lines depict the pericentre and apocentre positions in a static orbit, respectively. Each curve in the plot considers a different mass resolution.

- *Solid red line*: the satellite is a point mass orbiting in a static NFWT potential in the absence of dynamical friction or mass loss. Its equations of motion are given by B.31 and are integrated numerically.
- *Dotted lime line*: the satellite is represented by a single particle in the simulation with a mass $M_p = 1\,M_\odot$.
- *Solid green line*: the satellite is represented by a single particle in the simulation with a mass $M_p = 7.138 \times 10^8\,M_\odot$, the standard mass per particle.
- *Solid blue line*: the satellite is represented by a single particle in the simulation with a mass $M_p = 2.5 \times 10^{13}\,M_\odot$, the standard total satellite mass.
- *Dash-dotted purple line*: the satellite is represented by many particles as in our standard simulations. These results are identical to that shown in Fig. 2.6.
- *Dashed vertical line*: the radial orbital period in a static orbit given by Eq. B.25.

In all cases, the central halo is represented using many particles with our standard particle mass as outlined in Section 2.2.1. From the plot, we find the satellite's orbit mirrors the static case when its mass is less than $7.138 \times 10^8 M_\odot$, our standard mass per particle. This implies dynamical friction has little effect on the orbit when the mass ratio of the merger is sufficiently small. At late times, the results from the $N$-body simulations start to diverge from the static case due to the central halo having finite resolution. On the other hand, dynamical friction causes the orbit to decay in the simulation once the satellite is given its total mass. However, since the satellite is represented by a single particle, it does not lose mass, and it cannot move back out after pericentre. Thus, the satellite must be represented using many particles in the simulations in order to get an accurate measure for its orbit.

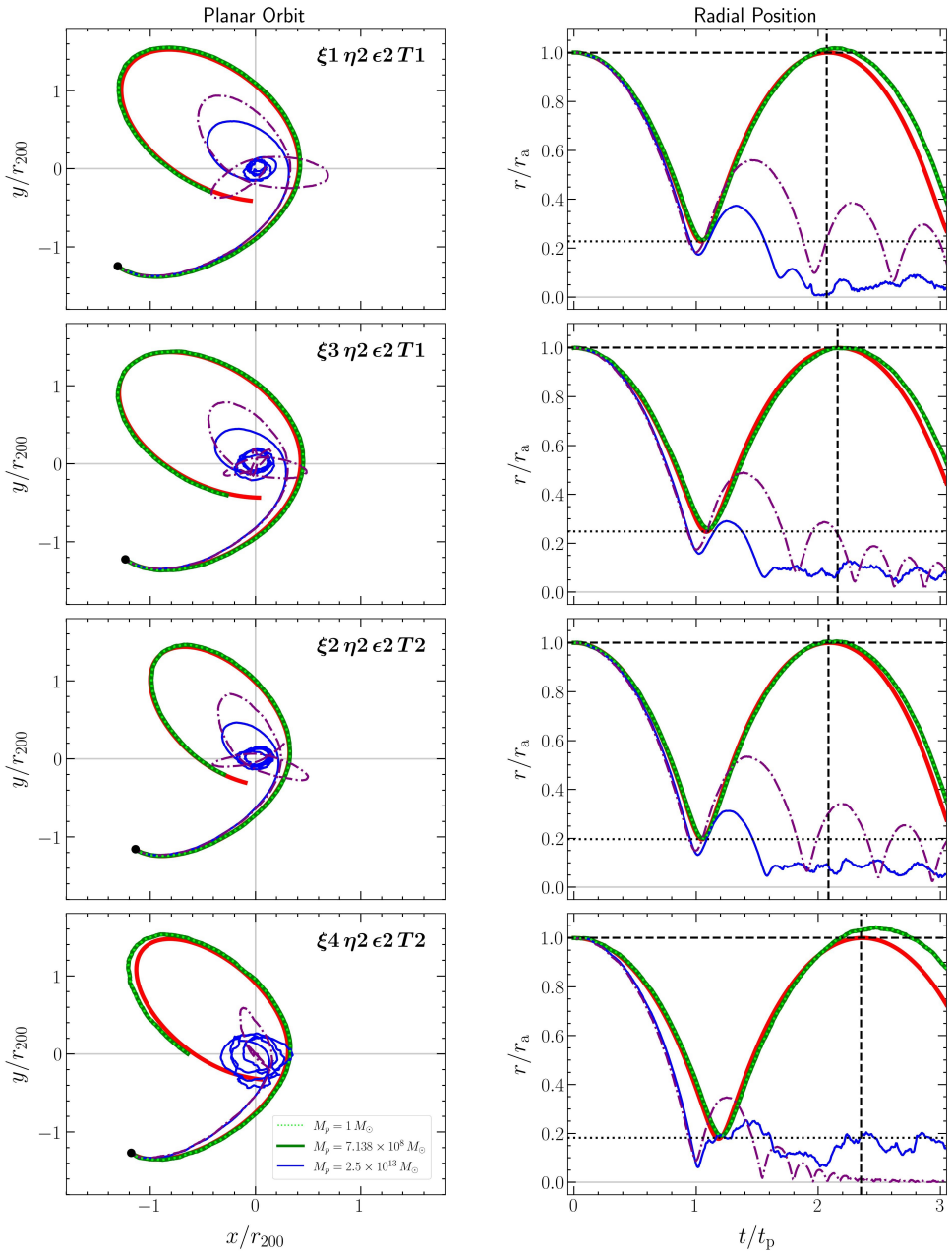



Figure A.6: Comparing the motion of the satellite in the orbital plane (left) and its radial separation from the central halo (right) during the merger. The coordinates of the orbit are shown relative to the virial radius of the central halo. Each curve considers a simulation with a different mass resolution. See the text for a detailed discussion.

## A.5 Measuring Changes in Structural Properties for Different Satellite Masses

In this work, our entire analysis and modeling relies on a satellite with one specific mass, $M_s = 2.5 \times 10^{13} M_\odot$. We chose this mass since we were interested in studying how mergers affect the measured properties of cluster halos. However, this was an arbitrary choice, and we could have selected a different mass scale. In this section, we investigate how the choice of satellite mass influences its orbit and the properties we measure for the remnant system in a set of simulations. Our results are shown in the plots below. Each curve considers a different mass for the satellite.

- *Solid lime line*: $M_s = 2.5 \times 10^{11} M_\odot$, galaxy scale central halos $M_c \sim 10^{12} M_\odot$.
- *Dashed teal line*: $M_s = 2.5 \times 10^{12} M_\odot$, group scale central halos $M_c \sim 10^{13} M_\odot$.
- *Dash-dotted purple line*: $M_s = 2.5 \times 10^{13} M_\odot$, cluster scale central halos $M_c \sim 10^{14} M_\odot$.

For a given simulation, the initial conditions ($\xi$, $v_r/v$, $v/v_{200}$) were kept identical to their default values (see Table 2.1) except we adjusted the mass per particle, $M_p$, used in the simulation to get the correct satellite mass (i.e. $M_p = M_s/N_t$). We also changed the concentrations of the two halos and their virial radii for their new masses to keep them consistent with cosmological values. Doing this will modify the length scale of the merger to its proper scale. Overall, we find the properties we measure for the satellite and remnant system are largely independent of the choice of satellite mass. There are some minor differences which we highlight below.

1. After the first apocentre, the radial separation of the satellite decays faster with decreasing satellite mass. Furthermore, the satellite experiences more precession in its orbit for lower mass satellites. Differences in the mass loss curves can be attributed to differences in the orbits.

2. The amplitude of the primary oscillations for the central halo and remnant scale radii increases with increasing satellite mass. The drop in scale radius after pericentre for the remnant system is larger for lower mass satellites.

3. Both the initial and final minor-to-major axis ratios for the remnant system decrease with decreasing satellite mass.

4. The initial spin of the remnant system increases with increasing satellite mass, except for when we have high mass ratio mergers (e.g. $\xi 4\, \eta 2\, \epsilon 2\, T2$).

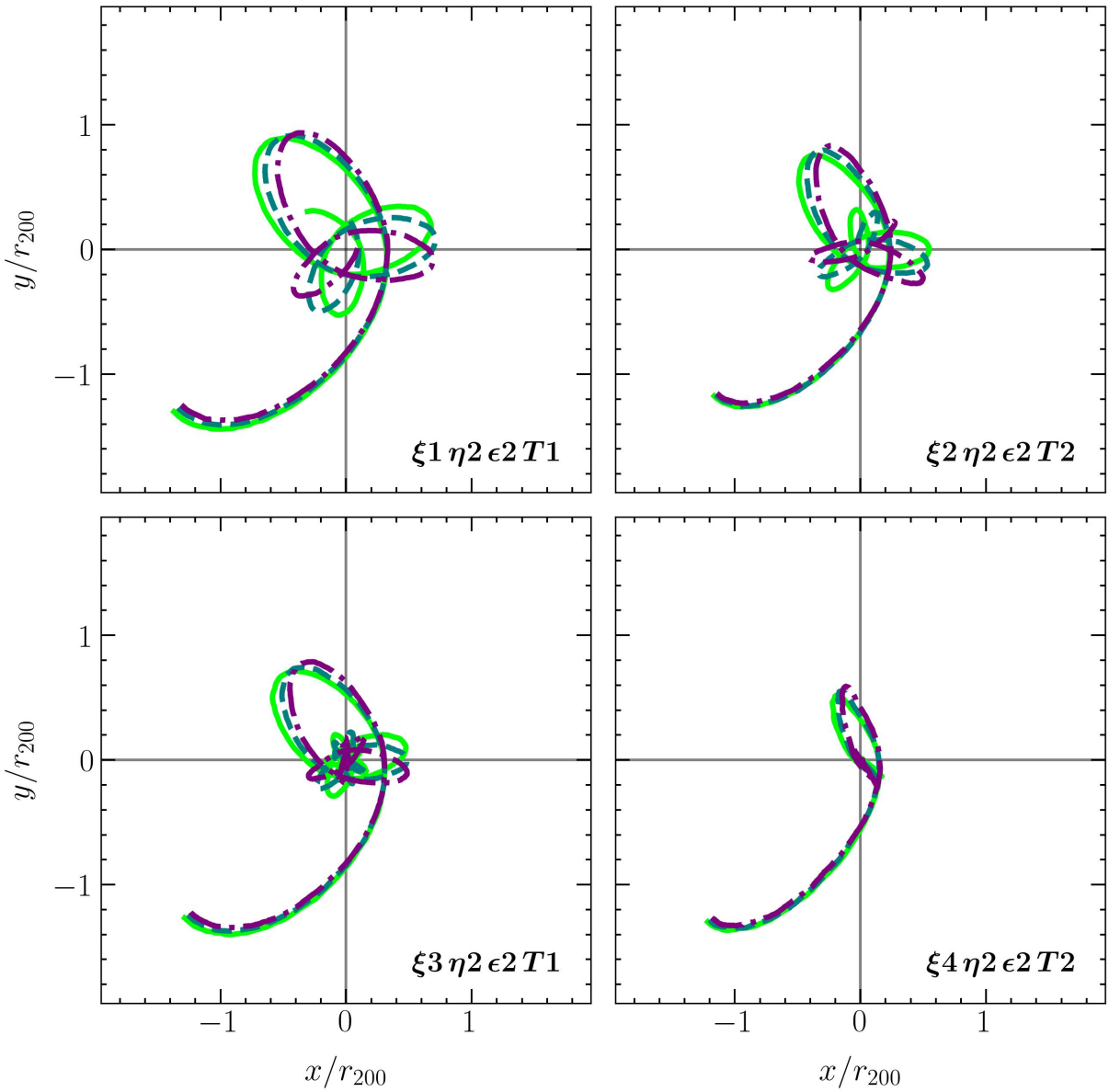



Figure A.7: Measured motion of the satellite in the orbital plane in simulations with different satellite masses.

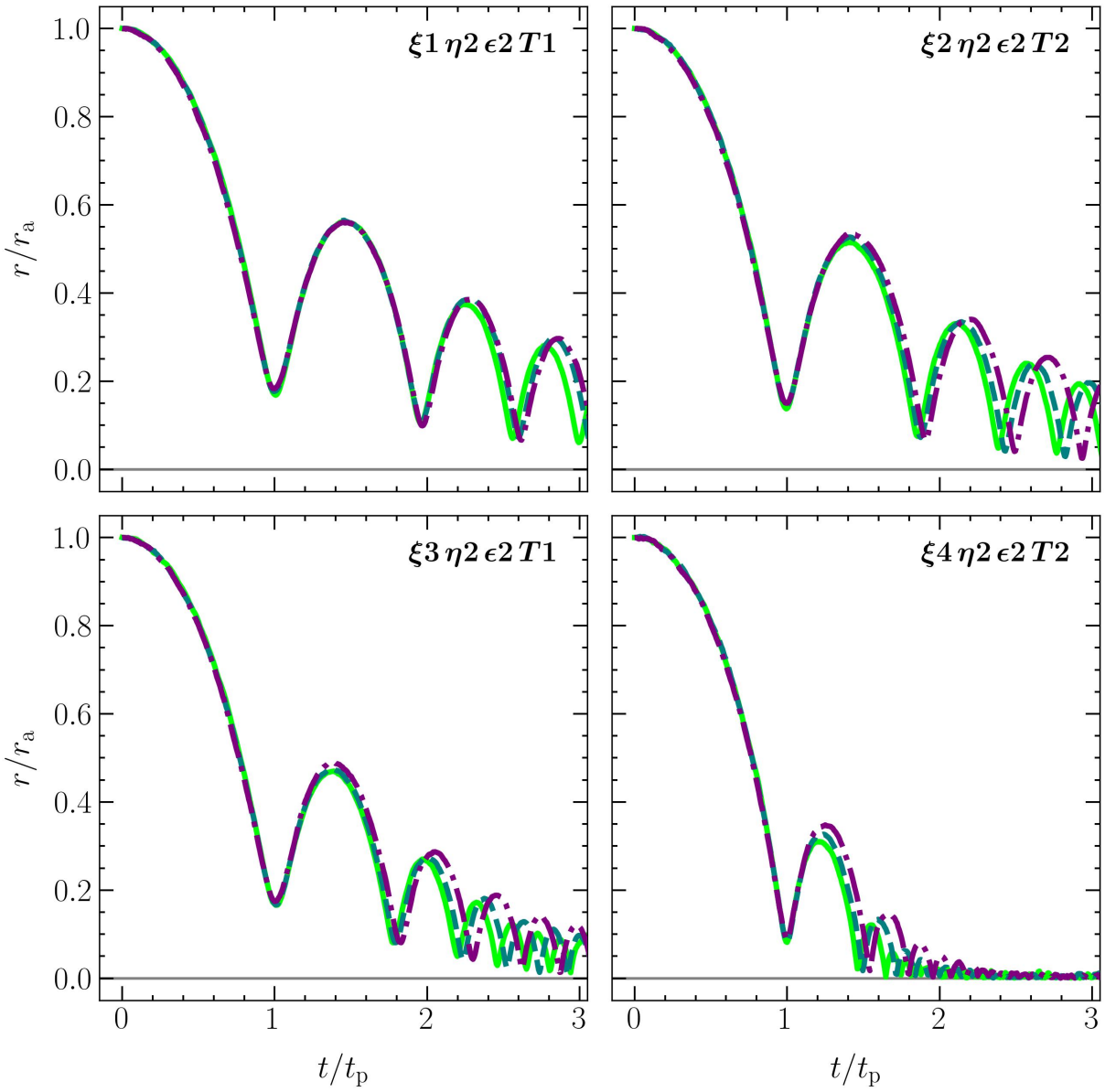



Figure A.8: Measured radial separation between the satellite and central halos' positions of highest local density in simulations with different satellite masses.

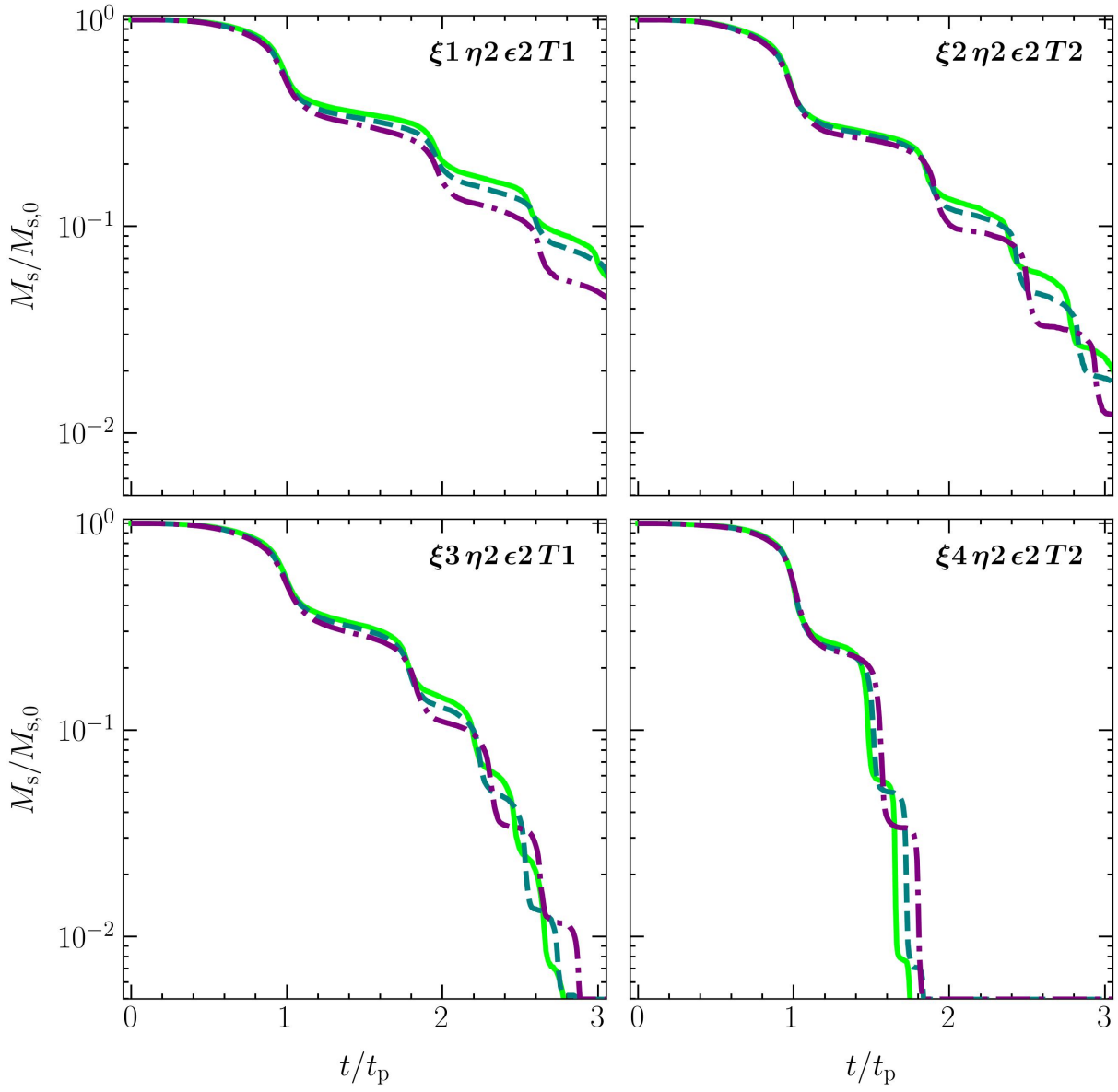



Figure A.9: Measured satellite mass loss in simulations with different satellite masses.

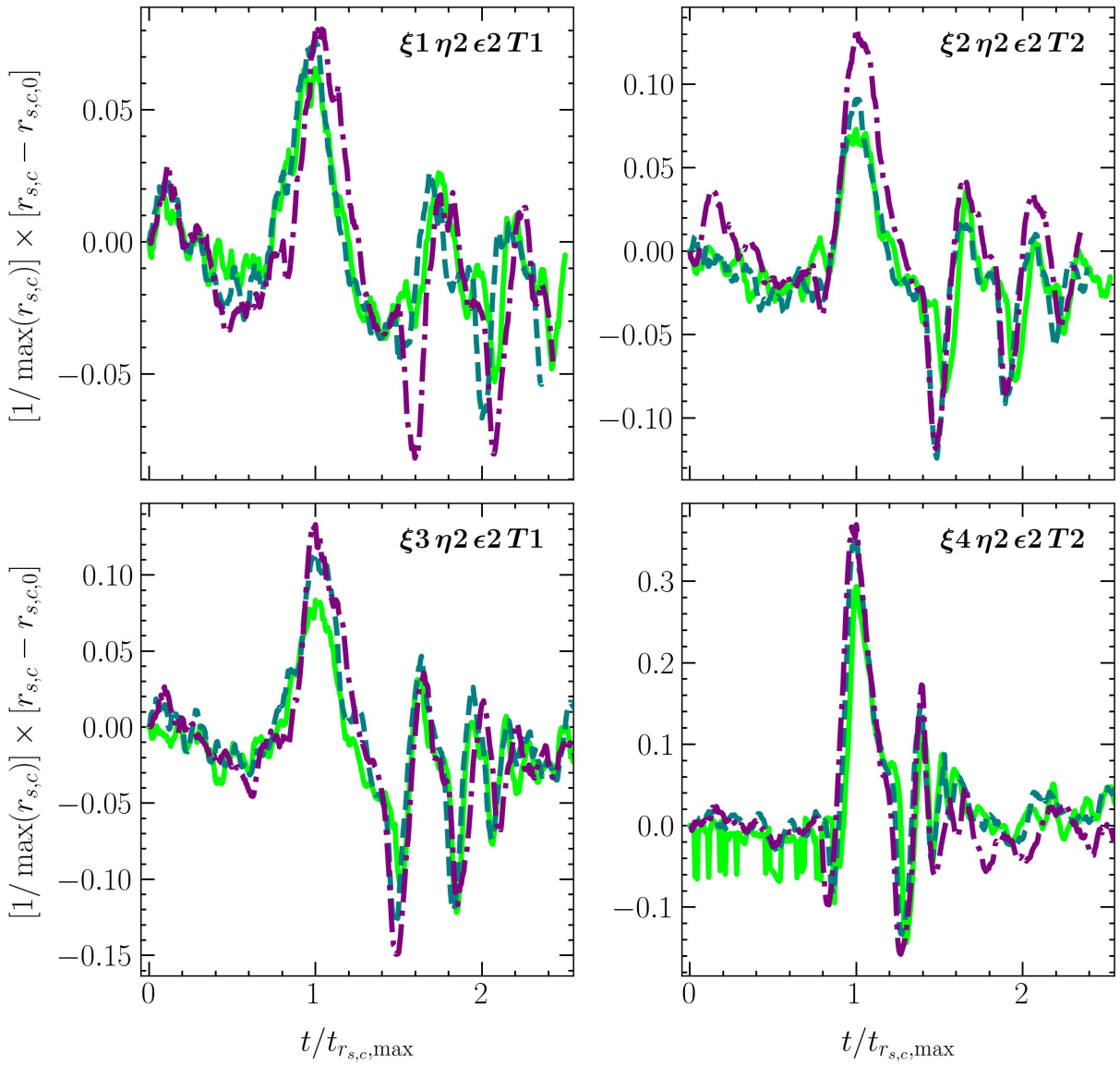



Figure A.10: Measured central halo scale radius in simulations with different satellite masses.

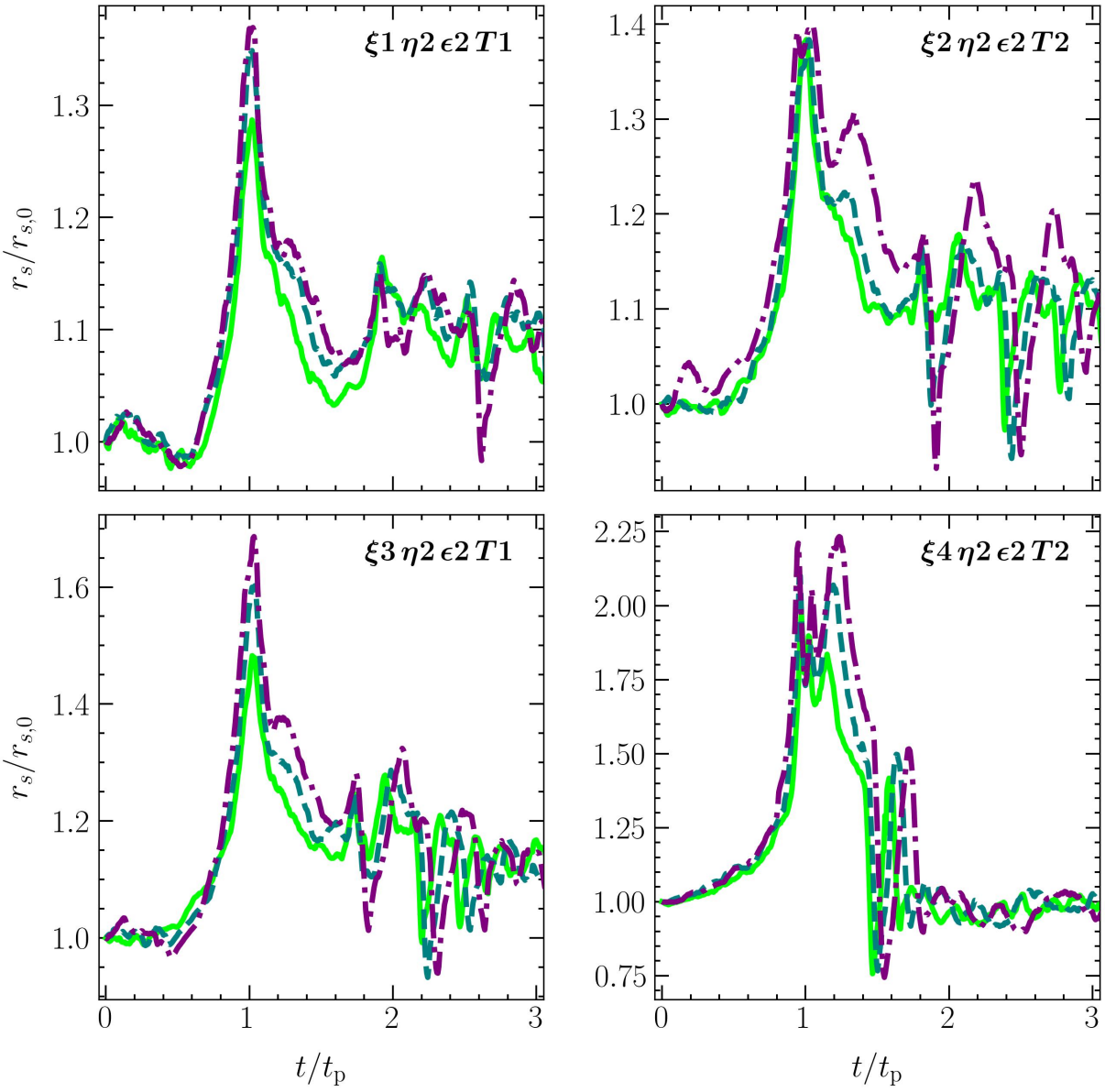



Figure A.11: Measured remnant system scale radius in simulations with different satellite masses.

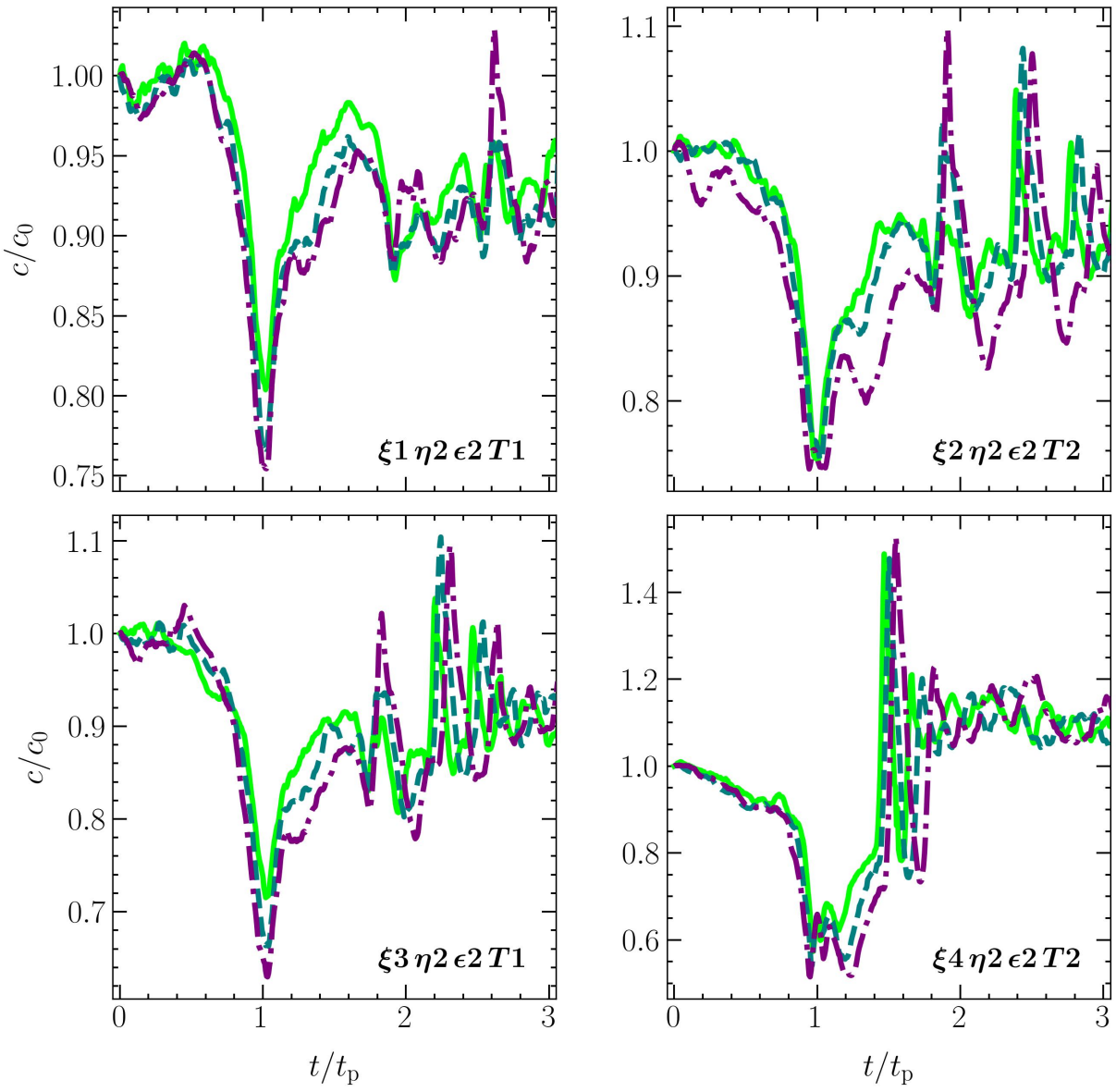



Figure A.12: Measured remnant system concentration in simulations with different satellite masses.

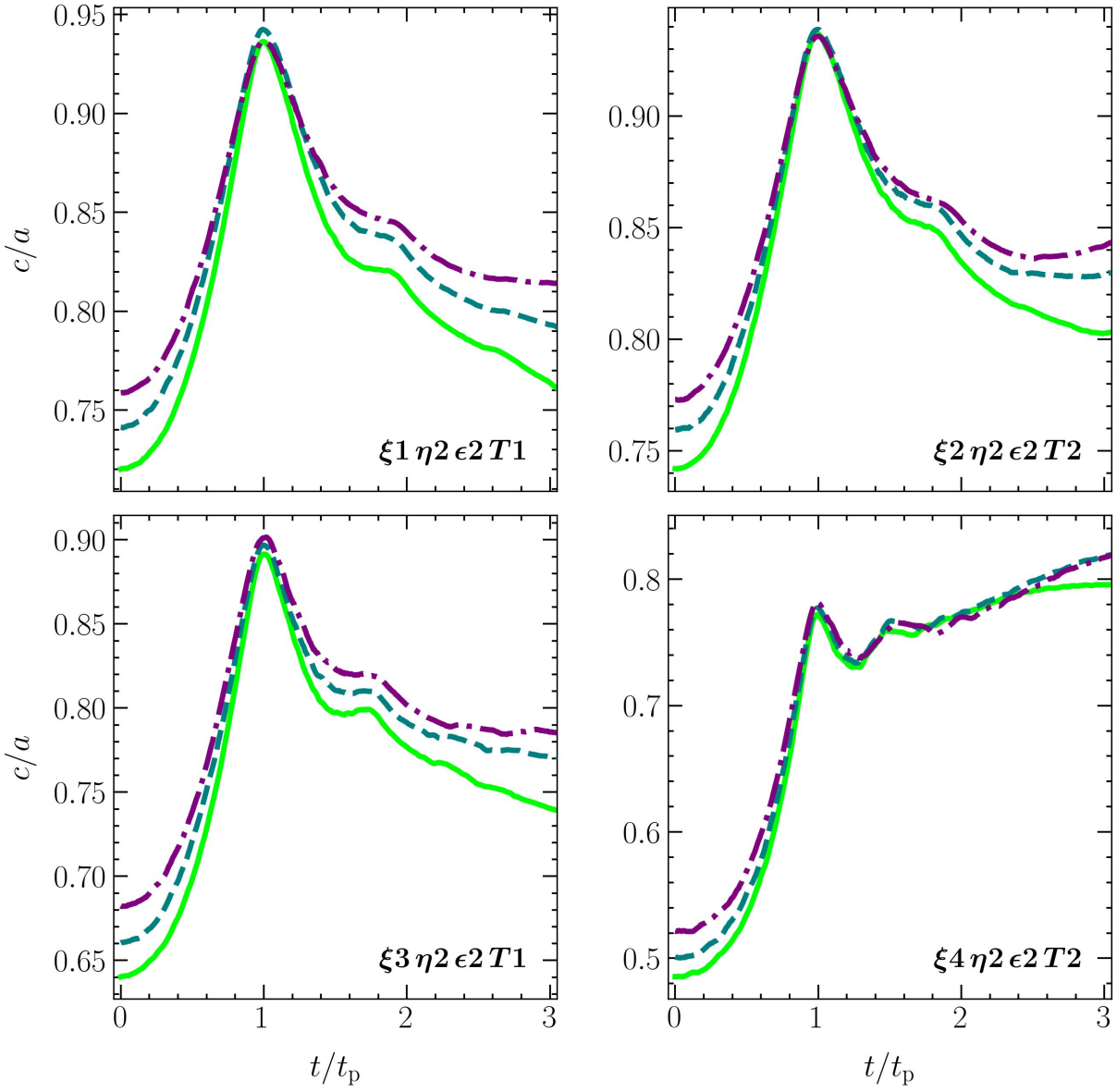



Figure A.13: Measured remnant system minor-to-major axis ratio in simulations with different satellite masses.

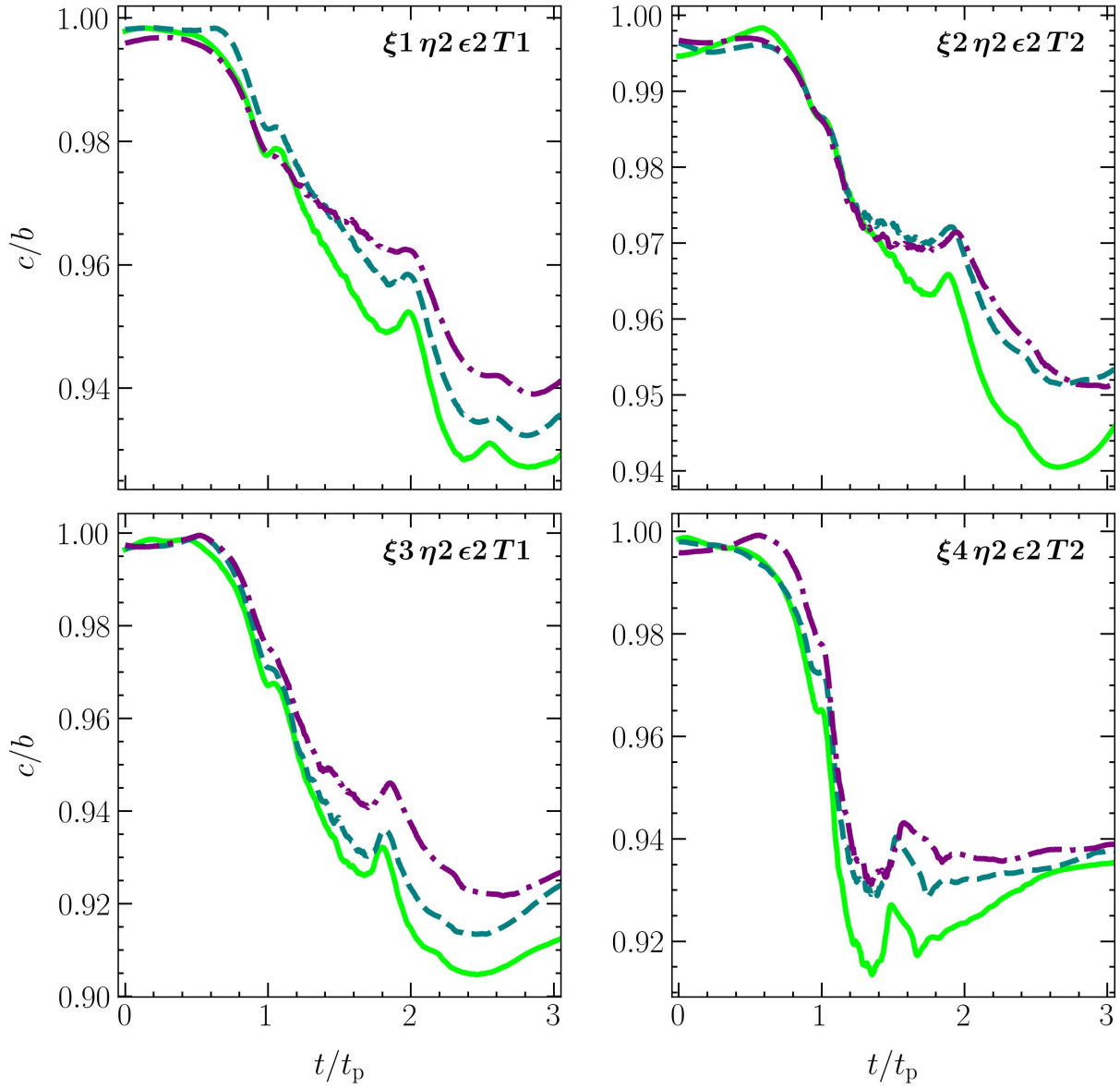



Figure A.14: Measured remnant system minor-to-intermediate axis ratio in simulations with different satellite masses.

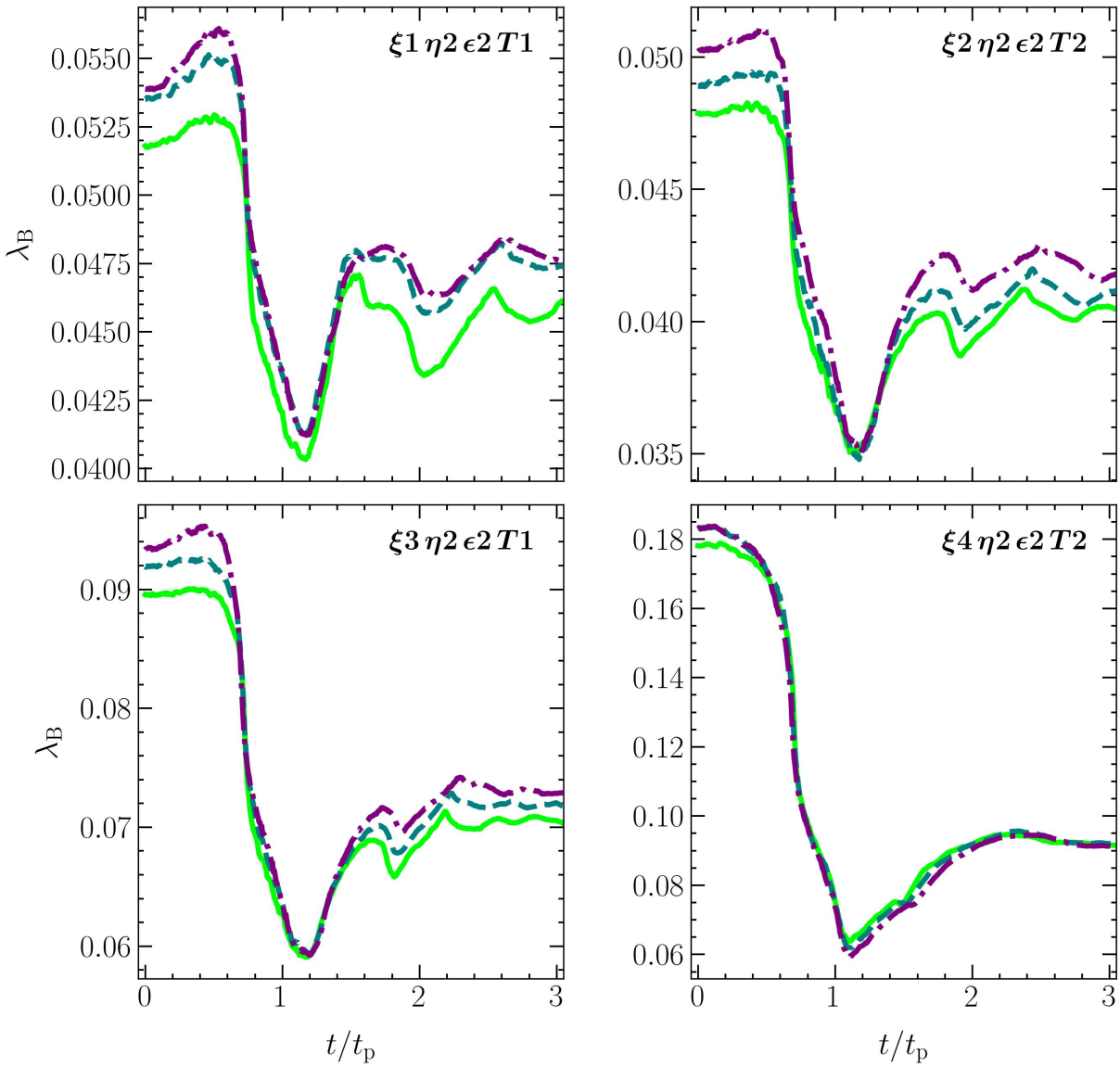



Figure A.15: Measured remnant system spin in simulations with different satellite masses.

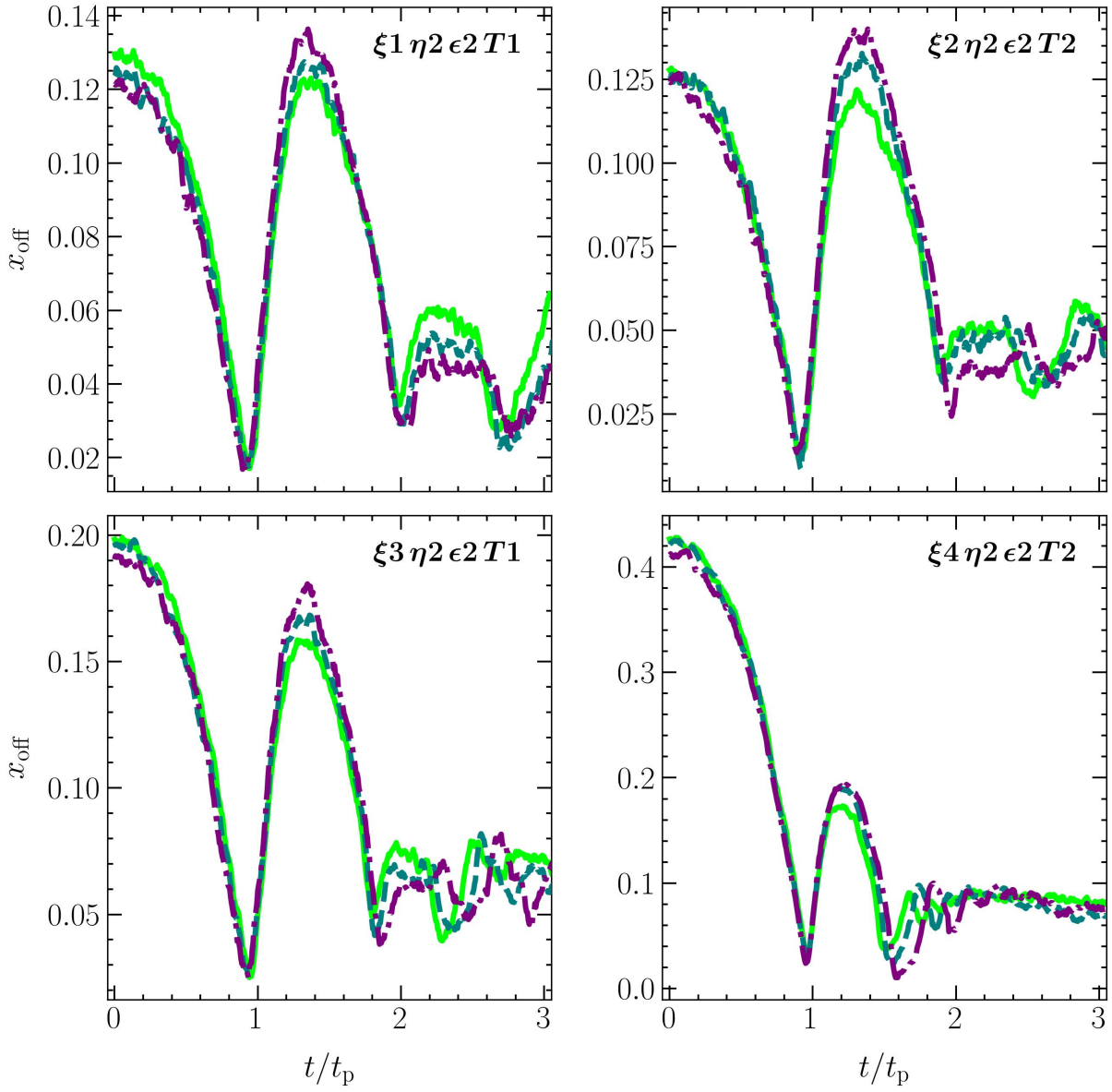



Figure A.16: Measured remnant system asymmetry in simulations with different satellite masses.

# Appendix B

# Supplemental Modeling Results

## B.1 Static Orbit in a Spherically Symmetric Potential

Suppose there exists a system consisting of a spherically symmetric gravitational field which is centrally directed, as is the case with an NFW potential. If a point mass is placed in this field, and its position with respect to the centre of the field is denoted by $\vec{r} = r\hat{r}$, then the equation of motion governing its orbit is,

$$\ddot{\vec{r}} = g(r)\hat{r} \tag{B.1}$$

where we use the radial acceleration on the point mass, $\vec{g} = g(r)\hat{r}$. From this result, we can show that the quantity $\vec{r} \times \dot{\vec{r}}$ is conserved.

$$\frac{d}{dt}\left(\vec{r} \times \dot{\vec{r}}\right) = \dot{\vec{r}} \times \dot{\vec{r}} + \vec{r} \times \ddot{\vec{r}} \tag{B.2}$$

$$\frac{d}{dt}\left(\vec{r} \times \dot{\vec{r}}\right) = \vec{0} + r\hat{r} \times g(r)\hat{r} \tag{B.3}$$

$$\frac{d}{dt}\left(\vec{r} \times \dot{\vec{r}}\right) = \vec{0} \tag{B.4}$$

where in the above we have used the identity $\vec{a} \times \vec{a} = \vec{0}$. Thus, we find that the angular momentum per unit mass, $\vec{L} \equiv \vec{r} \times \dot{\vec{r}}$, is constant. It is also perpendicular to the plane of motion, defined by the point mass's instantaneous position and velocity vectors. We can then conclude that the motion of the point mass is confined to this plane, the orbital

plane. This allows us to represent its orbit using simple planar polar coordinates $(r, \theta)$ in which the centre of the gravitational field is at $r = 0$ and $\theta$ is the azimuthal angle in the orbital plane. In these coordinates, we can calculate the magnitude of $\vec{L}$.

$$L_0 = \|\vec{r} \times \dot{\vec{r}}\| \tag{B.5}$$

$$L_0 = \|r\hat{r} \times (r\dot{\theta}\hat{\theta} + r\dot{\hat{r}})\| \tag{B.6}$$

$$L_0 = r^2\dot{\theta} \tag{B.7}$$

The orbit of the point mass in the plane can be derived using the Euler-Lagrange equations. In polar coordinates, the Lagrangian per unit mass is given by (see e.g. Binney & Tremaine, 2008, Appendix D.3),

$$\mathcal{L} = \frac{1}{2}\left[\dot{r}^2 + (r\dot{\theta})^2\right] - \Phi(r) \tag{B.8}$$

where $\Phi$ is the gravitational potential and $g(r) = -\frac{d\Phi}{dr}$. From the Lagrangian, the equations of motion for the point mass are,

$$0 = \frac{d}{dt}\frac{\partial \mathcal{L}}{\partial \dot{r}} - \frac{\partial \mathcal{L}}{\partial r} = \ddot{r} - r\dot{\theta}^2 + \frac{d\Phi}{dr} \tag{B.9}$$

$$0 = \frac{d}{dt}\frac{\partial \mathcal{L}}{\partial \dot{\theta}} - \frac{\partial \mathcal{L}}{\partial \theta} = \frac{d}{dt}(r^2\dot{\theta}) \tag{B.10}$$

where the second of these equations gives the same result as Eq. B.7. We can use this expression to relate derivatives of $t$ and $\theta$ since it implies,

$$\frac{d}{dt} = \frac{L_0}{r^2}\frac{d}{d\theta} \tag{B.11}$$

and the equation of motion for $r$ becomes,

$$0 = \frac{d}{dt}\left(\frac{dr}{dt}\right) - r\left(\frac{d\theta}{dt}\right)^2 + \frac{d\Phi}{dr} \tag{B.12}$$

$$0 = \frac{L_0}{r^2}\frac{d}{d\theta}\left(\frac{L_0}{r^2}\frac{dr}{d\theta}\right) - r\left(\frac{L_0}{r^2}\right)^2 + \frac{d\Phi}{dr} \tag{B.13}$$

$$0 = \frac{L_0^2}{r^2}\frac{d}{d\theta}\left(\frac{1}{r^2}\frac{dr}{d\theta}\right) - \frac{L_0^2}{r^3} + \frac{d\Phi}{dr} \tag{B.14}$$

This equation can be simplified with the substitution $u = \frac{1}{r}$ putting it into the form,

$$0 = u^2 L_0^2 \frac{d}{d\theta}\left(-\frac{du}{d\theta}\right) - u^3 L_0^2 - u^2 \frac{d\Phi}{du} \tag{B.15}$$

$$0 = \frac{d^2u}{d\theta^2} + u + \frac{1}{L_0^2}\frac{d\Phi}{du} \tag{B.16}$$

where we used the result $du = -\frac{1}{r^2}dr$. This expression has two types of solutions: unbound orbits as $r \to \infty$ and hence $u \to 0$, and bound orbits where $r$ and $u$ oscillate between finite limits. This expression is related to another conserved quantity if we multiply it by $\frac{du}{d\theta}$.

$$\frac{d}{d\theta}\left[\left(\frac{du}{d\theta}\right)^2 + \frac{2\Phi}{L_0^2} + u^2\right] = 2\frac{du}{d\theta}\frac{d^2u}{d\theta^2} + \frac{2}{L_0^2}\frac{d\Phi}{du}\frac{du}{d\theta} + 2u\frac{du}{d\theta} \tag{B.17}$$

$$\frac{d}{d\theta}\left[\left(\frac{du}{d\theta}\right)^2 + \frac{2\Phi}{L_0^2} + u^2\right] = 2\frac{du}{d\theta}\left(\frac{d^2u}{d\theta^2} + \frac{1}{L_0^2}\frac{d\Phi}{du} + u\right) \tag{B.18}$$

$$\frac{d}{d\theta}\left[\left(\frac{du}{d\theta}\right)^2 + \frac{2\Phi}{L_0^2} + u^2\right] = 0 \tag{B.19}$$

where in the last expression we used the result of Eq. B.16. Thus, we find that,

$$\left(\frac{du}{d\theta}\right)^2 + \frac{2\Phi}{L_0^2} + u^2 \equiv \frac{2E_0}{L_0^2} \tag{B.20}$$

is constant, where $E_0 = \frac{1}{2}\left(\dot{r}^2 + r^2\dot{\theta}^2\right) + \Phi(r)$ is the energy of the orbit per unit mass. For bound orbits, we have that $\frac{du}{d\theta} = 0$ and the above expression simplifies to,

$$u^2 + \frac{2}{L_0^2}\left(\Phi - E_0\right) = 0 \tag{B.21}$$

This expression normally has two roots $u_p$ and $u_a$ between which the point mass oscillates radially as it revolves in $\theta$. As a result, the orbit of the point mass is confined between an inner radius $r_p = u_p^{-1}$ known as **pericentre** and an outer radius $r_a = u_a^{-1}$ known as **apocentre**. For a circular orbit, these two values are equal.

The radial orbital period, $t_r$, describes the time required for the point mass to travel from apocentre to pericentre and back again. To calculate this, we use Eq. B.11 to

eliminate $d\theta$ from Eq. B.20.

$$\frac{2E_0}{L_0^2} = \left(-\frac{1}{r^2}\frac{r^2}{L_0}\frac{dr}{dt}\right)^2 + \frac{2\Phi(r)}{L_0^2} + \left(\frac{1}{r}\right)^2 \tag{B.22}$$

$$2E_0 = \dot{r}^2 + 2\Phi(r) + \frac{L_0^2}{r^2} \tag{B.23}$$

$$\dot{r} = \sqrt{2\left[E_0 - \Phi(r)\right] - \frac{L_0^2}{r^2}} \tag{B.24}$$

If we compare this expression to Eq. B.21, we find that $\dot{r} = 0$ at the pericentre and apocentre radii, $r_p$ and $r_a$, as it should. It then follows that the radial orbital period is,

$$t_r = 2\int_{r_p}^{r_a} \frac{dr}{\sqrt{2\left[E_0 - \Phi(r)\right] - \frac{L_0^2}{r^2}}} \tag{B.25}$$

and the time to pericentre is $t_p = \frac{t_r}{2}$. As the point mass completes a full orbit, the azimuthal angle increases by an amount,

$$\Delta\theta = 2\int_{r_p}^{r_a} \frac{d\theta}{dr}dr = 2\int_{r_p}^{r_a} \frac{L_0}{r^2}\frac{dt}{dr}dr \tag{B.26}$$

$$\Delta\theta = 2L_0\int_{r_p}^{r_a} \frac{dr}{r^2\sqrt{2\left[E_0 - \Phi(r)\right] - \frac{L_0^2}{r^2}}} \tag{B.27}$$

leading to precession in the orbit in a direction opposite to the rotation of the point mass. The precession rate is given by,

$$\Omega_p = \frac{\Delta\theta - 2\pi}{t_r} \tag{B.28}$$

If we were in a frame co-rotating with the point mass at an angular velocity $\Omega_p$, the orbit would appear as a closed ellipse. Finally, we can convert our coordinates into Cartesian coordinates using,

$$x = r\cos(\theta) \qquad \dot{x} = \dot{r}\cos(\theta) - r\dot{\theta}\sin(\theta) \tag{B.29}$$

$$y = r\sin(\theta) \qquad \dot{y} = \dot{r}\sin(\theta) + r\dot{\theta}\cos(\theta) \tag{B.30}$$

assuming that the orbital plane coincides with the $xy$-plane.

## B.2 Testing Integration Schemes for Evaluating Ordinary Differential Equations (ODEs)

Our model for the isolated merger between dark matter halos involves a satellite halo orbiting and infalling towards a central halo. The equations of motion for this two halo system do not have a closed-form analytic solution. Thus, the differential equations describing the motion need to be integrated numerically. This section explores several integrators on a simple test case to determine a suitable integrator to be used in evaluating our model.

For this test, we consider a point mass, orbiting in a static, extended distribution as discussed in Appendix B.1. In Cartesian coordinates, the equations of motion for the point mass are,

$$\ddot{\vec{x}} = -\frac{\partial \Phi}{\partial \vec{x}} \tag{B.31}$$

where $\vec{x} = (x, y, z)$ is the 3D position of the point mass, and $\Phi(\vec{x})$ is the potential of the extended distribution. Several potentials including the homogeneous sphere, harmonic, isochrone, and NFW potential (see e.g. Binney & Tremaine, 2008, Section 2.2) were tested and yielded similar results. However, in this section, we only present results for the NFW distribution since this distribution is closest to the one used in our model. For an NFW potential, the equations of motion for the point mass become,

$$\ddot{\vec{x}} = -4\pi G \rho_0 \left(\frac{r_s}{r}\right)^3 \left[\ln\left(1 + \frac{r}{r_s}\right) - \frac{r/r_s}{1 + r/r_s}\right] \vec{x} \tag{B.32}$$

We will test each integrator by numerically solving for the orbit of the point mass defined by these equations of motion. Suppose we have an initial value problem for a system of ODEs:

$$\dot{\vec{y}} = \vec{f}(t, \vec{y}), \qquad \vec{y} = \vec{y}_0 \tag{B.33}$$

where $t$ is an independent variable and $\vec{y}$ is an $n \times D$ vector dependent variable. The ODEs are characterized by the $n \times D$ dynamics function $\vec{f}(t, \vec{y})$. The simplest integrator to solve this problem is described by Euler's method (Burden & Faires, 2010).

$$\vec{y}_{n+1} = \vec{y}_n + h\vec{f}(t, \vec{y}), \qquad t_{n+1} = t_n + h \tag{B.34}$$

where $h$ is the step size between integration steps. Typically, the accuracy of each integration scheme is accessed by its local and global error. The local error describes the difference between the solution curve through the $n^{\text{th}}$ point and the estimate from the ODE method, while the global error measures the difference between the exact solution at the $n^{\text{th}}$ point

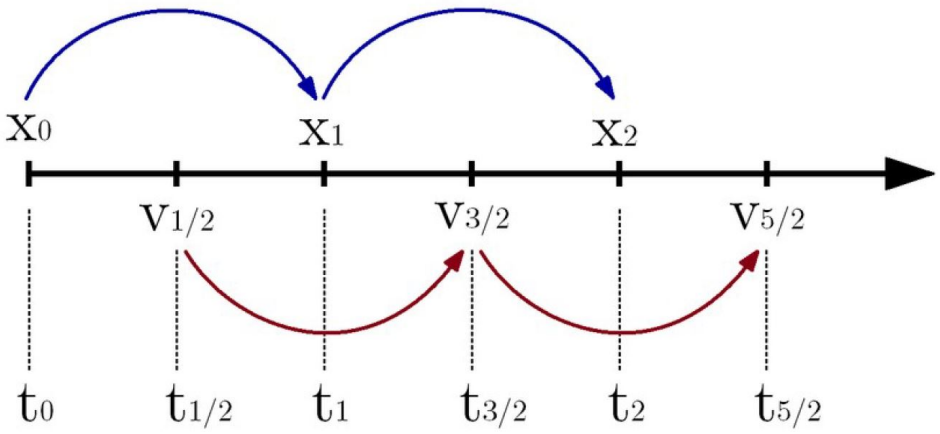



Figure B.1: Schematic illustrating the leapfrog integration scheme.

and the estimate from the ODE method. For Euler's method, the local and global errors are $\mathcal{O}(h^2)$ and $\mathcal{O}(h)$, respectively (Burden & Faires, 2010).

The most commonly used higher order integration schemes are the so-called Runge-Kutta (RK) methods. These integrators differ from Euler's method by using several evaluations of $\vec{f}$ at different points between $t_n$ and $t_{n+1}$. For example, Heun's method uses 2 slope evaluations, while RK4 uses 4 slope evaluations (Burden & Faires, 2010). The number of slope evaluations is related to the local and global errors of a particular method. For example, suppose that a Runge-Kutta method evaluates the slope $q$ times. Then, the corresponding local and global errors for the method are $\mathcal{O}(h^{q+1})$ and $\mathcal{O}(h^q)$, respectively (Burden & Faires, 2010). Note that adaptive time step versions of Runge-Kutta methods exist that attempt to limit the local error to a fixed tolerance. The idea here is to take as large a time step as possible that keeps the local error just smaller than the tolerance. The advantage of this is that fewer dynamics function evaluations are required for integration, which depending on the problem, could substantially decrease the integration time required while preserving accuracy.

A different class of higher order integration schemes are the Leapfrog methods. These methods involve updating the positions and velocities of the particles in the dynamical system studied. The second-order version of Leapfrog uses Heun's method to get the first midpoint between $\vec{y}_0$ and $\vec{y}_1$,

$$\vec{y}_{1/2} = \vec{y}_0 + \frac{h}{2}\vec{f}\left(t_0 + \frac{h}{4}, \vec{y}_0 + \frac{h}{4}\vec{f}(t_0, \vec{y}_0)\right) \tag{B.35}$$

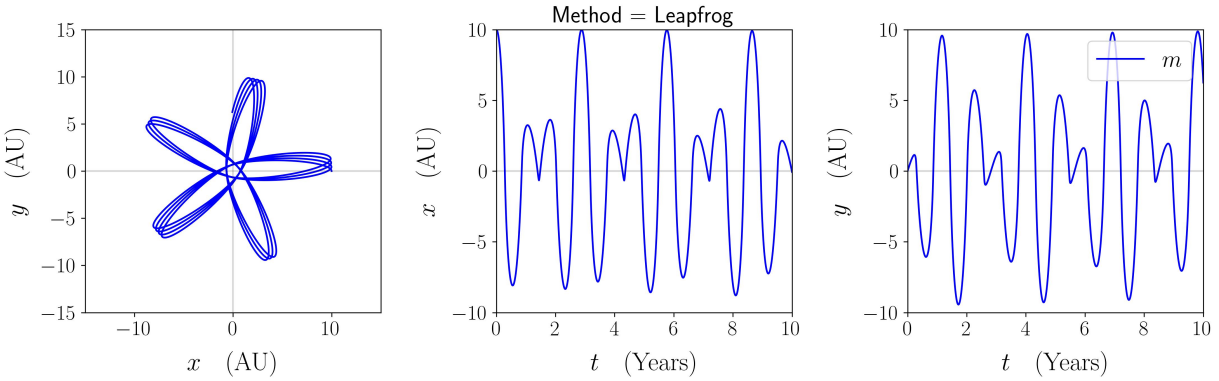



Figure B.2: Motion of a point mass in an NFW potential where its equations of motion were evaluated using Leapfrog integration.

Then, given the initial conditions and the midpoint $\vec{y}_{1/2}$, the Leapfrog method is described by the following equations (Newman, 2013):

$$\vec{y}_{n+1} = \vec{y}_n + h\vec{f}(t_{n+1/2}, \vec{y}_{n+1/2}), \qquad t_{n+1} = t_n + h \tag{B.36}$$

$$\vec{y}_{n+3/2} = \vec{y}_{n+1/2} + h\vec{f}(t_{n+1}, \vec{y}_{n+1}), \qquad t_{n+1/2} = t_n + \frac{h}{2} \tag{B.37}$$

The local and global errors for the Leapfrog method are $\mathcal{O}(h^3)$ and $\mathcal{O}(h^2)$, respectively. There are two distinct advantages to Leapfrog integration when applied to mechanics problems like orbits (Newman, 2013). The first is time-reversibility. If we forward integrate to a certain point along the orbit and then backwards integrate from that point, we will arrive back at the same starting position. The second is integrals of motion are bounded. The consequence of this is orbital quantities that are conserved remain conserved as the orbit evolves. This characteristic of the Leapfrog method is not found in the Runge-Kutta methods, where the values of integrals of motion can drift substantially over time.

To determine which integrator should be used to evaluate our model, we test the accuracy of each integration scheme by solving the equations of motion defined by Eq. B.32. An example of the resulting orbit of the point mass is shown in Fig. B.2. The accuracy of a given method will be accessed by examining the integrals of motion for the orbit. For a static spherical potential, the orbital energy and angular momentum of the point mass should be conserved. However, due to inaccuracies in the integration methods when updating the position and velocity of the point mass, the integrals of motion are only approximately conserved as the orbit evolves. The amount by which these quantities vary from their initial values will be our test of accuracy.

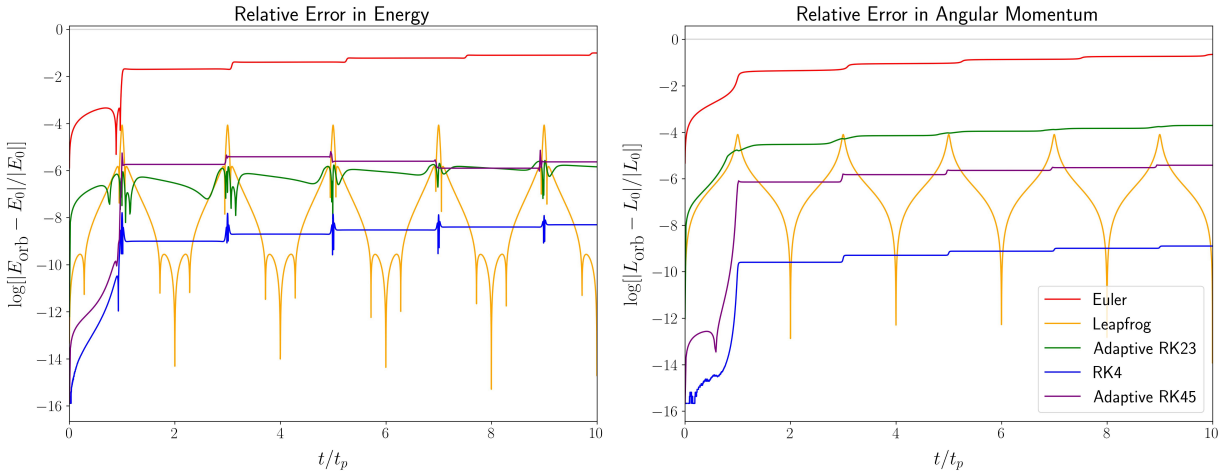



Figure B.3: Relative change in orbital energy (left) and angular momentum (right) for the point mass orbiting in an NFW potential calculated using various integration schemes.

Fig. B.3 illustrates the relative change in the orbital energy and angular momentum of the point mass as it orbits in an NFW potential, tested for several integration schemes. The five integrators we tested are as follows: (1) Euler's method, (2) Leapfrog method, (3) Adaptive RK23, (4) RK4, and (5) Adaptive RK45. After the point mass undergoes many orbits, we find that Euler's method has the worst accuracy, while RK4 has the best accuracy. The change in both integral of motions increases with every subsequent orbit for all integrators except for the Leapfrog method. For this method, the relative errors are bounded between maximum and minimum values. The maximum error occurs at the orbit's pericentre, while the minimum error occurs at the orbit's apocentre.

The results of this test indicate that the **Leapfrog method** should be the integration scheme we use. There are several advantages to this method. First, the error is bounded between a maximum and minimum value unlike the other methods tested, which should lead to a stable model. In addition, this integrator provides a good mixture of evaluation time and accuracy. The average error for the Leapfrog method is on the order of the Adaptive RK45 method, while its maximum error is roughly 0.01%, which is accurate enough for our purposes. Furthermore, the Leapfrog method requires fewer dynamics function evaluations than the Runge-Kutta methods. This is ideal since the dynamics function in our model can be expensive to evaluate, so the fewer times this is necessary the better. These advantages make the Leapfrog method the most suitable choice to evaluate our model.

## B.3 Rejection Sampling to Generate NFWT Profiles

In our model, we use particle realizations of the satellite and central halo to model the structural properties of the remnant system. Since the NFWT distribution cannot be inverted simply, rejection sampling of particles from an NFW distribution is used to sample our halos. We use the results from Robotham & Howlett (2018), where the authors implemented an efficient routine to sample particles from an NFW distribution given its model parameters ($r_s$, $\rho_0$) and a cutoff radius, $r_t$. Here they apply the standard technique of generating samples from a uniform distribution, finding where the sample sits on the cumulative distribution function (CDF), and inverting the CDF to obtain the random variate. In this case, the CDF is the enclosed mass distribution of the halo truncated at the cutoff radius.

Given samples from an NFW distribution, we can use rejection sampling to generate particles from an NFWT distribution. Suppose $f(r)$ is our target distribution and $q(r)$ is our sampling distribution. The idea behind rejection sampling is to sample points from $q(r)$ and apply some rejection criterion such that the samples we accept are distributed according to $f(r)$. Furthermore, this technique requires that our sampling distribution "covers" or envelops the target distribution, which is true in our case. The CDF of each distribution is the enclosed mass profile which indicates that the probability density functions (PDFs) are just the first derivative of the CDFs,

$$f(r) = 4\pi r^2 \frac{\rho(r)}{M(< r_t)} \qquad\qquad q(r) = 4\pi r^2 \frac{\rho_{\rm NFW}(r)}{M_{\rm NFW}(< r_t)} \tag{B.38}$$

Suppose we want to generate a halo with $N$ particles. The procedure for rejection sampling works as follows:

1. Generate a sample of particles with radii $r_i$ from an NFW distribution using the method in Robotham & Howlett (2018).
2. For the generated particles, calculate the PDFs $f(r_i)$ and $q(r_i)$. These are the NFWT and NFW distributions, respectively.
3. Apply the rejection sampling criterion. Particles are accepted if $u < \frac{f(r_i)}{c\, q(r_i)}$ and rejected otherwise, where $u \sim \text{Unif}[0, 1]$ is the uniform distribution and $c = \max\left(\frac{f(r_i)}{q(r_i)}\right)$.
4. Iterate this procedure until we have generated $N$ particles.

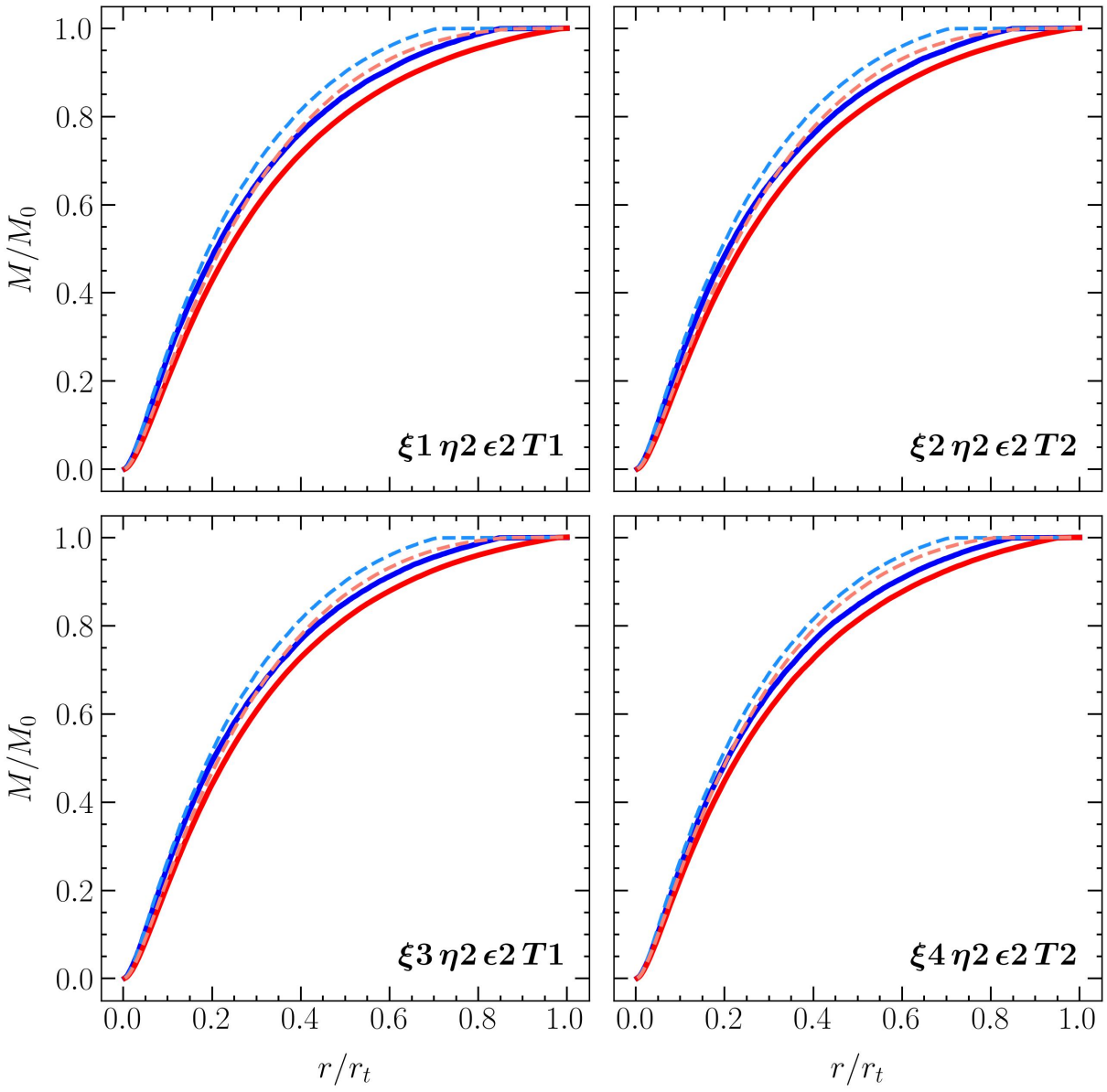



Figure B.4: Initial cumulative mass profiles of the satellite (blue) and central halo (red). The darker, solid lines represent the profiles used to model the remnant system structural properties, generated through rejection sampling. The lighter, dashed lines represent the profiles extracted directly from the simulation snapshots, generated using ICICLE. The radial position is shown relative to the truncation radius of the profile.

This will sample radii for each particle where the overall collection of particles follows an NFWT distribution. We then need to generate random angles for every particle to give them a 3D position. The angles are sampled from the following distributions.

$$\theta = 2\pi u \qquad\qquad \phi = \cos^{-1}(2u - 1) \tag{B.39}$$

These can then be converted into Cartesian coordinates using the transformation,

$$[x,\, y,\, z] = [r\sin(\phi)\cos(\theta),\, r\sin(\phi)\sin(\theta),\, r\cos(\phi)] \tag{B.40}$$

Fig. B.4 demonstrates how the initial mass profiles of the satellite and central halo generated using rejection sampling compare to their profiles generated in ICICLE, for a set of simulations. We find that the initial halos in the simulations are more compact than the initial halos we generate in our model. This is caused by the approximate nature of the NFWT profile. The truncation procedure applied by ICICLE is only approximated by the NFWT profile, whereas rejection sampling will generate the NFWT profile exactly given its model parameters ($r_s$, $\rho_0$, $y$). This difference has consequences for the initial values of some remnant properties in our model. In particular, since the halos created in our model are broader, the initial concentration and minor-to-major axis ratio, $c/a$, are generally slightly higher than that in the simulations.

## B.4 Model Predictions for the Fiducial Simulations

Our model predicts many properties for the satellite, its orbit, and the remnant system. In this section, we summarize our results by plotting all properties for every simulation in the fiducial set. From top to bottom, left to right, each subplot in a given figure below shows: (1) the satellite orbit, (2) the satellite radial separation, (3) the satellite mass loss, (4) the central halo scale radius, (5) the remnant scale radius, (6) the remnant concentration, (7) the remnant minor-to-major axis ratio, (8) the remnant minor-to-intermediate axis ratio, and (9) the remnant asymmetry. Simulation measurements are shown as purple dash-dotted lines. The other curves in the plots consider different versions of the model.

- *Dashed blue line*: the model neglects the central halo response and the orbital model parameters ($\gamma$, $\ln(\Lambda)$, $B$) are tuned directly using the simulation output.
- *Dotted yellow line*: the model includes the central halo response and the orbital model parameters ($\gamma$, $\ln(\Lambda)$, $B$) are tuned directly using the simulation output.
- *Solid green line*: the model includes the central halo response and the orbital model parameters ($\gamma$, $\ln(\Lambda)$, $B$) are predicted using the XGBoost model.

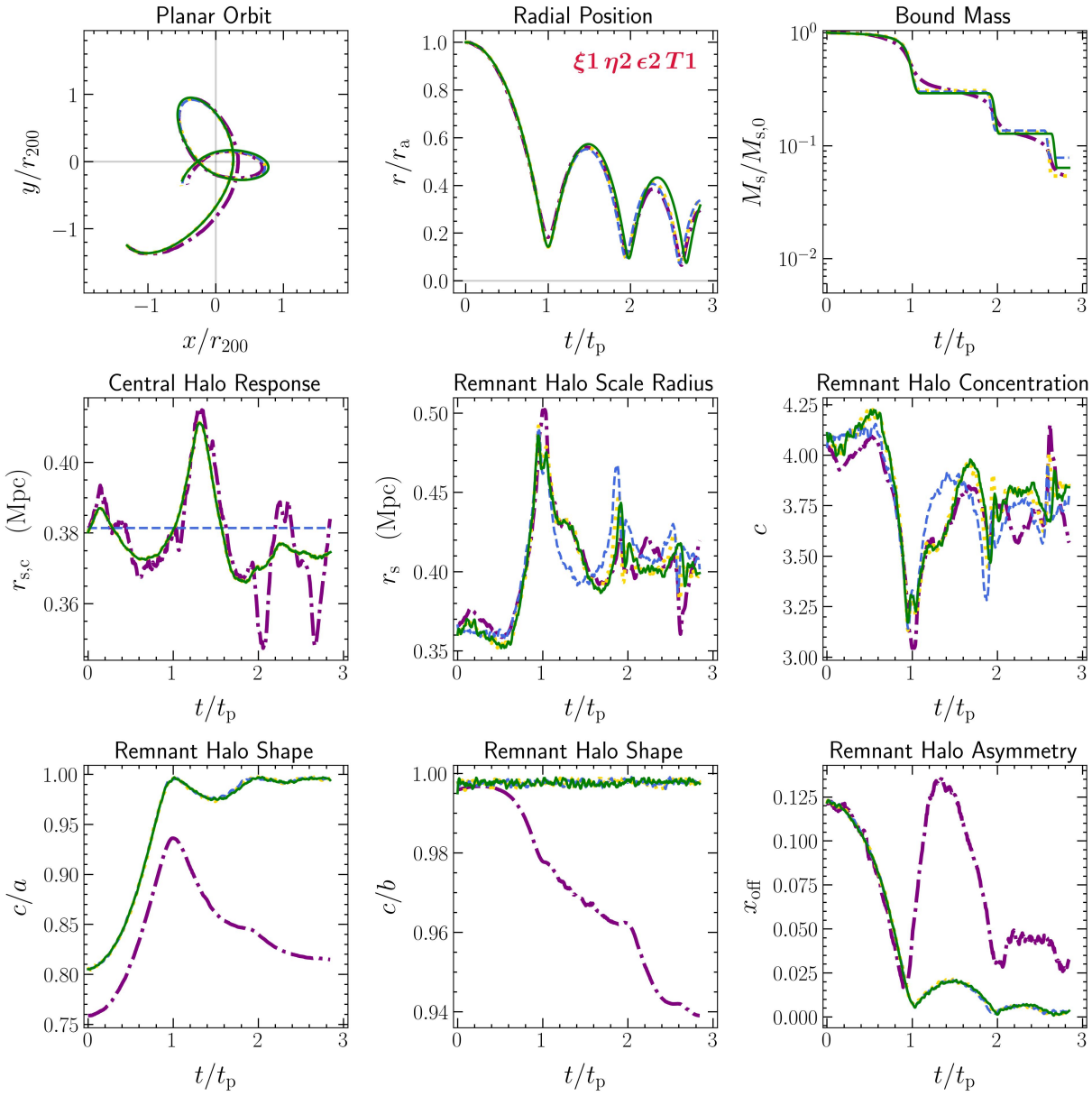



Figure B.5: Model predictions for all properties in the simulation $\xi 1\,\eta 2\,\epsilon 2\,T1$.

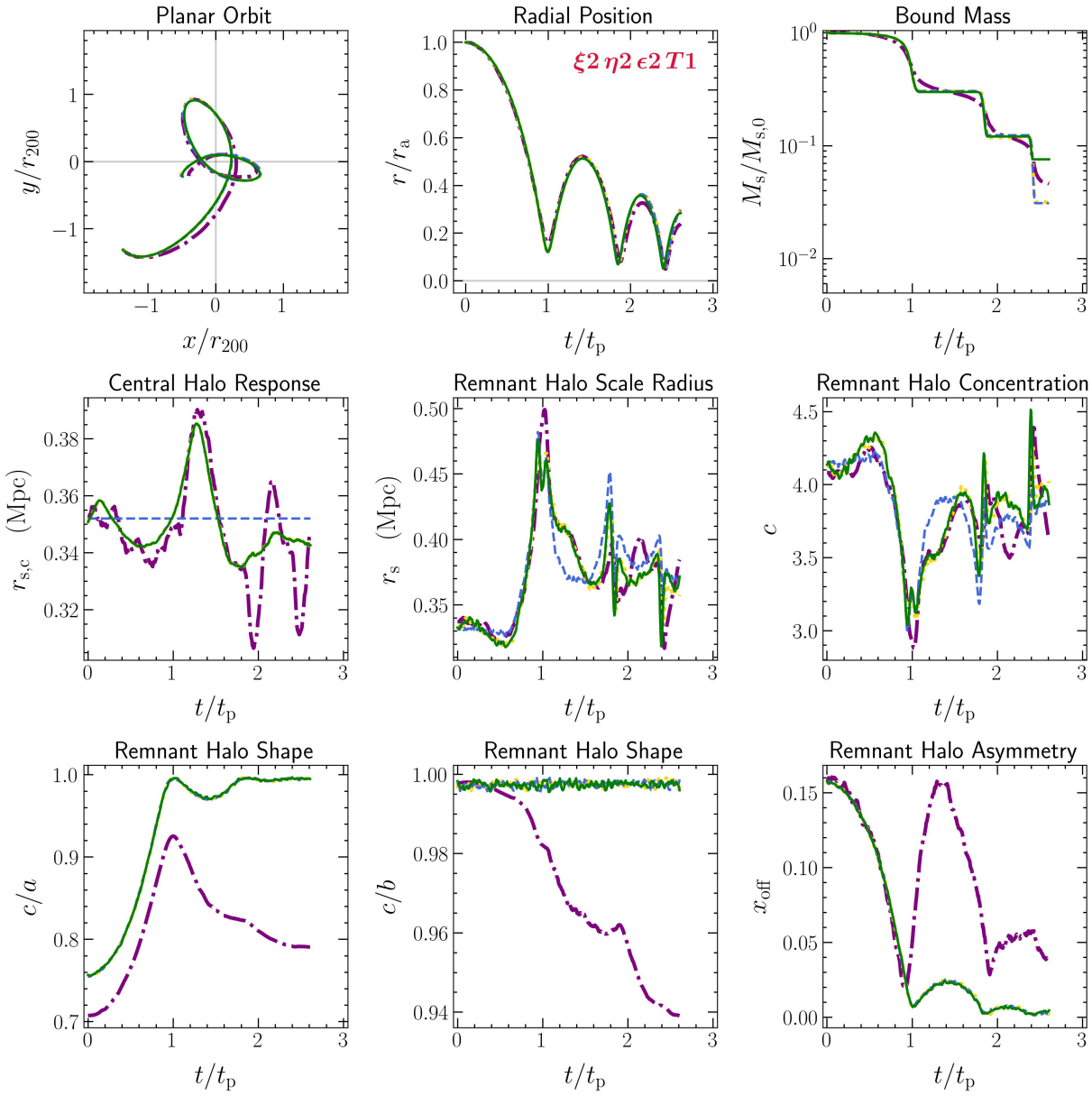



Figure B.6: Model predictions for all properties in the simulation $\xi 2\,\eta 2\,\epsilon 2\,T1$.

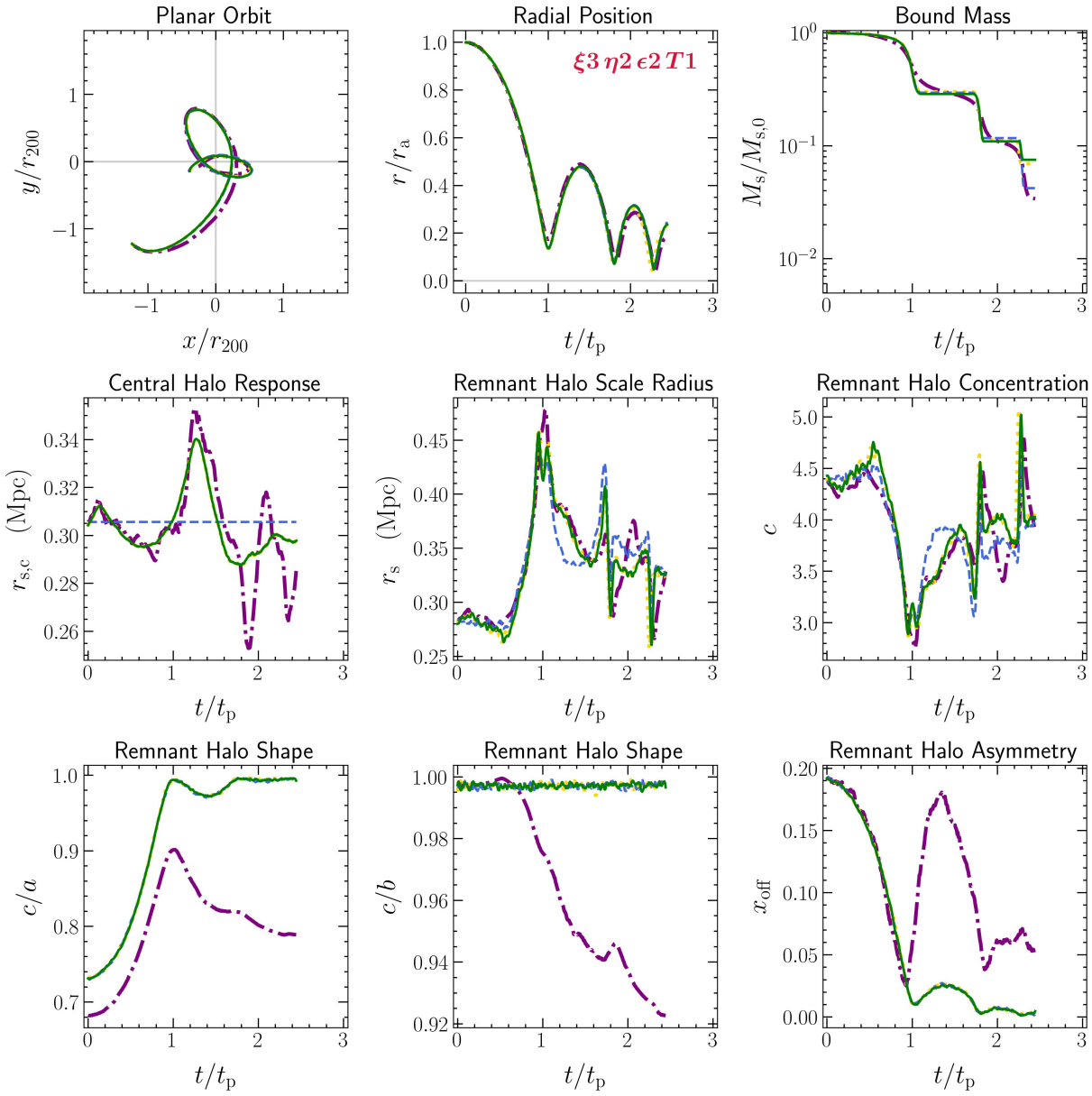



Figure B.7: Model predictions for all properties in the simulation $\xi 3\,\eta 2\,\epsilon 2\,T1$.

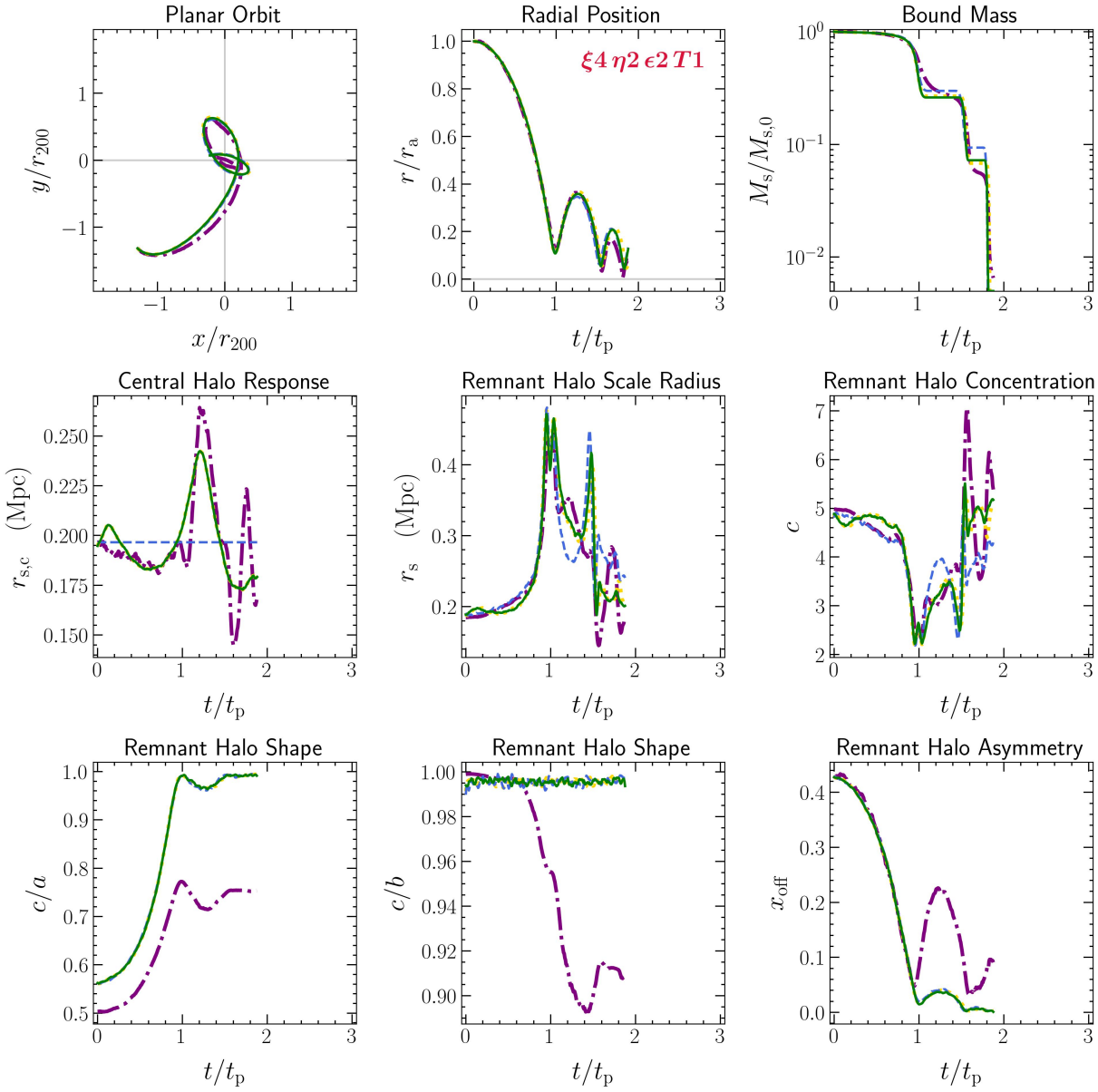



Figure B.8: Model predictions for all properties in the simulation $\xi 4\,\eta 2\,\epsilon 2\,T1$.

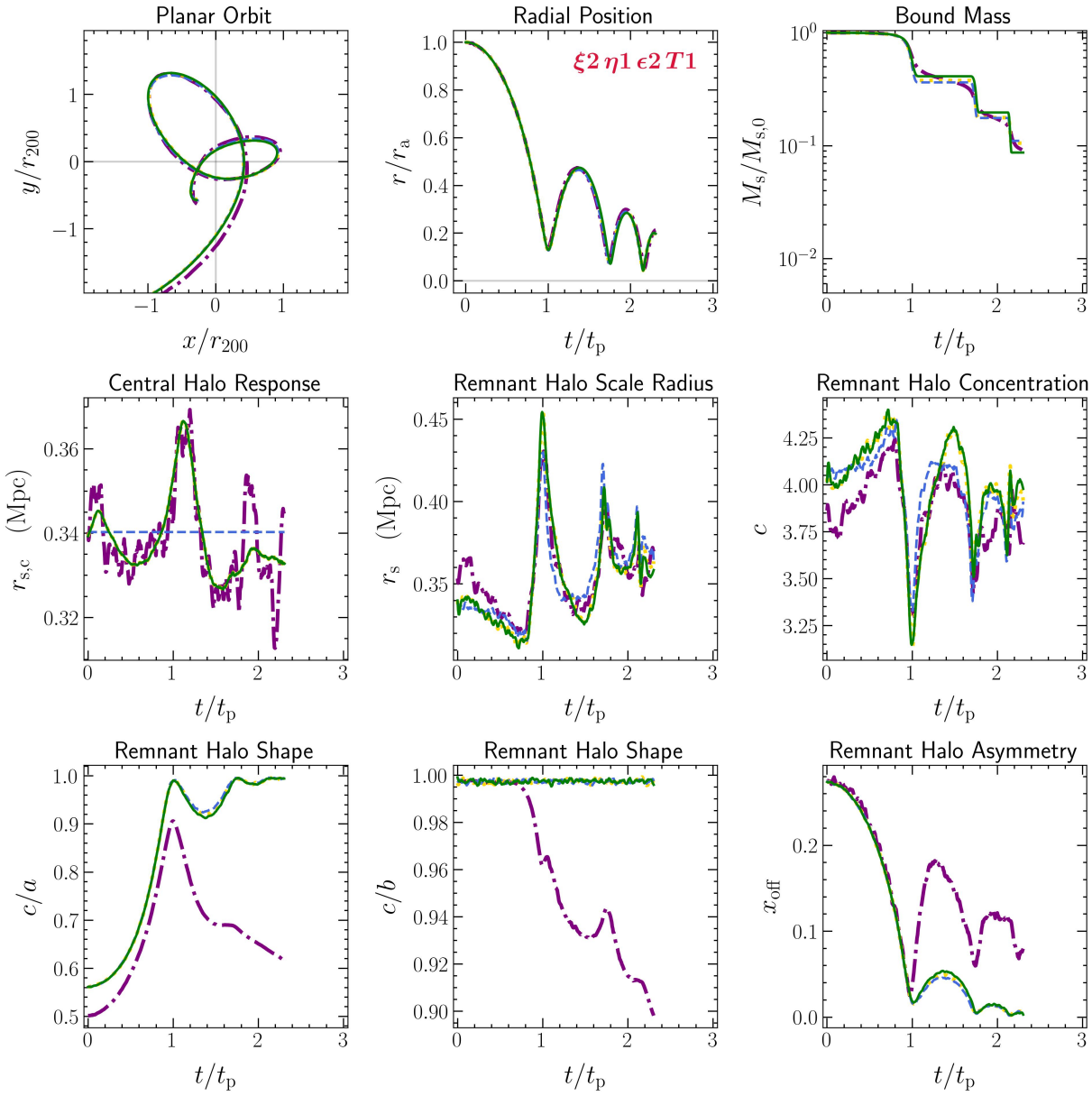



Figure B.9: Model predictions for all properties in the simulation $\xi 2\,\eta 1\,\epsilon 2\,T1$.

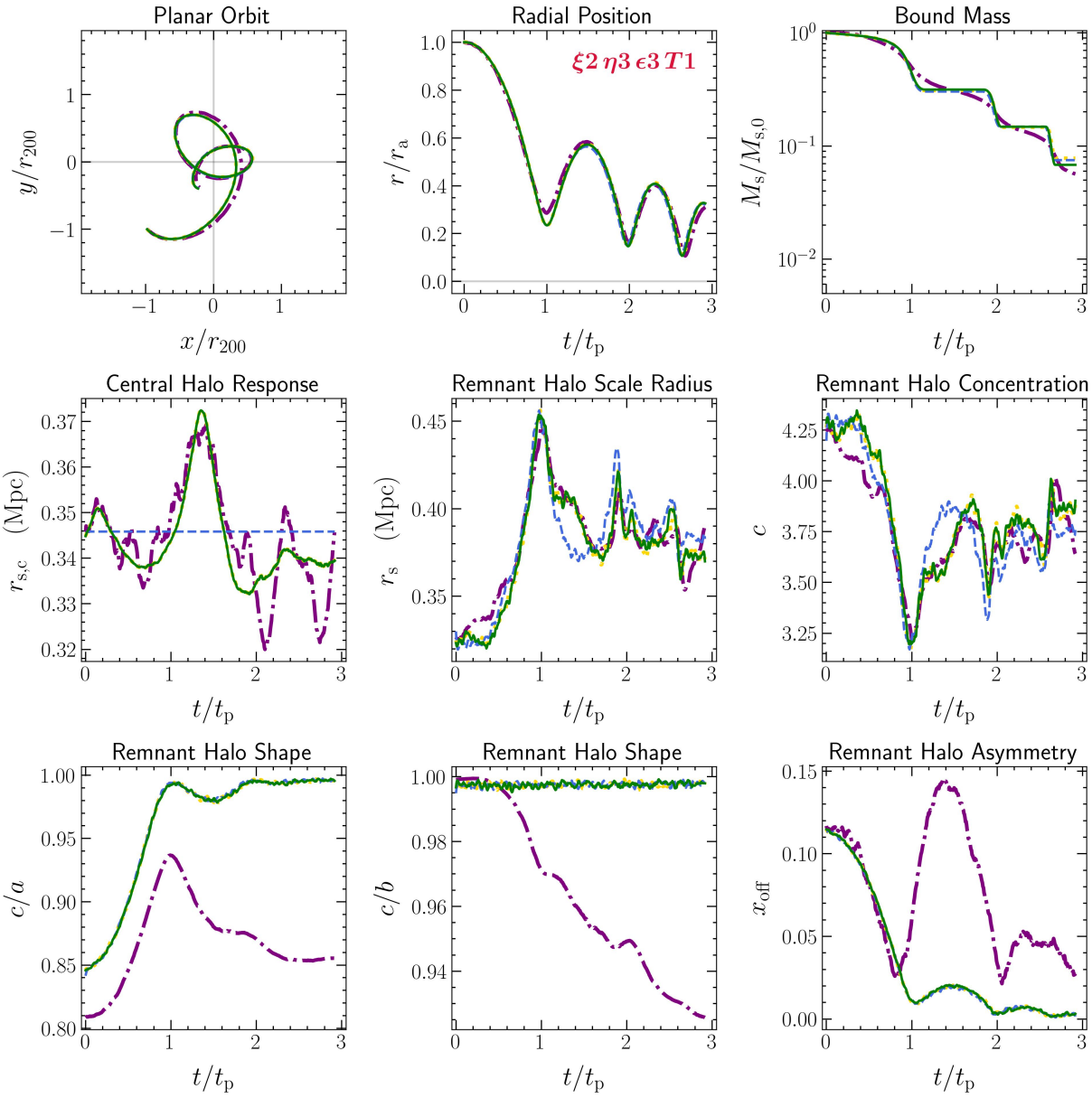



Figure B.10: Model predictions for all properties in the simulation $\xi 2\,\eta 3\,\epsilon 3\,T1$.

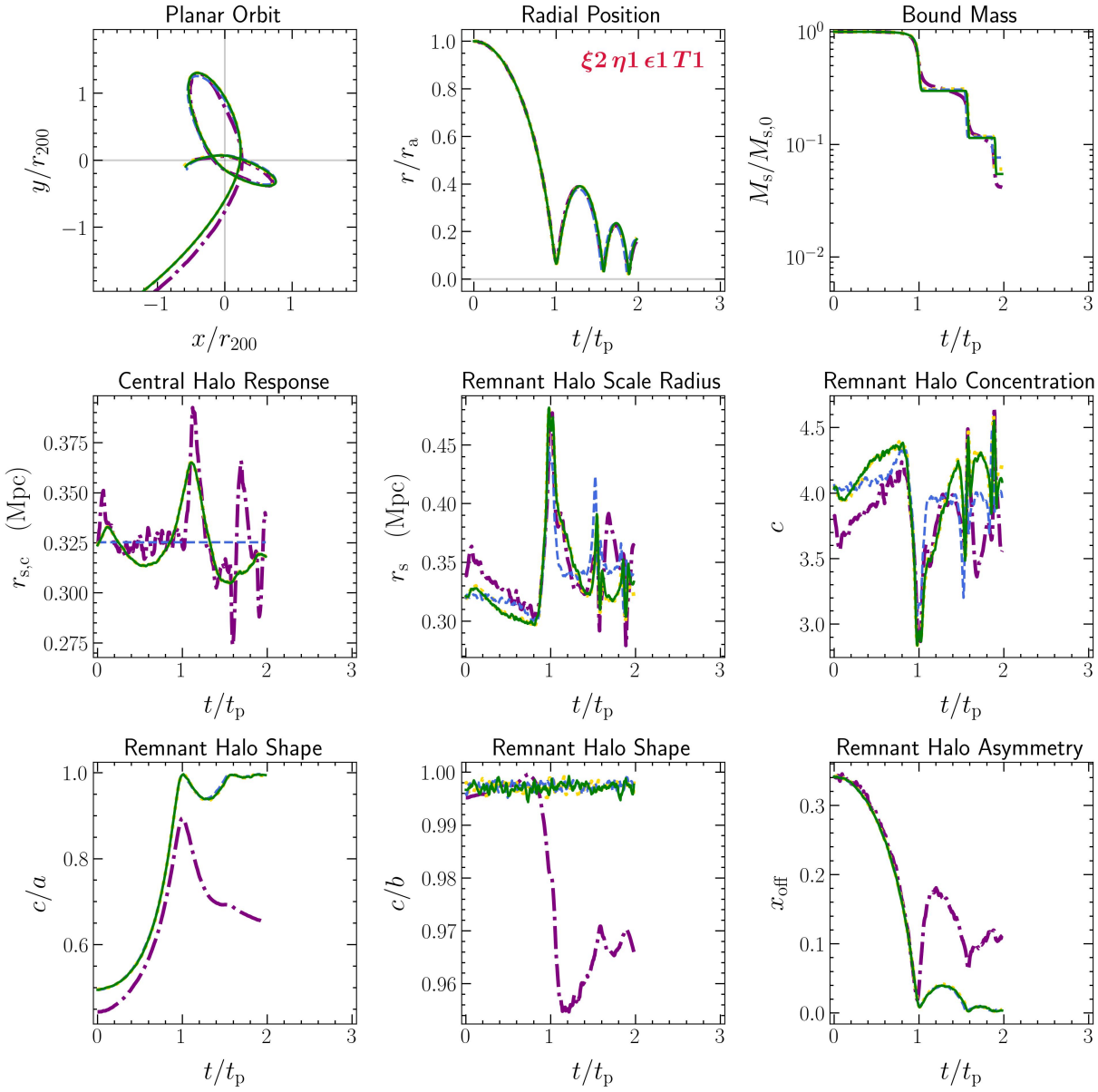



Figure B.11: Model predictions for all properties in the simulation $\xi 2\,\eta 1\,\epsilon 1\,T1$.

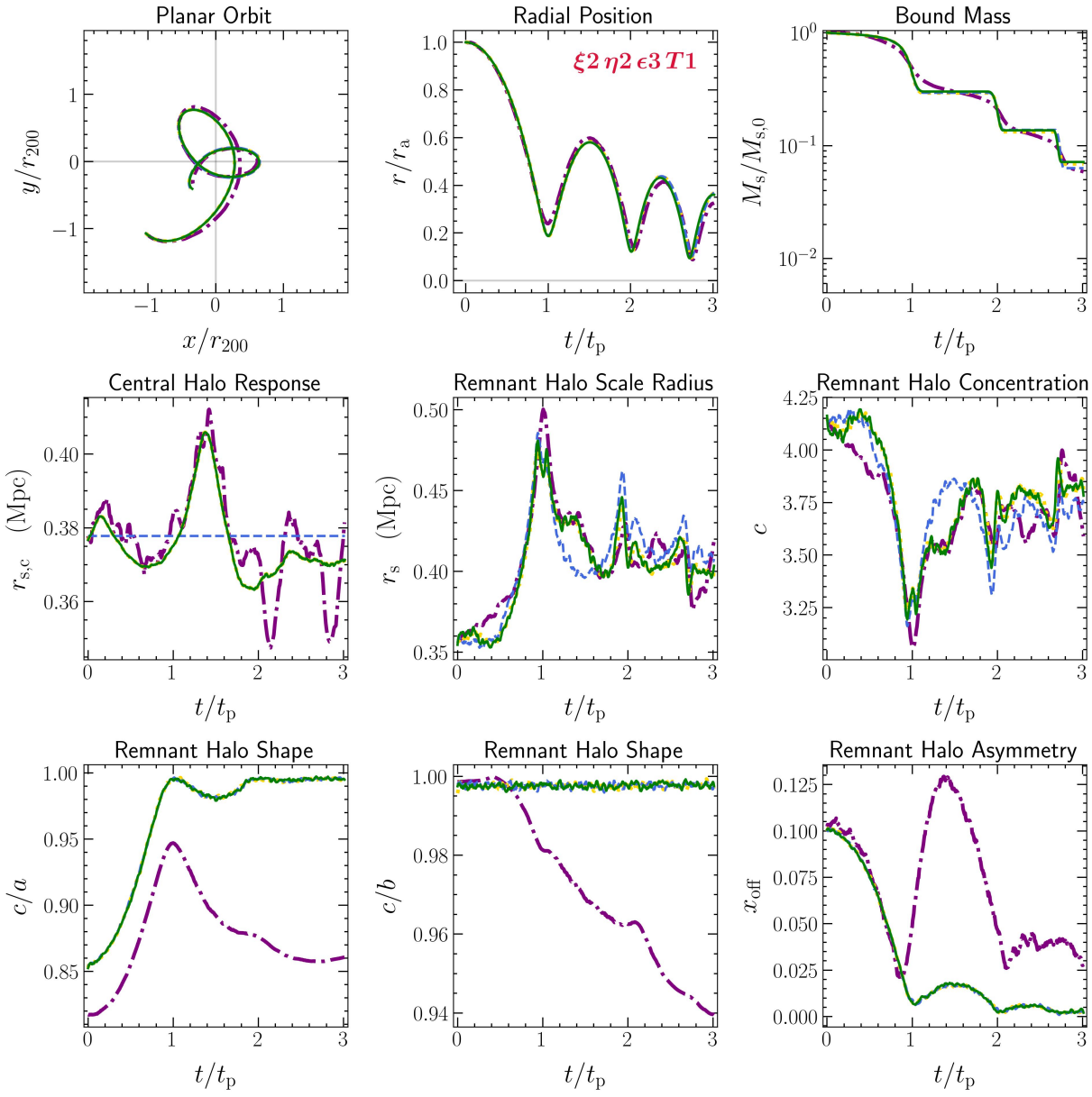



Figure B.12: Model predictions for all properties in the simulation $\xi 2\,\eta 2\,\epsilon 3\,T1$.

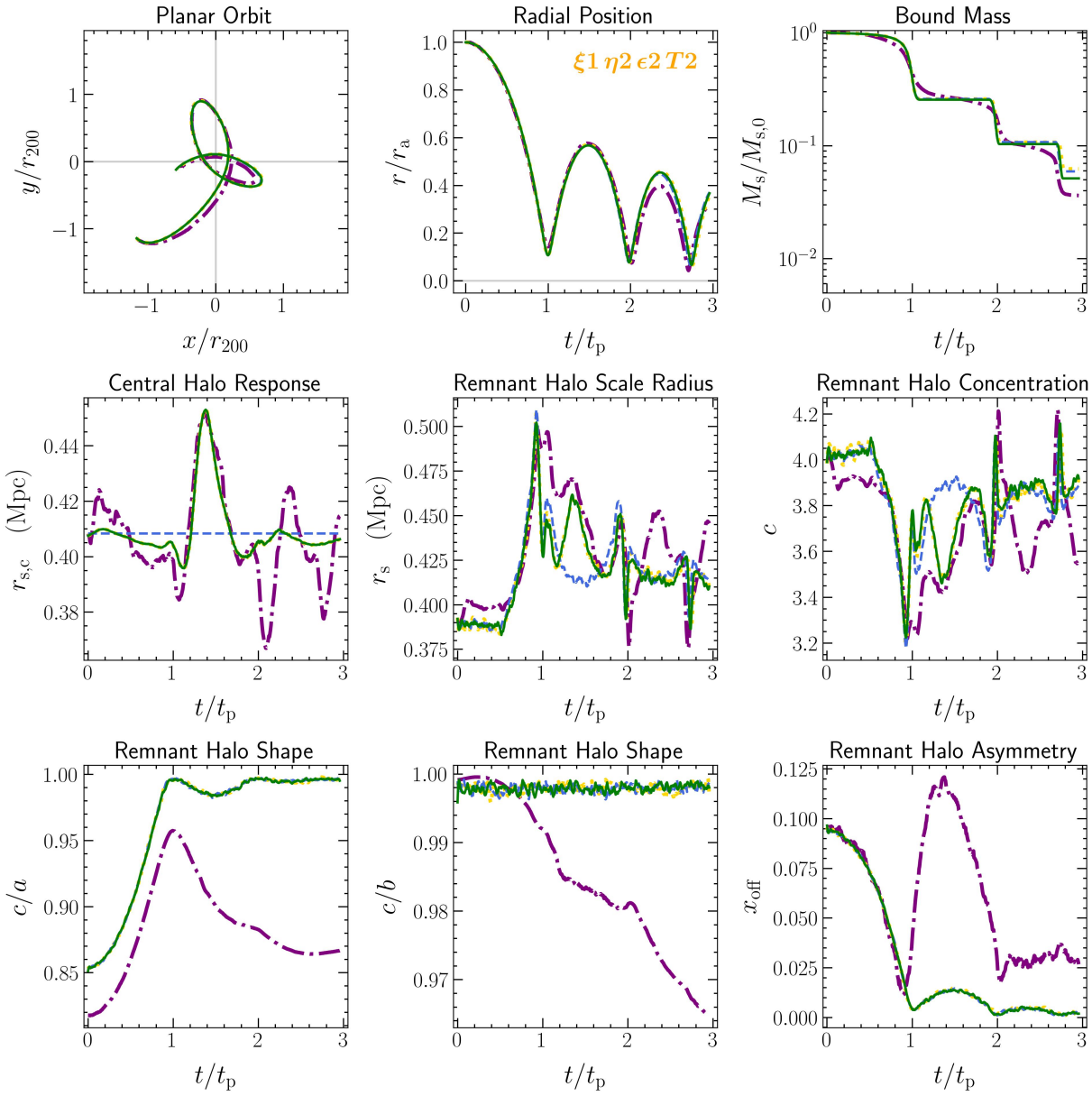



Figure B.13: Model predictions for all properties in the simulation $\xi 1\,\eta 2\,\epsilon 2\,T2$.

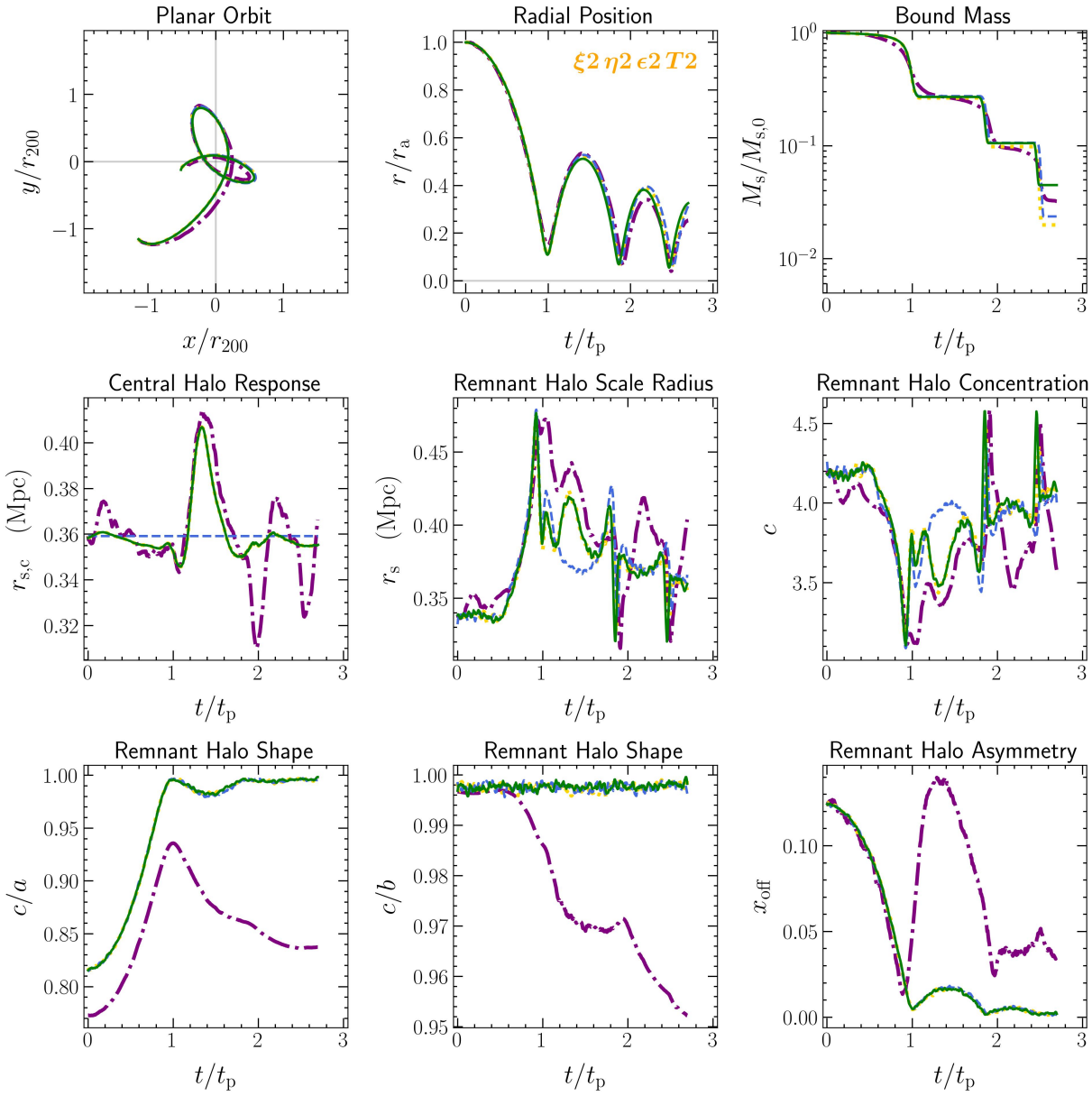



Figure B.14: Model predictions for all properties in the simulation $\xi 2\,\eta 2\,\epsilon 2\,T2$.

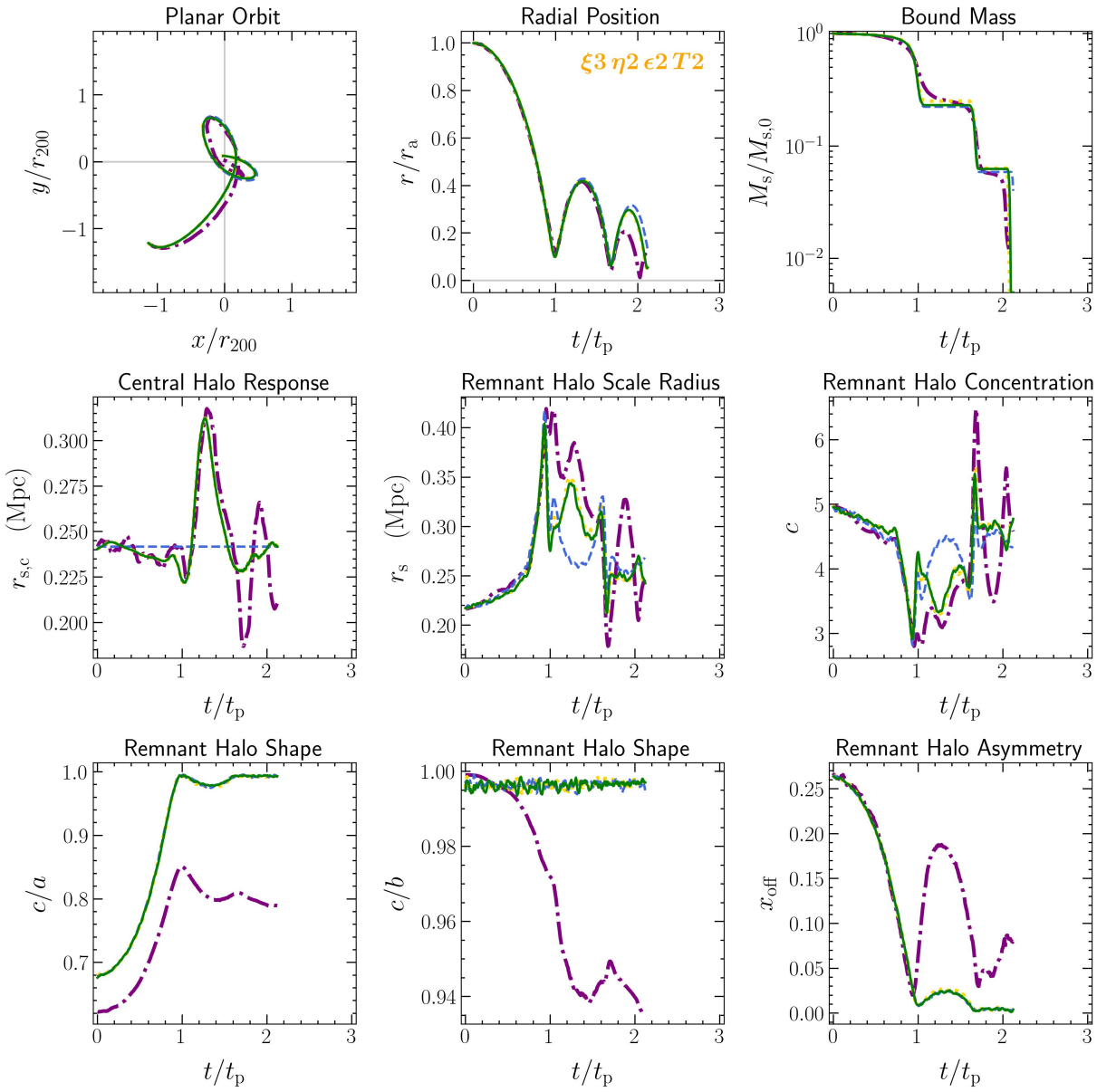



Figure B.15: Model predictions for all properties in the simulation $\xi 3\,\eta 2\,\epsilon 2\,T2$.

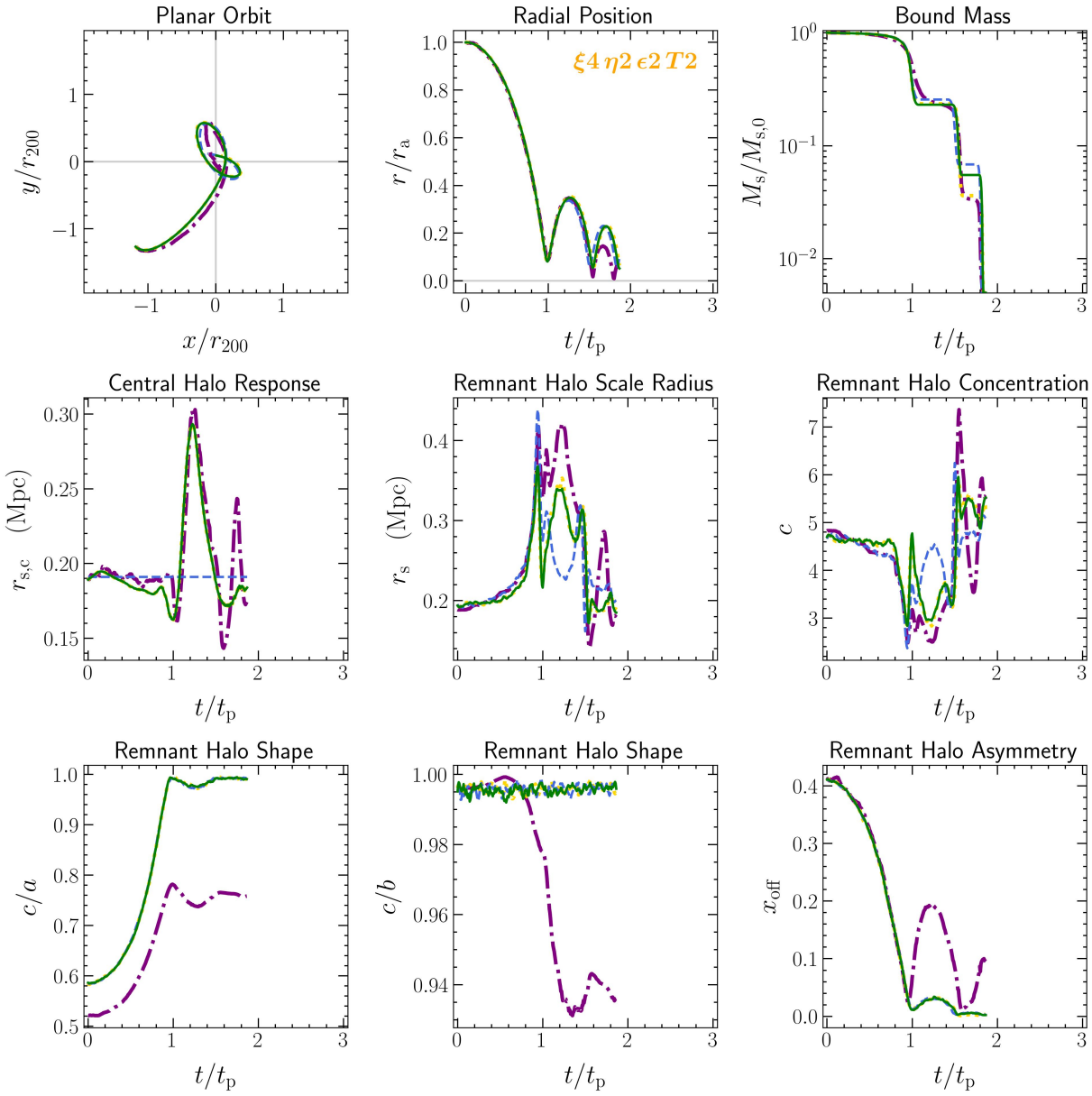



Figure B.16: Model predictions for all properties in the simulation $\xi 4\,\eta 2\,\epsilon 2\,T2$.

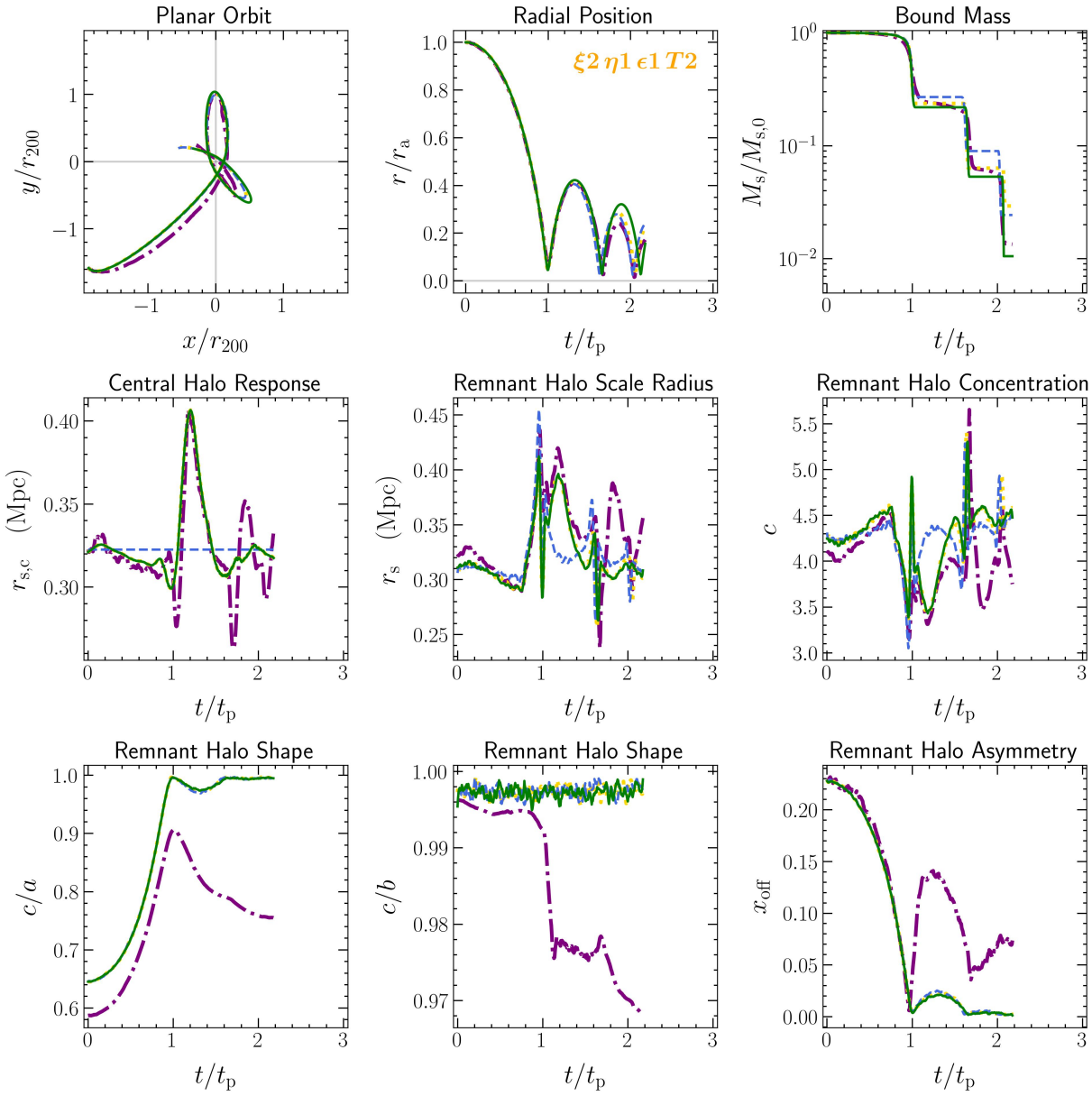



Figure B.17: Model predictions for all properties in the simulation $\xi 2\,\eta 1\,\epsilon 1\,T2$.

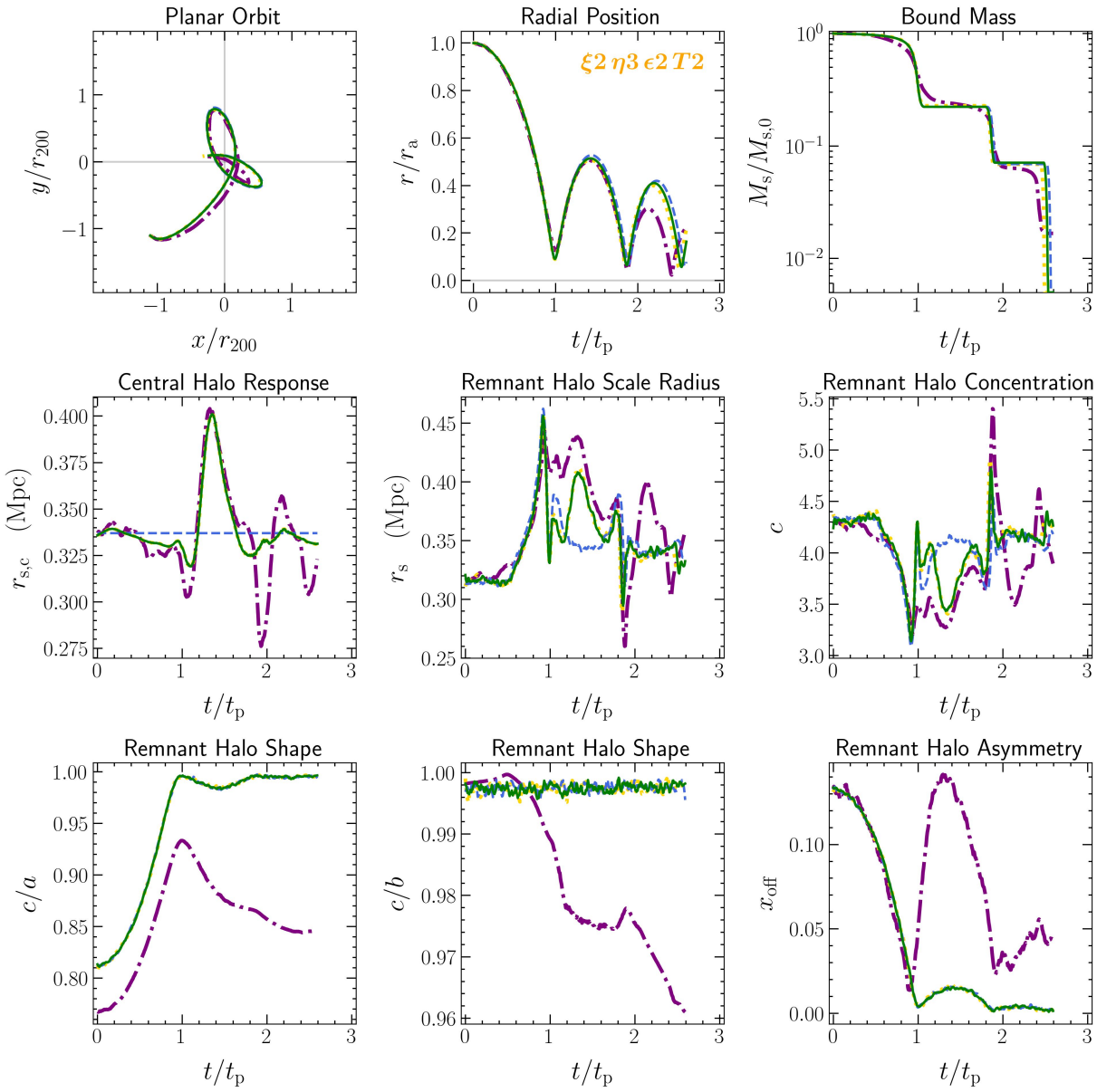



Figure B.18: Model predictions for all properties in the simulation $\xi 2\,\eta 3\,\epsilon 2\,T2$.

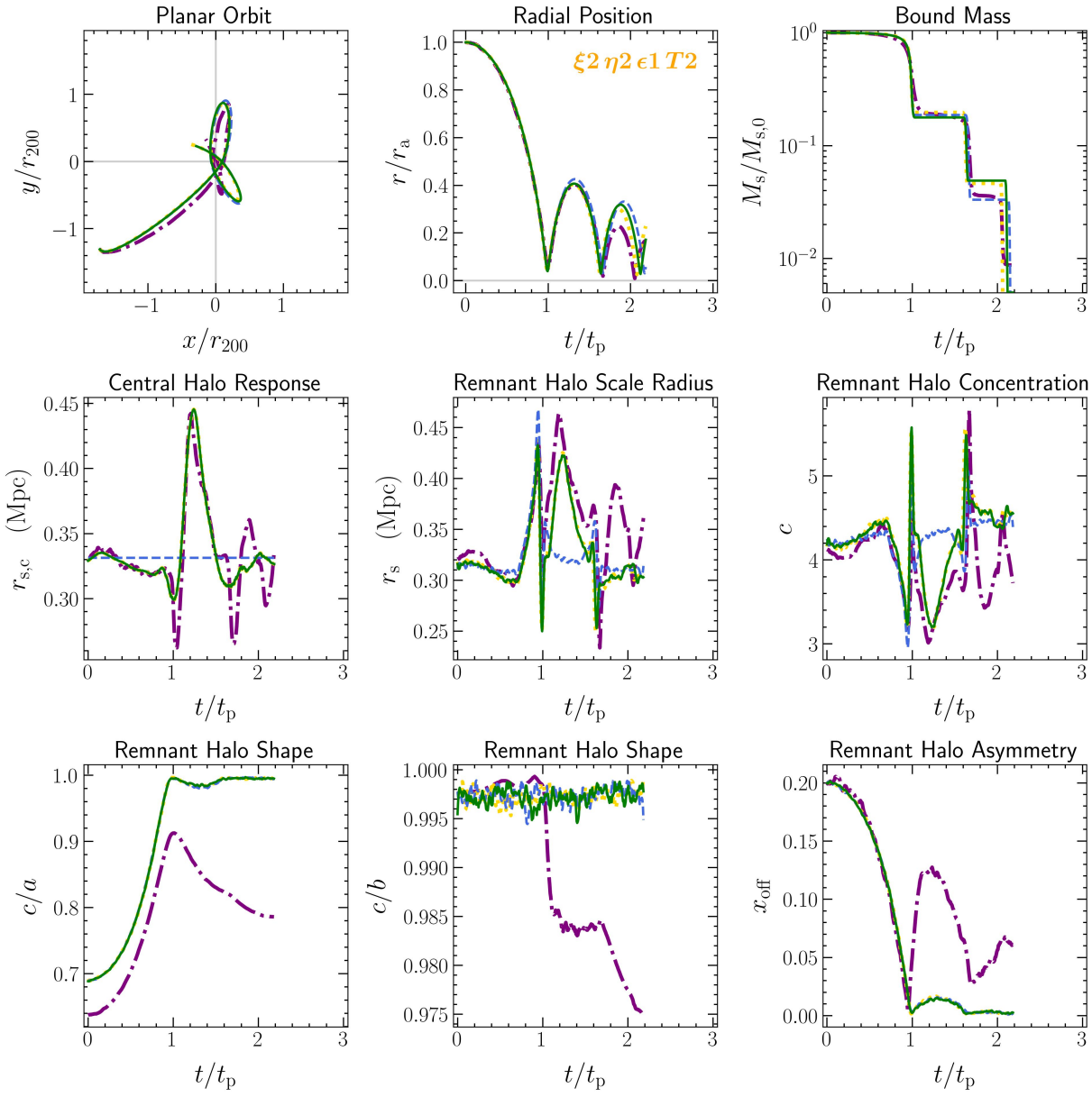



Figure B.19: Model predictions for all properties in the simulation $\xi 2\,\eta 2\,\epsilon 1\,T2$.

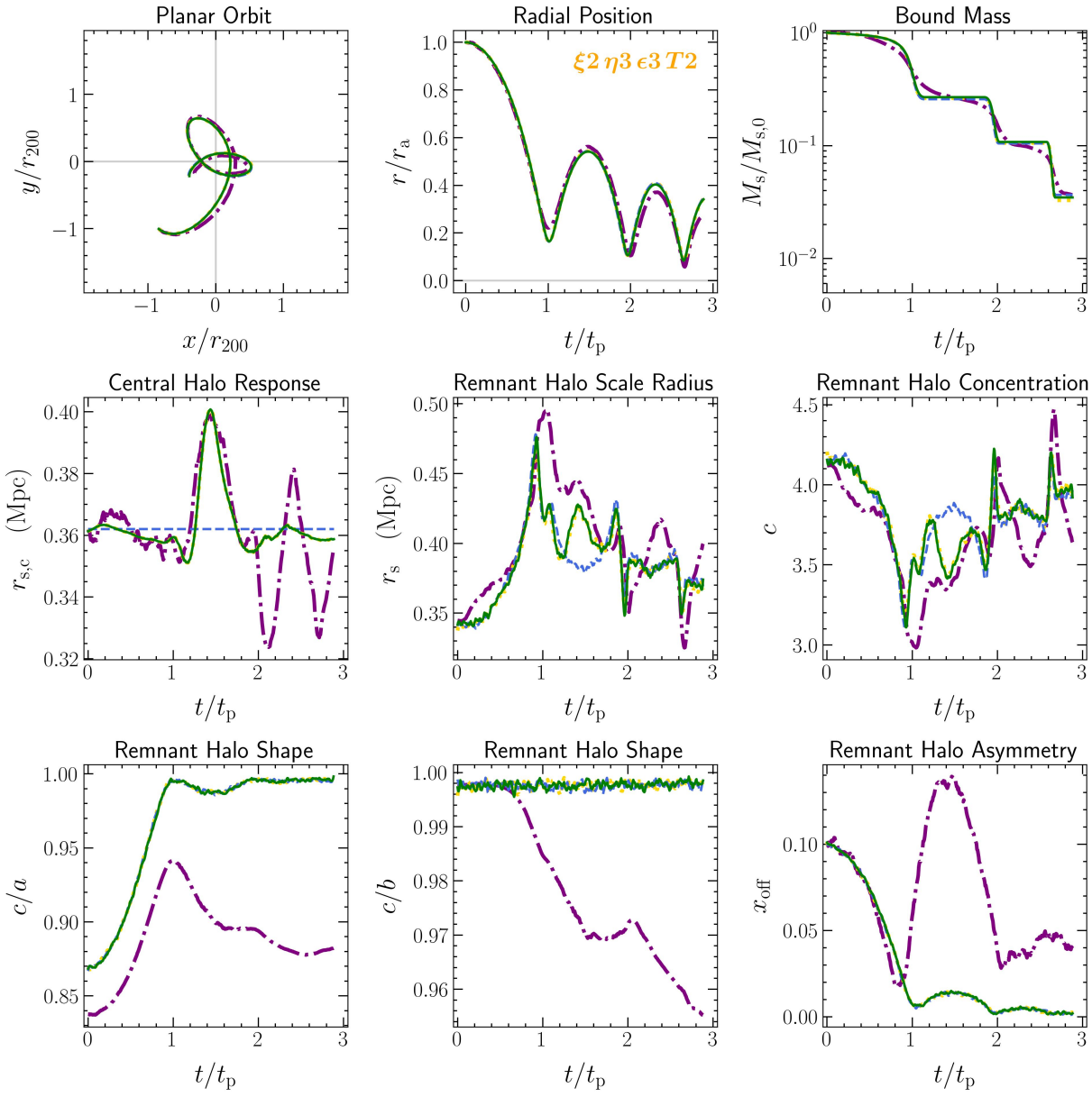



Figure B.20: Model predictions for all properties in the simulation $\xi 2\,\eta 3\,\epsilon 3\,T2$.